Polypyridinyl group VI metal complexes as catalysts for (photo)-electroconversion of CO2

Kabibi Charles Kamashanju

▶ **To cite this version:**

Kabibi Charles Kamashanju. Polypyridinyl group VI metal complexes as catalysts for (photo)-electroconversion of CO2. Other. Université Grenoble Alpes [2020-..], 2024. English. NNT : 2024GRALV001 . tel-04651642

HAL Id: tel-04651642

https://theses.hal.science/tel-04651642

Submitted on 17 Jul 2024

HAL is a multi-disciplinary open access archive for the deposit and dissemination of scientific research documents, whether they are published or not. The documents may come from teaching and research institutions in France or abroad, or from public or private research centers.

L'archive ouverte pluridisciplinaire **HAL**, est destinée au dépôt et à la diffusion de documents scientifiques de niveau recherche, publiés ou non, émanant des établissements d'enseignement et de recherche français ou étrangers, des laboratoires publics ou privés.

THÈSE

Pour obtenir le grade de

DOCTEUR DE L'UNIVERSITÉ GRENOBLE ALPES

École doctorale : CSV- Chimie et Sciences du Vivant
Spécialité : Chimie Physique Moléculaire et Structurale
Unité de recherche : Département de Chimie Moléculaire

Conversion du CO2 (photo)-électrocatalysée par les complexes polypyridinyl des métaux du groupe VI

Polypyridinyl group VI metal complexes as catalysts for (photo)-electroconversion of CO2

Présentée par :

Kabibi Charles KAMASHANJU

Direction de thèse :

Jerome CHAUVIN PROFESSEUR DES UNIVERSITES, Université Grenoble Alpes	Directeur de thèse

Rapporteurs :

Sabine SZUNERITS
PROFESSEURE DES UNIVERSITES, Université de Lille
Nicolas LE POUL
DIRECTEUR DE RECHERCHE, CNRS délégation Bretagne et Pays de la Loire

Thèse soutenue publiquement le **10 janvier 2024**, devant le jury composé de :

Jérôme CHAUVIN PROFESSEUR DES UNIVERSITES, Université Grenoble Alpes	Directeur de thèse
Sabine SZUNERITS PROFESSEURE DES UNIVERSITES, Université de Lille	Rapporteure
Nicolas LE POUL DIRECTEUR DE RECHERCHE, CNRS délégation Bretagne et Pays de la Loire	Rapporteur
Matthew MAYER DOCTEUR EN SCIENCES, Helmholtz-Zentrum Berlin	Examinateur
Cyrille TRAIN PROFESSEUR DES UNIVERSITES, Université Grenoble Alpes	Président

Acknowledgements

With an attitude of gratitude, I would like to express my sincere appreciation for people who have been there for me and with me through this chapter of my life. Like every other season of life, these past three consisted of challenging moments in the valley but also beautiful moments at the mountain tops. I have fallen, I have risen and most importantly I have learnt from it all. And indeed, I have been blessed to go through this journey with a number of people who have stayed committed to this course alongside me.

To my thesis director Jérôme Chauvin, thank you for being a kind supervisor for these past three years and a good teacher for the past five years. Thank you for the support and guidance that you have offered me every step of the way. Your advice, patience and presence for these past years have allowed me to learn and acquire competences and skills necessary for the successful completion of this thesis.

I would also like to express my sincere gratitude to Sabine Szunerits and Nicolas Le Poul for taking time to carefully review the quality of my thesis and for participating in the final defense of my work. Likewise, I would like thank Matthew Mayer and Cyrille Train for examining my thesis work and partaking in the final defense of my work. Furthermore, I would like to acknowledge Vincent Maurel, Bertrand Reuillard and Fabien Giroud for their support and for the discussions we have had in the past three years as members of my thesis follow-up committee.

A particular mention has to go to Florian Molton, who has been very helpful in the lab. For all the technical difficulties solved and the patience of helping me out in different experiments, I want to say thank you. Additionally, I would like to thank Fabrice Thomas for his effort in helping me with the DFT calculations that were necessary to finish this work. To Frederic Loiseau, Marcello Gennari, Damien Jouvenot and Nick Vlachopoulos, I appreciate you taking the time to assist me with the preparation of my final defense presentation.

During my time in the lab, I have come across different people who have offered their assistance to me in one way or another, I thank you all for your assistance and kindness. To Rana, Irene, Lorna, Lili, Guanqi and Leticia, thank you for being good friends who have been present for the past years. Largely, I would like to thank the whole DCM team and also acknowledge the ANR for funding this project for the past three years.

Special thanks to my parents (Amina Kabale and Charles Kamashanju) who have been the great source of inspiration and support ever since I was born. Thank you so much for loving me, praying for me and giving me the best of what life has to offer. To my siblings (Kevin, Irene and Ruge), thank you for amazing siblings who make sure I do not miss out on all that is happening back at home. To my Schatz Victor, thank you for being supportive and understanding every step of the way. To my dear friends (Grace, Sarah, Belinda, Celia), thank you for cheering me on during this chapter of my life. Lastly and very importantly, I want to express my deepest gratitude to the Almighty God for being the lamp that guides me and the light for my path in these past years. Thank you for being my ever-present and perfect source of strength in my moments of weakness. I am grateful that you have bestowed upon me the grace to complete this PhD degree successfully.

Table of contents

List of abbreviations

Bpy: 2,2'-bipyridine

BIH: 1,3-dimethyl-2-phenyl-2,3-dihydro-1H-benzo[d]imidazole

Cat: Catalyst

CB: Conduction Band

CE: Counter Electrode

CO2R: Carbon dioxide Reduction

CV: Cyclic Voltammogram

SD: Sacrificial Electron Donor

DMF: 2,5-dimethylfuran

DFT: Density Functional Theory

EPR: Electron Paramagnetic Resonance

FT-IR: Fourier transformed Infrared

FTO: Fluorine-doped Tin Oxide

GC: Gas Chromatography

HOMO: Highest Occupied Molecular Orbital

IC: Ionic Chromatography

IP: Ionization potential

Ipy: Imidazole pyridine

LC: Ligand-Centered

LUMO: Lowest Unoccupied Molecular Orbital

MC: Metal-Centered

MO: Molecular Orbital

MLCT: Metal-to-Ligand Charge Transfer

MS: Mass Spectroscopy

NHE: Normal Hydrogen Electrode

NMR: Nuclear Magnetic Resonance

PEC: Photoelectrochemical

PCET: Proton-Coupled Electron Transfer

PS: Photosensitizer

Qpy: Quaterpyridine ligand

RE: Reference Electrode

RT: Room Temperature

SSCE: Saturated Sodium Calomel Electrode

$TBAPF_6$: tetrabutylammonium hexafluorophosphate

TEA: Triethylamine

TEOA: Triethanolamine

TEM : Transmission Electron Microscopy

UV-vis : Ultraviolet-visible

VB: Valence Band

WE: Working Electrode

General context

From an increase in consumption of fossil fuels, emission of greenhouse gases such as CO_2 has led to a considerable climatic change. Numerous research works are being conducted towards converting CO_2 into more valuable small carbon-based products such as CO, HCOOH, CH_4; which in turn could be utilized as raw materials in industries. Parallel to this climate challenge, the transition from the use of fossil fuels to the use of renewable energy has brought forth a need to develop sustainable energy storage systems due to the intermittent nature of most renewable energy sources.

In such a context, I was enrolled in a European research project namely Hybrid Interfaces for Photoelectrochemical CO_2 conversion (HYPEC) entailing the use of photoelectrochemical (PEC) carbon dioxide reduction (CO2R) process as a solution to both challenges. By employing this PEC-CO2R process, an electrochemical conversion of CO_2 into chemical fuels using solar energy as the driving force could be achieved while realizing energy storage through the conversion of solar energy into chemical energy. This broad project suggested a systematic investigation of molecular inorganic catalysts incorporated with inorganic semiconductor photoelectrodes. The focus of this investigation centered on improving the fundamental understanding of how interfacial effects influence CO2R reactivity; and exploiting that knowledge to design devices that can perform an efficient solar-driven conversion of CO_2 to valuable synthetic fuel using Earth-abundant and scalable materials.

The HYPEC project gathers a consortium of expertise in inorganic redox electrochemistry, semiconductor photoelectrochemistry, and semiconductor materials physics constituted of four research institutions: Helmholtz-Zentrum Berlin (HZB), École Polytechnique Fédérale de Lausanne (EPFL) together with Uppsala university and University of Grenoble Alpes (Department of Molecular Chemistry).

My work in the Department of Molecular Chemistry (DCM) was mainly dedicated to the development and characterization of molecular inorganic complexes as catalysts for CO_2 reduction. In this work, the use of group VI metal complexes has been advocated given the abundance of their metal centers.

This manuscript is divided into four chapters;

- Chapter **I** describes the general context of this study and presents two major challenges faced worldwide, i.e. global warming and lack of sustainable energy as a result of a continuous increase of greenhouse gas emissions. With CO_2 being one of the major contributing gases, efforts have been implemented towards CO_2 capture and utilization. On a fundamental level, a catalytic conversion of CO_2 to value-added carbon products using molecular catalysts has been one of the most investigated approach as inspired by nature, i.e. photosynthesis. A review of some relevant catalysts for this study is depicted.
- Chapter **II** presents a family of bipyridyl tetracarbonyl complexes $[M(bpy)(CO)_4]$ (with M= Cr, Mo, W and bpy = 2,2'-bipyridine ligand) that has been investigated for its electrochemical properties in CO_2 saturated environments. As an attempt to lower the energy input for CO_2 conversion, a new family of anionic complexes $[M(bpy)(CO)_3X]^-$ (X=halide ligand) was developed and investigated for their catalytic properties.
- Chapter **III** introduces another tetracarbonyl family $[M(Ipy)(CO)_4]$ with a different diimine ligand (Ipy= imidazole pyridine ligand). This family was investigated mainly due to its specific photophysical properties that could be useful in achieving photocatalysis of CO_2 under light irradiation. A complex of this family was associated with a cuprous oxide photocathode ($Cu_2O/Ga_2O_3/TiO_2$).
- Chapter **IV** is based on the development of a different type of metal complex $[Cr(qpy)(Cl)_2]Cl.4H_2O$ with a tetradentate ligand (qpy = quaterpyridine). This complex of chromium with a high oxidation state (+3) was notably associated in a photocatalytic cycle and studied in the presence of p-type photocathode ($Cu_2O/Ga_2O_3/TiO_2$) as a working electrode to research on the photoelectrocatalysis of CO_2.

This research work develops conclusive studies and some novel findings on group VI metal complexes, which can pave way to a better understanding of CO_2 reduction using these abundant metal centers. By further integrating these metal complexes with semiconductors, a design of photochemical devices capable of conducting a solar-driven conversion of CO_2 into valuable synthetic fuel looks promising.

CHAPTER I. VALORIZATION OF CO_2 USING METAL COMPLEXES

1. Introduction

Ever since the industrial era, the world has mainly depended on the use of fossil fuels as a source of energy and as raw materials for several industrial products, which has eventually led to several challenges. Firstly, with the reserves of fossil fuels being finite there is a risk of depletion. Secondly, the combustion of these fossil fuels has led to a considerable rise of atmospheric carbon dioxide levels.[1]

The accumulation of CO_2 as well as other greenhouse gases has led to some serious greenhouse effects such as ocean acidification, polar ice melting, droughts, hurricanes; all these events occurring as a result of climate change. Associated with the greenhouse effect, the average global temperature of Earth has risen causing global warming. Inevitable changes in the thermal structure of the atmosphere, and of the Earth's solid surface, are causing the temperatures of the planet's waters to rise and their volume to increase, to a point where the rising water levels on the Earth's surface are seen as a major problem, especially in coastal areas.[2]

A closer look into greenhouse gas emissions as reported in the Emissions Database for Global Atmospheric Research (EDGAR)[3] indicated a decrease in the global emissions by 3.7% in 2020 compared to 2019 levels as a result of the COVID-19 pandemic. However, this decrease was nullified soon after the pandemic with global GHG emissions reaching the level of 53.8 Gt CO_2eq in 2022, which is 2.3% higher than 2019 and 1.4% higher than 2021. A report on worldwide greenhouse gas emissions by sector was reported by EDGAR as indicated in **Figure I.1.**

Figure I. 1 Greenhouse gas emissions in different sectors worldwide.[3]

Based on climate modelling study,[4] it has been shown that this climate change will have a long-lasting effect due to a continuous increase of greenhouse gases in the atmosphere as a result of energy consumption and anthropogenic activities due population growth. In addressing this challenge, the 2015 United Nations Climate Change Conference in Paris led to the drawing of the Paris Agreement.[5] This legally binding international treaty focuses on combating climate change by limiting the global temperature rise to 1.5°C through declining 43% of greenhouse gas emissions by 2030.

In lieu of searching for one idealistic technology that can single handedly provide a definite solution to minimizing atmospheric CO_2 emissions, a correct blend of technologies could be identified in achieving the most affordable and effective solution towards mitigating CO_2 emissions. Such a strategy employs different technologies that include the use of non-carbon-based fuels such as nuclear energy, implementation of carbon dioxide capture and storage, use of integrated gasification combined cycle (IGCC), use of perennial and renewable energy sources and CO_2 utilization. The accomplishment of energy sustainability is also made more attainable by effectively allocating the use of these technologies toward various energy needs in accordance with the various intensities of energy required (i.e., energy density).[2]

With the steady increase of worldwide energy demand, fossil fuels accounts for 81% of total energy consumption in 2022.[6] The use of nuclear and renewable energy (solar, wind and hydro power) are of necessity as they play an important role in compensating the decline of fossil fuels consumption. As the cheapest power option in most parts of the world, the use of renewable energy sources has become more interesting. Cheap electricity from renewable sources could provide 65% of the world's total electricity supply by 2030. It could decarbonize 90 percent of the power sector by 2050, massively cutting carbon emissions and helping to mitigate climate change.[7]

However, the intermittency of these renewable energy sources makes energy storage an immediate challenge. Plus, these energy sources do not provide combustible fuels for use in the transport sector, in particular aviation and heavy freight over long-distances, nor feedstock chemicals for making plastics, rubbers, fertilizers, and pharmaceuticals. New approaches are therefore needed to provide sustainable resources for fuels and commodity production.[8]

With carbon dioxide being the ultimate source of fossil fuels that can exist as gases, liquids, and solids, there is a possibility of utilizing CO_2 as a safe, cheap and abundant chemical feedstock for a variety of industrial applications. The different existing forms of fuel offer a possibility of selecting a form most suitable for a particular application. This flexibility in fuel choice will be beneficial for the foreseeable future.[9]

In nature, the process that drives carbon fixation into fuel is photosynthesis, the biological conversion of sunlight, water, and carbon dioxide into reduced organic materials. This process plays a major role in controlling land-atmosphere CO_2 exchange, providing the capacity of terrestrial ecosystems to partly offset anthropogenic CO_2 emissions. Moreover, this process provides an attractive solution for storing the tremendous amount of sunlight energy falling on earth.

In this context, natural photosynthesis is a great source of inspiration for the scientific community. With this inspiration, the carbon fixation process has paved way for industrial utilization of CO_2 through technological, chemical, or enhanced biological methods that may lead to the decline of CO_2 emissions.[10]

By developing efficient technologies capable of converting CO_2 into fuels and different usable products, the results of these technologies will close the cycle of carbon and demonstrate a significant step towards chemical and energy production with minimum to zero carbon-emission level. But in achieving this, there is a need to ensure that the technology implemented is cost effective in terms of energy and materials used plus environmentally friendly.

2. Utilization of CO_2

2.1. Reactivity of CO_2

Carbon dioxide is a non-polar, linear molecule composed of a very short C=O bond distance of 1.16 Å that possesses a high dissociation energy of ~750 kJ.mol^{-1}, hence thermodynamically stable. Despite being non-polar, CO_2 contains polar bonds due to the difference in electronegativity between the carbon and the oxygen. Its electronic structure is best represented as $O^{-\delta}$–$C^{+2\delta}$–$O^{-\delta}$, highlighting its susceptibility to nucleophilic attack on the carbon and electrophilic attack on the oxygen, often discussed in terms of its quadrupole moment.[9]

For the discussion of different electroreduction pathways of CO_2 reduction, it is worthwhile to start with a consideration of its molecular properties and coordination chemistry. As shown in **Figure I.2**, CO_2 is a $16e^-$ molecule with a linear equilibrium structure in its electronic ground state, therefore belonging to the $D_{\infty h}$ symmetry group.[11]

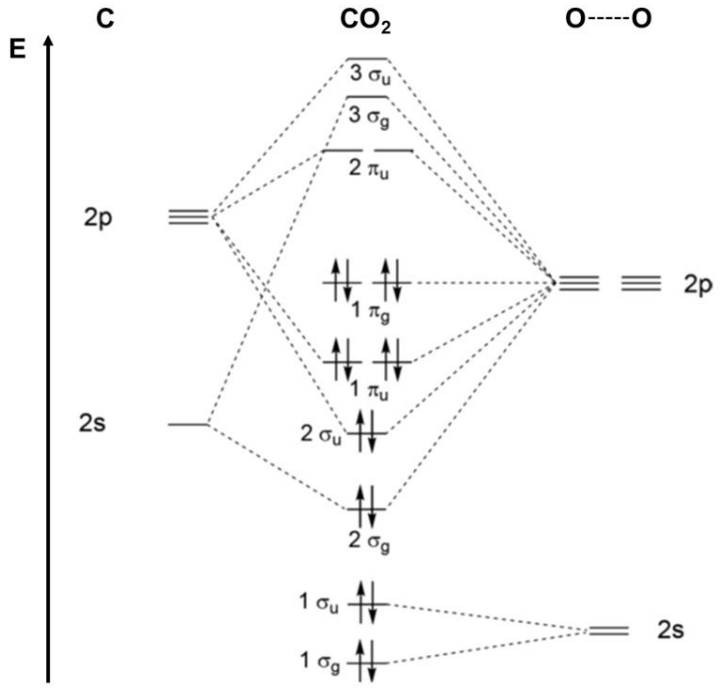

Figure I. 2 Molecular orbital (MO) diagram of carbon dioxide

The molecular orbitals with the highest relevance to the reactivity are the $1\pi_g$ and $2\pi_u$ orbitals, which play the role of HOMO and LUMO, respectively. The doubly occupied nonbonding $1\pi_g$ MOs are mainly localized at the terminal oxygen atoms, whereas the empty antibonding $2\pi_u$ orbitals are mostly centered on the carbon atom. Hence, the electronic transition between the two states occurs with a low extinction coefficient (**ε**) and in the deep UV-C around 100 nm causing the molecule to have no photoreactivity.

Despite CO_2 being an amphoteric molecule where the oxygen atoms display a Lewis basic character and the carbon atom behaves as a Lewis acid center. With a slightly negative electron affinity (E_a) of about −0.6 eV[12] and a first ionization potential (IP) of about 13.8 eV,[13] carbon dioxide is a better electron acceptor than donor and the reactivity of the molecule is dominated by the electrophilic character of the carbon atom rather than the weak nucleophilic properties of the oxygen atoms.

With carbon in the CO_2 at its highest possible oxidation state (+IV), this electrophilic character of CO_2 can result into the reducing of the oxidation state of carbon in CO_2 towards a large variety of products with different carbon oxidation states ranging from CO (+II) to higher hydrocarbons in the gaseous phase CH_4 (-IV), as well as various oxygenates in the liquid phase such as CH_3OH and HCOOH.[14-16] **Figure I. 3** summarizes the reduction routes of CO_2 towards various products at the surface of an electrode.

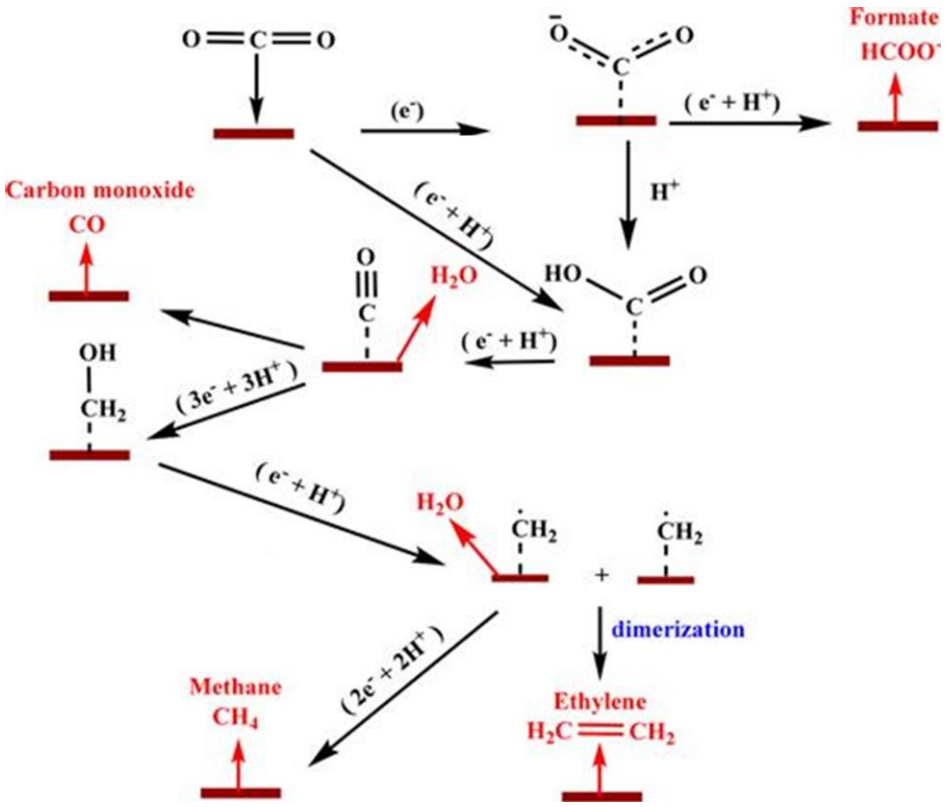

Figure I. 3 Hypothesized mechanisms for formation of some products of CO_2 reduction: HCOOH, CO, CH_4 and C_2H_4.[17]

2.2. Electrochemical reduction of CO_2

Electrochemical reduction of CO_2 towards the formation of value-added carbon-based products involves an "activation of CO_2" step, which entails the LUMO orbitals of CO_2 being filled via an electron transfer, resulting to a lowest energy state corresponding to a bent geometry of CO_2 radical.

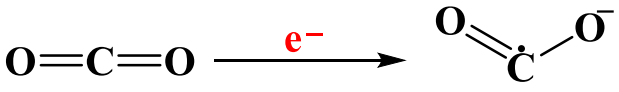

However, this activation step requires a significant amount of energy input for the large structural rearrangement of the linear CO_2 to a bent $CO_2^{\bullet-}$ radical through cleavage of the C=O bond.[9] This energy cost is demonstrated by a high thermodynamic barrier and a competitive potential energy as presented in **Table I. 1**. These energetic requirements for CO_2 reduction are usually dependent on the pH and the number of electrons associated in the half-reactions as shown below. (**Table I. 1**)

Table I. 1 Standard potential values of chemical products from proton assisted CO_2 reduction.[14]

	Electrochemical half reaction	Standard potential, E°[V] (vs SHE at pH=7)
$CO_2^{\bullet-}$ radical	$CO_2 + e^- \rightarrow CO_2^{\bullet-}$	-1.90
Oxalic acid	$2CO_2 + 2H^+ + 2e^- \rightarrow C_2H_2O_4$	-0.89
Formic acid	$CO_2 + 2H^+ + 2e^- \rightarrow HCOOH$	-0.61
Carbon monoxide	$CO_2 + 2H^+ + 2e^- \rightarrow CO + H_2O$	-0.53
Formaldehyde	$CO_2 + 4H^+ + 4e^- \rightarrow H_2CO + H_2O$	-0.48
Methanol	$CO_2 + 6H^+ + 6e^- \rightarrow CH_3OH + H_2O$	-0.38
Ethanol	$2CO_2 + 12H^+ + 12e^- \rightarrow C_2H_5OH + 3H_2O$	-0.33
Methane	$CO_2 + 8H^+ + 8e^- \rightarrow CH_4 + 2H_2O$	-0.24
Hydrogen	$2H^+ + 2e^- \rightarrow H_2$	-0.42

As indicated in **Table I. 1**, the $CO_2/CO_2^{\bullet-}$ has a standard potential of -1.9 vs NHE which makes the $CO_2^{\bullet-}$ formation, a rate determining step for the CO_2 reduction process. Then, a series of proton-coupled two-electron transfer processes (PCET) will follow, leading to a formation of different products, such as HCOOH, CO, CH_4 and CH_3OH. In the same potential range, H_2O can be reduced to H_2, making the H_2 evolution reaction a competing reaction against other CO_2 reduction processes.

To lower/minimize this energy penalty acting as a thermodynamic(activation) barrier for CO_2 reduction, involvement of a catalyst is of great importance as it plays a role of lowering the overpotential values required for an electrochemical reaction, opening up routes for less energy demanding reactions by stabilizing the intermediate transition states between the linear CO_2 molecules and the intended product.[18] A range of catalysts have been studied for the reduction of CO_2, such as enzymes, solid-state materials and synthetic molecules.

Based on a number of studies done previously, the use of molecular inorganic complexes as catalysts was found to be more advantageous due to their well-defined structures that are readily characterized, with catalytic mechanisms that can be interpreted with clarity, and the opportunity to optimize catalytic activities through molecular design. These catalysts structures are often single atom transition-metal complexes stabilized by ligands in environments that tune the redox potentials of the catalyst and may increase the selectivity of the reaction.[19,20]

2.3. Different catalytic conversion mechanisms

While working with different molecular catalysts in converting carbon dioxide gas into other carbon-based value-added products, different valorization techniques can be employed. These techniques have different operating principles based on the working conditions in place. Examples of conversion techniques that have been previously used include biochemical conversions,[21] chemical conversions,[22] and thermal reforming processes.[23] However, a number of limiting factors were observed in most of these conversion processes such as: low conversion rate, poor selectivity and harsh conditions (severe temperature and high energy input).

In this work we mainly explored three conversion techniques in solution with optimized operating conditions that involve minimal energy consumption and better conversion rates by involving the use of a catalyst. These conversion techniques also known as catalytic mechanisms for CO_2 reductions are electrocatalysis, photocatalysis and photo-electrocatalysis mechanisms.

i. Electrocatalysis of CO_2 in solution

This mechanism usually occurs in mild experimental conditions where CO_2 gas is converted into valuable carbon-based products by applying an external bias/ potential on an electrode surface in the presence of a catalyst in solution i.e. electrocatalytic conversion of CO_2 **(Figure I. 4)**. The applied external bias tends to provide an electrical energy that supplies electrons to a given catalyst which in succession launches the CO_2 reduction process through formation of active species which favor the adsorption of CO_2 on a catalytic site. [24-27]

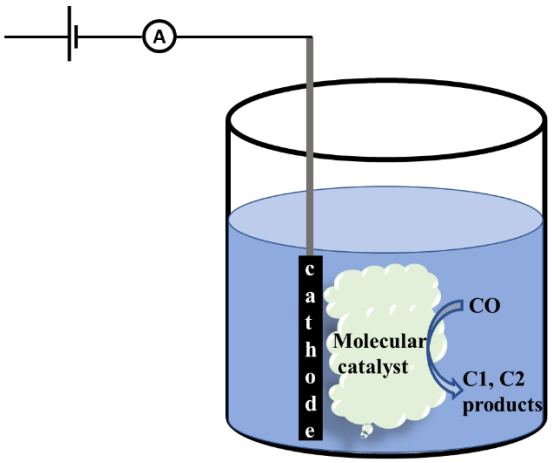

Figure I. 4 Electrocatalysis of CO_2 to various carbon-based products in solution.

Depending on the availability of electrons and protons as well as the nature of the catalyst used, these active species can result in the formation of various products. Additionally, the formation of these different carbon reduced products is dependent on the thermodynamics and kinetics of the appropriate electrochemical reactions. (see **Table I. 1)**.

However, this mechanism does present a couple of drawbacks such as high overpotentials causing low faradaic efficiency (FE), low product selectivity, poor CO_2 solubility in the electrolyte (solvent) and formation of unstable intermediates. Nevertheless, this mechanism can still provide a better insight into the reaction mechanism of the CO_2 reduction process through studying the thermodynamics and kinetics of the corresponding reactions.

To mitigate the given drawbacks, different conditions can be optimized (by changing electrolytes, controlling the pH) but the most important step in improving the performance of this mechanism lies in the choice of a catalyst. By choosing an appropriate electrocatalyst that can undergo reduction easily as a result of a high electron affinity, an efficient electron transfer can be promoted between an electrode surface and a catalyst. Moreover, the use of an electrocatalyst that forms stable and reactive intermediates can aid in increasing the rate of chemical reactions occurring during the reduction process of CO_2.

A variety of carbon-based, metallic, molecular and metal–organic frameworks (MOFs) catalysts have been widely utilized as electrocatalysts in achieving an efficient electrochemical conversion of CO_2. Among all these catalysts, the polypyridyl transition metal complexes are

the most researched molecular catalysts, which exhibit high CO_2 reduction reaction efficiency and high activity in aprotic solvents.[28]

In this work, the study of electrocatalysis of CO_2 was mainly centered on investigating electrochemical properties of homogeneous electrocatalysts which exist in the same phase as the CO_2 reactant i.e. both catalyst and CO_2 are solubilized in an organic electrolyte.

ii. Photocatalysis of CO_2

Photocatalysis of CO_2 is a reduction mechanism of CO_2 that occurs mainly in the presence of a catalyst and a light source that acts as the driving force for the reaction. This mechanism usually occurs in three major steps: **1.** light absorption, **2.** charge separation and electron transfer, and **3.** surface catalytic reaction. Each step involves a crucial component that facilitates the photoreduction of CO_2 as indicated in **Figure I. 5**.

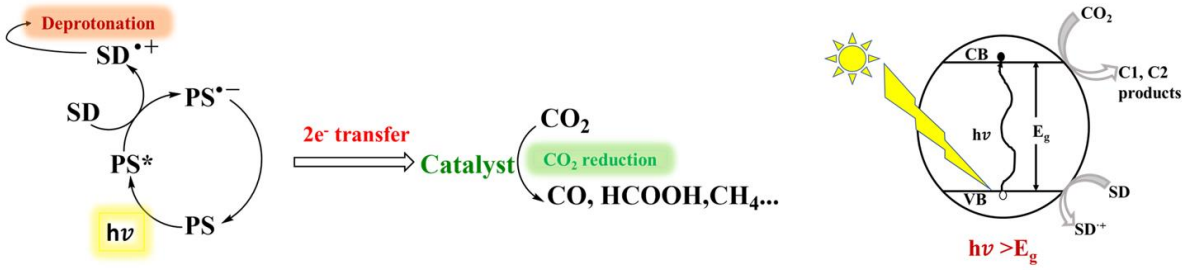

Figure I. 5 Photocatalysis of CO_2 in homogeneous (left) and heterogeneous (right) environments (**PS**: photosensitizer, **SD**: sacrificial electron donor).

The key component in step **1** is a redox photosensitizer (**PS**) possessing light absorption properties. Upon light irradiation, photoexcitation of electrons from a ground state (HOMO for complexes or VB for semiconducting materials) to an excited level (LUMO for complexes or CB for semiconducting materials) will occur forming $\mathbf{PS^*}$. Consecutively in step **2**, an electron transfer process will take place between a $\mathbf{PS^*}$ and a sacrificial electron donor (**SD**) resulting into the formation of $\mathbf{PS^{\bullet-}}$ and $\mathbf{SD^{\bullet+}}$ respectively. This reduced state $\mathbf{PS^{\bullet-}}$ will successively relay its accumulated electrons to CO_2 gas, hence achieving the photocatalytic reduction of CO_2 molecules into other carbon reduced products.

It is important for all components involved in each step of the photocatalytic reaction to possess the required photophysical and electrochemical properties. The following are the general prerequisites for an efficient photocatalysis of CO_2;

i. For an efficient utilization of the light source, the **PS** should absorb more than the **SD** and **Cat** in the visible region at a given excitation wavelength.
ii. An excited $\mathbf{PS}^*$ should have a long lifetime to ensure an efficient reductive quenching process between itself and a **SD**.
iii. A $\mathbf{PS}^*$ should possess a strong oxidation power to promote capturing of electrons from a **SD** and $\mathbf{PS}^{\bullet-}$ a strong reducing power to favor the activation of a catalyst.
iv. Upon reduction, $\mathbf{PS}^{\bullet-}$ species should remain stable enough to ensure an electron transfer between a **Cat** and $\mathbf{PS}^{\bullet-}$, hence an efficient surface catalytic reaction.
v. The $\mathbf{SD}^{\bullet+}$ species need to be decomposed (e.g., by deprotonation thus losing its oxidation power), in doing so the back-electron transfer reaction between $\mathbf{SD}^{\bullet+}$ and $\mathbf{PS}^{\bullet-}$ will be suppressed.

It should be noted that, in some cases the redox **PS** might play a double role as catalyst and as a **PS** respectively (i.e. photocatalyst). In such cases, there are only two crucial components involved in the photocatalytic reaction, a photocatalyst and a sacrificial electron donor. As a photocatalyst, this molecular component should possess strong absorption properties in the visible region, strong oxidizing power to promote an electron transfer from the **SD** and finally it should also have catalytic properties towards CO_2 reduction in its reduced form.[29-32]

The photocatalysis of CO_2 has been previously investigated in heterogeneous conditions using semiconducting surface with light harvesting properties such as TiO_2;[33] and in homogeneous conditions using metal complexes,[15,34] supramolecular photocatalysts i.e. dyads (molecular structure bridging a photosensitizer and catalyst) in solution.[35,36]
In this work, the photocatalysis of CO_2 was investigated using molecular complexes as redox photosensitizers and catalysts in homogeneous conditions (i.e. all molecular components were solubilized in a liquid phase).

iii. Photoelectrocatalysis of CO_2

This mechanism is based on the photoelectroreduction of CO_2 that incorporates the working conditions of electrocatalysis and photocatalysis of CO_2 in one operating system. In such a mechanism, CO_2 is reduced in the presence of a catalyst that is linked to a surface of a working electrode which possesses light harvesting properties i.e. photoelectrode. In addition to using a

light source as the driving force of the reaction, an external bias is applied on an electrode surface to sustain the flow of electrons.

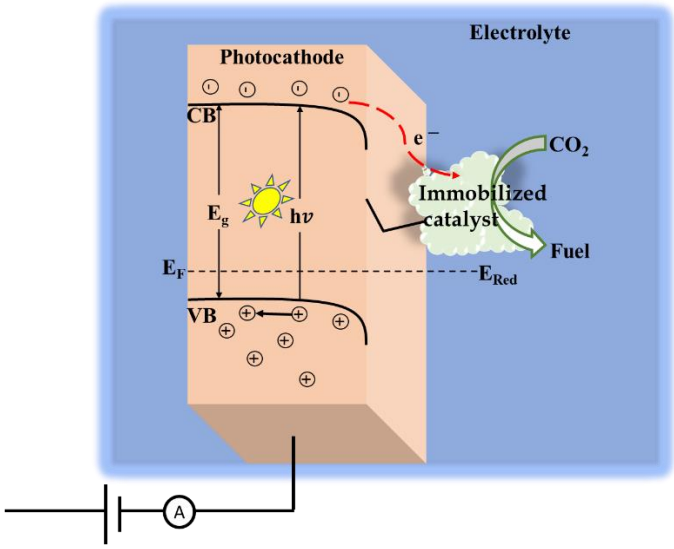

Figure I. 6 Photoelectrochemical catalysis of CO_2 on the surface of a p-type photocathode under light irradiation.

As depicted in **Figure I. 6**, in this mechanism, the use of a normal conducting electrode is replaced with that of a semi-conducting electrode (either p-type or n-type). The two driving forces of this given mechanism (solar and electrical energy) are responsible for launching the photoexcitation of electrons and charge transportation processes. In CO_2 reduction, p-type semiconductors are of particular interest as photocathodes due to their highly negative conduction bands resulting in an expected flow of electrons down the potential gradient in the conduction band toward the interface as shown in **Figure I. 6**.

A p-type photocathode with a suitable energy bandgap (E_g) can harvest incident photons from a light source causing photoexcitation of an electron from the valence band to the conduction band proceeding to the generation of electron-hole pairs (i.e. excitons). It is important that the bandgap of this photocathode overlaps with the visible solar spectrum ($E_g \sim 1.75–3.0$ eV) to ensure an efficient photoexcitation process.

In addition to light energy, an applied external bias on this electrode can result to a band bending at the semiconductor-electrolyte interface creating an electric field within the semiconductor that aids in the oriented transfer of the photogenerated electrons and consequently decreasing the recombination rate of the photogenerated e^- /h^+ pairs. There are different commonly used semiconductors as indicated in **Figure I. 7**.

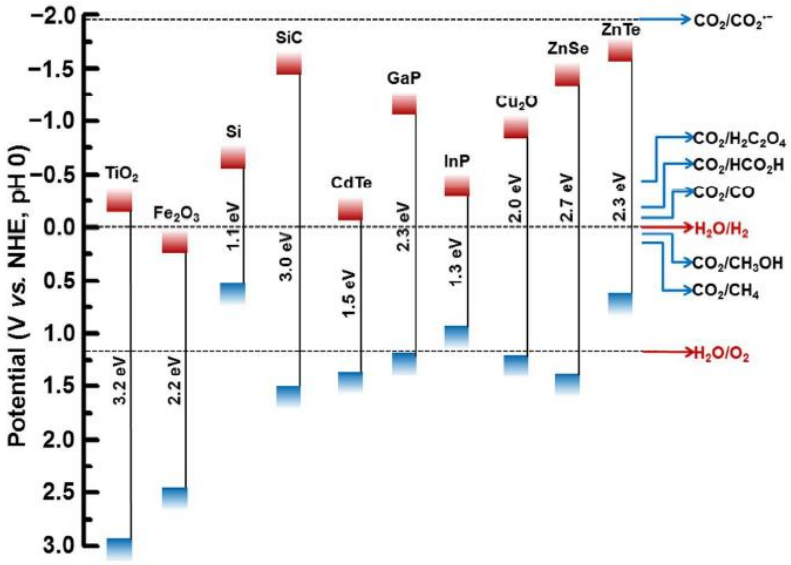

Figure I. 7 Conduction (red) and valence (blue) band positions of some commonly used semiconductors with indicated redox potentials of several CO_2 and H_2O redox couples at pH 0, plotted versus NHE.[37,38]

Consecutive to the photoexcitation, these excited electrons will be oriented towards an interface of a photocathode and electrolyte where these electrons will be relayed to the CO_2 molecule through a reduction process of a loaded catalyst. However, it is important to ensure that the conduction band edge of a photocathode lies at a potential that is more negative than the onset potential of a given catalyst to promote the proton-assisted multielectron reduction reaction of CO_2.

As means of realizing an efficient CO_2 photoreduction process, the design of a photoelectrode can be optimized through developing a buried junction structure between a p-type and an n-type semiconductor. This heterojunction feature will be beneficial in offering a sufficient charge layer space for charge separation (preventing charge recombination) and transfer as well as ensure an overall stability of an electrode.[39]

Loading of a catalyst on the surface of a photocathode can be done physically (physical adsorption), chemically through covalent bonding, or through polymerization resulting to a formation of a heterogeneous/hybrid system for CO_2 reduction.[40-44] By incorporating a catalyst on a surface of a photoelectrode along with generating photovoltage from the absorption of photons, the required external bias for CO_2 reduction is expected to be minimized.

By combining the electrocatalytic and photocatalytic CO_2 reduction processes, this mechanism tends to mitigate the weaknesses of both catalytic techniques to ensure an efficient CO_2 conversion. The photoelectrocatalytic mechanism offers many advantages such as: better diffusional electron transfer kinetics, minimum electricity consumption and a sustainable energy utilization and storage system that converts solar energy into chemical energy which winds up being stored in different forms of fuel.

The photoelectrocatalytic reduction of CO_2 using a p-type semiconductor as a photocathode leading to the formation of different organic products has been investigated in the absence and presence of different forms of catalysts.[45,46]

As part of the project, we focused on the photoelectrochemical reduction of CO_2 using a heterogeneous system consisting of a metal complex loaded on the surface of a metal oxide semiconductor (i.e. a $Cu_2O/Ga_2O_3/TiO_2$ photocathode) under light irradiation which will further be discussed in the coming chapters.

2.4. Different types of catalysts

Generally, a good electrocatalyst has to reduce CO_2 at a potential (E) close to the thermodynamic potential (E°) of the given reaction, resulting in a low overpotential value. Experimentally, this reduction potential should be less negative than that of a direct CO_2 reduction (in the absence of a catalyst) while working in the same conditions. And since the electrocatalytic reduction of CO_2 is initiated by the interaction between CO_2 and an active form of a catalyst, the kinetics involved in the chemical step (formation of an active intermediate of a catalyst) have to be fast in order to facilitate a rapid turnover.

Given the reduction potential of the catalyst is within the appropriate range, while the reduced form of the catalyst is sufficiently stable, and the chemical step is feasible under the desired electrolysis conditions (reaction medium, temperature, etc.), an efficient electrocatalytic reaction of CO_2 should be achievable. For molecular inorganic complexes, these factors can be adjusted by choice of a suitable metal and optimized by ligand tuning. In the last few decades, the progress which has been made in this area is truly impressive, both in optimizing the electrocatalytic performance and in mechanistic understanding.

There exist two different types of catalysis that have been explored and studied for the electrocatalytic reduction of CO_2 in the past decades using molecular inorganic catalysts, homogeneous and heterogeneous catalysis.

i. Homogeneous catalysis

Homogeneous catalysis is a catalytic system in which a CO_2-reducing catalyst diffuses freely within the same environment as that saturated with CO_2 as the reactant, thus having the reduction of CO_2 occurring mainly in one phase (i.e. a liquid phase). In this mechanism, a metal complex solubilized in solution behaves as an electron mediator between an electrode surface and CO_2. This relay of electrons is carried out by reducing a catalyst at the surface of an electrode, giving a more reduced state of a catalyst which then donates electrons to CO_2 in solution and returns to its initial state.[11]

The transfer of an electron between the catalyst and CO_2 can proceed through an outer sphere (redox) mechanism or an inner sphere (chemical) mechanism. The latter one requires a binding step between a catalyst and CO_2.

Generally, the use of homogeneous catalysts can exhibit high activity and selectivity towards specific reactions because of their well-defined active sites and tunability. By readily adjusting the molecular structure and composition of homogeneous catalysts (through changing metal centers or ligands) the product distribution can be tailored through taking advantage of the detailed kinetic and mechanistic understanding that can often be deduced, whereas for heterogeneous catalysts rational modification is more difficult.

Examples of homogeneous catalysts

The structures of the complexes discussed below are depicted in **Figure I. 8** and **I. 9**;

Ru and Os complexes

Ruthenium-based homogeneous metal complexes investigated for electroreduction of CO_2 date back to the 1980s, when the catalytic properties of $[Ru(bpy)_2(CO)Cl]^+$ (with bpy=2, 2'-bipyridine), were described by Tanaka and co-workers. Upon $2e^-$ reduction and dehalogenation, a five-coordinated active species of $[Ru(bpy)_2(CO)]$ catalyzed CO_2 reduction at −1.5 V vs SCE in buffered H_2O/DMF (9:1 v/v) solutions. The product selectivity of these complexes displayed a strong dependence on the pH value, with acidic conditions (pH 6) favoring CO and H_2 formation while basic conditions (pH 9.35) induced $HCOO^-$ production. [47-49] (**Figure I. 8a**)

Analogous to the Ru complexes, a more recent study on the photo-induced electron-transfer reactions of $[Os(bpy)(CO)_2(Cl)_2]$ and $[Os(dmbpy)(CO)_2(Cl)_2]$ (dmbpy=4,4'-dimethyl 2,2'-bipyridine) was reported by Chauvin and co-workers.[34] These complexes under visible irradiation in the presence of a sacrificial electron donor, TEOA (triethanolamine) led to a two-electron, two-proton conversion of CO_2 into CO, revealing how these osmium complexes act as both photosensitizers and catalysts (i.e. photocatalyst). (**Figure I. 8b**)

Re and Mn complexes

Among the most efficient and selective homogeneous molecular catalysts for CO_2 reduction is the archetype $[Re(bpy)(CO)_3X]$ complex (with bpy=2,2'-bipyridine and X= Cl, Br) first developed by J.M Lehn in the 1980's.[30]

This family of complex was found to be an efficient and stable homogeneous catalyst for photochemical and electrochemical reduction of CO_2 to CO in a solution of TEA: DMF (TEA= triethylamine), giving a quantum yield of 14% and a faradaic efficiency of 98%. From mechanistic studies, the rhenium complex acted as both the catalyst and the photosensitizer, with the TEA acting as an electron and proton donor. (**Figure I. 8c**)

And because $[Re(bpy)(CO)_3X]$ absorbs mainly in the UV, later the group of O. Ishitani developed a series of supramolecular systems where this Re-based complex was linked to visible redox photosensitizer units (i.e. $[Ru(bpy)_3]^{2+}$) for an efficient photocatalysis under visible light irradiation in the presence of various sacrificial electron donors.[50,51](**Figure I. 8d**)

From investigating carbonyl polypyridyl manganese complexes as electrocatalysts for the reduction of CO_2, Deronzier et al., described the activity of $[Mn(bpy\text{-}R)(CO)_3Br]$ with bpy-R = 4,4′-disubstituted 2,2′-bipyridine (R=Me, H) towards CO formation.[52] (**Figure I. 8e**)

Compared to the Re analogues, the reduction occurred at a significantly lower overpotential value (with a gain of 0.4V). This catalyst turned out to be highly selective towards CO formation and stable over several hours. However, in contrast to their Re congeners, the use of Mn complexes requires the addition of a proton source such as water. Moreover, this catalyst has a low photostability and needs to be protected from direct light excitation when used in photocatalysis or photo-electrocatalysis.[53,54]

Fe-based complexes

In the 1980s, Savéant and co-workers initiated a series of studies by close examination of the tetraphenyl porphyrin complex $[Fe^{III}(tpp)]Cl$ as a catalyst for CO_2 electroreduction. In the absence of a proton source in a NEt_4ClO_4:DMF electrolyte, the catalytic activity of this complex promoted CO2R to mainly CO formation.[55,56] However, this catalytic process under such aprotic conditions was accompanied by rapid deactivation of the catalyst, presumably caused by carboxylation and hydrogenation of the ligand, resulting to only a few turnovers.

Later on, this family of complex was further modified using phenyl rings with the trimethylammonium substituent groups in para positions, resulting to a formation of a water-soluble catalyst capable of efficiently catalyzing the conversion of CO_2 into CO both in DMF containing a proton donor and in pH-neutral aqueous electrolyte.[57] The latter finding is particularly remarkable, since the byproduct H_2 was found only in small quantities. (**Figure I. 8f**)

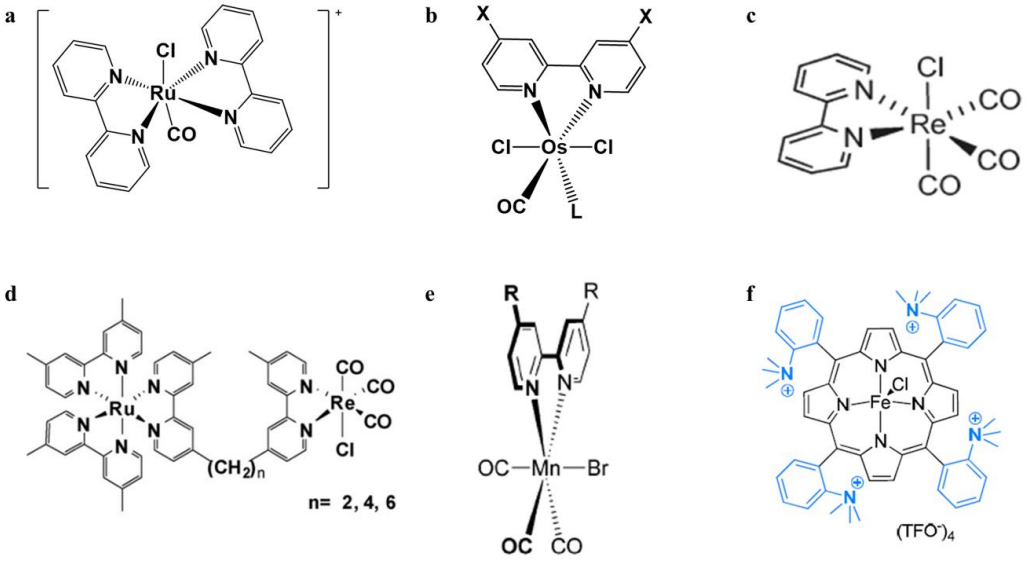

Figure I. 8 Different molecular structures (Group VII and VIII) of metal complexes used in the homogenous catalysis of CO_2.

Ni-based complexes

On the basis of the pioneering work of Eisenberg et al.[58] and Sauvage et al.[59] in the 1980s, a number of studies on $[Ni(cyclam)]^{2+}$ for CO_2 electroreduction were reported. This complex appeared to be an active and selective electrocatalyst for reduction of CO_2 in aqueous medium leading to the formation of CO. (**Figure I. 9a**)

However, the selectivity of this catalyst was affected by the choice of the electrolyte system. In aqueous medium, CO is the main reduction product whereas in anhydrous medium (with [H_2O] <0.2%), the catalytic properties of the complex varied, leading to formate being produced preferentially to CO.[60]

Co-based complexes

Among the first family of Co-based metal complexes reported for CO_2 reduction was the cobalt porphyrins (CoTCPP and $CoTPPS_3$ with TCPP: mesotetracarboxyphenylporphine and $TPPS_3$: tetraphenylporphinesulfonate). These complexes reported by Toshima et al., displayed catalytic activities for CO_2 reduction in aqueous solution.[61] Later on, cobalt complexes of terpyridine $[Co(tpy)_2]^{2+}$ and vinyl-terpyridine $[Co(v\text{-}tpy)_2]^{2+}$ were also reported to be CO_2 reducing catalysts in organic solvents; with the polymeric films of the $[Co(v\text{-}tpy)_2]^{2+}$ complex resulting to a reduction of CO_2 at less negative potential (-0.9V vs SSCE) in comparison to the $[Co(tpy)_2]^{2+}$ complex (-1.91 V vs SSCE) under similar conditions.[62] (**Figure I. 9 b, c**)

Recently, the group of Marc Robert reported the (photo)-electroreduction of CO_2 in water using a cobalt quaterpyridine complex immobilized on a surface of a photocathode. Overall, photo-electroreduction of CO_2 resulted to a better selectivity (97%) and FE (89%) of CO in comparison to electroreduction of CO_2 with 80% selectivity and 63% FE.[63]

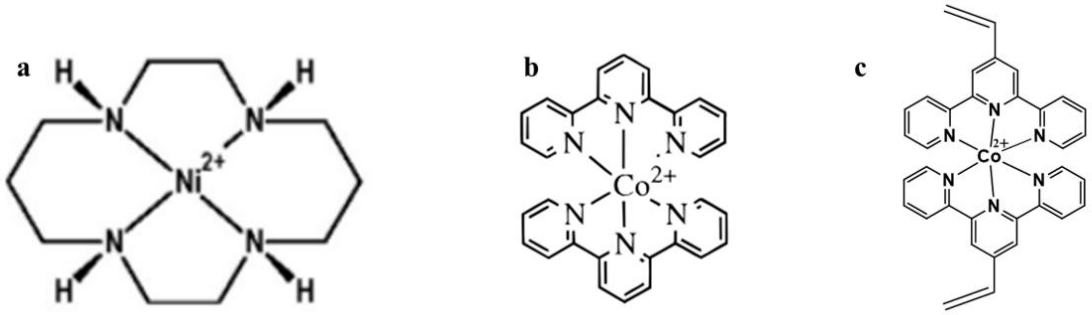

Figure I. 9 Examples of group IX and X metal complexes used in the homogenous catalysis of CO_2.

Conclusively, it is important to note that these molecular complexes employed in homogeneous catalysis of CO_2 can also be used in heterogeneous catalysis of CO_2 upon molecular structure modification of these complexes using different anchoring groups that permit the immobilization of these molecular catalysts on different surface of conducting electrodes. Such an approach has been investigated before as means of improving the efficiency of CO2R.

ii. Heterogeneous catalysis

This type of catalysis mainly involves the reduction of CO_2 in an environment that consists of two different phases; a solid phase consisting of a cathode and a catalyst in close proximity and a liquid or gas phase which usually consists of a CO_2 substrate (i.e. CO_2 reduction at a solid-liquid interphase or solid-gas interphase). Usually, a heterogeneously catalyzed CO_2 reduction occurs on a surface of an electrode acting as the main catalyst or with a co-catalyst immobilized in form of a metal, metal oxide or a molecular complex.

A variety of electrode materials have been reported to be used in the heterogeneous catalysis of CO_2 such as metal-based nanoparticles (Ag, Au, Cu),[64-66] carbon-based electrodes (MWCNT, graphene),[67] and semiconductors (p-Si, p-Cu_2O, p-GaP).[45] Despite the reported high faradaic efficiencies of most metal electrodes in the CO_2 reduction process, the use of these metals proves to be expensive given their rarity.

To overcome this challenge, efforts were made towards developing heterogeneous systems composed of semiconducting electrode surfaces modified with homogeneous molecular catalysts through chemical bonding, noncovalent bonding, or polymerization. This approach presents an advantage of selectivity and tunability of molecular catalyst systems as well as the advantages of heterogeneous systems including high concentrations of the catalysts at the reaction site, bypassing poor solubility of catalyst in certain electrolytes, elimination of the diffusion and mass-transport limitations, improved lifetime of a loaded catalyst, and easy separation of the catalyst from the reaction mixture.

As part of this project, we have investigated heterogeneous catalysis of CO_2 based on some molecular catalysts we developed for CO_2 reduction, which were then loaded on the surface of a semiconducting metal oxide (Cu_2O) as means of improving the catalytic efficiency of CO_2 reduction at less negative reducing potentials in organic solvents.

2.5. Group VI metal complexes as catalysts for CO2R

As it has been stated in this chapter, the use of catalysts is of necessity when it comes to an efficient CO_2 reduction process. Despite a variety of catalysts that have been previously reported, maximum efforts of chemically transforming CO_2 have been implemented in the presence of molecular metal complexes acting as catalysts for the electrochemical reduction of CO_2.

These efforts of designing and studying different metal complexes for CO2R were mainly done on complexes with metal centers from group VII (Mn, Re), group VIII (Fe, Ru, Os), group IX (Co) and group X (Ni). And despite remarkable development and efforts in trying to find the best CO2R catalyst, there are still some limitations encountered in the already existing molecular structure such as instability (for Mn-carbonyl complexes), heavy synthesis (for Fe porphyrins and Ni cyclams) and use of rare-earth metals which could in turn lead to high cost upon large scale production.

With the prospect of designing molecular catalysts with earth-abundant elements as their metal centers, group VI metals complexes regained interest. In particular, a series of bipyridyl complexes of Group VI metals $[M(bpy)(CO)_4]$ (M=Cr, Mo, W, Cr) were studied by different research teams.

The group of Kubiak reported electrocatalytic properties of the metal tetracarbonyl bipyridine $[M(R\text{-}bpy)(CO)_4]$ (M=Mo, W; R=H, tBu) complexes for CO_2 reduction using a glassy carbon electrode. Through a two-electron reduction process, these complexes were transformed into active species for CO_2 reduction at an onset potential of -2.3 V vs. saturated calomel electrode (SCE) in acetonitrile. From this work it was also evident that the addition of substituent groups on the bipyridine ligand can result to an increase of the catalytic density of these complexes.[68]

Later on, from the research work of Hartl et al., it was discovered that the catalytic reduction of CO_2 in the presence of $[M(CO)_4(bpy)]$ (M=Cr, Mo, W) complexes was quite sensitive to the electrode material employed. Using a gold working electrode, these complexes displayed a shifted catalytic onset potential towards less negative potential values.[69] In this family of complexes, the pentacoordinate species of $[M(CO)_3(bpy)]^{2-}$ formed upon two-electron reduction were hinted to be the active catalytic species for CO2R.

In further studies reported by Hartl et al., the formation of these active species $[M(CO)_3(bpy)]^{2-}$ was investigated by photo-assisted electrochemical reduction of $[M(CO)_4(bpy)]$. This was achieved by irradiating a mono-reduced radical anion (i.e. $[M(CO)_4(bpy)]^{\bullet-}$) with UV light, generating these pentacoordinate dianion species which were detected at a potential value that is, ~ 0.4V less negative than the standard potential of bi-reduced metal complex in the absence of UV light.[70] Despite these reported works, the group VI metal complexes still remain underexplored compared to complexes of group VII or group VIII.

Apart from the discussed metal complexes with carbonyl ligands that tend to stabilize the low valent species, there are scarce examples of metal complex structures without carbonyl ligands. Among these rare examples is the Cr (III) complex published by Machan et al., this complex structure consists of a 2,2'-bipyiridine based ligand with two phenolate moieties (**Figure I. 10a**). This complex is capable of selectively reducing CO_2 into CO with phenol as the proton source in acetonitrile.[71]

Another example of a Cr (III) complex was reported by Abruña et al., where a Cr (III) complex was designed with a bis-4'-vinylterpyridine ligand (**Figure I. 10b**). Upon electropolymerization of the complex onto a surface of a glassy carbon electrode, this polymer film exhibited an electrocatalytic activity towards the reduction of CO_2 with formaldehyde as a predominant reduction product.[72] This formation of formaldehyde was attributed to a cooperative effect between two or more metals in the electrodeposited film. These given examples show that the designing of polypyridyl group VI complexes do not necessarily require only low valent species.

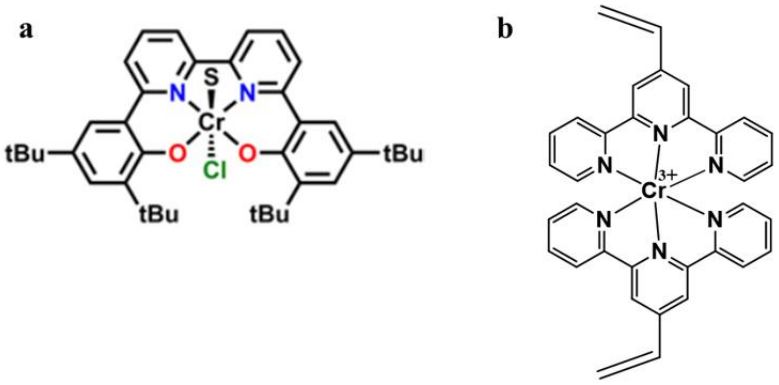

Figure I. 10 Cr (III) molecular complexes investigated for CO_2 reduction.

3. Scope of this research work

In this research project, we focus on studying the catalytic conversion of CO_2 using polypyridyl group VI metal complexes, based on non-noble and non-rare elements (for instance W earth's abundance is 1.2 ppm whereas Re is 0.0026ppm).

Notably, the electrochemical behavior of the designed complexes will be investigated in non-aqueous systems which offer some advantages, and have shown some interesting trends for CO2R.[73,74] The solubility of CO_2 in organic solvents can be more significant than in water

(e.g. >8 times higher in acetonitrile), potentially leading to enhanced reaction rates and selectivity for CO2R.

The investigation of the electrocatalytic behavior of these molecular complexes in the dissolved state will be investigated using different electro-characterization techniques (cyclic voltammetry, electrolysis) in order to test their efficiency as electrocatalysts especially in the presence of different weak acids to favor the $2H^+$ coupled $2e^-$ reduction of CO_2 into CO.

With the aim of achieving CO2R at low onset reduction potentials, modification of ligand structure and alteration of the metal center's oxidation state will be explored. In doing so we hope to lower the overpotential (η) value which indicates a relatively small electrochemical drive required to convert CO_2 to certain desired products.

$$\eta = E^{\circ}_{CO_2} - E_{app}$$

With;

$E^0_{CO_2}$ as the thermodynamic standard potential for CO2R

E_{app} as the experimental applied onset potential at which electrolysis is run

Another electrocatalytic metric that will be presented in this manuscript is the Faradaic efficiency (FE) value that is determined by product quantification (gas chromatography, ion chromatography). This value is essential in correlating the electric charge quantity passing through the electrochemical system with products being formed, which tends to reveal as to whether the electron flow is directed towards the intended reactions or other parasitic (undesirable) reactions such as solvent decomposition, catalyst degradation, H_2 production and even CO_2 reduction to non-desired products.

$$Faradaic\ efficiency\ (\%) = \frac{zFn_{product}}{Q} \times 100$$

With; z = number of electrons required for the reduction reaction,

F = Faraday constant (96 485 C mol^{-1}),

Q = Total charge passed (in coulombs).

Apart from studying the electrocatalytic properties, photophysical properties will also be studied to explore the possibility of performing photocatalysis of CO_2 in homogenous conditions and photoelectrocatalysis of CO_2 in heterogeneous conditions by integrating these

molecular complexes with suitable semiconducting electrodes and investigating these systems under photo-irradiation.

In the next chapters, our results are reported in the following order;

Chapter II presents a summary of the work done on the bipyridyl metal complexes $[M(bpy)(CO)_4]$ with M= Cr, Mo, and W. These complexes will be synthesized and investigated for their electrocatalytic properties in organic solvents. Using this family of complexes as the foundation of understanding the CO_2 reduction mechanism, further complex modifications will be carried out to develop a new family of complexes, triscarbonyl metal complexes $[M(bpy)(CO)_3Cl]^-$.

Chapter III focuses on a new family of complex built with pyridyl imidazole-based ligands $[M(\mathbf{L})(CO)_4]$ which will mainly be investigated for their photophysical properties as means of carrying out photocatalysis of CO_2 in the presence of a sacrificial electron donor. Prior to this investigation the electrocatalytic properties of this family of complexes will also be investigated for CO_2 reduction. In collaboration to our project members, the photoelectrocatalysis of CO_2 using the tungsten complex $[W(\mathbf{L1})(CO)_4]$ (with **L1** = 2-(1H-imidazol-2-yl)pyridine) ligand) will be studied in the presence of a cuprous oxide semiconductor.

Chapter IV presents a chromium (III) metal complex with a tetradentate ligand. The electrocatalytic behavior of this complex in dissolved state will be further studied in detail in the presence of varying concentrations of added weak acids. Further studies of this complex will involve the investigation of photocatalysis and photoelectrocatalysis of CO_2 using a molecular photosensitizer and a Cu_2O photocathode respectively, under light irradiation.

Bibliography

1. P. Friedlingstein, M. O'Sullivan, M. W. Jones, R. M. Andrew, et al., *Earth Syst. Sci. Data*., **Global Carbon Budget 2022,** *14*, 4811–4900.
2. M. Aresta, *Carbon Dioxide as Chemical Feedstock*., **2010**.
3. M. Crippa, D. Guizzardi, F. Pagani, M. Banja, M. Muntean, E. Schaaf, W. Becker, F. Monforti-Ferrario, R. Quadrelli, A. R. Martin, P. Taghavi-Moharamli, J. Köykkä, G. Grassi, S. Rossi, J. Brandao De Melo, D. Oom, A. Branco, J. San-Miguel, E. Vignati, GHG emissions of all world countries, Publications Office of the European Union, Luxembourg, **2023**, doi:10.2760/953332, JRC134504.
4. S. Solomon, J. S. Daniela, T. J. Sanford, D. M. Murphya, G.-K. Plattner, R. Knutti, P. Friedlingstein, *Proc. Natl. Acad. Sci USA*., **2010**, *107*(43), 18354–18359.
5. Parties to the United Nations Framework Convention on Climate Change, Paris Agreement, United Nations, **2015**.
6. Economist Intelligence Unit **2022**.
7. World Energy Transitions Outlook by the International Renewable Energy Agency (IRENA) **2021-2022**.
8. K. E. Dalle, J. Warnan, J. J. Leung, B. Reuillard, I. S. Karmel, E. Reisner; *Chem. Rev.*, **2019,** *119*, 2752–2875.
9. A.M. Appel, J.E. Bercaw, A. B. Bocarsly, H. Dobbek, D. L. DuBois, M. Dupuis, J. G. Ferry, E. Fujita, R. Hille, P. J. A. Kenis, C. A. Kerfeld, R. H. Morris, C. H. F. Peden, A. R. Portis, S. W. Ragsdale, T. B. Rauchfuss, J. N. H. Reek, L. C. Seefeldt, R. K. Thauer, G. L. Waldrop, *Chem. Rev*., **2013**, *113* (8), 6621–6658.
10. E. S. Andreiadis, M. Chavarot-Kerlidou, M. Fontecave, V. Artero, *Photochem. Photobiol*., **2011**, *87*, 946–964.
11. R. Francke, B. Schille, M. Roemelt, *Chem. Rev*., **2018**, *118*, 4631−4701.
12. G. L. Gutsev, R. J. Bartlett, R. N. Compton, *J. Chem. Phys*., **1998**, *108*, 6756−6762.
13. L.-S. Wang, J. E. Reutt, Y. T. Lee, D. A. Shirley, *J. Electron. Spectrosc. Relat. Phenom*., **1988**, *47*, 167−186.
14. X. Chang, T. Wang, J. Gong, *Energy Environ Sci*., **2016**, *9*, 2177-2196.
15. J. M. Lehn, R. Ziessel, *Proc. Natl. Acad. Sci. U.S.A*., **1982**, *79*, 701-704.
16. A. H. Shah, Y. Wang, A. R. Woldu, L. Lin, M. Iqbal, D. Cahen, T. He, *J. Phys. Chem. C*., **2018**, *122*, 18528–18536.

17. M. Bellardita, V. Loddo, F. Parrino, L. Palmisano; *ChemPhotoChem*., **2021**, *5*, 767–791.
18. B. Kumar, M. Llorente, J. Froehlich, T. Dang, A. Sathrum, C. P. Kubiak, *Annu. Rev. Phys. Chem*., **2012**, *63*, 541-569.
19. H. Ishida, C. Machan, M. Robert, N. Iwasawa, *Front. Chem*., **2020**, 8.
20. S. Zhang, Q. Fan, R. Xia, T. J. Meyer, *Acc Chem Res*., **2020**, *53*(1), 255-264.
21. P. Chen, M. Min, Y. Chen, L. Wang, Y. Li, Q. Chen, C. Wang, Y. Wan, X. Wang, Y. Cheng, S. Deng, K. Hennessy, X. Lin, Y. Liu, Y. Wang, B. Martinez, R. Ruan, *Int J Agric & Biol Eng*., **2010**, *2* (4), 1–30.
22. M. Aresta, A. Dibenedetto, A. Angelini, *Chem. Rev*., **2013**, 114 (3), 1709–1742.
23. O.-S. Joo, K.-D. Jung, I. Moon, A.Y. Rozovskii, G.I. Lin, S.-H. Han, S.-J. Uhm, *Ind. Eng. Chem. Res*., **1999**, *38* (5), 1808–1812.
24. R. Kortlever, J. Shen, K. J. P. Schouten, F. Calle-Vallejo, M. T. M. Koper, *J. Phys. Chem. Lett*., **2015**, *6*, 4073–4082.
25. J. Wu, T. Sharifi, Y. Gao, T. Zhang, P. M. Ajayan, *Adv. Mater*., **2019**, *31*, 1804257.
26. E. E. Benson, C. P. Kubiak, A. J. Sathrum, J. M. Smieja, *Chem. Soc. Rev*., **2009**, *38*, 89–99.
27. V. Kumaravel, J. Bartlett, S. C. Pillai, *ACS Energy Lett*., **2020**, *5*, 486–519.
28. J.P. Collin, J.P. Sauvage, *Coord. Chem. Rev*., **1989**, *93*, 245 -268.
29. C. Kutal, M.A. Weber, G. Ferraudi, D. Geiger, *Organometallics*., **1985**, *4*, 2161–2166.
30. J. Hawecker, J.M. Lehn, R. Ziessel, *Helv. Chim. Acta*., **1986**, *69*, 1990-2012.
31. S. Sato, T. Morikawa, T. Kajino, O. Ishitani, *Angew. Chem. Int. Ed*., **2013**, *52*, 988–992.
32. D. Behar, T. Dhanasekaran, P. Neta, C. M. Hosten, D. Ejeh, P. Hambright, E. Fujita, *J. Phys. Chem. A*., **1998**, *102*, 2870–2877.
33. H. Abdullah, M. M. R. Khan, H. R. Ong, Zahira Yaakob, *J. CO2 Util*., **2017**, *22*, 15–32.
34. J. Chauvin, F. Lafolet, S. Chardon-Noblat, A. Deronzier, M. Jakonen, M. Haukka, *Chem. Eur. J*., **2011**, *17*, 4313.
35. B. Gholamkhass, H. Mametsuka, K. Koike, T. Tanabe, M. Furue, O. Ishitani, *Inorg. Chem*., **2005**, *44*, 2326–2336.
36. Y. Tamaki, K. Koike, T. Morimoto, Y. Yamazaki, O. Ishitani, *Inorg. Chem*., **2013**, *52*, 11902–11909.

37. M. Grätzel, *Nature*., **2001**, *414*, 338−344.
38. J. Li, N. Wu, *Catal. Sci. Technol*., **2015**, *5*, 1360-1384.
39. C. Li, T. Hisatomi, O. Watanabe, M. Nakabayashi, N. Shibata, K. Domen, J.-J. Delaunay, *Energy Environ. Sci*., **2015**, *8*, 1493–1500.
40. S. Sato, T. Arai, T. Morikawa, K. Uemura, T. M. Suzuki, H. Tanaka, T. Kajino, *J. Am. Chem. Soc*., **2011**, *133*, 15240-15243.
41. K. L. Materna, R. H. Crabtree, G. W. Brudvig, *Chem. Soc. Rev*., **2017**, *46*, 6099−6110.
42. J. Willkomm, K. L. Orchard, A. Reynal, E. Pastor, J. R. Durrant, E. Reisner, *Chem. Soc. Rev*., **2016**, *45*, 9−23.
43. B. J. Brennan, M. J. Llansola Portolés, P. A. Liddell, T.A. Moore, A. L. Moore, D. Gust, *Phys. Chem. Chem. Phys*., **2013**, *15*, 16605−16614.
44. L. A. Martini, G. F. Moore, R. L. Milot, L. Z. Cai, S.W. Sheehan, C. A. Schmuttenmaer, G. W. Brudvig, R. H. Crabtree, *J. Phys. Chem. C*., **2013**, *117*,14526−14533.
45. M. Halmann, *Nature*., **1978**, *275*, 115-116.
46. J. White, M. F. Baruch, J. E. Pander Lii, Y. Hu, I. C. Fortmeyer, J. E. Park, T. Zhang, K. Liao, J. Gu, Y. Yan, T. W. Shaw, E. Abelev, A. B. Bocarsly, *Chem. Rev*., **2015**, *115* (23), 12888–12935.
47. H. Ishida, K. Tanaka, T. Tanaka, *Chem. Lett*., **1985**, *14*, 405−406.
48. H. Ishida, K. Tanaka, T. Tanaka, *Organometallics*., **1987**, *6*, 181−186.
49. H. Ishida, H. Tanaka, K. Tanaka, T. Tanaka, *J. Chem. Soc., Chem. Commun*., **1987**, 131−132.
50. Z. -Y. Bian, K. Sumi, M. Furue, S. Sato, K. Koike, O. Ishitani, *Inorg. Chem.*, **2008**, *47* (23), 10801–10803.
51. K. Koike, S. Naito, S. Sato, Y. Tamaki, O. Ishitani, *J. Photochem. Photobiol*., A **2009**, *207*, 109– 114.
52. M. Bourrez, F. Molton, S. Chardon-Noblat, A. Deronzier, *Angew. Chem., Int. Ed*., **2011**, *50*, 9903−9906.
53. G. J. Stor, S. L. Morrison, D. J. Stufkens, A. Oskam, *Organometallics*., **1994**, 13, 2641−2650.
54. M. Stanbury, J.-D. Compain, S. Chardon-Noblat, Coord. Chem. Rev., **2018**, *361*, 120-137.
55. M. Hammouche, D. Lexa, J. M. Savéant, M. Momenteau, *J. Electroanal. Chem*., **1988**, *249*, 347−351.

56. M. Hammouche, D. Lexa, M. Momenteau, J. M. Savéant, *J. Am. Chem. Soc*., **1991**, *113*, 8455−8466.
57. C. Costentin, M. Robert, J.-M. Savéant, A. Tatin, *A. Proc. Natl. Acad. Sci. U. S. A.*, **2015**, *112*, 6882−6886.
58. B. J. Fisher, R. Eisenberg, *J. Am. Chem. Soc*., **1980**, *102*, 7361−7363.
59. M. Beley, J.-P. Collin, R. Ruppert, J.-P. Sauvage, *J. Chem. Soc., Chem. Commun*., **1984**, 1315-1316.
60. J. P. Collin, A. Jouaiti, J. P. Sauvage, *Inorg. Chem*., **1988**, *27*, 1986−1990.
61. K. Takahashi, K. Hiratsuka, H. Sasaki and S. Toshima, *Chem. Lett*., **1979**, *8*, 305-308.
62. H.D. Hurrell, A.-L. Mogstad, D.A. Usifer, K.T. Potts, H.D. Abruña, *Inorg Chem*., **1989**, *28*, 1080-1084.
63. P. B. Pati, R. Wang, E. Boutin, S. Diring, S. Jobic, N. Barreau, F. Odobel, M. Robert, *Nat Commun*., **2020**, *11*, 3499.
64. S. Nitopi, E. Bertheussen, S. B. Scott, X. Liu, A. K. Engstfeld, S. Horch, B. Seger, I. E. L. Stephens, K. Chan, C. Hahn, J.K. Nørskov, T. F. Jaramillo, I. Chorkendorff, *Chem. Rev*., **2019**, *119* (12), 7610−7672.
65. W. Zhu, Y.-J. Zhang, H. Zhang, H. Lv, Q. Li, R. Michalsky, A. A. Peterson, S. Sun, *J. Am. Chem. Soc*., **2014**, *136* (46), 16132−16135.
66. Y. Hori, *Modern Aspects of Electrochemistry*., **2008**, *42*, 89−189.
67. M. Zhu, J. Chen, L. Huang, R. Ye, J. Xu, Y.-F. Han, *Angew. Chem., Int. Ed*., **2019**, *58*, 6595-6599.
68. M. L. Clark, K. A. Grice, C. E. Moore, A. L. Rheingold, C. P. Kubiak, *Chem. Sci*., **2014**, *5*, 1894–1900.
69. J. Tory, B. Setterfield-Price, R. A. W. Dryfe, F. Hartl, *ChemElectroChem.*, **2015**, *2*, 213–217.
70. J. O. Taylor, Y. Wang, F. Hartl, *ChemCatChem*., **2020**, *12*, 386-393.
71. S. L. Hooe, J. M. Dressel, D. A. Dickie, C. W. Machan, *ACS Catal*., **2020**, *10*(2), 1146-1151.
72. J. A. Ramos Sende, C. R. Arana, L. Hernandez, K. T. Potts, M. Keshevarz-K, H. D. Abruña, *Inorg. Chem*., **1995**, *34* (12), 3339–3348.
73. Y. Tomita, S. Teruya, O. Koga, Y. Hori, *J. Electrochem. Soc*., **2000**, *147*, 4164.
74. M. Jitaru, D. A. Lowy, M. Toma, B. C. Toma and L. Oniciu, *J. Appl. Electrochem*., **1997**, *27*, 875–889.

CHAPTER II. BIPYRIDYL-CARBONYL METAL COMPLEXES

1. Introduction

As stated in the previous chapter, the group VI metal complexes (M= Cr, Mo, W) have gained interest due to the prospect of synthesizing molecular catalysts for CO_2 reduction with earth-abundant metals as their metal centers. Despite these metals being commonly found in the active sites of formate dehydrogenase (FDH) enzymes, which interconvert CO_2 and formate,[1] there are noticeably few groups that have deeply investigated these metal complexes as potential catalysts for reduction of carbon dioxide.[2-4]

In efforts of establishing a foundation for this research work, the first step involved reproducing the synthesis and characterization of the group VI tetracarbonyl metal complexes. Through this step, a defined synthetic route was determined, which was then employed in the preparation of other metal complexes to be discussed in chapters to come.

2. Bipyridyl tetracarbonyl metal complexes [M(bpy)(CO)$_4$], M= Cr, Mo, W

2.1. Synthesis

The synthesis of tetracarbonyl metal complexes [M(bpy)(CO)$_4$] with (M= Cr, Mo, W) was conducted following two different synthesis routes; the reflux route and the irradiation route. The reflux route was firstly reported in the work of Stiddard[5] in which metal hexacarbonyl [M(CO)$_6$] as the metal source was refluxed with an excess of the bipyridine ligand in either dry toluene (for Cr, Mo) or xylene (for W) under inert atmosphere, leading to a reaction yield of 50% to 70% (**Scheme II. 1**).

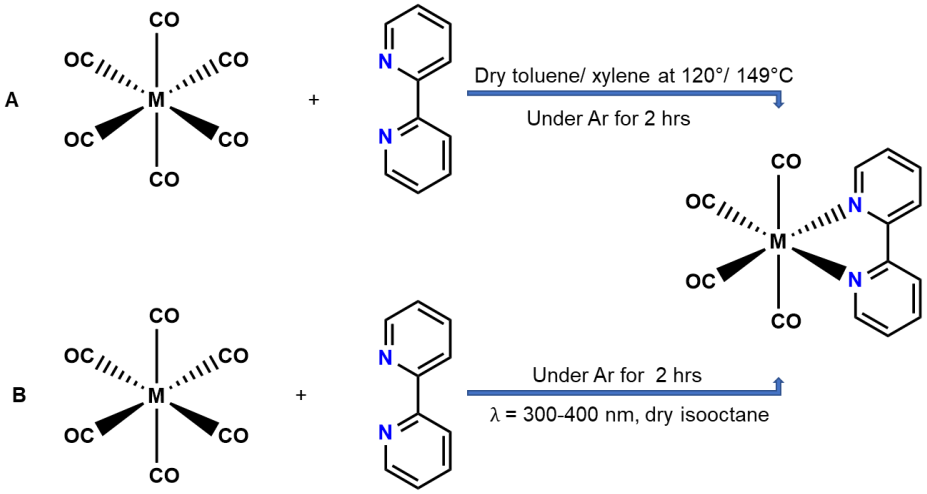

Scheme II. 1 Two different synthetic routes for the synthesis of [M(bpy)(CO)$_4$] complexes (M=Cr, Mo, W); reflux (**A**) and irradiation (**B**) routes.

The irradiation route involved UV irradiation of the parent hexacarbonyl [M(CO)$_6$] with an excess of the bipyridine ligand in N_2-saturated isooctane,[6] leading to the formation of the [M(bpy)(CO)$_4$] product that precipitated out of solution, resulting to a reaction yield of less than 10%. From ^{1}H NMR measurements, the two different synthetic routes led to the formation of similar complexes (see experimental part). These complexes were also reported to have common electronic features as previously shown by density functional theory (DFT) calculations of [M(bpy)(CO)$_4$] complexes.[7-8]

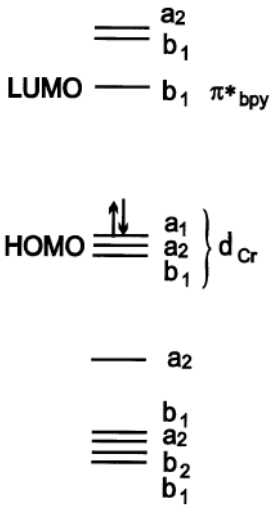

Figure II. 1 Molecular orbital diagram of [Cr(bpy)(CO)$_4$] as a representative example of other [M(bpy)(CO)$_4$] complexes.[7]

These complexes were found to be stable in solid form and were stored in the dark, under vacuum to ensure their long-term stability. These complexes demonstrate a distorted octahedral geometry, with four moderate band maxima which are characteristic of C_{2v} symmetry of the carbonyl ligands coordinated to the metal center and are correlated to the $2A_1$, B_1, B_2 vibration CO modes. [9-10] (**Table II. 1**)

Table II. 1 IR spectral data and assignments for the [M(bpy)(CO)$_4$] complexes in the carbonyl stretching region.

Complexes	Bands, cm^{-1}			
	A_1	B_1	A_1	B_2
Cr(bpy)(CO)$_4$	1999	1892	1859	1828
Mo(bpy)(CO)$_4$	2006	1912	1858	1825
W(bpy)(CO)$_4$	2000	1906	1826	1802

2.2. Photophysical properties

The UV-Vis absorption spectra of strongly colored [M(bpy)(CO)$_4$] complexes in toluene exhibited three absorption bands; the first band in the UV region (~302 nm) associated to the $\pi \rightarrow \pi^*$ ligand centered (LC) transitions, the second band in the near UV region (~360 nm) and the third one located in the visible range (430-600 nm). Given the intensity of the latter absorption band, it was assigned to the metal to ligand charge transfer (MLCT). A number of theoretical studies and calculations reported the orbital excitation from the b_1 (HOMO of the metal center) to the b_1 π^* (LUMO of the bpy) to be the main electronic transition represented by absorption band in the visible region (**Figure II. 2**).[8]

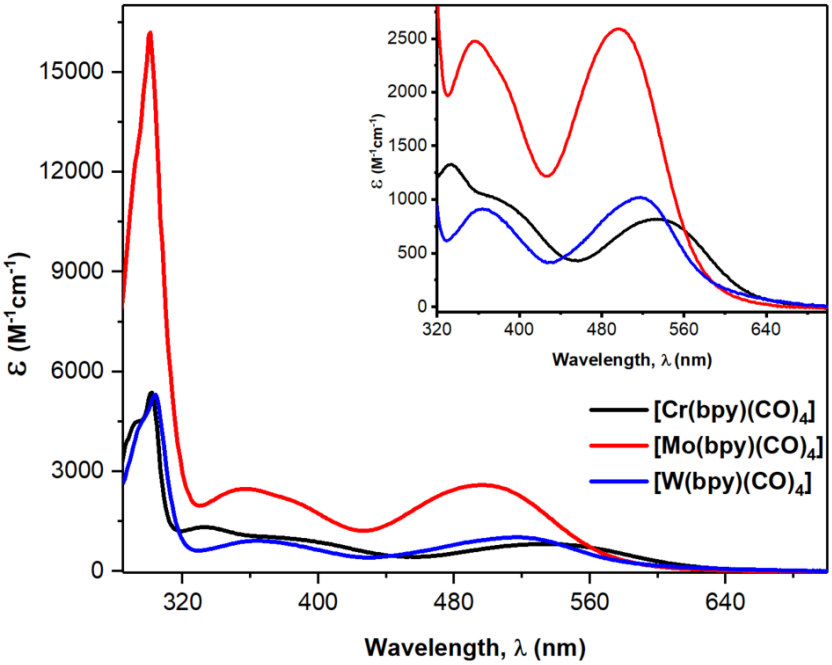

Figure II. 2 UV-Vis absorption spectra of [M(bpy)(CO)$_4$] complexes in toluene; indicating [Cr(bpy)(CO)$_4$] in black, [Mo(bpy)(CO)$_4$] in red and [W(bpy)(CO)$_4$] in blue.

Through calculated changes of electron density distribution on the individual molecular fragments of the complex upon MLCT excitation suggest an occurrence of another lowest possible electronic transition which involves a charge transfer from the metal and axial CO orbitals to the π^* (bpy) orbital.[7] The near UV region band around 360 nm was previously assigned to a LF transition arising from excitation between d-orbitals.[11] However, recent research through experimental and theoretical studies[12-15] strongly suggest that this band originates in low-lying metal center to carbonyl charge transfer.

Interestingly, upon recording the absorption spectra of these complexes in different organic solvents, the MLCT maxima band in the visible range indicated a solvent dependency behavior (**Figure II. 3**).

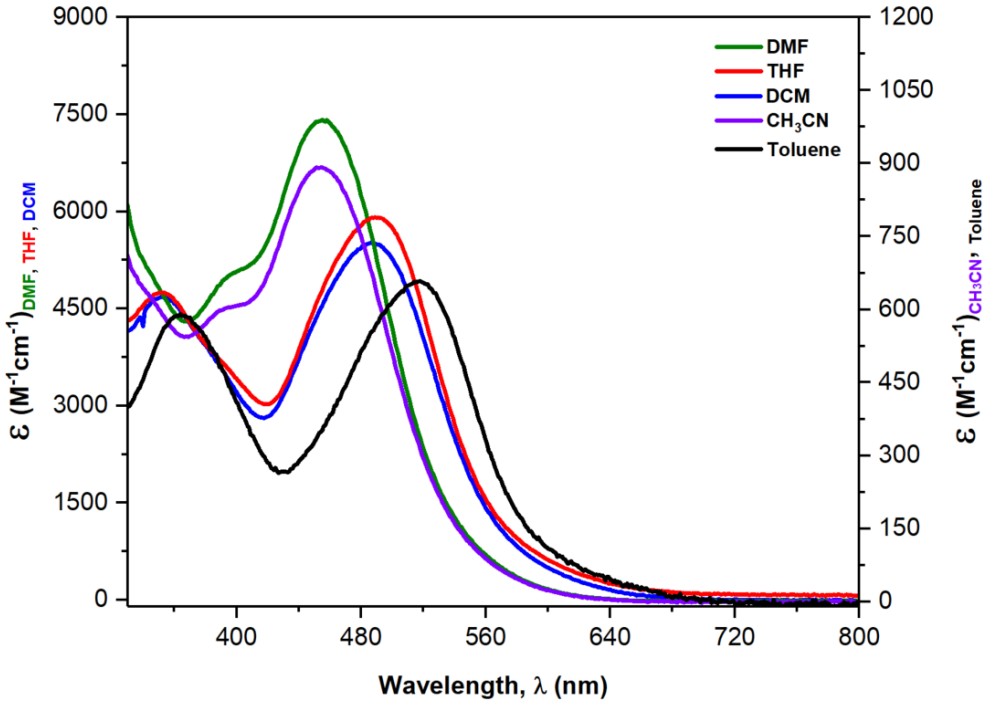

Figure II. 3 UV-Vis absorption spectra of $[W(bpy)(CO)_4]$ complexes in different organic solvents

Unlike the higher energy absorption bands in the near UV region which remain unshifted upon changing solvent medium, the MLCT band demonstrated some solvatochromic properties which have been reported in other substituted metal carbonyl complexes.[16-17]

Table II. 2 MLCT band shift of the $[M(bpy)(CO)_4]$ complexes in different organic solvents

Solvents (Solvent polarity)[a]	λ_{max}, nm [extinction molar coefficient ε, $M^{-1}cm^{-1}$]		
	$[Cr(bpy)(CO)_4]$	$[Mo(bpy)(CO)_4]$	$[W(bpy)(CO)_4]$
Toluene (2.4)	534 (810)	497 (2460)	518 (980)
DCM (3.1)	504 (2700)	470 (4800)	486 (5200)
THF (4)	506 (990)	473 (5000)	489 (5600)
CH_3CN (5.8)	471 (2700)	444 (4000)	455 (9000)
DMF (6.4)	470 (3200)	442 (4700)	454 (7000)

[a]Rohrschneider's polarity parameter

These [M(bpy)(CO)$_4$] complexes indicate a negative solvatochromism which manifests itself by a shift of the intense visible MLCT absorption band to higher energies (i.e. shorter wavelengths) as the solvent polarity increases (see **Table II. 2**). This solvatochromism characteristic of the MLCT transition of the [M(bpy)(CO)$_4$] complex is usually interpreted by different stabilization of the ground and excited states by electrostatic (mainly dipole-dipole) interactions with polar solvents.[6,11,18-21]

2.3. Electrochemical characterization of [M(bpy)(CO)$_4$] complexes

The electrochemical characterization of 1mM of [M(bpy)(CO)$_4$] complexes was done using cyclic voltammetry (CV) measurements. These CV measurements were performed at room temperature in acetonitrile with 0.1M $TBAPF_6$ as the supporting electrolyte. A three-electrode cell configuration saturated with argon was used, with the glassy carbon electrode (GCE) as the working electrode and all potential values recorded against Ag/10^{-2}M $AgNO_3$ as the reference electrode.

i. Electro-oxidation of [M(bpy)(CO)$_4$] complexes under argon

Under argon saturated conditions, two irreversible oxidation waves are detected in the anodic scan of the CV. As previously discussed in literature, these oxidation waves were reported to be metal centered.[22] **Figure II. 4a** displays the behavior of the [Mo(bpy)(CO)$_4$] in CH_3CN as an example.

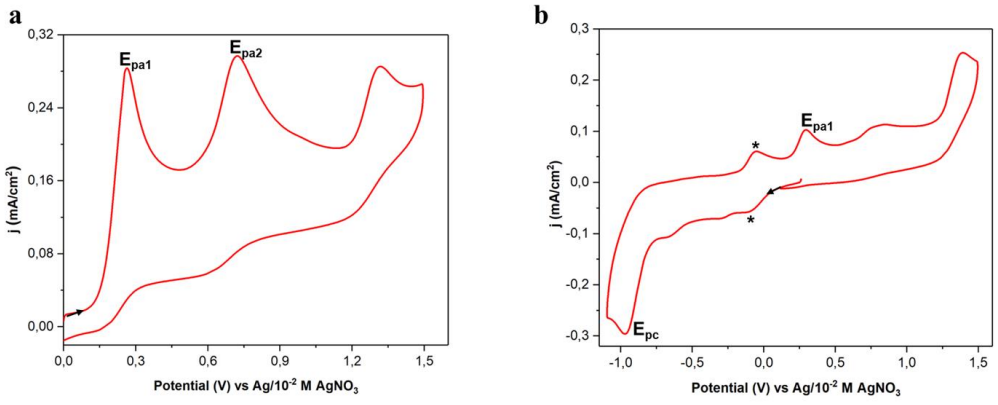

Figure II. 4 CV scans of the [Mo(bpy)(CO)$_4$] complex in CH_3CN/0.1M $TBAPF_6$ under argon, prior electrolysis (**a**) and after electrolysis (**b**) at +0.26V vs Ag/10^{-2}M $AgNO_3$ on a GCE at v =0.1Vs^{-1}. *Appearance of a new redox system after electrolysis at +0.26V

After the first oxidation wave at E_{pa1}= +0.26V, a release of one CO ligand is expected to occur leading to the coordination of a solvent molecule to the metal center; thus formation of the $[Mo^{I}(bpy)(CO)_3(CH_3CN)]^+$ cation. The second oxidation process at E_{pa2}= +0.72V induces the formation of transient $[Mo^{II}(bpy)(CO)_3(CH_3CN)]^{2+}$ species that lead to the formation of the heptacoordinate species of $[Mo^{II}(bpy)(CO)_3(CH_3CN)_2]^{2+}$.[22]

Similarly, to the work reported by Johnson et al., a CV scan performed after an exhaustive electrolysis at Epa_1 suggests the reduction of the $[Mo^{I}(bpy)(CO)_3(CH_3CN)]^+$ cation to its neutral form of $[Mo(bpy)(CO)_3(CH_3CN)]$ at E_{pc}= -0.97V (**Figure II. 4b**). As presented in the timescale of electrolysis (**Scheme II. 2**), this reduction wave is irreversible which suggests a formation of new chemically transformed species upon the release of the solvato ligand i.e. CH_3CN leading to $[Mo(bpy)(CO)_3]$. Re-coordination of the CO ligand to the metal center is likely to occur resulting in a partial regeneration of the starting $[Mo(bpy)(CO)_4]$ species as confirmed by the appearance of the oxidation peak at E_{pa1} on the reverse scan (**Figure II. 4b**).

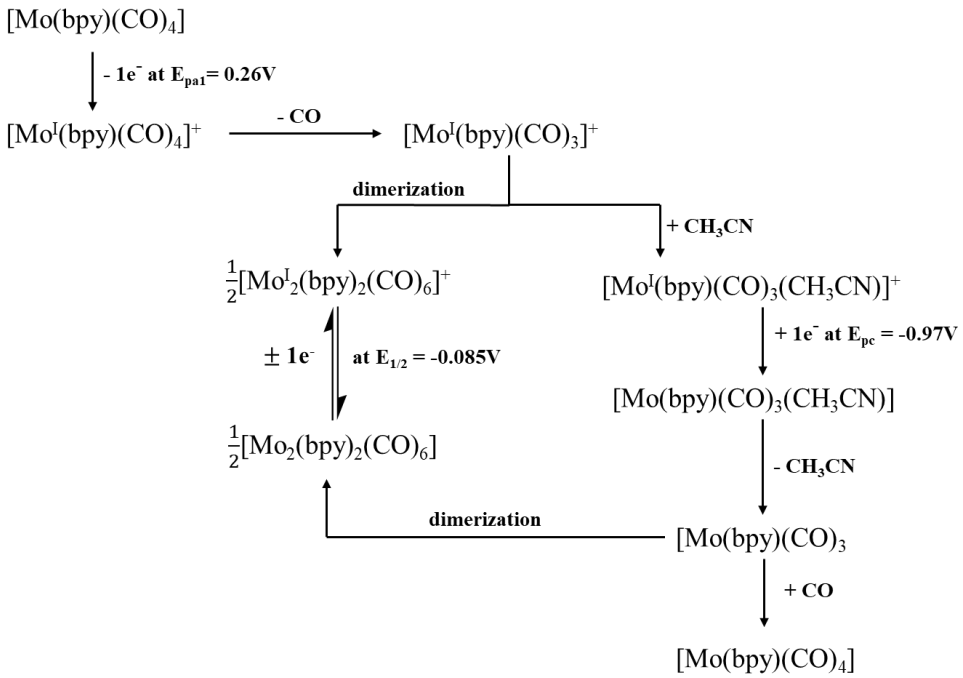

Scheme II. 2 Possible reaction mechanisms after electrolysis at E_{pa1} leading to the formation of different species upon oxidation, reduction, and ligand dissociation.

Additionally, an appearance of a minor redox system at -0.085V (***Figure II. 4b**) might suggest a formation of dimer species $[Mo_2(bpy)_2(CO)_6]^+$ and $[Mo_2(bpy)_2(CO)_6]$ from the $[Mo(bpy)(CO)_3]^+$ and $[Mo(bpy)(CO)_3]$ species respectively formed after CO and CH_3CN dissociation as depicted in **Scheme II. 2**.

ii. Electroreduction of [M(bpy)(CO)$_4$] complexes under argon

As depicted in **Figure II. 5** and **Table II. 3**, these [M(bpy)(CO)$_4$] complexes show two successive reduction steps. The first one-electron reduction detected at ca. -1.7V to -1.9V vs Ag/10^{-2}M $AgNO_3$ in CH_3CN is reversible (R1/O1) at the time scale of the CV, producing the corresponding radical-anions [M(bpy)(CO)$_4$]$^{\bullet-}$ with the added electron occupying the bpy-based SOMO,[3] indicating that the first reduction potential depends strongly on the diimine ligand while the metal atom has a much smaller influence.[12, 23-27] The second one-electron reduction (R2) of [M(bpy)(CO)$_4$]$^{\bullet-}$ to [M(bpy)(CO)$_4$]$^{2-}$ which occurs ca. 0.6 V more negatively, is chemically irreversible due to a fast dissociation of a CO ligand; hence, leading to the formation of [M(bpy)(CO)$_3$]$^{2-}$ species.[3]

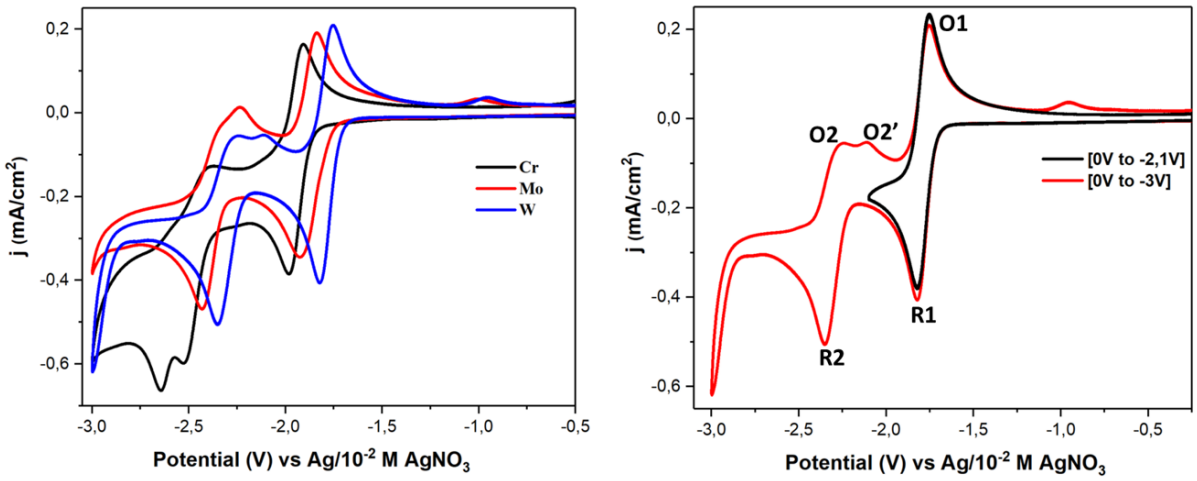

Figure II. 5 Cathodic CV scans of 1mM [M(bpy)(CO)$_4$)] complexes under argon atmosphere (left); and of a 1mM [W(bpy)(CO)$_4$)] complex under argon, showing a study of different reduction waves (right) on a GCE in CH_3CN/0,1M $TBAPF_6$ at v = 0.1Vs^{-1}.

This CO ligand loss results in the appearance of new anodic wave (O2') on the reverse scan, belonging to the oxidation of the strongly π-delocalized pentacoordinated dianion [M(bpy)(CO)$_3$]$^{2-}$ to [M(bpy)(CO)$_3$]$^{-}$, which is subsequently followed by a rapid re-coordination of the carbonyl ligand resulting to [M(bpy)(CO)$_4$]$^{\bullet-}$ species.

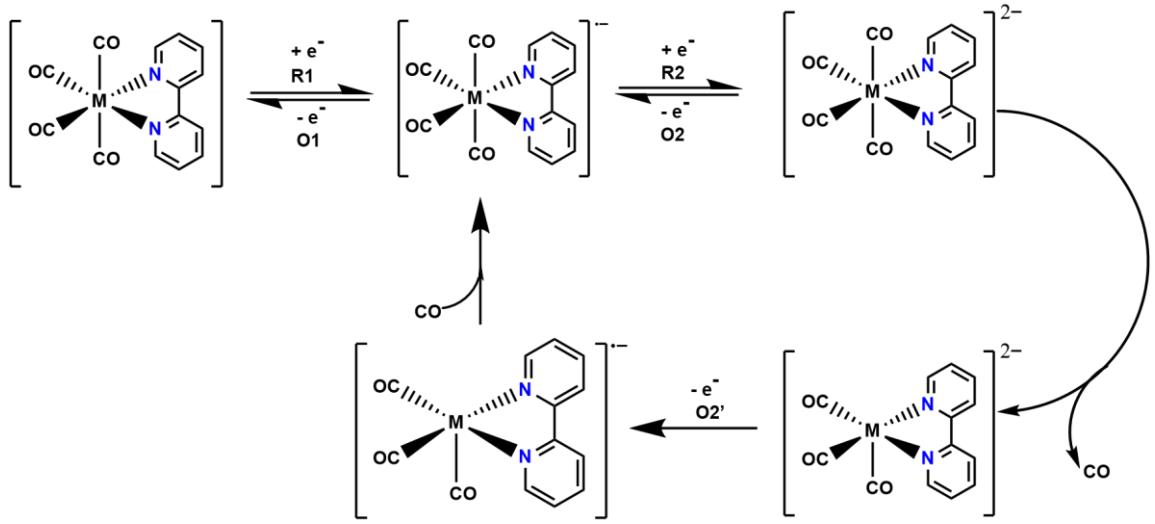

Scheme II.3 The electrochemical reduction and oxidation pathways of the $[M(bpy)(CO)_4]$ complexes (M=Cr, Mo, W) under argon saturated environment.

Depending on the rate of the CO dissociation after R2, the anodic wave (O2) represents the oxidation of the remaining $[M(bpy)(CO)_4]^{2-}$ species. While studying the second reduction system, a small oxidation wave (≈ -1V) is observed in the reverse scan of the $[M(bpy)(CO)_4]$ complex. This wave is suspected to represent the oxidation of less concentrated dimer species $[M_2(bpy)_2(CO)_6]^{2-}$ formed by the pentacoordinate $[M(bpy)(CO)_3]^-$ species or oxidation of the solvato complex $[M(bpy)(CO)_3(CH_3CN)]^-$.

Interestingly, the $[Cr(bpy)(CO)_4]$ complex displays two consecutive reduction waves at -2.53V and -2.64V after the first reduction event. This electrochemical behavior is attributed to a partial dissociation of the CO ligand from the $[Cr(bpy)(CO)_4]^-$ complex leading to $[Cr(bpy)(CO)_3]^-$. The latter complex is reduced at -2.53V whereas $[Cr(bpy)(CO)_4]^-$ is reduced at -2.64V.

The shift of the reduction potentials towards less negative values for the $[M(bpy)(CO)_4]$ complexes in the order of Cr >Mo >W indicates how the electron-withdrawing properties of the metal center can also play an important role in influencing the structure, reactivity and properties of a molecule, hence enhancing possible catalytic properties of these complexes.

Table II. 3 Electrode potentials of the [M(bpy)(CO)$_4$] complexes in CH_3CN/0.1M $TBAPF_6$ on a GCE.

Complexes	E (V) vs Ag / 0.01M $AgNO_3$			
	$E_{1/2}$ (ΔE_p)	R2	O2	O2'
Cr(bpy)(CO)$_4$	-1.95 (0.077)	-2.52; -2.64	-	-2.37
Mo(bpy)(CO)$_4$	-1.87 (0.093)	-2.43	-2.33	-2.23
W(bpy)(CO)$_4$	-1.78 (0.091)	-2.34	-2.24	-2.11

In-situ spectro-electrochemical measurements were recorded in CH_3CN at room temperature in the glove box. A modified three-electrode cell coupled with an UV-Vis probe was used as described in the experimental part. A UV-Vis absorption spectrum of the [Mo(bpy)(CO)$_4$] in CH_3CN solution was recorded parallel to the exhaustive electrolysis measurements at different reduction potentials.

As shown in **Figure II. 6**, one-electron reduction of the [Mo(bpy)(CO)$_4$] in CH_3CN at -1.95V led to the formation of bipyridine radical anion characterized by appearance of broad π-π* intraligand electronic absorption band (~380nm) in the high-energy near UV region, and a red shift of the MLCT transition bands was also observed.[28] Remarkably, a new weak and broad band was found around 840 nm, which may be the result of dimer formation.[29]

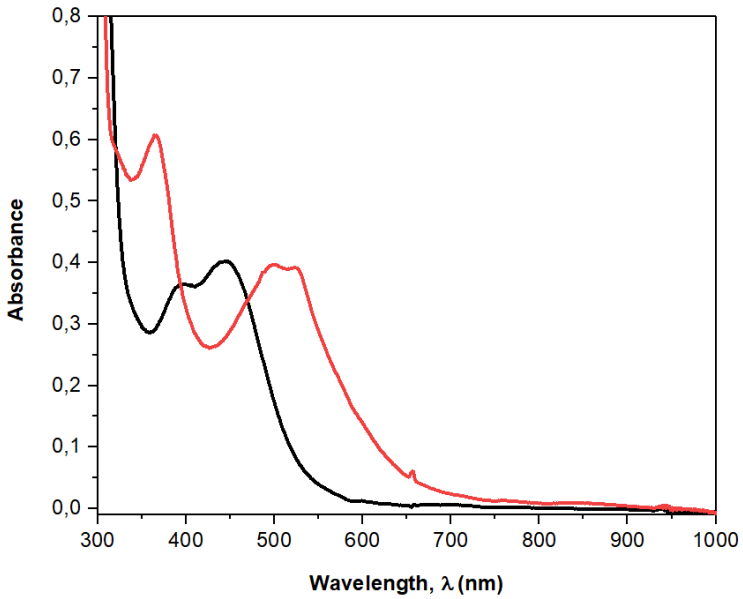

Figure II. 6 Absorption spectra of [Mo(bpy)(CO)$_4$] complex; prior electrolysis (black), after electrolysis (red) at -1.95V vs Ag/10^{-2}M $AgNO_3$ in CH_3CN.

Two novel reduction waves at -2.15V and -2.54V that were previously absent in the CV of the initial complex $[Mo(bpy)(CO)_4]$ are presented in a recorded CV following exhaustive electrolysis at -1.95V versus Ag/10^{-2}M $AgNO_3$ (**Figure II. 7, Table II. 3**). This finding implies that the complex's initial reduction process leading to $[Mo(bpy)(CO)_4]^{\bullet-}$ species, may not be entirely reversible and may trigger a chemical transformation of $[Mo(bpy)(CO)_4]^{\bullet-}$ to $[Mo(bpy)(CO)_3]^{\bullet-}$ as a result of CO dissociation. It is anticipated that this new pentacoordinate complex will coordinate with CH_3CN to generate $[Mo(bpy)(CO)_3(CH_3CN)]^{\bullet-}$ species that might be accountable for the new reduction waves.

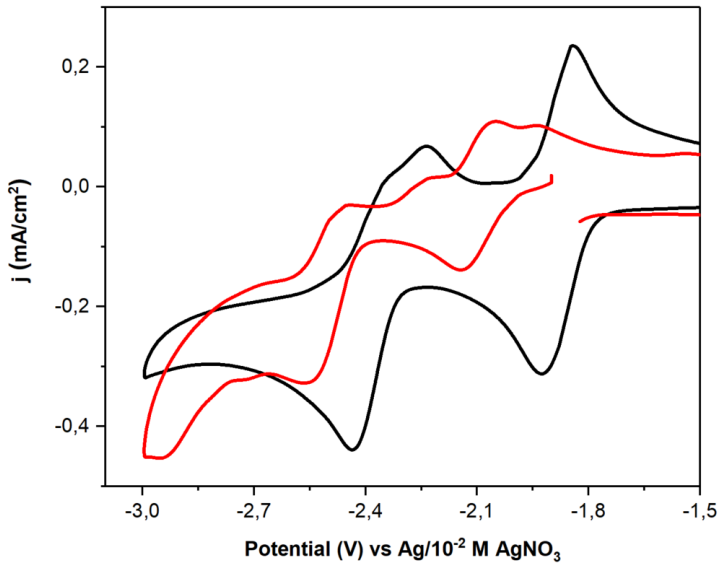

Figure II. 7 Cathodic CV scans of a 1mM $[Mo(bpy)(CO)_4)]$ complexes under argon prior (black) and after (red) electrolysis at -1.95V vs Ag/10^{-2}M $AgNO_3$ on a GCE in CH_3CN/0,1M $TBAPF_6$ at v = 0.1Vs^{-1}.

iii. Electrocatalytic reduction of CO_2 using $[M(bpy)(CO)_4]$ complexes

With the goal of investigating the electrocatalytic properties of the $[M(bpy)(CO)_4]$ complexes, CV measurements were carried out in a CO_2 saturated environment. A three-electrode cell configuration containing 1mM of the $[M(bpy)(CO)_4]$ complex in 10 mL of CH_3CN solution was purged with CO_2 gas prior running the CV measurements.

Under CO_2 as shown in **Figure II. 8**, each of the investigated complexes showed a minor reversibility loss occurring at the first reduction wave and a cathodic current enhancement on the second reduction wave in the potential range of -2.3 V to -2.5 V, in comparison to the CV

scans obtained under argon. Interestingly, the onset potential value (at which a catalytic current response is observed in the presence of a catalyst) is noticeably at less negative values in comparison to the experimental cathodic potential value of the direct electroreduction of CO_2 (in the absence of a catalyst), proving the catalytic properties of the $[M(bpy)(CO)_4]$ complexes.

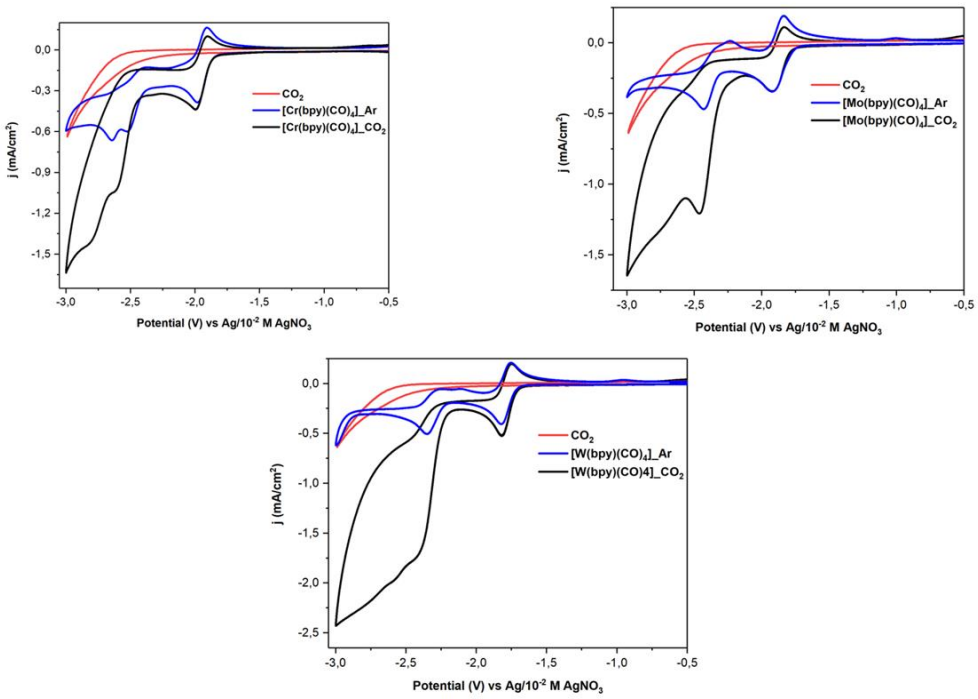

Figure II. 8 Cathodic CV scans of a 1mM $[M(bpy)(CO)_4)]$ complexes under argon and CO_2 saturated conditions on a GCE in CH_3CN/0,1M $TBAPF_6$ at v= 0.1Vs^{-1}.

The loss of reversibility suggests an improved chemical transformation of the $[M(bpy)(CO)_4]^{\bullet-}$ species in the presence of carbon dioxide. So far, electrocatalytic studies of CO_2 reduction by $[M(bpy)(CO)_4]$ complexes have shown the inactivity of $[M(bpy)(CO)_4]^{\bullet-}$ species in reducing CO_2.[2,3]

Given the cathodic current enhancement on the second reduction wave coincides with cathodic potential where the pentacoordinate dianion $[M(bpy)(CO)_3]^{2-}$ species are formed, this points to the five-coordinate dianion species as the active catalytic species for the reduction of carbon dioxide.[3,28] As shown in **Scheme II. 4**, there are two possible reduction pathways depending on the conditions in place. In anhydrous condition, the interaction of these active species with CO_2 leads to the formation of reduced carbon-based products such as CO, whereas in hydrous condition the formation of H_2 gas will occur as a result of the hydrogen proton reduction.

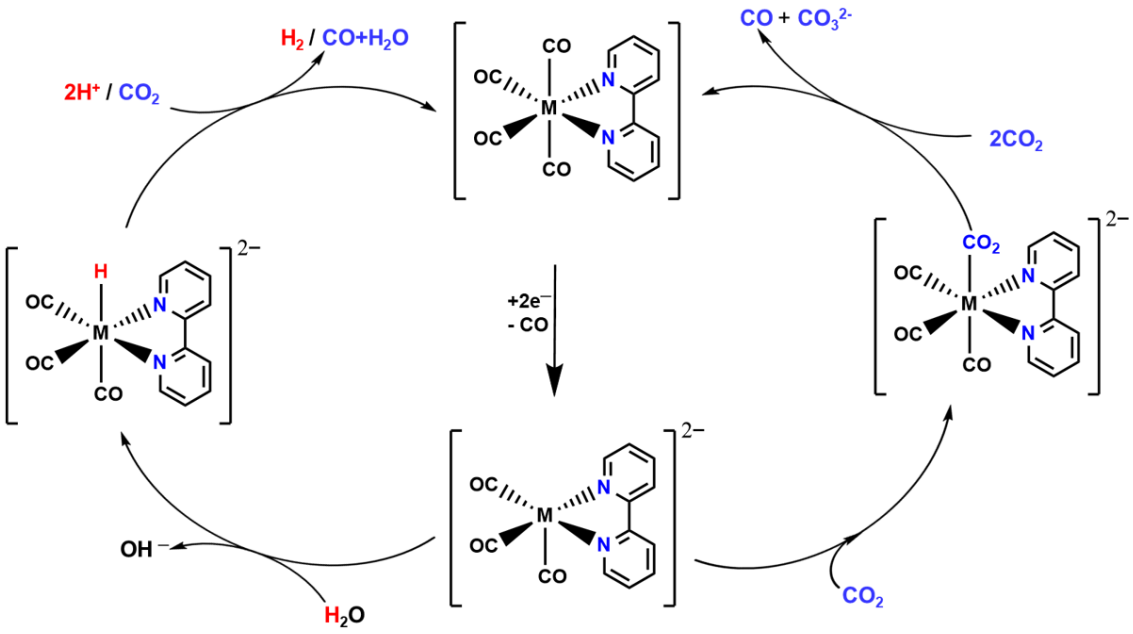

Scheme II. 4 The electrochemical reduction pathways of the [M(bpy)(CO)$_4$] complexes (M=Cr, Mo, W) under a CO_2 saturated environment in the presence (left) and absence(right) of protons.

The ratio of a catalytic peak current i_{cat} at the second reduction peak under CO_2 to the non-catalytic response i_p under argon atmosphere (i_{cat}/i_p) is useful in evaluating the catalytic activity of a complex. The [W(bpy)(CO)$_4$] and [Mo(bpy)(CO)$_4$] complexes were reported to have better catalytic activities than the [Cr(bpy)(CO)$_4$] complex as depicted in **Table II. 4**. This difference in catalytic activity could be due to a possible interaction of $[Cr(bpy)(CO)_3]^{2-}$ species with an acetonitrile molecule.

Moreover, the [Cr(bpy)(CO)$_4$] complex exhibits a catalytic peak current at a negative reduction potential about 100mV and 180mV higher than that of [Mo(bpy)(CO)$_4$] and [W(bpy)(CO)$_4$] respectively. This observation makes the chromium carbonyl complexes less efficient as catalysts compared to the corresponding Mo and W analogous systems.

Table II. 4 i_{cat}/i_p ratios of the [M(bpy)(CO)$_4$] complexes at the second reduction peak in CH_3CN/0.1M $TBAPF_6$

Complexes	i_{cat}/i_p
[Cr(bpy)(CO)$_4$]	1.03
[Mo(bpy)(CO)$_4$]	2.43
[W(bpy)(CO)$_4$]	2.76

Additionally, by employing the "Foot of the wave" (FOW) analysis developed by Savéant and Constentin[30,31] a kinetic rate constant (k_{cat}) of a catalytic reaction can be estimated using **Eq II. 1**. A linear correlation between the current ratio ip/i_p^0 and the term $1/(1+exp[F/RT(E\text{-}E_{cat}^0)])$ was developed using standard CV measurements of the $[M(bpy)(CO)_4]$ complexes in the absence and presence of the CO_2 substrate as presented in **Figure II. 9**.

$$\frac{i_p}{i_p^0} = \frac{2.24\sqrt{\frac{RT}{Fv}\,2k_{cat}c_{cat}}}{1+exp\left[\frac{F}{RT}(E-E_{cat}^0)\right]} \qquad \textbf{Eq II. 1}$$

From **Eq II. 1**, i_p represents the catalytic current in the presence of CO_2, i_p^0 is the peak current intensity in the absence of CO_2 (under argon), F is the Faraday constant, R is the perfect gas constant, T is the absolute temperature, v is the scan rate expressed in Vs^{-1}, c_{cat} is the initial concentration of a catalyst, E is the applied potential and $E_{cat}^0$is the standard potential of the reversible reduction peak of the active form of the catalyst.

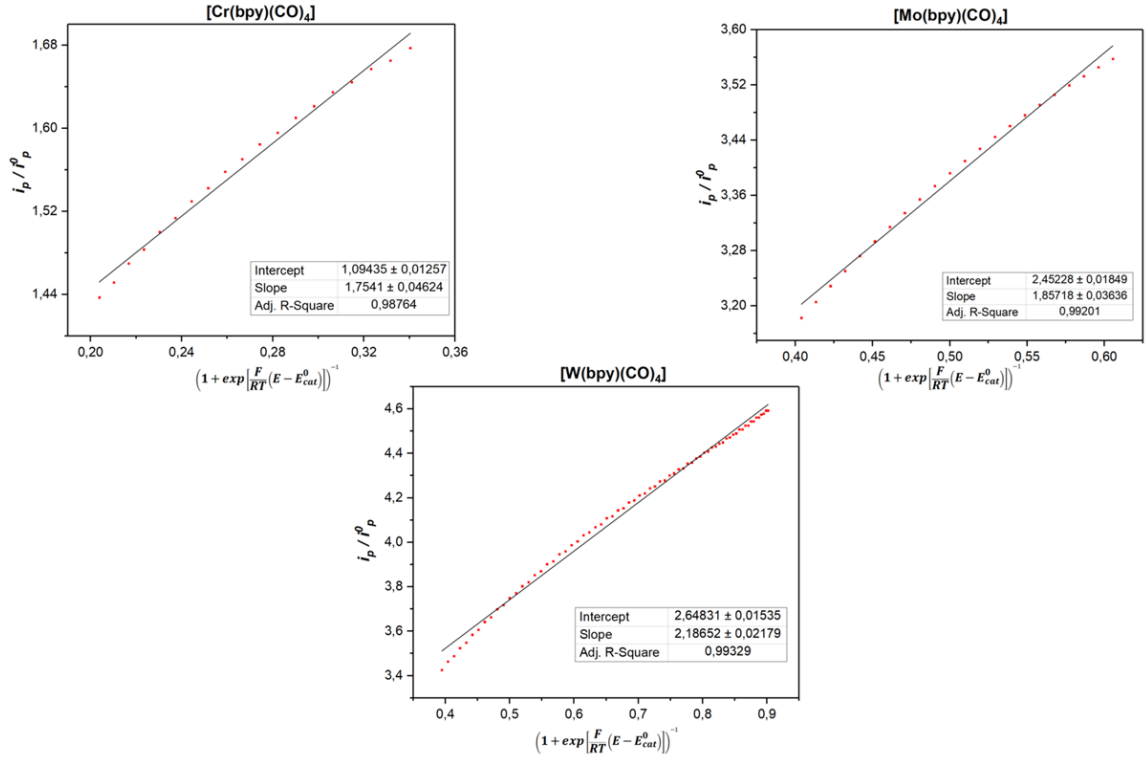

Figure II. 9 FOW analysis of the catalysis of CO_2 reduction by 1 mM $[M(bpy)(CO)_4]$ complexes on a GCE in CH_3CN/0,1M $TBAPF_6$ at v =0.1Vs^{-1}.

Theoretical k_{cat} values of these complexes were calculated by equating the slope of the linear correlation presented in **Figure II. 9** to the slope of the linear correlation presented in **Eq II.1** i.e. $2.24\sqrt{\frac{RT}{Fv}\,2k_{cat}c_{cat}}$.

Table II.5 Theoretical k_{cat} values of the catalysis of CO_2 reduction by 1 mM [M(bpy)$(CO)_4$] complexes on a GCE in CH_3CN/0,1M $TBAPF_6$ at v =0.1Vs^{-1}.

[M(bpy)$(CO)_4$]	Slope	k_{cat} ($M^{-1}s^{-1}$)
[Cr(bpy)$(CO)_4$]	1.7541	1194
[Mo(bpy)$(CO)_4$]	1.8572	1338
[W(bpy)$(CO)_4$]	2.1865	1855

From **Table II. 5**, the theoretical k_{cat} values are presented in an ascending order, with the k_{cat} values of the [Cr(bpy)$(CO)_4$] being the lowest. This observation is similar to that of the i_{cat}/i_p ratios of the [M(bpy)$(CO)_4$] complexes reported in **Table II.4**, which further confirms the [Cr(bpy)$(CO)_4$] complex being the least efficient catalyst in this family of complexes.
Besides this observation it is important to take note of the deviation of the linear correlation presented in **Figure II. 9** to that presented in **Eq II.1**. With the y-intercept not equating to zero, the reaction mechanism for this family of complexes is expected to be different to that reported in literature for the iron porphyrins that presented fast and efficient catalysis.[30]

Depending on the rate to which these active catalytic [M(bpy)$(CO)_3]^{2-}$ species are formed, only a small quantity can be available for the reduction of CO_2. However, in the presence of a weak acid as a source of protons, alternative active species could be formed [M(bpy-H)$(CO)_3]^-$ which can result in an increase of a catalytic current.[3] With the aim of achieving the latter, the [W(bpy)$(CO)_4$] complex was investigated electrochemically in the presence of two different types of proton sources (H_2O and phenol).

CV scans of 1mM of complex in CH_3CN/0,1M $TBAPF_6$ were recorded step by step, starting with a CV under argon conditions followed by a purging of CO_2 in the complex solution to create a CO_2 saturated environment. After this CV scan, either 0.3M of phenol (**Figure II. 10**) or 1% v/v of H_2O (**Figure II. 11**) was introduced into the complex solution then after another CV scan was recorded.

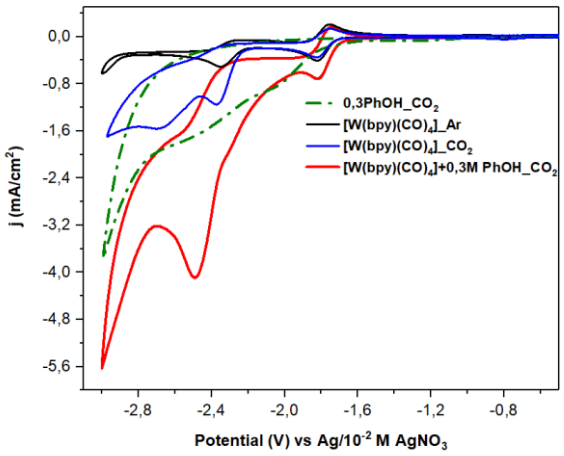

Figure II. 10 Cathodic CV scans of a 1mM [W(bpy)(CO)$_4$)] complex under argon (blue), under CO_2 (black), under CO_2 in the presence of phenol (red) and of phenol in the absence of a complex under CO_2 (green, dash lines) on a GCE in CH_3CN/0,1M $TBAPF_6$ at v = 0.1Vs^{-1}.

For either of these weak acids to be appropriate sources of protons, an increase of catalytic current and/or shift of the onset potential towards lesser negative values is anticipated. However, it is important to confirm that the current response detected is mainly due to the catalytic properties of the complex and not due to direct reduction of these weak acids. To confirm this, separate CV scans of these proton sources in blank electrolytes were recorded within the same potential range as that of other CVs and then added on **Figure II. 10** and **Figure II. 11** for 0.3M phenol and 1% v/v H_2O respectively.

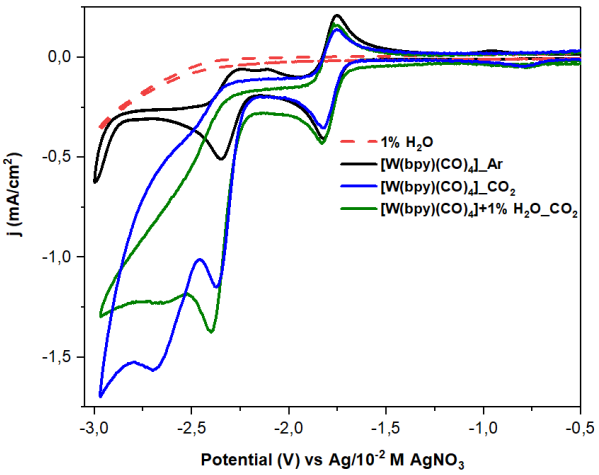

Figure II. 11 Cathodic CV scans of a 1mM [W(bpy)(CO)$_4$)] complex under argon (black), under CO_2 (purple), under CO_2 in the presence of H_2O (green) and of H_2O in the absence of a complex under CO_2 (red, dash lines) on a GCE in CH_3CN/0,1M $TBAPF_6$ at v = 0.1Vs^{-1}.

Among these two weak acids (water and phenol), the use of water was found to be more favorable than phenol due to the direct reduction of phenol within the same potential range as that of the catalytic activity.

In investigating the efficiency and selectivity of the $[M(bpy)(CO)_4]$ complex, gas chromatography measurements were carried out parallel to exhaustive electrolysis on mainly the $[Mo(bpy)(CO)_4]$ and $[W(bpy)(CO)_4]$ complex at given onset potentials in the presence of water as the source of protons. (See **Table II. 6**). The production of HCOOH acid was detected using an ionic chromatography technique at the end of the conducted experiment.

Table II. 6 Faradaic efficiencies of 1mM $[M(bpy)(CO)_4]$ complexes (with M=Mo, W) in the presence of 1%v/v H_2O in CH_3CN/0.1M $TBAPF_6$ at v =0.1Vs^{-1}.

Complex	E_{onset} (V)	Time (mins)	Q (C)	%CO	%HCOOH
$[Mo(bpy)(CO)_4]$	-2.35	75	-15	38	
		170	-38	21	
		240	-54	14	5
$[W(bpy)(CO)_4]$	-2.3	120	-20	15	
		140	-36	12	11

From faradaic efficiency values of these complexes, it is evident that the $[Mo(bpy)(CO)_4]$ complex is much more reactive towards the production of CO compared to the $[W(bpy)(CO)_4]$ complex that produced more HCOOH than $[Mo(bpy)(CO)_4]$.

A different and new approach was investigated as a possibility of lowering the catalytic onset potential for CO_2 reduction by substituting one of the carbonyl ligands with a halide ligand. This was done by synthesizing a new family of tris-carbonyl metal complexes $[M(bpy)(CO)_3Cl]^-$ (M=Mo, W) presented in the following part of this chapter.

3. Bipyridyl tricarbonyl halide metal complexes $[M(bpy)(CO)_3Cl]^-$, M=Mo, W

3.1. Synthesis

The synthesis of $PPh_4[M(bpy)(CO)_3Cl]$ complex was prepared by a reflux reaction of $[M(bpy)(CO)_4]$ complex with Ph_4PCl in either a mixture of toluene/acetonitrile for **M=Mo** or in a mixture of xylene/acetonitrile for **M=W**. Upon cooling, the product was collected from filtration, rinsed with cold methanol and dried under vacuum.[32]

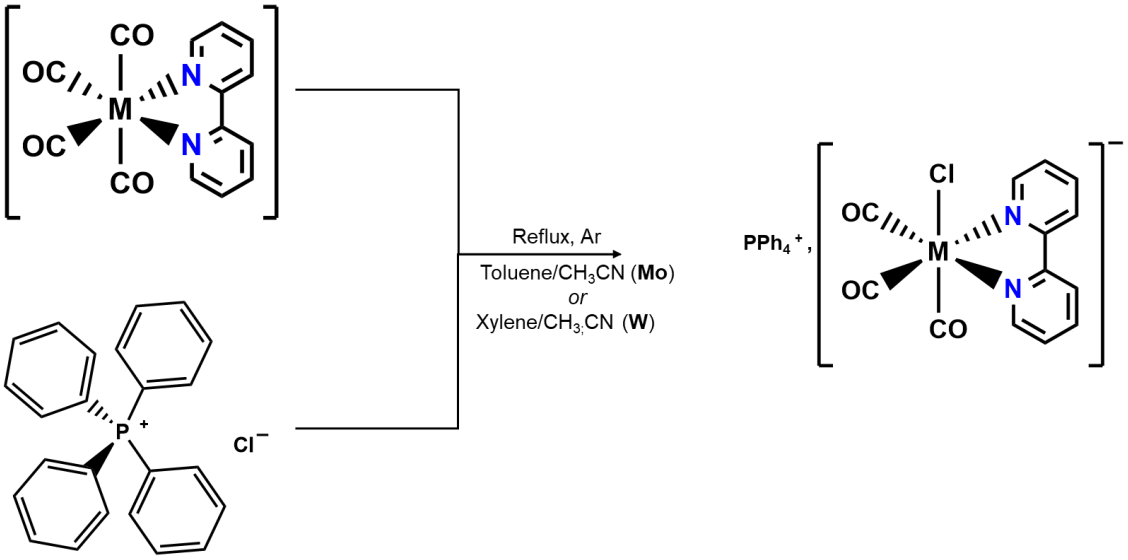

Scheme II. 5 Synthesis of $PPh_4[M(bpy)(CO)_3Cl]$ complexes.

These anionic complexes were obtained in low yields as solid powder that was sparingly soluble in most non-coordinating and low polar solvents such as $CHCl_3$ and CH_2Cl_2 and readily soluble in coordinating and polar solvents such as CH_3CN.

Complexes of stoichiometry $[ML_2(CO)_3X]^-$ with L_2 as a bidentate chelating ligand were found to possibly exist in either of two isomeric forms, both of which should give rise to three infrared-active terminal carbonyl stretching vibrations. In general, the fac-isomer may be distinguished from the mer-isomer by band intensity measurements, since in the former case three strong absorptions are predicted whereas one weak and two strong bands are expected for the latter.[33]

Both of the anionic complexes under discussion show three strong carbonyl stretching vibrations attributed to the symmetry species A_1 and E in the solid state, hence assigned to the fac-configuration of local pseudo-C_{3v} symmetry. [34,35] (**Table II. 7**)

Table II. 7 FT-IR spectral data and assignments for the anionic $[M(bpy)(CO)_3Cl]^-$ complexes in the carbonyl stretching region.

Complex	Bands, cm^{-1}		
	A_1	E	E
$[Mo(bpy)(CO)_3Cl]^-$	1885	1765(sh)	1744
$[W(bpy)(CO)_3Cl]^-$	1874	1759(sh)	1739

3.2. Photophysical properties

From the UV absorption spectra, the electronic absorption properties of the $[M(bpy)(CO)_3Cl]^-$ anionic complexes were hardly noticeable in most organic solvents except in CH_3CN as shown in **Figure II. 12**.

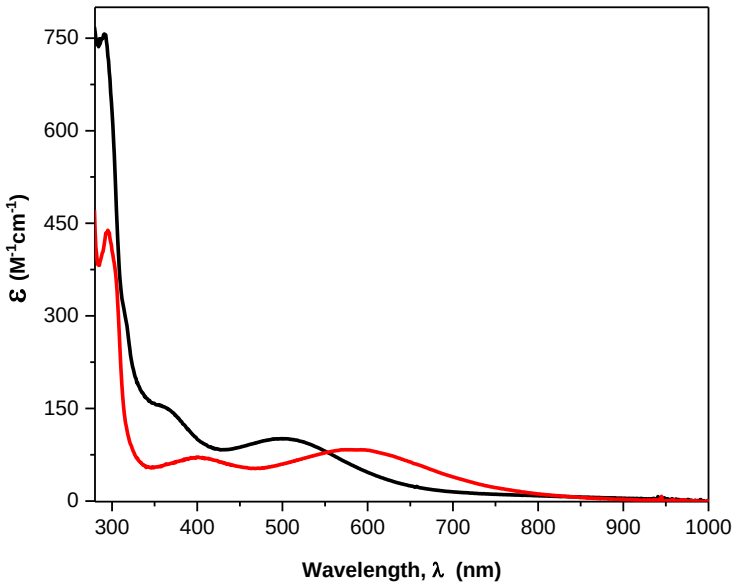

Figure II. 12 Absorption spectra of $[M(bpy)(CO)_3Cl]^-$ anionic complexes in CH_3CN; $[W(bpy)(CO)_3Cl]^-$ complex (red) and $[Mo(bpy)(CO)_3Cl]^-$ complex(black).

The absorption bands in the visible range (~350-800 nm) correlates to the metal centered electronic transitions, and it may be noted that these forbidden d-d electronic transitions are generally at lower energies than the corresponding tetracarbonyl complexes $[M(bpy)(CO)_4]$. The absorption band in the UV region (~300 nm) is attributed to the LC electronic transitions.

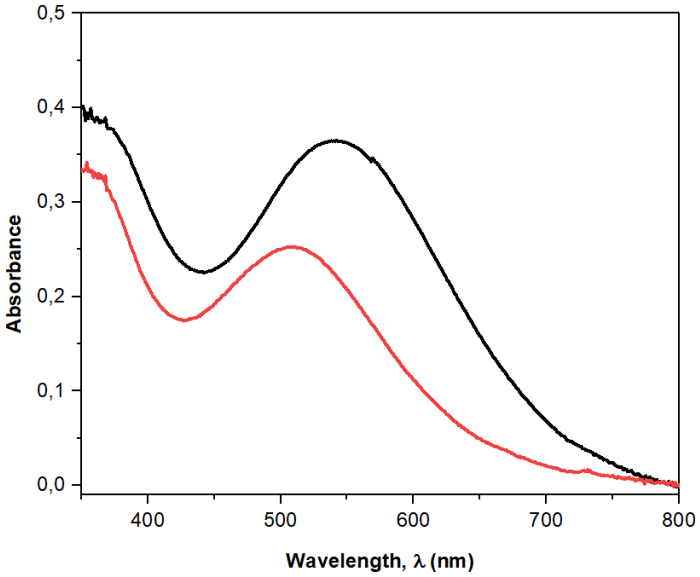

Figure II. 13 UV-Vis absorption spectra of $[Mo(bpy)(CO)_3Cl]^-$ anionic complex in CH_3CN (red) and DMF (black).

Given the poor solubility of these complexes in most of the organic solvents, the investigation of the solvatochromism effect was hardly obtained with an exception of the $[Mo(bpy)(CO)_3Cl]^-$ complex which was soluble in both CH_3CN and DMF (**Figure II. 13)**. From this spectrum, this anionic $[Mo(bpy)(CO)_3Cl]^-$ complex displays a solvent dependency behavior of the MLCT band in the visible range similar to the tetracarbonyl metal complexes. Among these two reported polar solvents, a significant red-shift of the MLCT transition band is observed in DMF which is more polar than CH_3CN i.e. positive solvatochromism.

3.3. Electrochemical characterization of $PPh_4[M(bpy)(CO)_3Cl]$ complex

i. Electro-oxidation of $[M(bpy)(CO)_3 Cl]^-$ complex under argon

The anodic CV scans of the $[M(bpy)(CO)_3Cl]^-$ complexes in **Figure II. 14** presents three and two irreversible oxidation waves for the M= Mo and W respectively. The first irreversible wave of these complexes at -0.38V and -0.31V for M= Mo and W respectively, can be associated with the oxidation of the metal center ($M^{0/+}$). A potential shift of 70 mV between the $[Mo(bpy)(CO)_3Cl]^-$ and $[W(bpy)(CO)_3Cl]^-$ complexes demonstrates a favorable oxidation of the Mo metal in comparison to the W metal center.

Upon 1e$^-$ oxidation, a release of the halide ligand is to be expected which will then result in the formation of $[M^I(bpy)(CO)_3(CH_3CN)]^0$ species. Evidently, these latter species will be reduced in the reverse scan at the reduction peaks of around -1.3 to -1.5V (see **Figure II. 15)**.

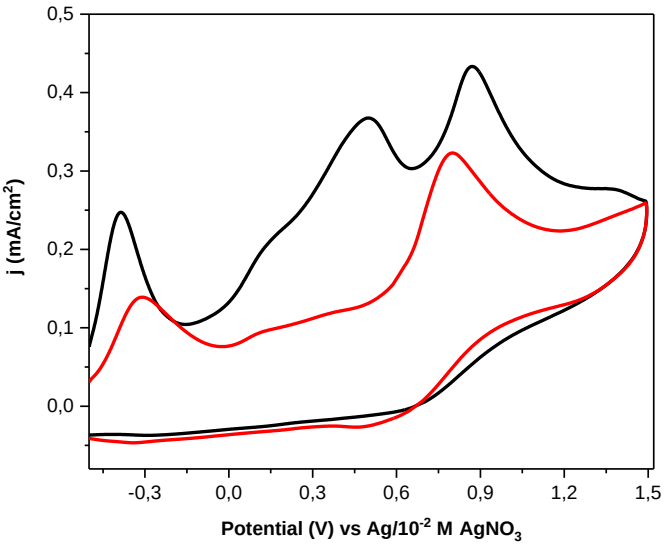

Figure II. 14 Anodic CV scans of 1mM complex; $[Mo(bpy)(CO)_3Cl]^-$ (black) and $[W(bpy)(CO)_3Cl]^-$ (red) under argon on a GCE in CH_3CN/0,1M $TBAPF_6$ at v = 0.1Vs^{-1}.

In addition to the first irreversible peak, other oxidation peaks observed are almost similar in characteristics to the oxidation peaks detected in the PPh_4Cl salt (see **Table II. 8)**. This observation might suggest that these oxidation peaks may not only represent further oxidation of the metal center but a possible oxidation process of the PPh_4Cl salt.

Table II. 8 Oxidation potentials of the $[M(bpy)(CO)_3Cl]^-$ complexes in CH_3CN/0.1M $TBAPF_6$ on a GCE.

Complexes	**E (V) vs Ag / 0.01M $AgNO_3$**		
	E_{pa1}	**E_{pa2}**	**E_{pa3}**
PPh_4^+, $[Mo(bpy)(CO)_3Cl]^-$	-0.38	0.5	0.86
PPh_4^+, $[W(bpy)(CO)_3Cl]^-$	-0.31	-	0.8
PPh_4Cl	-	0.5	0.8

ii. Electroreduction of $[M(bpy)(CO)_3 Cl]^-$ complex under argon

This anionic complex was electrochemically characterized with cyclic voltammetry, in an CH_3CN/0.1M $TBAPF_6$ electrolyte using a glassy carbon electrode (d = 3 mm) as a WE. In the cathodic scan of the CV presented in **Figure II. 15**, these anionic complexes demonstrated one reversible system followed by two successive irreversible reduction waves at E_{pc1} = -2.2 V and E_{pc2} = -2.5 V vs Ag/10^{-2}M $AgNO_3$ as shown in **Table II.9**.

Table II. 9 Electrode potentials of 1mM $[M(bpy)(CO)_3Cl]^-$ complexes in CH_3CN/0.1M $TBAPF_6$ on a GCE.

Complexes	E (V) vs Ag / 0.01M $AgNO_3$			
	$E_{1/2}$	ΔE_p	E_{pc1}	E_{pc2}
PPh_4^+, $[Mo(bpy)(CO)_3Cl]^-$	-1.96	0.059	-2.22	-2.56
PPh_4^+, $[W(bpy)(CO)_3Cl]^-$	-1.88	0.049	-2.22	-2.54

The half-wave potential values ($E_{1/2}$) of the reversible system were -1.96V and -1.88V for $[Mo(bpy)(CO)_3Cl]^-$ and $[W(bpy)(CO)_3Cl]^-$ respectively. The difference in the $E_{1/2}$ potential value of about 80mV between these anionic metal complexes is associated with the electron withdrawing properties of the metal center. The same effect was observed for the tetracarbonyl relative species.

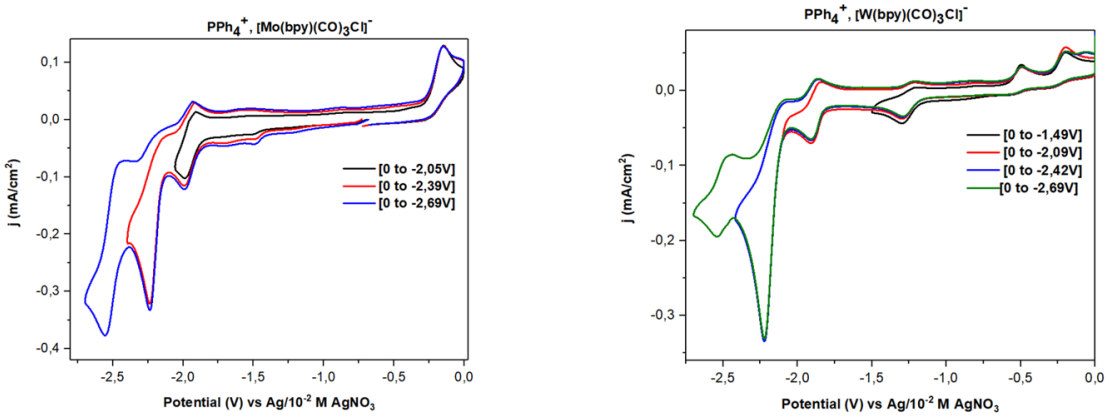

Figure II. 15 Cathodic scan CVs of 1mM complex; $[Mo(bpy)(CO)_3Cl]^-$ (left) and $[W(bpy)(CO)_3Cl]^-$ (right) under argon on a GCE in CH_3CN/0,1M $TBAPF_6$ at v = 0.05Vs^{-1}.

In comparison to the potential values of the tetracarbonyl complexes, the $E_{1/2}$ potential values of the $[M(bpy)(CO)_3Cl]^-$ complexes were shifted by 100mV towards higher negative potentials.

This shift is possibly due to an electron rich environment around the metal center associated with the presence of a chloride ligand, which could eventually result in an electron repulsion towards the first incoming electron from the WE.

Additionally, an interesting reduction wave is detected at less negative potential values of around -1.3 ~ -1.5V for the $[W(bpy)(CO)_3Cl]^-$ and $[Mo(bpy)(CO)_3Cl]^-$ respectively. This could be a consequence of a halide release process in solution leading to an equilibrium between $[M(bpy)(CO)_3Cl]^-$ and $[M(bpy)(CO)_3(CH_3CN)]$ species, with the latter species being reduced at -1.3V in the case of M=W and -1.5V for M=Mo.

It should be noted that the reduction of these species is fully irreversible in the case of M=Mo whereas it is partially reversible for M=W. In this case the reverse scan shows an oxidation peak around E_p= -1.25V close to the oxidation peak attributed to $[W(bpy)(CO)_3(CH_3CN)]^-$ or $[W_2(bpy)_2(CO)_6]^{2-}$ by analysis of the CV of $[W(bpy)(CO)_4]$ in CH_3CN as previously mentioned in the former part of this chapter.

Interestingly, a distinct reduction wave was observed at -2.22V vs $Ag/10^{-2}M$ $AgNO_3$ which was found to be common in both of the $[M(bpy)(CO)_3Cl]^-$ complexes. In an attempt to assign this reduction process to the proper species, 1mM of the PPh_4Cl salt was electrochemically investigated.

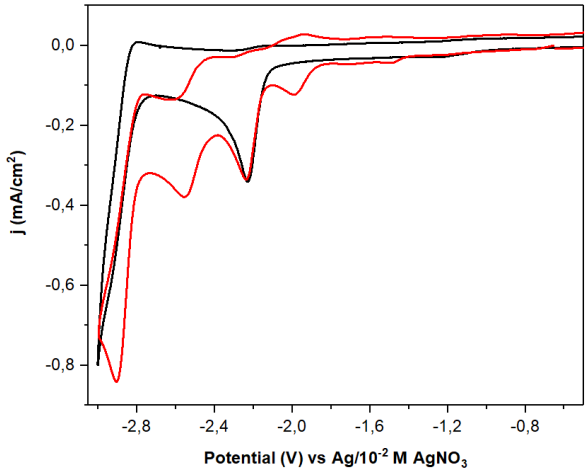

Figure II. 16 Cathodic scan CVs of a 1mM PPh_4Cl salt (black) and 1mM $[Mo(bpy)(CO)_3Cl]^-$ complex (red) under argon conditions on a GCE in CH_3CN/0,1M $TBAPF_6$ at ν = $0.1Vs^{-1}$.

Through CV measurements, this peak was confirmed to be a reduction wave associated to the counter ion of these complexes, i.e. Ph_4P^+. As presented in **Figure II. 16**, upon complexation the presence of this PPh_4^+ cation was still detected in the CV scans of the $[M(bpy)(CO)_3Cl]^-$ complexes.

From the in-situ spectro-electrochemical measurements done parallel to electrolysis of these complexes under inert atmosphere led to the evolution of the absorption spectra as shown in **Figure II. 17**. Electrolysis at the -1.95V led to an intense band formation around 365 nm linked to the formation a bipyridine radical anion as a result of having the incoming electron density centered on the bipyridine ligand.[4]

During this step, a broadening and a blue shift of the MLCT band in the visible range was also detected. When investigating electrolysis -2.5V vs $Ag/10^{-2}M$ $AgNO_3$, a new broad absorption band around 840 nm was formed, suggesting a possible metal-metal dimer formation.[29,36]

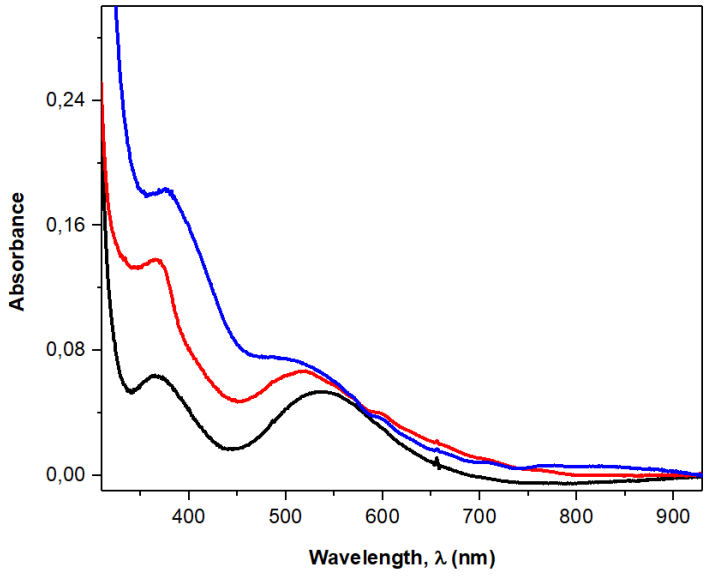

Figure II. 17 Absorption spectra of $[W(bpy)(CO)_3Cl]^-$ complex; prior electrolysis (black), after electrolysis at -1.9V vs $Ag/AgNO_3$ (red) and at -2.5V vs $Ag/AgNO_3$ (blue).

The spectro-electrochemical data thus shows upon one-electron reduction of the $[M(bpy)(CO)_3Cl]^-$ complex, bis-reduced species $[M(bpy)(CO)_3Cl]^{2-}$ are formed (**Eq 1**). These species could afterwards undergo partial loss of the Cl^- ligand (**Eq 2**) resulting in the co-existence of $[M(bpy)(CO)_3]^-$ and $[M(bpy)(CO)_3Cl]^{2-}$ species. This heterolytic splitting of the metal-halide bond is in fact a typical property of the radical anions $[M(L)(CO)_3X]^-$ (M = Mn, Re) with strongly basic diimine $[L]^-$ radical ligands.[29]

$$[M(bpy)(CO)_3Cl]^- + e^- \xrightleftharpoons{R1/O1} [M(bpy)(CO)_3Cl]^{2-} \quad \textbf{Eq 1}$$

$$[M(bpy)(CO)_3Cl]^{2-} \longrightarrow [M(bpy)(CO)_3]^- + Cl^- \quad \textbf{Eq 2}$$

$$[M(bpy)(CO)_3]^- + CH_3CN \longrightarrow [M(bpy)(CO)_3\ (CH_3CN)]^- \quad \textbf{Eq 3}$$

and /or

$$[M(bpy)(CO)_3]^- + [M(bpy)(CO)_3]^- \longrightarrow [M(bpy)(CO)_3]_2^{2-} \quad \textbf{Eq 4}$$

$$[M(bpy)(CO)_3\ (CH_3CN)]^- + e^- \xrightarrow{R2} [M(bpy)(CO)_3]^{2-} + CH_3CN \quad \textbf{Eq 5}$$

and / or

$$[M(bpy)(CO)_3]_2^{2-} + e^- \xrightarrow{R2} 2\ [M(bpy)(CO)_3]^{2-} \quad \textbf{Eq 6}$$

With the $[M(bpy)(CO)_3]^-$ species being unstable, the formation of the $[M(bpy)(CO)_3(CH_3CN)]^-$ and $[M_2(bpy)_2(CO)_6]^{2-}$ species inevitably occurs as a result of CH_3CN coordinating to the metal center (**Eq 3**) and the creation of a bond between the two metal centers (**Eq 4**) respectively. At the third reduction wave, the one-electron reduction reaction could propagate the formation of the bis-reduced species i.e. $[M(bpy)(CO)_3]^{2-}$ through further reduction of either the $[M(bpy)(CO)_3(CH_3CN)]^-$ or $[M_2(bpy)_2(CO)_6]^{2-}$ species in **Eq. 5** and **6** respectively. The indicated reduction potentials for **equations 1-6** are presented in **Table II.10**.

Table II.10 Summary of reduction potentials of the PPh_4^+, $[M(bpy)(CO)_3Cl]^-$ complexes in CH_3CN/0.1M $TBAPF_6$ on a GCE.

Complexes	**E (V) vs Ag / 0.01M $AgNO_3$**	
	R1	**R2**
PPh_4^+, $[Mo(bpy)(CO)_3Cl]^-$	-1.96	-2.56
PPh_4^+, $[W(bpy)(CO)_3Cl]^-$	-1.88	-2.54

iii. Electrocatalytic reduction of CO_2 using $[M(bpy)(CO)_3\ Cl]^-$ complexes

These complexes were studied using CV in organic medium CH_3CN/0.1 M $TBAPF_6$ under a CO_2 atmosphere to observe if they do contribute to the electroreduction of CO_2 by acting as a catalyst. From **Figure II. 18**, current enhancement is detected from around at -2 V vs $Ag/AgNO_3$.

The current response under a CO_2 saturated environment suggests a possible catalytic activity. The current enhancement observed from the first wave could be a result of CO_2 coordinating to the metal center soon after the chloride ligand is released.

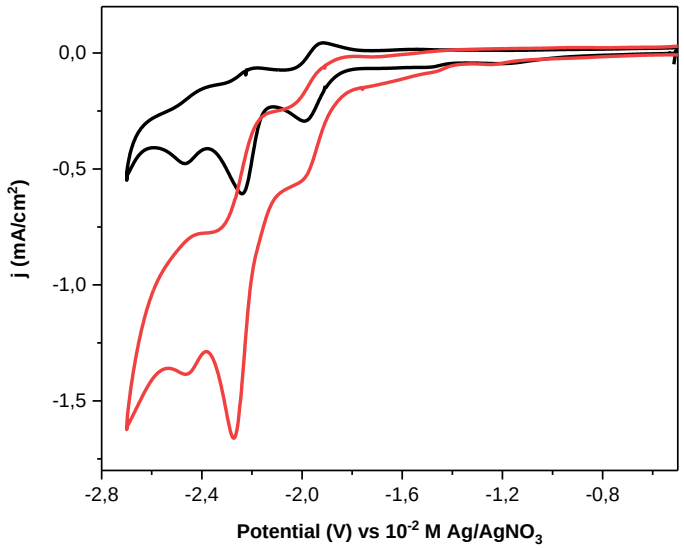

Figure II. 18 Cathodic scan CVs of a 1mM $[W(bpy)(CO)_3Cl]^-$ complex; under argon (black) and under CO_2 (red) on a GCE in CH_3CN/0,1M $TBAPF_6$ at v =0.1Vs^{-1}.

From the electrochemical measurements, it is possible to suggest two different types of active species; the mono- and bi-reduced species of the $[W(bpy)(CO)_3Cl]^-$ complex i.e. $[W(bpy)(CO)_3]^-$ and $[W(bpy)(CO)_3]^{2-}$ respectively (**Scheme II. 5**). Further electrolysis coupled with GC measurements could further confirm the hypothesis.

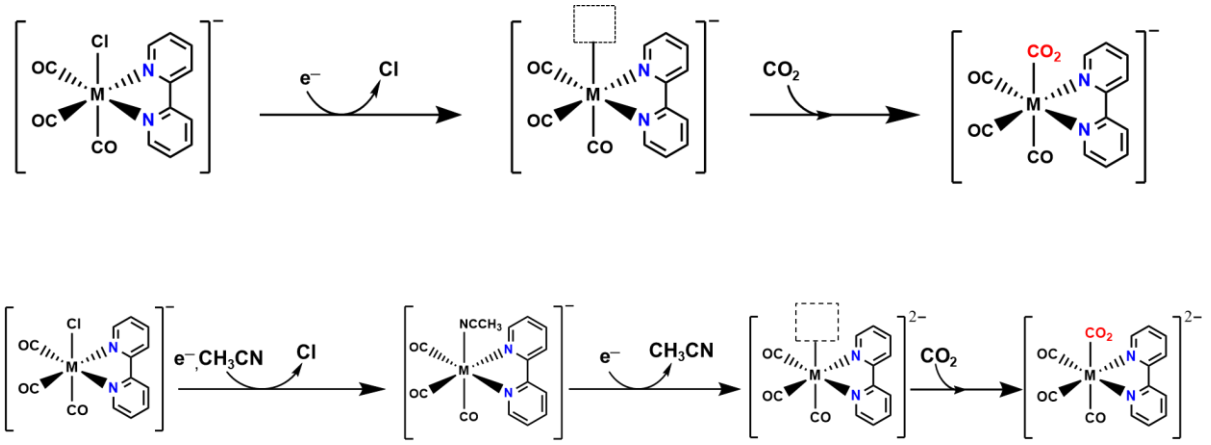

Scheme II. 6 Possible formation mechanism of active catalytic species from reduction of the $[M(bpy)(CO)_3Cl]^-$ complexes (M=W, Mo) under carbon dioxide saturated conditions.

FE measurements of the $[Mo(bpy)(CO)_3Cl]^-$ complex in the presence of 1%v/v H_2O at E_{onset} = -2.25V (after the first reduction wave of the $[Mo(bpy)(CO)_3Cl]^-$ complex) revealed just a modest quantity of CO generated (FE~2%) throughout the five hours of exhaustive electrolysis. This observation may indicate that, despite the reduction onset potential shift and current augmentation seen under CO_2 saturation conditions, these complexes are not effective catalysts as anticipated.

4. Conclusion

From investigating the tetracarbonyl complexes, the foundation of the synthesis of these complexes was established as well as a better understanding of their catalytic role in the reduction of CO_2. However, these complexes were found to have onset potential values that were more negative in comparison to other families of complexes such as those of rhenium and manganese tricarbonyl.

As an attempt to reduce the overpotential and achieve the reduction of CO_2 at less negative potentials, a different family of complexes were synthesized. With almost a similar geometry as that of the rhenium and manganese tricarbonyl complexes, tricarbonyl complexes of the group VI metals were synthesized by replacing one carbonyl ligand with a halide ligand, i.e. chloride.

From electrochemical measurements, these complexes were found to have some catalytic properties yet at almost similar onset potential values as those of the tetracarbonyl family given in both families the same active catalytic species of $[Mo(bpy)(CO)_3]^{2-}$ are formed. Nevertheless, since the halide ligand is more readily released than the carbonyl ligand in the case of the $[M(bpy)(CO)_4]$ complexes, beginning with the $[Mo(bpy)(CO)_3Cl]^-$ anionic complex may facilitate an easier generation of catalytic species.

Compared to Group 7 counterparts, the group VI tetracarbonyl compounds have significant lower reaction rates. DFT calculations previously reported in literature showed a stronger π-back bonding into the CO ligands with Group 6 metals compared to the Rhenium complexes,[2] this observation can explain the difference in reaction rates. Hence, the hindered release of CO from $[M(bpy)(CO)_4]^{2-}$ might limit the CO_2 reduction rates of these complexes.

Bibliography

1. T. Reda, C. M. Plugge, N. J. Abram, J. Hirst, *Proc. Natl. Acad. Sci. USA*., **2008**, *105* (31) 10654-10658.
2. M. L. Clark, K. A. Grice, C. E. Moore, A. L. Rheingold, C. P. Kubiak, *Chem. Sci*., **2014**, *5*, 1894–1900.
3. J. Tory, B. Setterfield-Price, R. A. W. Dryfe, F. Hartl, *ChemElectroChem.*, **2015**, *2*, 213–217.
4. C. G. Bellido, L. A. Miguel, D. Miguel, N. Lalaoui, N. Cabon, F. Gloaguen, N. Le Poul, *ChemElectroChem.*, **2021**, *8*, 1899–1910.
5. Stiddard., *J. Chem. Soc.*, **1962**, 4712-4715.
6. D. M. Manuta, A. J. Lees, J. *Inorg. Chem*., **1983**, *22*, 25, 3825–3828.
7. S. Záliš, C. Daniel, A. Vlček, C. Daniel, A. Vlček Jr, *J. Chem. Soc., Dalton Trans*., **1999**, 3081-3086.
8. A. Vlček Jr, *Coord. Chem. Rev*., **2002**, *230*, 225-242.
9. C. S. Kraihanzel, F. A. Cotton, *Inorg. Chem*., **1963**, *2* (3), 533–540.
10. S. Chun, E. G. Getty, A. J. Lees, *Inorg. Chem*., **1984**, *23*, 2155.
11. D. M. Manuta, A. J. Lees, *J. Inorg. Chem*., **1986**, *25*, 1354–1359.
12. I.R. Farrell, F. Hartl, S. Záliš, T. Mahabiersing, A. Vlček Jr, *J. Chem. Soc., Dalton Trans*., **2000**, 4323-4331.
13. S. Záliš, I.R. Farrell, A. Vlček Jr, Inorg. Chem., *J. Am. Chem. Soc*., **2003**, *125*(15), 4580–4592.
14. D. Guillaumont, A. Vlček Jr, C. Daniel, *J. Phys. Chem. A*., **2001**, *105* (7), 1107–1114.
15. I.R. Farrell, J. van Slageren, S. Záliš, A. Vlček, *Inorg. Chim. Acta*., **2001**, *315* (1), 44-52.
16. M. S. Wrighton, H. B. Abrahamson, D. L. Morse, *J. Am. Chem. Soc*., **1976**, *98* (14), 4105–4109.
17. H. B. Abrahamson, M. S. Wrighton, *Inorg. Chem*., **1978**, *17* (12), 3385-3388.
18. D.J. Stufkens, *Coord. Chem. Rev*., **1990**, *104*, 39-112.
19. H. Saito, J. Fujita, K. Saito, *Bull. Chem. Soc. Jpn*., **1968**, *41* ,863-874.
20. S. Ernst, Y. Kurth, W. Kaim, *J. Organomet. Chem*., **1986**, *302* (2), 211-215.
21. W. Kaim, S. Kohlmann, S. Ernst, B. Olbrich-Deussner, C. Bessenbacher, A. Schultz, *J. Organomet. Chem*., **1987**, *321* (2), 215-226.
22. R. Johnson, H. Madhani, J. P. Bullock, *Inorg. Chim. Acta*., **2007**, *360*, 3414–3423.
23. S. Ernst, W. Kaim, *J. Am. Chem. Soc*., **1986**, *108* (13), 3578-3586.

24. S. Ernst, W. Kaim, *Inorg. Chim. Acta*., **1986**, *114* (2),123-125.
25. W. Kaim, S. Kohlmann, *Inorg. Chem.*, **1987**, *26* (1), 68-77.
26. H. Tom Dieck, K.-D. Franz, F. Hohmann, *Chem. Ber*., **1975**, *108*, 163-173.
27. D. Miholová, B. Gaš, S. Záliš, J. Klíma, A. A. Vlček, *J. Organomet. Chem*., **1987**, *330*, 75-84.
28. J. O. Taylor, R. D. Leavey, F. Hartl, *ChemElectroChem*., **2018**, *5* (21), 3155-3161.
29. G.J. Stor, F. Hartl, J.W.M. van Outersterp, D.J. Stufkens, *Organometallics*., **1995**, *14*, 1115-1131.
30. C. Costentin, S. Drouet, G. Passard, M. Robert, J.-M. Savéant, *J. Am. Chem. Soc*., **2013**, *135*, 9023–9031.
31. C. Costentin, J.-M. Savéant, *ChemElectroChem*., **2014**, *1*, 1226–1236.
32. B. J. Brisdon, D. A. Edwards, J. W. White, *J. Organomet. Chem.* **1978**, *156*, 427-437.
33. L. E. Orgel, *Inorg.Chem*., **1962**, *1*, 25-29.
34. H. Behrens, E. Lindner, G. Lehnert, *J. Organomet. Chem*., **1970**, *22*, 439−448.
35. M. J. Hollas, Modern Spectroscopy, 4th edition, John Wiley & Sons, Inc, 2004.
36. F. Hartl, T. Mahabiersing, P. Le Floch, F. Mathey, L. Ricard, P. Rosa, S. Záliš, *Inorg. Chem*., **2003**, *42*, 4442–4455.

CHAPTER III. PYRIDINE IMIDAZOLE METAL COMPLEXES

1. Introduction

As discussed in chapter I, achieving solar driven CO_2 reduction into valuable carbon-based fuel products is an answer that can address both challenges of global warming and energy demand. It is evident that the excessive CO_2 emission from consumption of fossil fuels, has surpassed the conversion load of natural photosynthesis.[1,2] With inspiration from nature, artificial photosynthesis has been employed in the conversion of CO_2 to value-added products by utilizing inexhaustible solar energy.[3-5]

As one category of a solar-driven CO_2 reduction reaction, photocatalytic (PC) reaction requires the use of a photosensitive unit that can initiate an electron transfer process for the conversion of CO_2 in the presence of light and electron source, mimicking the natural photosynthetic reaction. These photoactive systems exist in different forms that range from semiconducting metal oxides particles to molecular structures such as molecular complexes.

As it is fairly known, a semiconducting nanoparticle needs to possess some photophysical properties that will enable it to absorb light energy. Through photoexcitation, electrons will migrate from the valence band to the conduction band. And eventually these energized electrons will then favor the CO_2 reduction process at the surface of nanoparticles.

On the other hand, molecular photocatalytic reactions involve three crucial components; a photosensitizer (**PS**), acting as an electron transfer mediator, a sacrificial electron donor (**SD**) and a catalyst (**Cat**) as presented in **Scheme III. 1A**. However, in some literature work it has been reported that a photosensitizer could also possess some catalytic properties towards reduction of CO_2. In such cases, only two crucial components are needed in the photocatalytic process: a photocatalyst (**PC**) and an electron donor (**SD**) as shown in **Scheme III. 1B**.

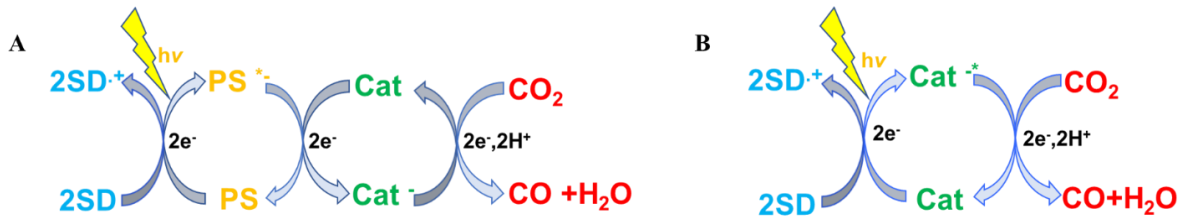

Scheme III. 1 Two possible reaction mechanisms for CO_2 photocatalysis**; A**: when a **Cat** lacks the required photophysical properties hence the use of a **PS** is required, and **B**: when a **Cat** possesses the required photophysical properties as a **PS** i.e. a photocatalyst (**PC**).

Examples of photocatalysts include some Re(I) complexes reported to act as photocatalysts for CO_2 reduction due to their sufficient long lifetimes in their excited state.[6-8] Other examples of photocatalysts include Ir(III)[9,10], Co and Fe porphyrin.[11-13]

Considering that the complexes described in the previous chapter were electrocatalysts and not photocatalysts due to their weak photophysical properties, further studies were made. These consequent efforts were centered on investigating molecular metal complexes analogue to complexes described in Chapter II that may exhibit interesting photophysical characteristics, i.e. possess absorption properties in the visible region and a long lifetime in their excited state (> 10 ns) in order to be photoreduced in the presence of a sacrificial donor.

From literature, [W(**L1**)$(CO)_4$] complex (**L1** = 2-(1H-imidazol-2-yl)pyridine ligand) was reported to display a long-lived photoluminescence behavior in toluene with a lifetime greater than 100ns.[14] Hence, our initial course of action was to examine the possibility of this metal complex acting as a catalyst for the reduction of CO_2 and then explore its ability in acting as a photocatalyst.

2. Synthesis and characterization of pyridine imidazole family of complexes

2.1. Synthesis of [M(L1)$(CO)_4$] complexes (M= Cr, Mo, W)

Following previously reported literature by Stiddard,[15] a series of pyridine imidazole tetracarbonyl complexes were synthesized using hexacarbonyl metal complexes, $[M(CO)_6]$ with M= Cr, Mo, W and a 2-(1H-imidazol-2-yl)pyridine ligand in a reflux reaction under argon atmosphere. Upon filtration, a greenish-yellow precipitate was collected and rinsed with diethyl ether. (Yield ~ 50%, see experimental part).

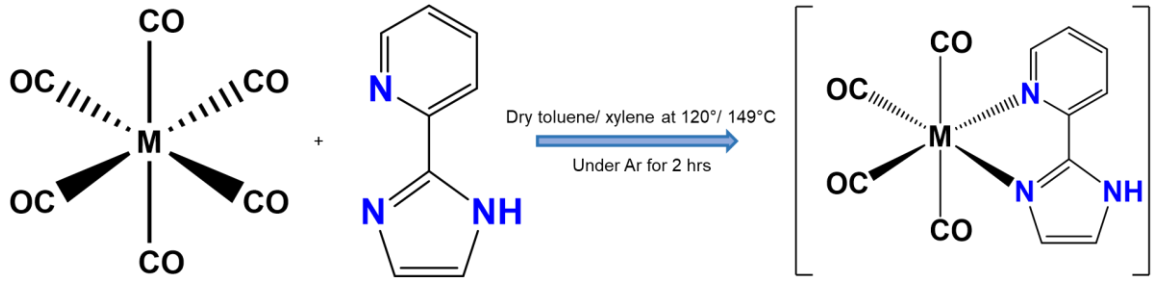

Scheme III. 2 Synthetic procedure for the [M(**L1**)$(CO)_4$] complexes (M=Cr, Mo, W).

These complexes demonstrated long-term stability in dark and vacuum storage conditions. Through infrared measurements, these complexes were found to have four CO stretching frequencies in the carbonyl region (2100-1700 cm^{-1}) as indicated in **Table III. 1**.

Table III.1 IR spectral data and assignments for the [M(**L1**)$(CO)_4$] complexes in the carbonyl stretching region.

Complexes	Bands, cm^{-1}			
	A_1	B_1	A_1	B_2
Cr(**L1**)$(CO)_4$	2004	1908	1851	1767
Mo(**L1**)$(CO)_4$	2010	1912	1851	1762
W(**L1**)$(CO)_4$	2002	1902	1846	1753

2.2. Photophysical characterization

The absorption spectra of the synthesized complexes are reported in **Figure III. 1**. The absorption band in the UV region around 300 nm detected in all the complexes, is associated to the $\pi \rightarrow \pi^*$ intraligand electronic transition. The absorbance band in the visible region (~ 440 nm to 470 nm) is attributed to a low-lying metal-ligand charge transfer of dπ-π* (MLCT).

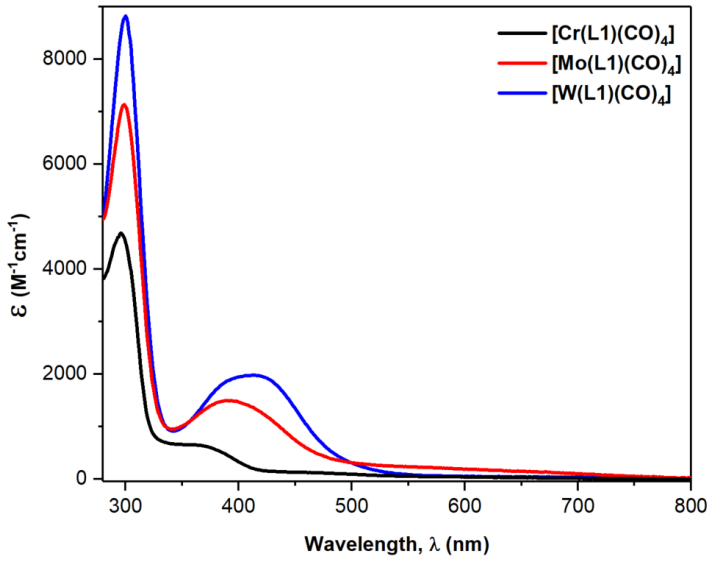

Figure III. 1 UV-Vis absorption spectra of [M(**L1**)$(CO)_4$] complexes in CH_3CN.

The MLCT absorption band of these complexes demonstrated a solvent-dependency behavior, marked by a hypsochromic shift (blue-shift) of the MLCT band in polar solvents. As the polarity of the organic solvent increases, the MLCT band shifts to shorter wavelengths as it was

previously observed with [M(bpy)(CO)$_4$]. **Table III. 2** gathers the wavelength values of the absorption maxima in different solvents.

Table III.2 Absorption properties of the [M(**L1**)(CO)$_4$] complexes in different organic solvents.

Solvents (Solvent polarity)[a]	λ_{max}, nm [extinction molar coefficient ε, $M^{-1}cm^{-1}$]		
	[Cr(**L1**)(CO)$_4$]	[Mo(**L1**)(CO)$_4$]	[W(**L1**)(CO)$_4$]
Toluene (2.4)	300(2900) 380 (110)	306(1680) 468 (530)	300 (1070) 463 (120)
DCM (3.1)	298 (6500) 367 (650)	301(6900) 430 (1400)	295 (3500) 450 (520)
THF (4)	300 (3250) 369 (180)	303 (10100) 430 (2050)	302 (10100) 448 (2300)
CH_3CN (5.8)	295(4700) 367 (650)	298 (7100) 389 (1550)	298 (8800) 410 (1970)
DMF (6.4)	298 (7000) 357 (2110)	300 (23000) 384 (2110)	300 (34700) 395 (2330)

[a]Rohrschneider's polarity parameter

The shift of the MLCT band maxima of different complexes in different organic solvents with varying solvent polarity as shown in **Table III. 2** indicates a solvatochromic behavior. This solvatochromic behavior can be explained through the stabilization of the ground state and the excited state by electrostatic interactions with the polar solvents.

At ground state, these complexes tend to be polar due to a diimine ligand (**L1**) to metal σ donation that results in the formation of charged metal and ligand species, $M^{\delta-}$ and $L1^{\delta+}$. Upon metal to **L1** ligand MLCT excitation, the negative charge on the metal center is transferred to the **L1** ligand causing a decrease of the dipole moment; causing these complexes to be less polar in their excited state than in their ground state.

In polar solvents, the polar ground state of the complex will be highly stabilized in comparison to the MLCT excited state; as an aftermath, the energy difference between the ground and excited state will be increased as the solvent polarity increases i.e. negative solvatochromism.

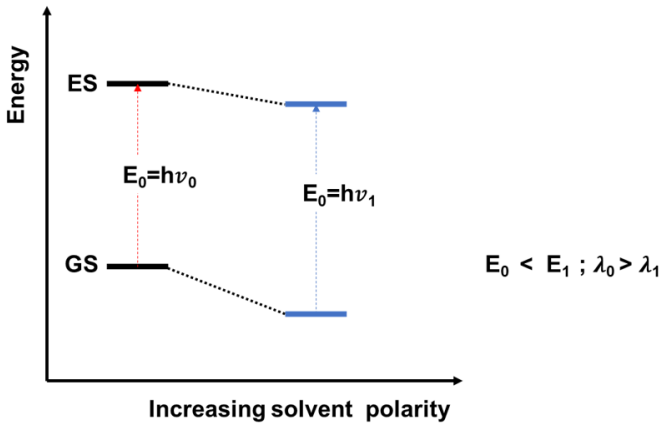

Scheme III. 3 Negative solvatochromism behavior observed with increasing solvent polarity (ES= excited state and GS= ground state).

Upon excitation of the [M(**L1**)$(CO)_4$] complexes at their corresponding wavelengths of absorption (λ_{abs}); emission spectra of these complexes were recorded in different solvents. From these measurements, most complexes were found to have weak to almost zero emission properties, with an exception of the [W(**L1**)$(CO)_4$] complex. This complex displayed a broad emission band at 588 nm with an emission lifetime of 70 ns in toluene. This emission band is shown in **Figure III. 2**, is associated with the luminescence light emission of the complex.

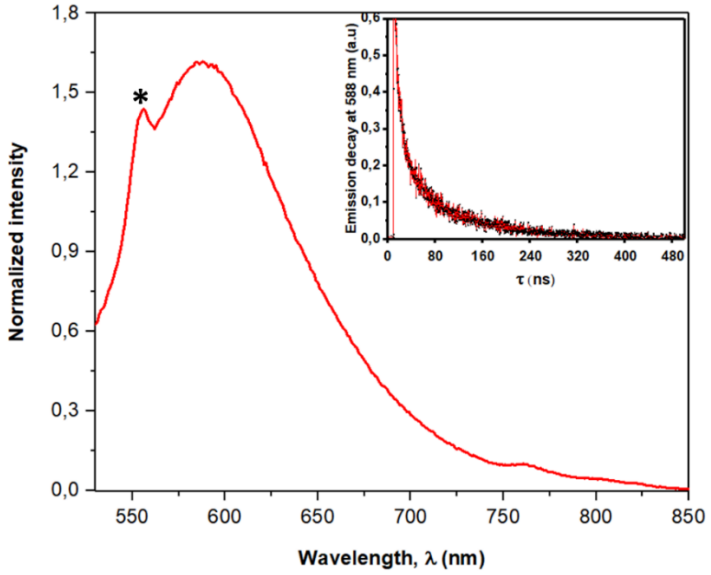

Figure III. 2 Emission spectra of the W(**L1**)$(CO)_4$ complex and emission lifetime decay of its excited state at 588nm (insert) in toluene under argon (*Raman scattering from organic solvent).

However, the [W(**L1**)$(CO)_4$] complex demonstrated strong emissive behavior and a long phosphorescence lifetime only in toluene which was not the case in other organic solvents. **Table III. 3** compares the photophysical properties of the [W(**L1**)$(CO)_4$] complex in different organic solvents.

Table III. 3 Absorption and emission properties of [W(**L1**)$(CO)_4$] complex in different organic solvents. (τ= emission lifetime and Φ^{em} =emission quantum yield).

Solvents	λ_{abs}	λ_{em}	τ, ns (%)	Φ^{em}
CH_3CN	411	685	16 (10) 2.2 (90)	0.0004
Toluene	460	588	70 (11) 5.4 (89)	0.003
DMF	395	550	9.1 (32) 2.6 (68)	0.005

2.3. Electrochemical characterization of [M(L1)$(CO)_4$] complexes

Electrochemical studies of these group VI metal complexes (1mM) were carried out in acetonitrile with 0.1M $TBAPF_6$ as the supporting electrolyte. The CV measurements were performed at room temperature using a three-electrode cell configuration with a glassy carbon electrode (GCE) as the working electrode and all potential values recorded against Ag/10^{-2}M $AgNO_3$ as the reference potential.

2.3.1. Electrochemical characterization of [M(L1)$(CO)_4$] complexes under argon

i. Electro-oxidation of [M(L1)$(CO)_4$] complexes under argon

In argon saturated conditions, the anodic CV scans of 1mM [Mo(**L1**)$(CO)_4$] showed two irreversible waves, at E_{pa1}= 0.2V vs Ag/$AgNO_3$ and E_{pa2}= 0.63 V vs Ag/$AgNO_3$. These oxidation waves are both associated with the oxidation of the metal center. The first oxidation wave at +0.2V is accompanied with the release of the CO ligand resulting in the coordination of the solvent ligand to the metal center, thus formation of the $[Mo^{I}$**(L1)**$(CO)_3(CH_3CN)]^+$ cationic species.

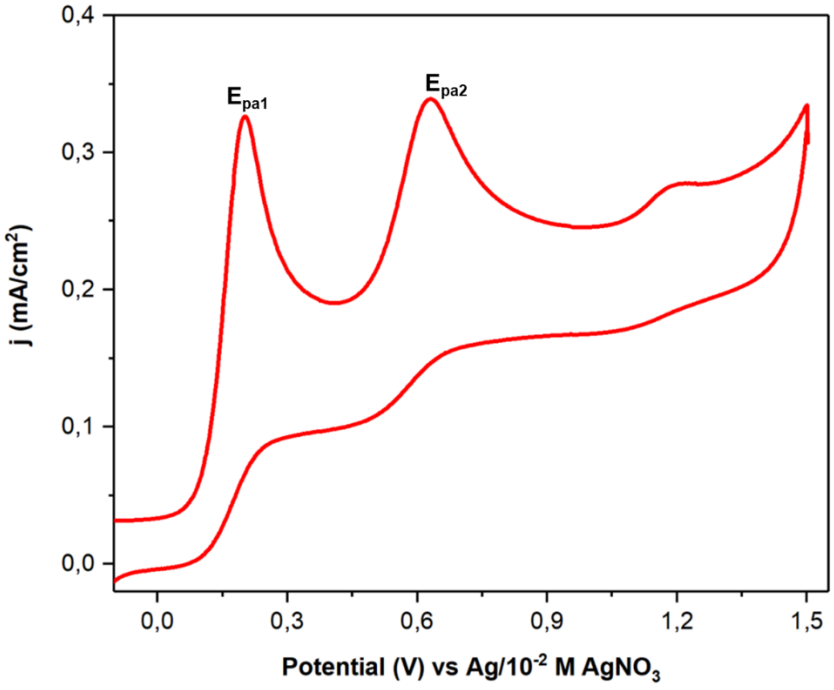

Figure III. 3 Anodic CV scans of a 1mM [Mo(**L1**)$(CO)_4$)] complexes under argon saturated conditions on a GCE in CH_3CN/0,1M $TBAPF_6$ at v = 0.1Vs^{-1}.

Upon second-electron oxidation, further oxidation of the metal center takes place accompanied with the formation of heptacoordinate species i.e. $[M^{II}(\mathbf{LI})(CO)_3(CH_3CN)_2]^{2+}$.[16] The oxidation processes of these complexes correspond to similar processes reported for the bipyridine family of metal complexes reported in the previous chapter. On the other hand, compared to the [M(bpy)$(CO)_4$] complexes, the pyridine imidazole-based complexes' oxidation processes occurred at less positive values, indicating an easier oxidation of the metal center for this particular family of complexes.

ii. Electroreduction of [M(L1)$(CO)_4$] complexes under argon

Cathodic CV scans of the pyridine imidazole metal complexes recorded under argon displayed two irreversible reduction waves for [Mo(**L1**)$(CO)_4$)] and [W(**L1**)$(CO)_4$)] complexes (**Figure III. 4**, **table III. 4**) . Both detected waves at high negative potentials correspond to ligand-centered reduction processes. A potential difference of ~80-90 mV is detected between the corresponding irreversible reduction waves of the [Mo(**L1**)$(CO)_4$)] complex and the [W(**L1**)$(CO)_4$)] complex, with [Mo(**L1**)$(CO)_4$)] complex having higher negative potential values compared to the [W(**L1**)$(CO)_4$)] complex. This potential difference can be attributed to the reactivity of the metal centers based on the 18-electron rule.

The irreversibility of the two reduction waves for the Mo and W complexes suggest an irreversible chemical formation of complex species upon each one-electron reduction reaction.

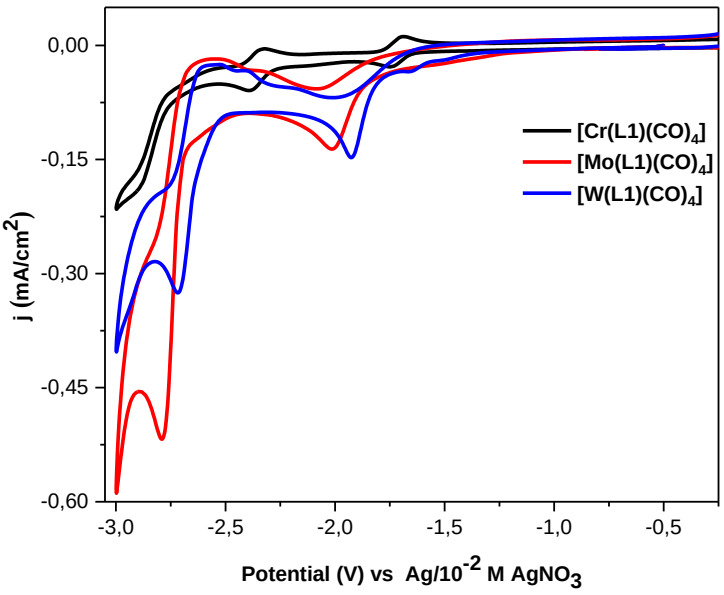

Figure III. 4 Cathodic CV scans of a 1mM [M(**L1**)$(CO)_4$] complex (with M = Cr, Mo, W) under argon saturated conditions on a GCE in CH_3CN/0,1M $TBAPF_6$ at v = 0.05Vs^{-1}.

This irreversibility behavior is different to what was observed for the [M(bpy)$(CO)_4$] family (see **Chap II**) where the first reduction localized on the ligand was reported to be reversible. The irreversibility behavior of the first wave of the [M(**L1**)$(CO)_4$)] complexes is attributed to the reactivity of the imidazole ring upon one-electron reduction. As it has previously been mentioned for some imidazolium salts, the reduction of this ligand may follow an EC mechanism with a release of H_2. (**Scheme III. 4**).[17]

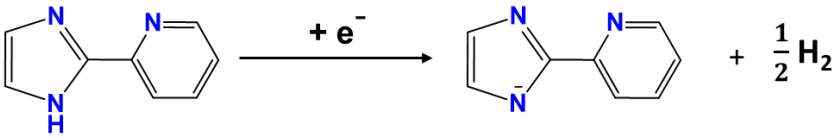

Scheme III. 4 Evolution of the 2-(1H-imidazol-2-yl)pyridine ligand upon one-electron reduction.

When the NH function is replaced by a NCH_3 function (ligand **L3** see further in the chapter at **section 5. 3i**) the first reduction wave becomes reversible. The second reduction is irreversible and associated to the release of CO after the second-electron reduction of the ligand, similar to

the observation made on the $[M(bpy)(CO)_4]^{\cdot-}$ complexes; thus, resulting to the formation of $[M(\mathbf{L1})(CO)_3]^{2-}$ species.

Interestingly, the $[Cr(\mathbf{L1})(CO)_4]$ complex displayed a different electrochemical system with two reversible waves at -1.72 and -2.35 V vs $Ag/AgNO_3$. This dissimilar electrochemical response could suggest a poor stability of the $[Cr(\mathbf{L1})(CO)_4]$ complex hence slow degradation of the complex in solution. This suggestion can be supported by observations previously made in literature work that reported a weak binding (i.e. coordination) of the 2-(2′-pyridyl) imidazole ligand to the first-row transition elements as a result of it being a poor π-acceptor ligand.[18-20] For this reason, this Cr complex will not be further characterized in solution.

Further electrochemical analysis conducted using a rotating disc electrode (RDE) as the working electrode confirmed the number of electrons (ne^-) involved at each of the irreversible wave (reduction and oxidation) equals 1. **Figure III. 5** indicates these one-electron reduction and oxidation processes in the cathodic and anodic scans respectively.

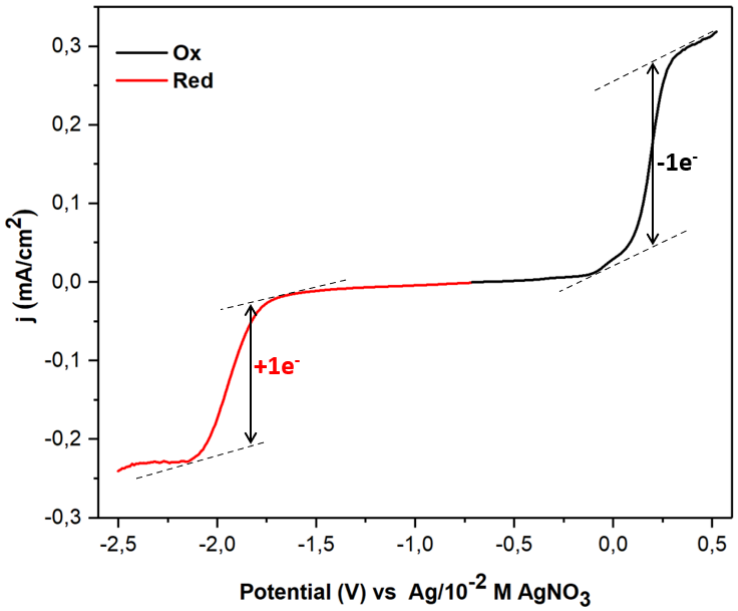

Figure III. 5 Anodic and cathodic CV scans of 1mM $[W(\mathbf{L1})(CO)_4]$ complex under argon atmosphere on a RDE in CH_3CN/0,1M $TBAPF_6$ at $\nu = 0.1Vs^{-1}$.

Conclusively, oxidation and reduction potential values for the electrochemical characteristics of these complexes under argon saturated conditions are summarized in **Table III. 4**.

Table III. 4 Reduction potentials of the [M(**L1**)$(CO)_4$] complexes in CH_3CN/0.1M $TBAPF_6$ recorded on a GCE at v = 0.1 mVs^{-1}.

Complexes	E (V) vs Ag / 0.01M $AgNO_3$		
	E_{pc1}	E_{pc2}	E_{pa}
[Mo(**L1**)$(CO)_4$]	-2.01	-2.79	0.2 0.63
[W(**L1**)$(CO)_4$]	-1.92	-2.71	0.2 0.48
[Cr(**L1**)$(CO)_4$]	$E_{1/2}$ = -1.73 (ΔE_p= 0.07)	$E_{1/2}$ = -2.36 (ΔE_p= 0.07)	0.57 0.93

2.3.2. Electrochemical reduction of CO_2 using [M(L1)$(CO)_4$] complexes

Consequently, the catalytic properties of these complexes were investigated under CO_2 saturated conditions using GCE as the working electrode, Ag/10^{-2}M $AgNO_3$ as the reference and Pt as the counter electrode in CH_3CN/0.1M $TBAPF_6$.

As shown in **Figure III. 6**, these complexes appeared to have a catalytic role in the reduction of CO_2, which was evidently indicated by the increase of current under CO_2 saturated atmosphere. This increase of current was observed to start slowly on the first reduction peak at an onset potential value of -2.1V vs Ag/10^{-2}M $AgNO_3$, and continuously increase at higher negative potentials.

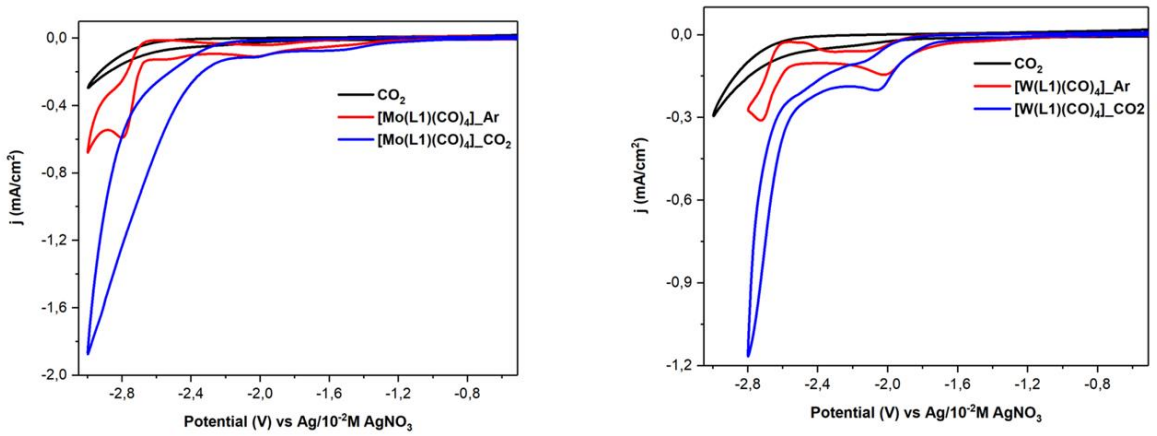

Figure III. 6 Cathodic CV scans of a 1mM [M(**L1**)$(CO)_4$)] complex under CO_2 saturated conditions on GCE in CH_3CN/0,1M $TBAPF_6$ at v = 0.05Vs^{-1}.

Upon the second electron-reduction, these bis-reduced complexes are presumed to release one carbonyl ligand which will then aid in coordinating CO_2 to the metal center. Upon exhaustive electrolysis, a flow of electrons towards these CO_2-adduct species will in time result to the reduction of CO_2. The faradaic efficiencies of these catalysts were calculated using gas analysis data from gas chromatography measurements performed during electrolysis measurements with a carbon foam as the working electrode.

Table III. 5 Faradaic efficiencies (%) of 1mM [M(**L1**)$(CO)_4$] complexes at given onset potential values vs $Ag/AgNO_3$ in 10 mL CH_3CN/0.1M $TBAPF_6$ at v = 0.05Vs^{-1} on a carbon foam (8 ppi) working electrode.

Complex	E_{app}(V)	Time (min)	Q(C)	%CO
[Mo(**L1**)$(CO)_4$]	-2.1	63	-9.5	29
[W(**L1**)$(CO)_4$]	-2.1	60	-2.9	18
		133	-8.8	21

As shown from **Table III. 5**, CO gas was found to be the main product obtained from reduction of CO_2 during electrolysis of these complexes. During the first hour, [Mo(**L1**)$(CO)_4$] had the leading amount of CO produced, followed by [W(**L1**)$(CO)_4$]. These compounds can be reported to be selective towards CO production and no other gaseous products such as H_2 and CH_4 were detected. Further investigation of the catalytic properties of this family of complexes was focused on the [W(**L1**)$(CO)_4$] complex.

In order to examine the effect of applied potential values and added proton sources on the complex's efficiency and selectivity for CO_2 reduction, this complex was subsequently characterized during electrolysis in the presence and absence of a proton source (methanol, CH_3OH) at various applied potential values (see different entries of **Table III. 6**).

Table III. 6 Different entries indicating the faradaic efficiencies of 1mM [W(**L1**)$(CO)_4$] complexes in 10 mL CH_3CN/0.1M $TBAPF_6$ at v = 0.05Vs^{-1} on a carbon foam (8 ppi) as the working electrode.

Entry	Complex (+/- proton source)	E_{app} (V)	Time (mins)	Q(C)	%CO	%H_2
1	[W(L1)$(CO)_4$]	-2.1	60	-2.9	18	0
2	[W(L1)$(CO)_4$]	-2.1	133	-8.8	21	0
3	[W(L1)$(CO)_4$]	-2.3	73	-6.2	14	0
4	[W(L1)$(CO)_4$] + 1.5M CH_3OH	-1.9	60	-2.5	4	50
5	[W(L1)$(CO)_4$] + 1.5M CH_3OH	-2.1	60	-9.1	8	52
6	[W(L1)$(CO)_4$] + 1.5M CH_3OH	-2.1	197	-23.1	9	56
7	[W(L1)$(CO)_4$] + 1.5M CH_3OH	-2.3	60	-12.4	3	47

At an applied potential of -2.1V, the [W(**L1**)$(CO)_4$] complex in the absence of methanol led to the production of CO which did not significantly improve with time nor with the amount of charge passed through the electrochemical system (**entry 1** and **2**). Moreover, in the absence of methanol at a much more negative applied potential of -2.3V, a lesser amount of CO gas was produced in comparison to the amount produced during a similar period of time at -2.1V. Strangely, the amount of charge passed at -2.3V was twice the charge quantity passed at -2.1V; this might suggest an occurrence of other reduction reactions or a formation of other carbon products undetectable by the gas chromatography system (**entry 1**, **2** and **3** of **Table III. 6**).

Additionally, failure to account for 100% faradaic efficiency could be associated with an occurrence of other two electron reduction processes (**Eq 1** and **2**) which might take place in the absence of protons, thus resulting in the formation of carbonates and oxalate.

$$2CO_2 + 2e^- \rightarrow CO + CO_3^{2-} \qquad \boldsymbol{Eq.1}$$

$$2CO_2 + 2e^- \rightarrow C_2O_4^{2-} \qquad \boldsymbol{Eq.2}$$

As an attempt of improving the efficiency of CO_2 reduction and lowering the probability of having **Eq 1** and **2** taking place, methanol CH_3OH was introduced as a proton source (**Figure III. 7)**. With the presence of protons in the given electrochemical process, CO_2 reduction reactions shown in **Eq 3** and **4** were more likely to occur.

$$CO_2 + 2H^+ + 2e^- \rightarrow CO + H_2O \qquad \textbf{Eq. 3}$$

$$CO_2 + 2H^+ + 2e^- \rightarrow HCOOH + H_2O \qquad \textbf{Eq. 4}$$

As represented in the cathodic CV scans of 1mM of [W(**L1**)$(CO)_4$] complex in the presence of 1.5M CH_3OH, an increase of catalytic current was detected at less negative potential values as shown in **Figure III. 7**.

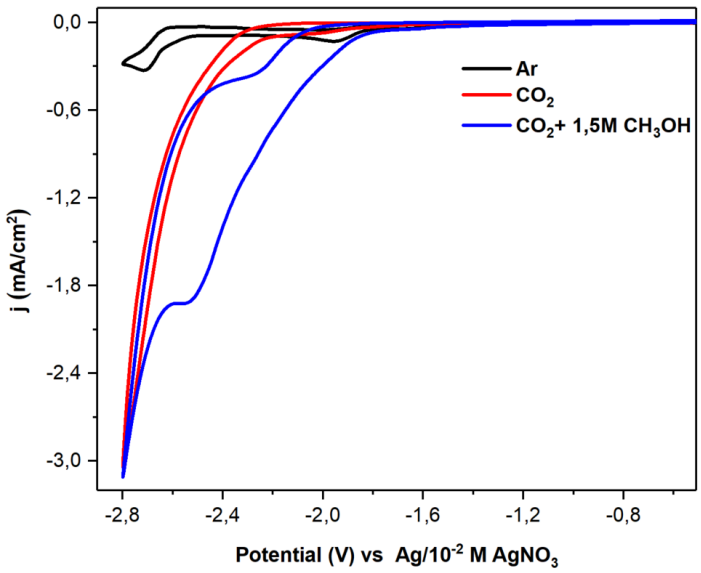

Figure III. 7 Cathodic CV scans of a 1mM [W(**L1**)$(CO)_4$)] complex under argon (black) and CO_2 (red) saturated conditions in the presence of methanol (blue) on a GCE in CH_3CN/0,1M $TBAPF_6$ at v = 0.05Vs^{-1}.

Faradaic efficiency measurements carried out during electrolysis of 1mM [W(**L1**)$(CO)_4$)] complex in a CO_2 saturated solution in the presence of methanol resulted to an overall improvement of the faradaic efficiency at different applied potentials (see **entry 4**, **5**, **6** and **7** of **Table III. 6**) . However, the addition of the proton source seemed to favor H_2 gas production over CO gas formation.

It is clear that the added protons in solutions experience an electroreduction process that results in the formation of hydrogen gas because there was essentially no improvement in CO production over the three hours of electrolysis at -2.1 V (**entry 5** and **6**), with the predominant gas created being H_2 (**Eq 5**).

$$2H^+ + 2e^- \rightarrow H_2 \qquad \textbf{Eq. 5}$$

This reaction has been previously reported as the main competing reaction against other reactions that favor formation of carbon-based products from the reduction of CO_2. Both species (protons and electrons) involved in the formation of hydrogen gas are crucial towards the reduction of CO_2 gas; hence, with these species being used in **Eq 5** to form H_2 gas will most definitely inhibit the reaction rate of **Eq 3** and **Eq 4**. To account for the remaining faradaic efficiency, reactions of **Eq 1** and **2** are still expected to happen leading to the formation of carbonates and possibly formate or formaldehyde.

In studying the influence of applied potential values on the faradaic efficiency of the complex (in the absence and presence of a proton source) and the products formed, electrolysis measurements were done at three different applied potential values (-1.9 V, -2.1 V and -2.3V vs $Ag/10^{-2}M$ $AgNO_3$). In the presence of CH_3OH, H_2 gas remained the predominant product after an hour of electrolysis, while CO gas continued to be produced in small amounts regardless of the potential values applied (**entry 4**, **5**, and **7** of **Table III. 6**); and in the absence of CH_3OH, only CO was detected as the primary product (**entry 1** and **3** of **Table III. 6**).

An attempt of using other proton sources such as phenol and water in equivalents amount to that of methanol did not yield any better result in terms of faradaic efficiency and selectivity. Conclusively, this family of complexes were indeed catalysts for CO_2 reduction with moderate faradaic efficiency that was mainly directed towards the production of H_2 gas when working in the presence of a proton source.

3. Photocatalysis of CO_2 in solution using $(W(L1)(CO)_4]$ complex

As stated in the beginning of this chapter, the investigation into this family of complexes was carried out with the intention of learning more about the photophysical characteristics of the [W(**L1**)$(CO)_4$] complex, which may be crucial to achieving the photocatalysis of CO_2 using this particular complex as the photocatalyst.

Further studies were conducted in investigating the possible photocatalytic behavior of this complex towards CO_2 reduction. With the appropriate catalytic and photophysical properties, the [W(**L1**)$(CO)_4$] complex could play a role of a photocatalyst (**PC**), that is expected to relay electrons to the CO_2 substrate from the sacrificial electron donor (**SD**), under light irradiation.

As prerequisites for this complex to act as a **PC** in photoreduction of CO_2, the [W(**L1**)$(CO)_4$] complex needs to absorb light in the UV-visible region and have adequate emission properties

with a long lifetime to promote an interaction between its excited state and the added electron donor (**SD**).

In its excited state (**PC***), the [W(**L1**)$(CO)_4$] complex is expected to accept electrons more easily (i.e. easier to reduce), thus achieving an efficient electron transfer from a **SD** to the complex. Additionally, an added **SD** needs to possess a strong reducing power, making it capable of donating step-by-step a minimum of two-electrons to the complex to facilitate the conversion of CO_2 to other carbon-based synthetic fuel products such as CO, HCOOH, CH_4 etc.

3.1. Spectroelectrochemistry of [W(L1)$(CO)_4$] complex under argon

Prior to studying the interaction between the [W(**L1**)$(CO)_4$] complex and different electron donors, spectroelectrochemical evolution of the [W(**L1**)$(CO)_4$] complex during exhaustive electrolysis at different applied potentials was recorded (see **Figure III. 8**).

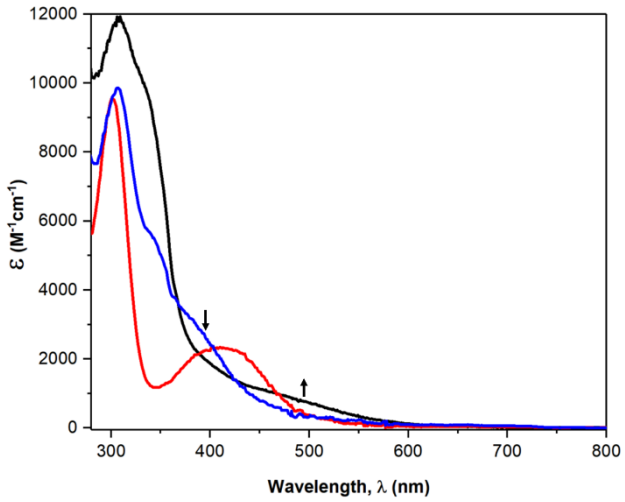

Figure III. 8 Absorption spectral evolution of 1mM [W(**L1**)$(CO)_4$)] complex under argon saturated conditions in CH_3CN/0,1M $TBAPF_6$ before (red) and after exhaustive electrolysis at -2.1V (blue) and -2.7V (black).

As presented in **Figure III. 8**, upon exhaustive electrolysis of 1mM [W(**L1**)$(CO)_4$)] complex at an applied potential of -2.1V the evolution of the absorption spectrum indicated a formation of two new shoulder bands at 344 nm and 395 nm accompanied with a disappearance of the broad MLCT band at 414 nm. Visually the color change was not significant as it changed from bright yellow to faint yellow.

Apart from the appearance of the new shoulder band in the near UV region, a minor red-shift of the absorption band assigned to the $\pi \rightarrow \pi^*$ intraligand electronic transition was also detected. These spectral changes mainly in the near UV region might suggest a structural modification of the ligand **L1** which correlates to the reactivity of the imidazole ring upon one-electron reduction as previously discussed (see part **2.3.1 ii** and **scheme III. 4**).[17]

Further exhaustive electrolysis was carried out at the second reduction peak (-2.7V) resulting in the two-electron reduced species of [W(**L1**)$(CO)_4$)] accompanied with a visible color change from faint yellow to orange. The overlay of absorption spectra indicates the broadening of the near UV absorption band (~315 nm), the disappearance of the shoulder band at ~ 395 nm accompanied with a slow formation of a broad absorption band at 491 nm which could suggest a low energy MLCT electronic transition. Using the obtained spectroelectrochemical results, a clear insight and understanding of the evolution of the absorption spectra of the reduced [W(**L1**)$(CO)_4$)] complex was deduced.

3.2. Photoreduction of [W(L1)$(CO)_4$] complex under argon

Following spectroelectrochemical studies, additional experiments were conducted between this complex and several sacrificial electron donors such as 1,3-dimethyl-2-phenyl-2,3-dihydro-1H-benzo[d]imidazole (BIH), triethylamine (TEA) and triethanolamine TEOA. Upon addition of an electron donor in a solution containing the [W(**L1**)$(CO)_4$)] complex, an instantaneous evolution of the absorption spectra was observed. This evolution of the spectra was very abrupt for the BIH and TEA electron donors, whereas with the TEOA the evolution was observed to be less abrupt (**Figure III. 9**).

As presented in **Figure III. 9**, addition of the TEOA resulted in a red-shift of the absorption band in the near UV region (from 301 to 310 nm), disappearance of the broad MLCT band at 411 nm and formation of a shoulder band at around 387 nm. This evolution spectra corresponds to that reported in **Figure III. 8**, in which a one-electron reduced [W(**L1**)$(CO)_4$)] complex was presented.

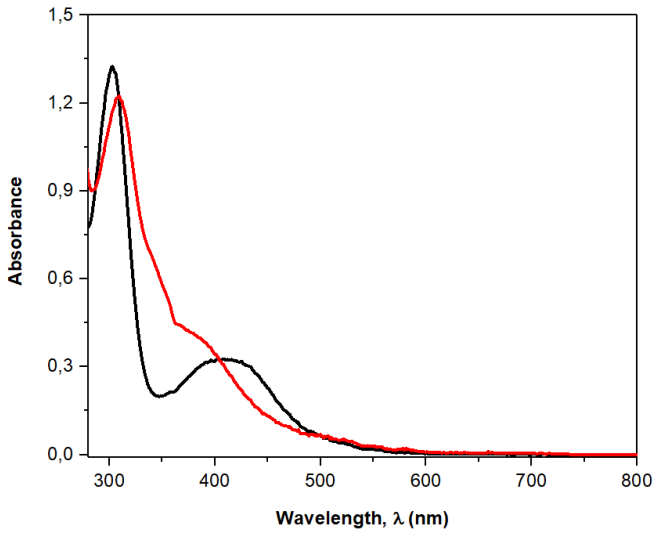

Figure III. 9 Absorption spectral evolution of 0.15 mM [W(**L1**)$(CO)_4$)] complex (black) in the presence of 1.5 M of TEOA (red) under argon saturated conditions in CH_3CN.

This observation clearly indicates a one-electron reduction process of the [W(**L1**)$(CO)_4$)] complex by TEOA that confirms a one-electron transfer between the complex and the donor. However, it is important to note that this electron transfer occurred in absence of light irradiation which suggests this transfer to be a thermal activated electron transfer instead of a light induced electron transfer.

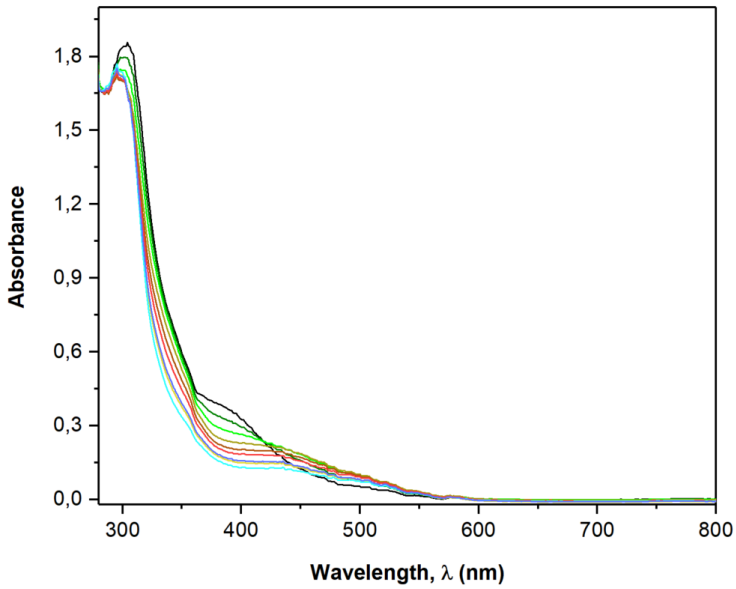

Figure III. 10 Absorption spectral evolution of 0.15 mM [W(**L1**)$(CO)_4$)] complex in the presence of 1.5 M of TEOA in argon saturated CH_3CN under light irradiation.

Upon light irradiation of the mono-reduced species of [W(**L1**)$(CO)_4$)] complex, the shoulder band (~387 nm) diminished in intensity overtime, while a broad absorption band (450-490 nm) appeared in the first 15 minutes of light irradiation (**Figure III. 10**).

As shown in **Figure III. 10**, this observed evolution of the absorption band is similar to that of the bis-reduced species of the [W(**L1**)$(CO)_4$)] complex upon second electron reduction at -2.7V (see **Figure III. 8**). However, this absorption band (450-490 nm) in **Figure III. 10** began to decrease upon further light irradiation which might indicate the photo-instability of the bis-reduced species under argon.

4. Photoelectrocatalysis of CO_2 in a heterogeneous system using [W(L1)$(CO)_4$] complex

Photoelectrocatalysis of CO_2 is a reduction mechanism that merges the principal steps involved in electrocatalytic (applied external bias) and photocatalytic (light irradiation) reduction processes towards CO_2 conversion. In doing so, the efficiency of CO_2 conversion is maximized by jointly involving the use of a light source upon an existing external bias. This energy input in the form of light helps also in diminishing the electricity consumption.

In a heterogeneous system, this mechanism involves the use of semi-conducting materials that play a role of a working electrode upon which a surface catalytic reduction of CO_2 takes place. These semi-conducting materials can be termed as co-catalysts since they indirectly influence the overall reduction process of CO_2.

In collaboration with our project partners at EPFL (a post-Doc student Bitao Dong), we decided to investigate the effects of integrating a photoactive semiconductor with a molecular catalyst as a heterogeneous system upon which the photoelectrochemical conversion of CO_2 takes place. In this work we involved the use of p-type semiconductor, an abundant and cheap cuprous oxide Cu_2O with a suitable band gap energy of 2 eV that ensures an absorption of a large portion of the solar spectrum, good electrical conductivity enabling the photo generated charge carrier extraction, and has a favorable band position to enable carrier injection and provide the required driving force for the reaction.[21]

Despite its advantages, this Cu_2O semiconductor was reported to have issues of instability and photo-corrosion in most aqueous and some non-aqueous solutions and under reductive

conditions.[22] As a solution in combating this instability issue, a deposition of thin protective layers on the Cu_2O electrode was considered necessary.

As means of attaining better band alignment that reduces interfacial charge recombination and increases photovoltage, an n-type Ga_2O_3 semiconductor was coated on Cu_2O photocathode as the first protective oxide layer resulting to a Cu_2O/Ga_2O_3 heterojunction. Consecutively, another protective layer of mesoporous TiO_2 was added with the intention of preventing photo-corrosion of the Cu_2O photoelectrode (under light and in solution);[23-25]thus formation of a $Cu_2O/Ga_2O_3/TiO_2$ photocathode.

A heterogeneous system (**Scheme III. 5)** can be designed in different ways depending on how the molecular catalyst is associated with the surface of the photoelectrode. This interface between a molecular catalyst and a photocathode can be developed in various ways such as electro-polymerization of a catalyst on an electrode surface, [26] chemical adsorption (covalent bonding of catalyst on a photoelectrode) and physical adsorption of a catalyst on a surface of a photocathode.[27-30]

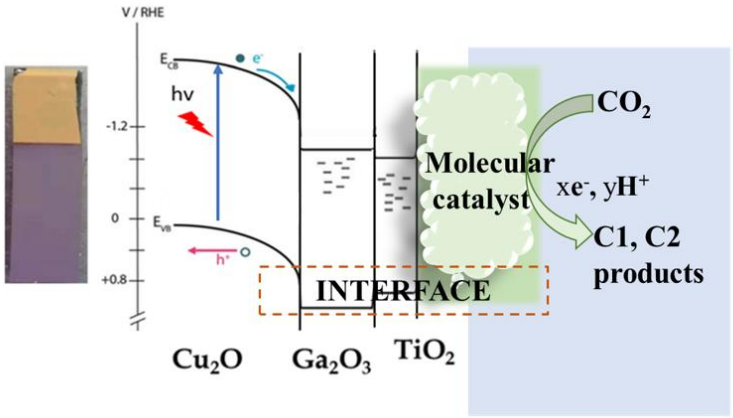

Scheme III. 5 Illustration of a photoelectrocatalysis of CO_2 in a heterogeneous system

Through this interface, photogenerated electrons from the conduction band of the Cu_2O layer are relayed through other oxide layers to reach the molecular catalyst adsorbed on the surface of the photocathode. (**Scheme III. 5)** In our collaborative work, we developed a heterogeneous system through physical adsorption of the group VI pyridyl imidazole metal carbonyl complexes on the surface of the $Cu_2O/Ga_2O_3/TiO_2$.

4.1. Preparation and characterization of a modified $Cu_2O/Ga_2O_3/TiO_2$ photocathode using a $[W(L1)(CO)_4]$ molecular catalyst.

Adsorption of the [W(**L1**)$(CO)_4$] complex on the surface of the $Cu_2O/Ga_2O_3/TiO_2$ photocathode was executed through a coating method where a $Cu_2O/Ga_2O_3/TiO_2$ photoelectrode of 1cm^2 surface area was dip coated for 24 hours at room temperature in 10mM [W(**L1**)$(CO)_4$] complex solubilized in acetonitrile.

A schematic illustration of the developed $Cu_2O/Ga_2O_3/TiO_2$-[W(**L1**)$(CO)_4$] photocathode for a photoelectrochemical CO_2 reduction system was represented in **Scheme III. 6.**

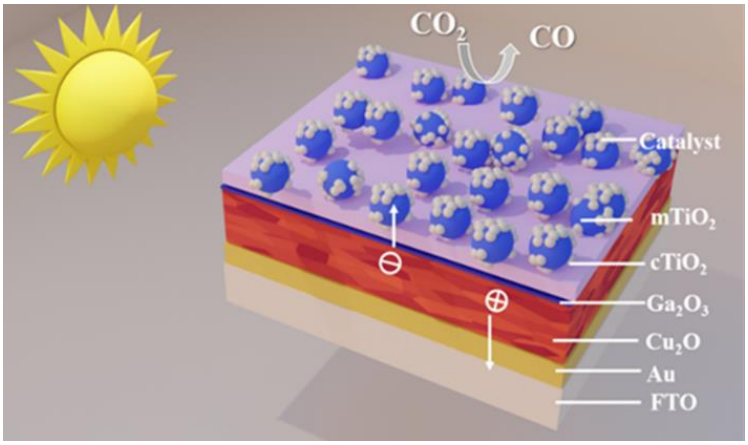

Scheme III. 6 A schematic representation of a $Cu_2O/Ga_2O_3/TiO_2$-[W(**L1**)$(CO)_4$] photocathode

The structure of this modified $Cu_2O/Ga_2O_3/TiO_2$-[W(**L1**)$(CO)_4$] photocathode consisted of different successive layers; a foundational layer of sputtered Au on an FTO surface, an electrodeposited Cu_2O film on Au, a compact and sequential Ga_2O_3 and TiO_2 compact layers onto the Cu_2O layer, a mesoporous TiO_2 layer on top of the compact TiO_2, and finally a [W(**L1**)$(CO)_4$] catalyst layer anchored on a TiO_2 surface via electrostatic adsorption.

The surface of the modified photocathode was investigated at different points during surface modification using scanning electron microscopy (SEM) technique that demonstrated an amorphous surface morphology of the modified $Cu_2O/Ga_2O_3/TiO_2$-[W(**L1**)$(CO)_4$] photocathode as shown in **Figure III. 11**.

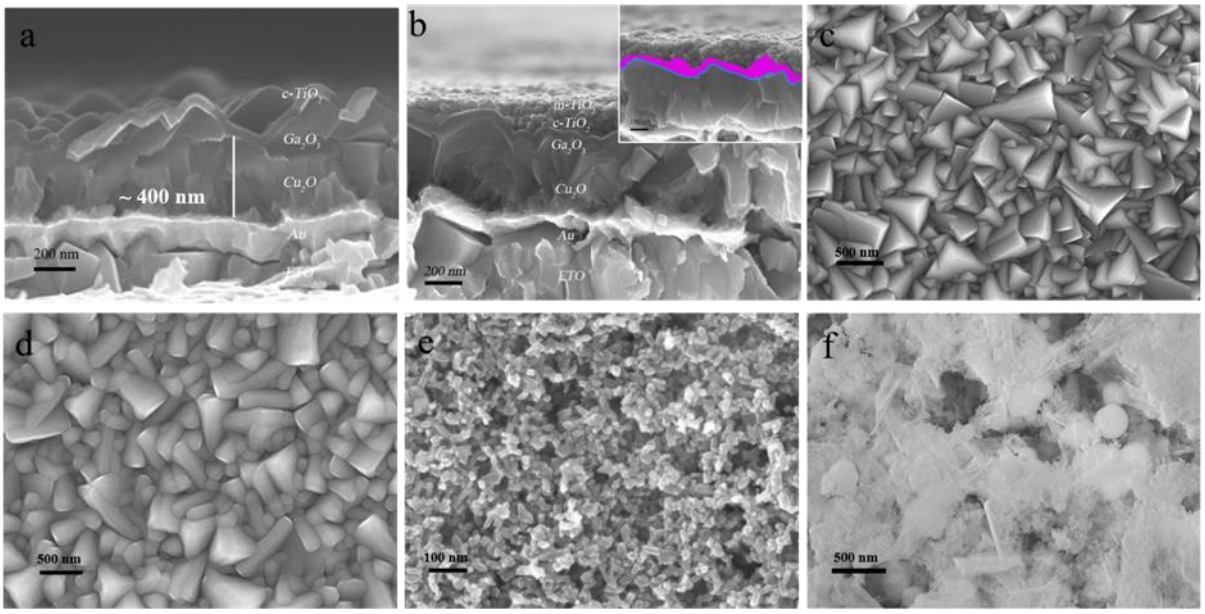

Figure III. 11 Cross-sectional scanning electron micrographs of a) $Cu_2O/Ga_2O_3/c\text{-}TiO_2$ electrode and b) $Cu_2O/Ga_2O_3/c\text{-}TiO_2$/ $m\text{-}TiO_2$. Top-view of scanning electron micrographs of c) Cu_2O surface, d) $c\text{-}TiO_2$ surface, e) $m\text{-}TiO_2$ surface and (f) [W(**L1**)$(CO)_4$] respectively.

The top-view of scanning electron micrograph images taken at different points during the preparation of the $Cu_2O/Ga_2O_3/TiO_2$-[W(**L1**)$(CO)_4$] photocathode clearly indicates the surface modification taking place.

i. Photoelectrochemical performance of a modified $Cu_2O/Ga_2O_3/TiO_2$-[W(L1)$(CO)_4$] photocathode in CO_2 reduction.

The photoelectrochemical characterization was conducted in a three-electrode system consisting of a platinum wire as the counter electrode, $Ag/AgNO_3$ as a reference electrode, and the as-fabricated photocathode as the working electrode in CH_3CN solution containing 0.1 M $TBAPF_6$ as a supporting electrolyte. The recorded potentials vs $Ag/AgNO_3$ were converted to E vs Fc/Fc^+ by the following equation:

$$\mathrm{E(vs\ Fc/}Fc^{+}) = \mathrm{E(vs\ Ag/}Ag^{+}) - 0.087\mathrm{V}$$

Photoelectrochemical measurements of the photocathode were carried out using the linear sweep voltammetry (LSV) under argon and CO_2 saturated conditions in the presence of simulated solar light (100mW/cm^2 AM 1.5G).

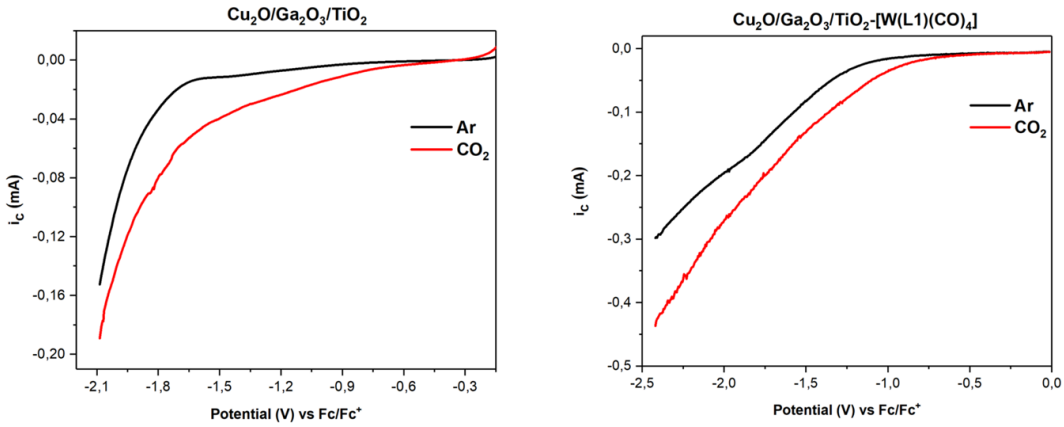

Figure III. 12 Cathodic LSV scans of pristine $Cu_2O/Ga_2O_3/TiO_2$ (left) and modified $Cu_2O/Ga_2O_3/TiO_2$-[W(**L1**)$(CO)_4$] (right) photoelectrodes under chopped simulated solar light in argon and CO_2 saturated CH_3CN/0.1M $TBAPF_6$ solution at v = 0.05mVs^{-1}.

As indicated in **Figure III. 12**, the pristine photocathode displayed low current values compared to the modified $Cu_2O/Ga_2O_3/TiO_2$ photocathode which demonstrated better catalytic current in CO_2 saturated condition as a result of the catalytic reduction of CO_2 substrate using the [W(**L1**)$(CO)_4$] catalyst.

Cathodic linear sweep voltammograms (LSVs) of $Cu_2O/Ga_2O_3/TiO_2$ in CO_2 saturated solution under chopped simulated solar light (100mW/cm^2 AM 1.5G) were recorded at 0.1 Vs^{-1} scan rate and presented in **Figure III. 13.**

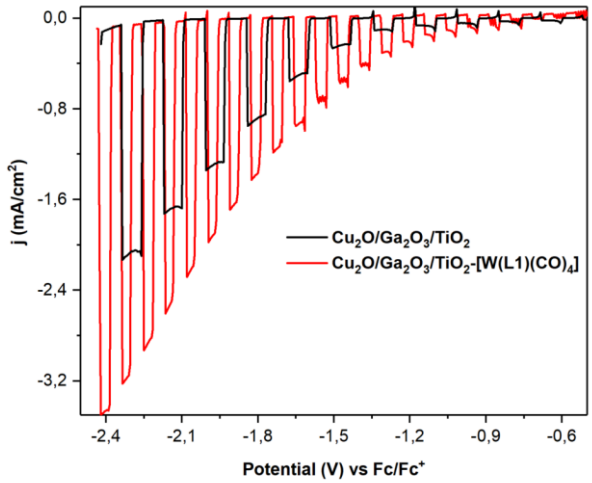

Figure III. 13 Cathodic LSV scans of pristine and modified $Cu_2O/Ga_2O_3/TiO_2$ photoelectrode under chopped simulated solar light in CO_2 saturated CH_3CN/0.1M $TBAPF_6$ solution at v = 0.05mVs^{-1}.

Evidently, the coating of the pristine $Cu_2O/Ga_2O_3/TiO_2$ photoelectrode with the [W(**L1**)$(CO)_4$] complex resulted to a noticeable increase of photovoltage from -1.3V vs Fc/Fc^+ as indicated in **Figure III. 13**. These observations clearly indicate the catalytic role of the [W(**L1**)$(CO)_4$] complex in the CO_2 reduction process.

The Faradaic efficiencies (FEs) of different products were quantified from the GC measurements of the modified $Cu_2O/Ga_2O_3/TiO_2$-[W(**L1**)$(CO)_4$] photoelectrode at different applied potentials values in a CO_2 saturated CH_3CN/0.1M $TBAPF_6$ electrolyte under simulated solar light irradiation.

Remarkably, the CO production at an applied potential of -2.1 V vs. Fc/Fc^+ reached a selectivity of 88%. Trace amounts of CH_4 and C_2H_4 were also detected at all applied potentials. Furthermore, a broad plateau of high CO yields was observed between -1.8 V and -2.2 V (vs. Fc/Fc^+). (**Figure III. 14A**)

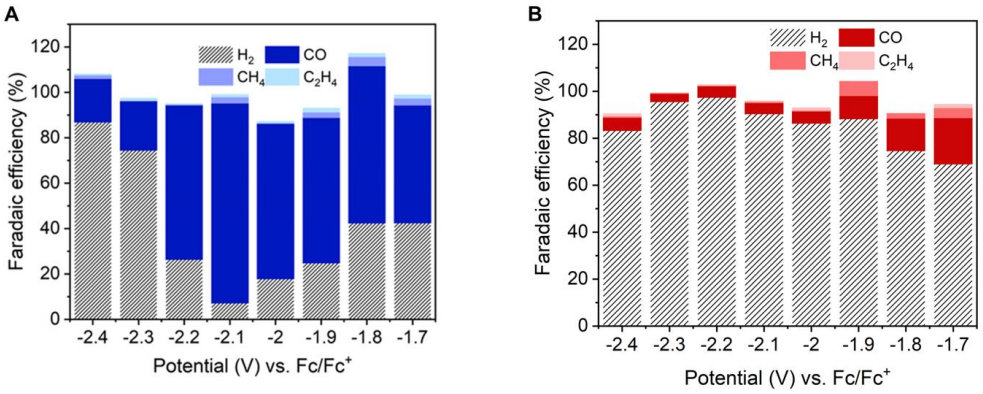

Figure III. 14 Faradaic efficiencies (FEs) of: **A**. $Cu_2O/Ga_2O_3/TiO_2$-[W(**L1**)$(CO)_4$] and **B**. $Cu_2O/Ga_2O_3/TiO_2$ photoelectrodes at different applied potentials values in a CO_2 saturated CH_3CN/0.1M $TBAPF_6$ electrolyte under simulated solar illumination (1 sun illumination at AM 1.5G)

As means of verifying that the CO produced is mainly from the modified $Cu_2O/Ga_2O_3/TiO_2$-[W(**L1**)$(CO)_4$] photoelectrode rather than $Cu_2O/Ga_2O_3/TiO_2$ or organic electrolyte decomposition, control experiments were performed on $Cu_2O/Ga_2O_3/TiO_2$ photoelectrode in CO_2 saturated conditions revealing H_2 gas as the major product formed as observed in **Figure III. 14B**.

In contrast to the modified photoelectrode, the bare $Cu_2O/Ga_2O_3/TiO_2$ photoelectrode produced a low amount of CO with a FE of 19.7% at applied potential -1.7 V (vs. Fc/Fc^+). This value gradually decreases at more negative potential; whereas H_2 gas was found to be the main product of the reduction process as a result of traces of H_2O in the solvent.

Chronoamperometry J−t measurements of the $Cu_2O/Ga_2O_3/TiO_2$ and $Cu_2O/Ga_2O_3/TiO_2$-[W(**L1**)$(CO)_4$] photoelectrode at a bias of -2.1V under interrupted light source for 2 minutes followed by 2 minutes of continuous lighting were conducted to verify a prolonged photoactivity of the modified photoelectrode. This measurement was also deemed to be important in confirming the generation of true photocurrent rather than corrosion current.

From **Figure III. 15**, the current density of the $Cu_2O/Ga_2O_3/TiO_2$-[W(**L1**)$(CO)_4$] photoelectrode increased during the first hour and gradually stabilized. After 10 hours of light irradiation, the $Cu_2O/Ga_2O_3/TiO_2$-[W(**L1**)$(CO)_4$] photoelectrode exhibited an excellent long-term stability. Whereas for the $Cu_2O/Ga_2O_3/TiO_2$ photoelectrode, current density increased during the first 20 min then steadily decreased throughout the photoirradiation measurements.

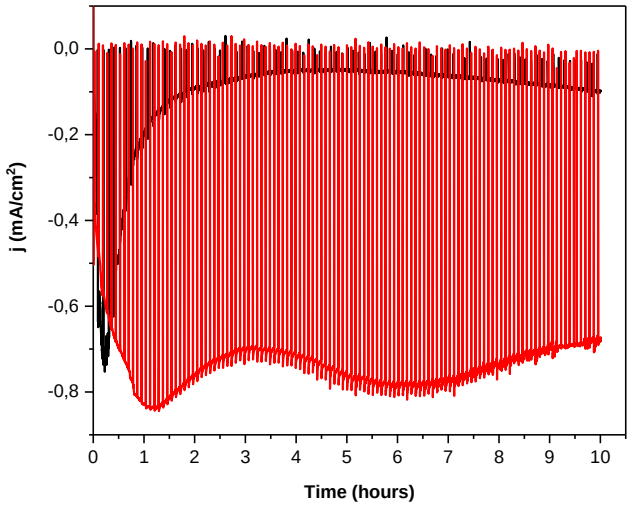

Figure III. 15 The chronoamperometry *J−t* curves of the $Cu_2O/Ga_2O_3/TiO_2$ (black) and $Cu_2O/Ga_2O_3/TiO_2$-[W(**L1**)$(CO)_4$] (red) under chopped simulated solar light (100mW/cm^2 AM 1.5G).

From this observation, it might be considered that the coated layer of [W(**L1**)$(CO)_4$] catalyst aids in preventing an immediate photodegradation of the $Cu_2O/Ga_2O_3/TiO_2$ photocathode during light irradiation. Conclusively, after 10 hours of the photoelectrochemical reaction under

these chopped light conditions resulted in a FE of 40% of CO which indicates a promising stability.

5. Pyridinyl benzimidazole family of complexes

The development of this family of complexes was done in an effort of further investigating the photophysical and electrochemical properties of metal complexes consisting of ligands analogous to the pyridine imidazole ligand. The photophysical and catalytic properties of the [W(**L1**)$(CO)_4$] complex could possibly be improved by an addition of substituent groups on the **L1** ligand, and these attributes combined together may promote the photocatalysis of CO_2. With this objective, two other metal complexes were synthesized and characterized as discussed in this part of the chapter.

5.1. Synthesis of [W(L)$(CO)_4$] complexes

Two different types of metal complexes [W(**L2**)$(CO)_4$] and [W(**L3**)$(CO)_4$] were synthesized using hexacarbonyl tungsten complexes, and two different types of pyridinyl benzimidazole (**L2** = 2-(pyridin-2-yl)-1H-benzo[d]imidazole and **L3** = 1-methyl-2-(pyridin-2-yl)-1H-benzo[d]imidazole) following previously reported literature by Stiddard (**Scheme III. 7**).[15] These complexes were synthesized in a reflux reaction under argon atmosphere, then collected through a filtration and a rinsing with diethyl ether.

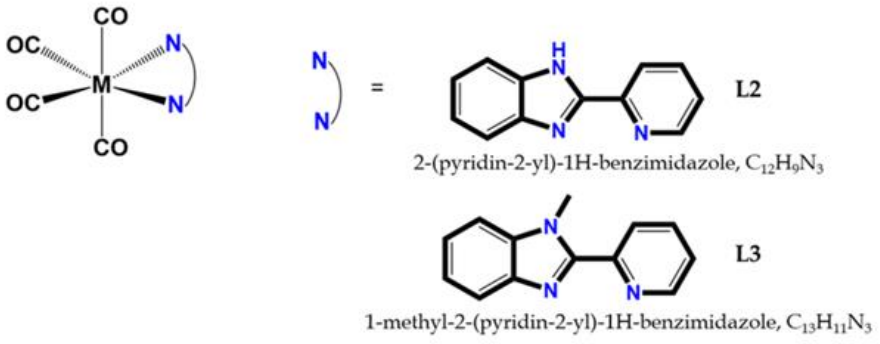

Scheme III. 7 Molecular structures of the ligands used in the synthesis of [M(**L**)$(CO)_4$] complexes.

5.2. Photophysical properties

In the absorption studies, samples to be analyzed were prepared by dissolving each of these complexes: [W(**L2**)$(CO)_4$] and [W(**L3**)$(CO)_4$] in an acetonitrile (CH_3CN) solution and then

deaerated by argon purging for 5 mins. From UV-Vis spectrometry measurements, these complexes displayed two absorption waves as shown in **Figure III. 16**.

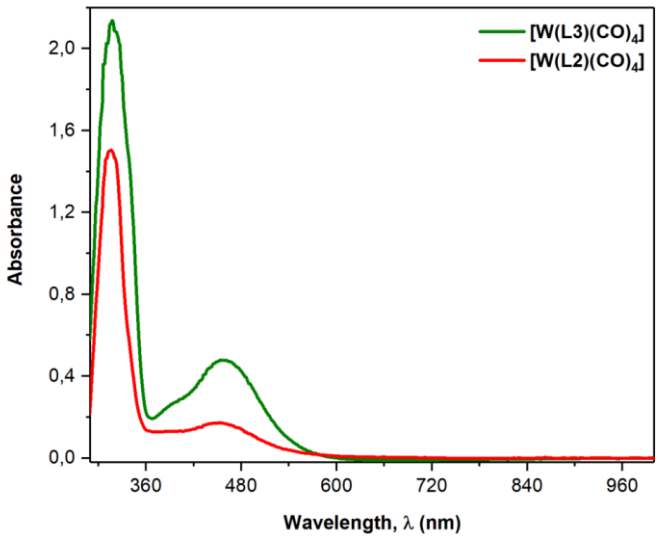

Figure III. 16 Absorption spectra of complexes [W(**L2**)$(CO)_4$] and [W(**L3**)$(CO)_4$] in CH_3CN solution. Inset: Zoomed-in spectra of the MLCT region of these complexes.

The two absorption bands were attributed to the ligand-centered $\pi \rightarrow \pi^*$ electronic transition (~ 315 nm) and a low-lying transition of the MLCT electronic transition around 445-455 nm. Upon excitation measurements in toluene, these complexes were found to have a much shorter lifetime compared to the [W(**L1**)$(CO)_4$] complexes as indicated in **Table III. 7**.

Table III. 7 Absorption, emission and excited state lifetime measurements of the [W(**L**)$(CO)_4$] complexes.

Complex	λ_{abs} in CH_3CN (nm)	λ_{em} in toluene (nm)	τ in toluene (ns)
[W(**L1**)$(CO)_4$]	460	588	70
[W(**L2**)$(CO)_4$]	450	640	26
[W(**L3**)$(CO)_4$]	454	675	5

5.3. Electrochemical characterization of [W(L)$(CO)_4$] complexes

Electrochemical studies of the [W(**L2**)$(CO)_4$] and [W(**L3**)$(CO)_4$] metal complexes (1mM) were carried out in acetonitrile with 0.1M $TBAPF_6$ as the supporting electrolyte. The cathodic cyclic

voltammetry (CV) measurements were performed at room temperature using a three-electrode cell configuration with glassy carbon electrode (GCE) as the working electrode and all potential values recorded against Ag/10^{-2}M $AgNO_3$ as the reference potential.

i. Electrochemical characterization of [M(L1)(CO)4] complexes under argon

In argon saturated solutions, these complexes displayed two different electrochemical systems as shown in **Figure III. 17A**. The cathodic CV scan of the [W(**L2**)$(CO)_4$] complex displayed two irreversible waves at -1.85 V and -2.45 V vs Ag/10^{-2}M $AgNO_3$. Despite this complex having an electrochemical response similar to that of the [W(**L1**)$(CO)_4$] complex; the irreversible waves of the [W(**L2**)$(CO)_4$] complex were positioned at less negative potential in comparison to the [W(**L1**)$(CO)_4$] complex. This noticeable potential gain of 70 mV and 260 mV for the first and second wave respectively as detected in the CV scan of the [W(**L2**)$(CO)_4$] complex can be attributed to the additional phenyl ring linked to the imidazole structure (**Table III. 8**).

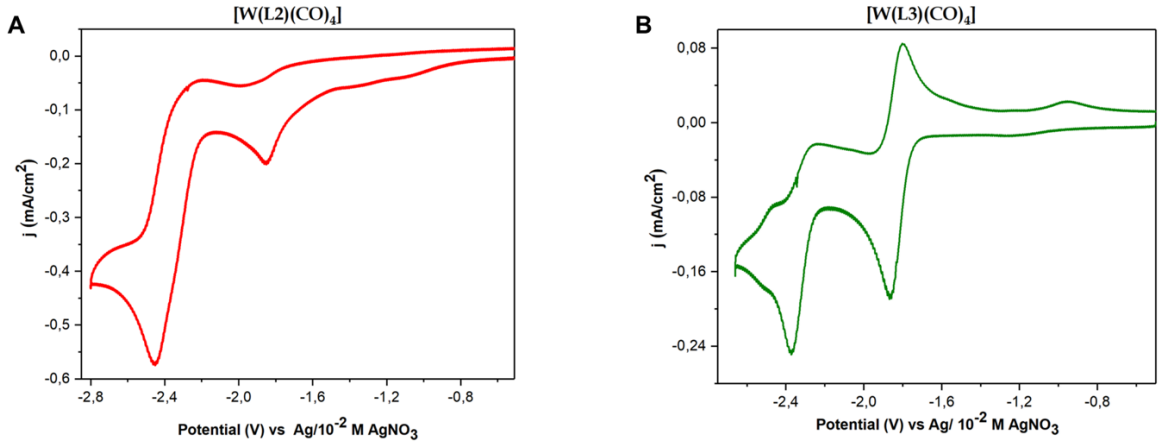

Figure III. 17 Cathodic CV scans of **A**: 1mM [W(**L2**)$(CO)_4$)] and **B**: 1mM [W(**L3**)$(CO)_4$)] complex under argon saturated conditions on a GCE in CH_3CN/0,1M $TBAPF_6$ at ν =0.1Vs^{-1}.

Interestingly, the [W(**L3**)$(CO)_4$] complex displayed a different electrochemical behavior in comparison to other complexes [W(**L1**)$(CO)_4$] and [W(**L2**)$(CO)_4$] complexes. An electrochemical response with a reversible wave followed by an irreversible one located respectively at -1.83V and -2.38V vs Ag/10^{-2}M $AgNO_3$ was reported for the [W(**L3**)$(CO)_4$] complex (**Figure III. 17B**).

The reversibility of the first wave is linked to the presence of the methyl substituted group on the imidazole ring. This methyl substitution prevents the chemical transformation of the

imidazole ring upon one-electron reduction. Among all complexes of the [W(**L**)(CO)$_4$] analogy reported in this chapter, the [W(**L3**)(CO)$_4$] complex displayed the least negative electrochemical potential values for the two reduction waves as shown in **Table III. 8**.

Table III. 8 Electrode potentials of the [W(**L**)(CO)$_4$] complexes in CH_3CN/0.1M $TBAPF_6$ on a GCE at ν =0.1Vs^{-1}

Complexes	**E (V) vs Ag / 0.01M $AgNO_3$**	
	E_{pc1}	**E_{pc2}**
[W(**L1**)(CO)$_4$]	-1.92	-2.71
[W(**L2**)(CO)$_4$]	-1.85	-2.45
[W(**L3**)(CO)$_4$]	$E_{1/2}$ = -1.83 (ΔE_p=0.07)	-2.37

ii. Electrochemical reduction of CO_2 using [W(L)(CO)$_4$] complexes

From **Figure III. 18**, cathodic CV scans of the [W(**L2**)(CO)$_4$] and [W(**L3**)(CO)$_4$] complexes under CO_2 saturated conditions presented an increase of current on the second reduction wave which confirms the catalytic role of these complexes towards CO_2 reduction.

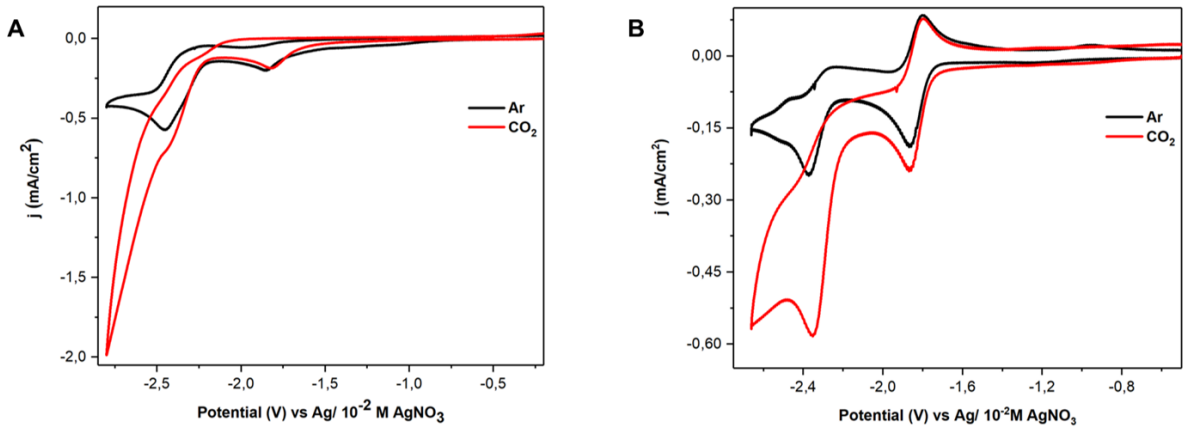

Figure III. 18 Cathodic CV scans of a **A**: 1mM [W(**L2**)(CO)$_4$] and **B**: 1mM [W(**L3**)(CO)$_4$] complex under CO_2 saturated conditions on a GCE in CH_3CN/0,1M $TBAPF_6$ at ν =0.1Vs^{-1}.

With the catalytic current response being detected at the second reduction wave, the active species of these complexes are assumed to be similar to the active species of the [W(**L1**)(CO)$_4$)] complex, i.e. tris-carbonyl reduced [W(**L**)(CO)$_3$]$^{2-}$ species.

As it was previously mentioned in this part of the chapter, these complexes were synthesized with an objective of improving the photophysical and electrochemical properties of this family of complexes. By introducing two different substituents groups, an improvement of photophysical properties was not observed; however, both complexes presented better electrochemical properties than the [W(**L1**)$(CO)_4$] complex.

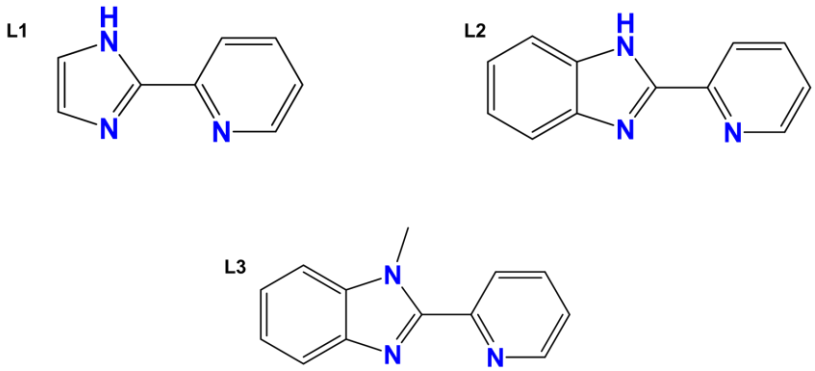

Scheme III. 8 Different structures of the pyridine imidazole-based.

Evidently, the addition of substituents groups on ligand **L1** leading to the formation of **L2** and **L3** ligands (**Scheme III.8**) resulted to metal complexes with better electrochemical properties.

6. Conclusion

In the course of this chapter, a different family of complexes [M(**L**)$(CO)_4$] were synthesized using pyridine-imidazole ligands. This family of complexes was developed with an intention of exploring and utilizing its possible photophysical properties in the photocatalysis of CO_2 reduction.

Evidently, only the [W(**L1**)$(CO)_4$] series of complexes displayed strong emissive properties with long excited lifetime. However, the long lifetimes of these complexes were reported in toluene which is an organic solvent that is rarely used in the CO_2 reduction processes (poor solubility of CO_2 in toluene).

Despite this hindering factor, we further investigated the electrochemical properties of these complexes which indeed confirmed the catalytic role of these complexes towards the reduction of CO_2. To our knowledge, the electrocatalytic role of this family of complexes towards CO_2 reduction has never been reported before till now.

Additionally, photoelectrocatalysis of CO_2 using mainly the [W(**L1**)$(CO)_4$)] complex was investigated using a $Cu_2O/Ga_2O_3/TiO_2$ photoelectrode. In such heterogeneous conditions, modification of the $Cu_2O/Ga_2O_3/TiO_2$ photocathode with the [W(**L1**)$(CO)_4$)] complex resulted in an efficient photoelectroreduction of CO_2 to CO with a FE of 88%.

And surprisingly, the [W(**L1**)$(CO)_4$] complex was reported to act as an additional protective layer towards the $Cu_2O/Ga_2O_3/TiO_2$ photoelectrode against corrosion which resulted to a prolonged photostability of the modified photoelectrode and a stable photocurrent density in the course of long-term photoirradiation. This finding shines an optimistic light on the possibility of developing a photoelectrochemical (PEC) carbon dioxide reduction (CO2R) system free of rare, expensive metals that can be used in tackling the climate and energy storage challenge.

Bibliography

1. T. J. Battin, S. Luyssaert, L. A. Kaplan, A. K. Aufdenkampe, A. Richter, L. J. Tranvik, *Nat. Geosci*., **2009**, *2*, 598−600.
2. D. W. Keith, *Science*., **2009**, *325*, 1654−1655.
3. D. Kim, K. K. Sakimoto, D. Hong, P. Yang, *Angew. Chem., Int. Ed*., **2015**, *54*, 3259−3266.
4. D. K. Dogutan, D. G. Nocera, *Acc. Chem. Res*., **2019**, *52*, 3143−3148.
5. J. Albero, Y. Peng, H. García, *ACS Catal*., **2020**, *10*, 5734−5749.
6. K. Kalyanasundaram, *J. Chem. Soc. Faraday Trans. 2*., **1986**, *82*, 2401–2415.
7. C. Kutal, M. A. Weber, G. Ferraudi, D. Geiger, *Organometallics*., **1985**, *4*, 2161–2166.
8. C. Kutal, A. J. Corbin, G. Ferraudi, *Organometallics*., **1987**, *6*, 553–557.
9. S. Sato, T. Morikawa, T. Kajino, O. Ishitani, *Angew. Chem. Int. Ed.*, **2013**, *52*, 988–992.
10. R.O. Reithmeier, S. Meister, B. Rieger, A. Siebel, M. Tschurl, U. Heiz, E.Herdtweck, *Dalton Trans*., **2014**, *43*, 13259–13269.
11. J. Grodkowski, D. Behar, P. Neta, P. Hambright, *J. Phys. Chem. A*., **1997**, *101*, 248–254.
12. D. Behar, T. Dhanasekaran, P. Neta, C.M. Hosten, D. Ejeh, P. Hambright, E. Fujita, *J. Phys. Chem. A*., **1998**, *102*, 2870–2877.
13. J. Bonin, M. Chaussemier, M. Robert, M. Routier, *ChemCatChem*., **2014**, *6*, 3200–3207.
14. J. J. Lee, C. P. Yap, T. S. Chwee, W. Y. Fan, *Dalton Trans*., **2017**, *46*, 11008-11012.
15. M. H. B. Stiddard, *J. Chem. Soc*., **1962**, 4712-4715.
16. R. Johnson, H. Madhani, J. P. Bullock, *Inorg. Chim. Acta*., **2007**, *360*, 3414–3423.
17. Encyclopedia of electrochemistry of the elements Ed A. J. Band, New York, **1973**, *xv*, 235.
18. W.J. Eilbeck, F. Holmes, G.G. Phillips, A.E. Underhill, *J. Chem. Soc. A.*, **1967**, 1161-1166.
19. W.J. Eilbeck, F. Holmes, *J. Chem. Soc. A*., **1967**, 1777-1782.
20. W.J. Eilbeck, F. Holmes, G. Phillips, *J. Chem. Soc. A*., **1970**, 689-690.
21. A. Paracchino, V. Laporte, K. Sivula, M. Grätzel, E. Thimsen, *Nat. Mater*., **2011**, *10*, 456–461.

22. M. Schreier, P. Gao, M. T. Mayer, J. Luo, T. Moehl, M. K. Nazeeruddin, S. D.Tilley, M. Grätzel, *Energy Environ. Sci*., **2015**, *8*, 855-861.
23. C. Li, T. Hisatomi, O. Watanabe, M. Nakabayashi, N. Shibata, K. Domen, J.-J. Delaunay, *Energy Environ. Sci*., **2015**, *8*, 1493–1500.
24. L. Pan, J. H. Hyun, M. T. Mayer, M. K. Son, A. Ummadisingu, J. S. Lee, A. Hagfeldt, J. Luo, M. Grätzel, *Nat. Catal*., **2018**, *1*, 412-420.
25. L. Pan, Y. Liu, L. Yao, D. Ren, K. Sivula, M. Grätzel, A. Hagfeldt, *Nat Commun*., **2020**, *11*(1), 318.
26. S. Rioual, B. Lescop, F. Quentel, F. Gloaguen, *Phys. Chem. Chem. Phys*., **2015**, *17*, 13374−13379.
27. K. L. Materna, R. H. Crabtree, G. W. Brudvig, *Chem. Soc. Rev*., **2017**, *46*, 6099−6110.
28. J. Willkomm, K. L. Orchard, A. Reynal, E. Pastor, J. R. Durrant, E. Reisner, *Chem. Soc. Rev*., **2016**, *45*, 9−23.
29. B. J. Brennan, M. J. Llansola Portolés, P. A. Liddell, T.A. Moore, A. L. Moore, D. Gust, *Phys. Chem. Chem. Phys*., **2013**, *15*, 16605−16614.
30. L. A. Martini, G. F. Moore, R. L. Milot, L. Z. Cai, S.W. Sheehan, C. A. Schmuttenmaer, G. W. Brudvig, R. H. Crabtree, *J. Phys. Chem. C*., **2013**, *117*,14526−14533.

CHAPTER IV. QUATERPYRIDINE COMPLEX OF Cr (III)

1. Introduction

After preparing different types of complexes using the group VI metals with an oxidation state of zero, a new approach was investigated. This approach involved synthesizing complexes with metal centers that have an oxidation state different from zero. From literature investigation, Cr (III) complexes have notably proven their efficiency as CO_2 electrocatalyst with 2,2'-bipyridine based ligand (see Chap I) substituted with 2 phenolate, leading to a tetradentate ligand. On the other hand, we came across the work of Constable who designed a Cr (III) complex with a quaterpyridine tetradentate ligand.[1]

As a polypyridyl complex of the first-row transition metals, the Cr (III) complexes[2-3] are underexplored in comparison to known Cu (II), Ni (II), Co (III) and Fe (II) complexes which have been widely investigated in the domain of electro/photo-catalysis of CO_2.[4-11] In the work of Constable, the formation of a hexacoordinated Cr (III) complexes possessing a $[Ar]3d^3$ configuration of the metal ion and a distorted octahedral symmetry was reported.

Use of a quaterpyridine (qpy) ligand proved to be advantageous in the synthesis of polypyridyl Cr (III) complex as a result of its properties. As a good π-acceptor ligand resistant to oxidation, its interaction with metal centers in high oxidation states can lead to the formation of stable metal complexes which could favor CO_2 reduction at relatively low potential values via a low-valent active intermediate.[12]

This $[Cr(qpy)(Cl)_2]Cl.4H_2O$ complex (**Scheme IV.1)** was characterized under argon by electrochemistry[1] but it had not been further investigated as to whether it can play a catalytic role in the reduction of CO_2, hence the following work is bound to be novel.

2. Preparation and characterization of $[Cr(qpy)(Cl)_2]Cl.4H_2O$ complex

2.1. Synthesis of $[Cr(qpy)(Cl)_2]Cl.4H_2O$ complex

The chromium bis-chloro [4',4''-diphenyl-2,2':6',2'':6'',2'''-quaterpyridine], complex with chloride counter anion was synthesized using a qpy ligand and a hydrated chromium (III) chloride salt as starting materials, as depicted in **Scheme IV.1**. Given the inert nature of the Cr^{3+}, the complexation procedure was found to be laborious. From a reflux reaction between $CrCl_3.6H_2O$ and qpy ligand that took place in ethanol for 30 hours under inert conditions, a grey solid powder was collected by filtration (Yield = 65~72%) .[1,5,13]

This pseudo-octahedral cation with the qpy ligand acting as an approximately planar tetradentate occupying the equatorial plane and the two chlorine ligands in the axial sites, is paramagnetic. Hence, it cannot be investigated with ^{1}H NMR spectroscopy.

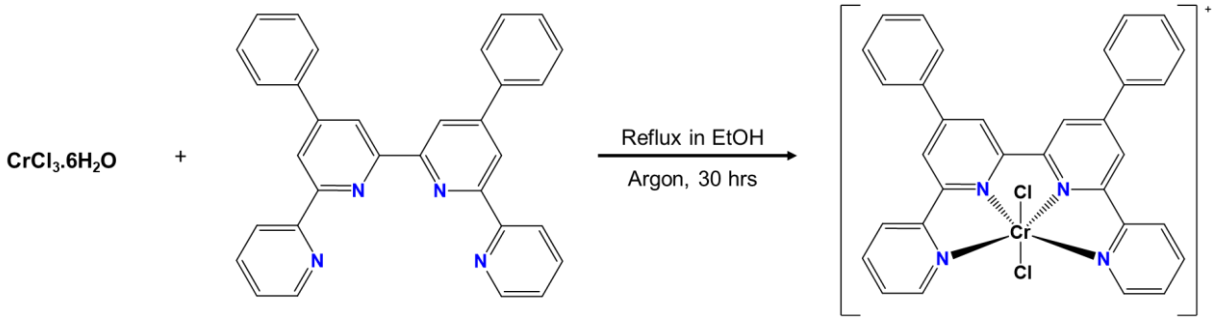

Scheme IV.1 Synthesis procedure for $[Cr(qpy)(Cl)_2]^+$ complex.

An effort of synthesizing the $[Mo(qpy)(Cl)_2]^+$ complex using $MoCl_3$ and quaterpyridine ligand proved futile despite various attempts.

2.2. Photophysical properties

The $[Cr(qpy)(Cl)_2]^+$ complex was found to be sparingly soluble in most of the organic solvents except in DMF, in which it was readily soluble displaying a faint brown-gold solution. Its absorption spectrum demonstrated a strong and a weak absorption band corresponding to the ligand centered (in the UV region) and metal centered (in the visible region) electronic transitions respectively (see **Figure IV. 1**).

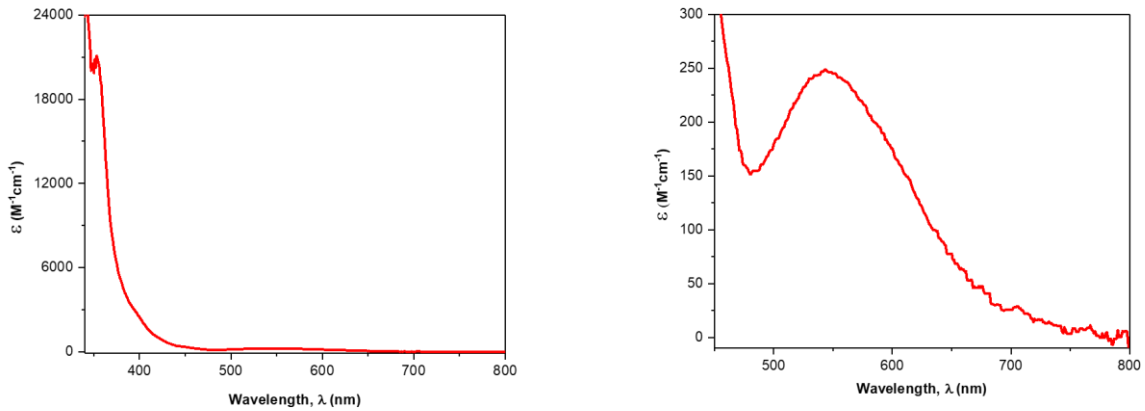

Figure IV. 1 UV-Vis absorption spectra of $[Cr(qpy)(Cl)_2]^+$ complexes in DMF; spectra on the left (zoom-out) and on the right (zoom-in).

As depicted in **Figure IV.1** (right), the strong absorption band localized at 353 nm in the UV region is associated to the allowed $\pi \rightarrow \pi^*$ intraligand electronic transition in accordance to its high absorption molar coefficient of 2×10^4 $M^{-1}cm^{-1}$. The subsequent weak absorption band with a maxima located around 540 nm (ε=250 $M^{-1}cm^{-1}$) can be associated to the forbidden metal centered transitions, i.e. Laporte forbidden d-d electronic transitions (see **Figure IV.1** (left)).

This Cr (III) complex with an electronic configuration of $[Ar]3d^3$ has three electrons in the HOMO π_M (t_{2g}) orbitals. As an octahedral complex the degeneracy of the chromium d-orbitals is lifted, resulting in two orbital subsets of t_{2g} and e_g symmetry. In the ground state, the electronic configuration $(t_{2g})^3$ with the d orbitals filled according to Hund's Rule renders the spin state S = $^3/_2$, hence the quartet ground state $^4A_{2g}$.[14]

Upon photon absorption, an electron can be promoted from a t_{2g} orbital to one of the two unoccupied e_g orbitals without changing its spin state as shown in **Scheme IV. 2**. But, it should be noted that this type of electronic transitions $\pi_M(t_{2g})^2\sigma_M^*(e_g)^1$ is forbidden according to the Laporte rule which states that electronic transitions that conserve parity are forbidden; i.e. g → g or u → u. And since all d-orbitals are gerade (g), the d → d transitions of this Cr (III) transition metal complex are forbidden transitions, hence the weak intense broad band in **Figure IV. 1**.

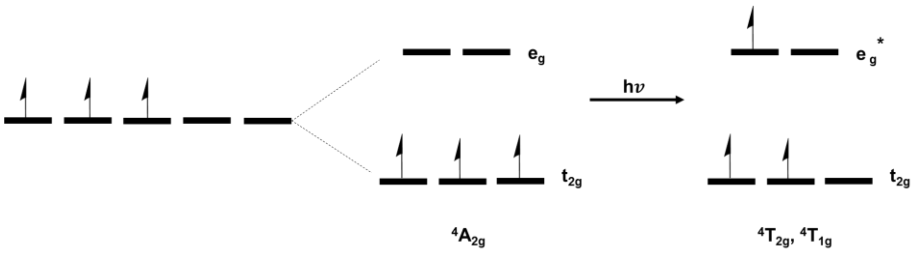

Scheme IV. 2 The d-orbital diagram for the electronic ground and excited states for d^3 Cr (III).

2.3. Electrochemical characterization under argon

i. Electroreduction of the 4',4''-diphenyl-2,2':6',2'':6'',2'''-quaterpyridine ligand

Prior to characterizing the Cr (III) complex, the synthesized 4',4''-diphenyl-2,2':6',2'':6'',2'''-quaterpyridine ligand (see experimental part) was investigated for its electrochemical properties in argon saturated DMF solution using cyclic voltammogram as presented in **Figure IV. 2**.

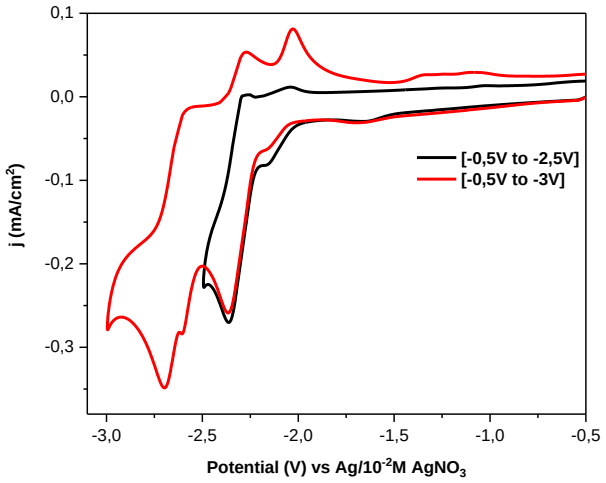

Figure IV. 2 Different cathodic CV scans of a 1mM of the diphenyl quaterpyridine ligand under argon atmosphere on a GCE in DMF/0,1M $TBAPF_6$ at $v = 0.1Vs^{-1}$.

As depicted in **Figure IV. 2**, two reduction waves (at -2.36V and -2.69 V vs $Ag/AgNO_3$) associated to the diphenyl quaterpyridine ligand were observed. The presence of a nitrogen atom on each of the four centered pyridine rings might suggest an equal probability for the localization of the first incoming electron on either of these four rings, whereas the localization of the second incoming electron might be dependent on the delocalization of electron density among these four pyridine rings.

The study of each reduction peak indicates an irreversibility behavior of these peaks, with the cathodic CV scan of the second reduction peak revealing three oxidation peaks (-2.56 V, -2.27 V and -2.02 V) on the reverse scan (red CV scan in **Figure IV. 2**). These oxidation peaks can be associated with oxidation of different reduced species of the ligand that vary depending on delocalization of the electron density in the quaterpyridine ring.

ii. Electroreduction of $[Cr(qpy)Cl_2]^+$ complex under argon

With almost no literature work reported on the electrochemical properties of this $[Cr(qpy)(Cl)_2]^+$ complex apart from that of Constable,[1] the first characterization technique employed in proving a successful synthesis of this complex was cyclic voltammetry (CV). In similar working conditions as the work of Constable, 1mM of the $[Cr(qpy)(Cl)_2]^+$ complex was

solubilized in CH_3CN/0.1 M $TBABF_4$ electrolyte with $Ag/10^{-2}$ M $AgNO_3$ as the reference electrode, Pt as the counter electrode and glassy carbon (GCE) as the working electrode.

As shown in **Figure IV.3**, this complex characterized at a scan rate of $0.1Vs^{-1}$ displayed three different reduction waves. However, this cathodic CV scan showed a low faradaic current response which could be associated with a low solubility of the $[Cr(qpy)(Cl)_2]^+$ complex in acetonitrile.

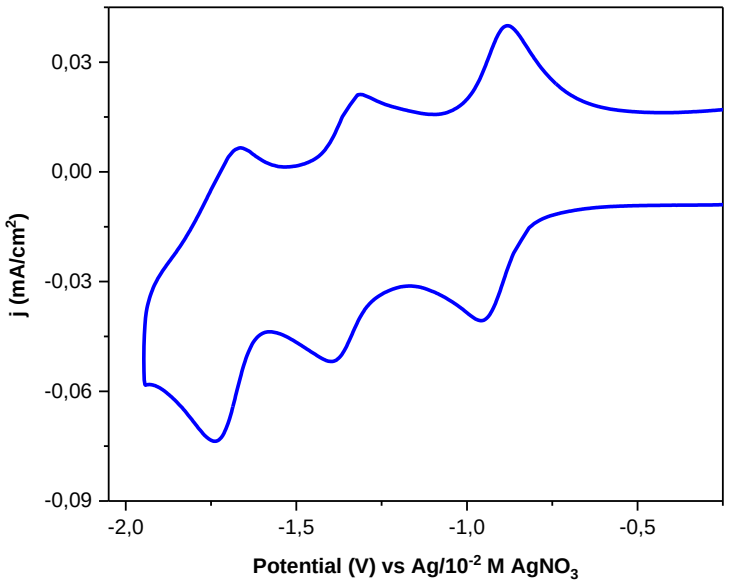

Figure IV. 3 Cathodic scan CV of a 1mM $[Cr(qpy)(Cl)_2]^+$ complex under argon atmosphere on a GCE in CH_3CN/0,1M $TBABF_4$ at $v = 0.1Vs^{-1}$.

Change of supporting electrolyte from $TBABF_4$ to $TBAPF_6$ did not visibly improve the solubility of the $[Cr(qpy)(Cl)_2]^+$ complex, and thus there was no significant improvement in current response associated to the metal complex in this given electrolyte.

Subsequent efforts towards improving the solubility of the complex involved studying of this Cr (III) metal complex in dimethylformamide while using $TBAPF_6$ as the supporting electrolyte which led to a complete solubilization of the complex in electrolyte resulting to a better current response as shown in **Figure IV. 4**.

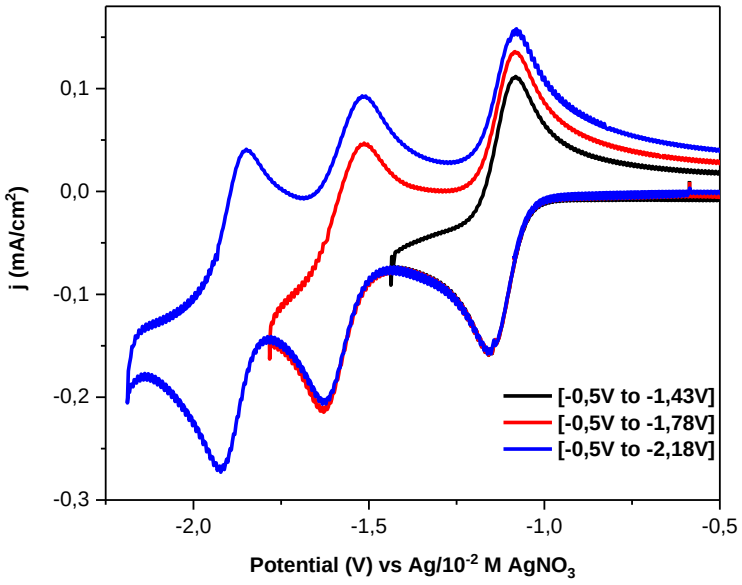

Figure IV. 4 Cathodic CV scan indicating different reduction waves of a 1mM $[Cr(qpy)(Cl)_2]^+$ complex under argon atmosphere on a GCE in DMF/0,1M $TBAPF_6$ at v = 0.1Vs^{-1}.

In the cathodic scanning of $[Cr(qpy)(Cl)_2]^+$ complex under inert conditions, this Cr(III) complex was found to be electrochemically active with a series of three reduction waves at $E_{1/2}$ (V) = -1.03, -1.49 and -1.8 vs $Ag/10^{-2}$ M $AgNO_3$ reference electrode. Given the difference in electrochemical response observed for the free ligand (**Figure IV. 3**), the reduction waves indicated in **Figure IV. 4** are mainly attributed to the metal complex. The reduction potential values of the free qpy ligand and Cr (III) metal complex in solution are summarized in **Table IV. 1**.

Table IV. 1 Electroreduction potential values of the $[Cr(qpy)(Cl)_2]^+$ complex and free quaterpyridine ligand in DMF/0.1M $TBAPF_6$ at v = 0.1 Vs^{-1}.

Reactants [1mM]	**$E_{1/2}$ (ΔE_p), V vs $Ag/10^{-2}$ M $AgNO_3$**				
	E_{red} *(1)*	**E_{red} *(2)***	**E_{red} *(3)***	**E_{red} *(4)***	**E_{red} *(5)***
$[Cr(qpy)(Cl)_2]^+$ (in DMF)	-1.03 (0.07)	-1.48 (0.11)	-1.79 (0.07)	-	-2.69
$[Cr(qpy)(Cl)_2]^+$ (in CH_3CN)	-0.96 (0.08)	-1.40 (0.09)	-1.74 (0.08)	-	-2.69
Quaterpyridine	-	-	-	-2.36	-2.69

From **Table IV. 1**, the cathodic waves between -0.5V to -2 V vs Ag/10^{-2} M $AgNO_3$ detected in the CV scan of the metal complex were absent in the cathodic CV scan of the free qpy ligand which displays two irreversible systems at -2.36V and -2.69 V vs Ag/10^{-2} M $AgNO_3$ (**Figure IV. 3**).

Each of the reduction waves detected in the cathodic CV scan of the Cr (III) complex were further investigated at different scan rates (from 0.005 to 0.5 Vs^{-1}) in order to interpret their kinetic behavior, i.e. reversible or irreversible. From calculating the ΔE_p **(Table IV. 1)** and the peak currents ratio i_{pc}/i_{pa} for the forward and reverse scans; the first reduction wave was deducted to be a reversible process while the second and third peak were quasi-reversible processes. Using CV measurements recorded at different scan rates, a correlation between the square root of scan rate and the peak current i_p of the first reduction wave was developed following **Eq. IV.1** and reported in **Figure IV. 5**.

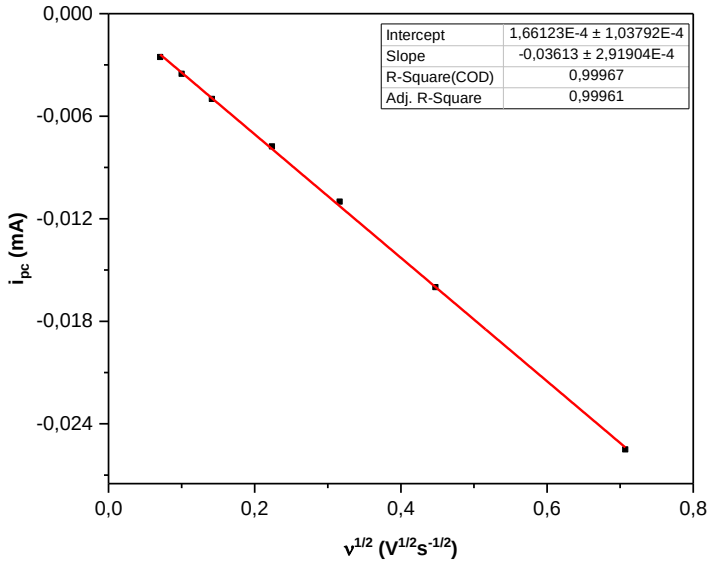

Figure IV. 5 The Randles–Ševčík plot for the first reduction wave of 1mM $[Cr(qpy)(Cl)_2]^+$ complex under argon atmosphere on a GCE in DMF/0,1M $TBAPF_6$ at different v = 0.005-0.5Vs^{-1}.

The linear trend of the Randles–Ševčík plot indicated in **Figure IV. 5** is common in all of the three redox processes, which indicates that these three redox waves are diffusion-controlled processes. From a Randles–Ševčík equation (**Eq. IV.1**), a diffusion coefficient of 3.59 ×10^{-6} cm^2s^{-1} was obtained for the $[Cr(qpy)(Cl)_2]^+$ species.

$$ip = 0.4463nFAC\left(\frac{nF\nu D}{RT}\right)^{\frac{1}{2}} \qquad \textbf{Eq. IV. 1}$$

Using the calculated diffusion coefficient, the hydrodynamic radius (R_H) of 7.58 Å was deduced using the Stokes-Einstein equation (**Eq. IV. 2**), where k is the Boltzmann constant, T is the temperature, η is the viscosity of the given medium.

$$R_H = \frac{kT}{6\pi\eta D} \qquad \textbf{Eq. IV. 2}$$

Exhaustive electrolysis was performed at each reduction potential and additional electrochemical studies were done using a rotating disc electrode (RDE) as means of investigating reaction mechanisms associated with each redox system. These redox processes appeared to have similar current magnitude prior and after electrolysis as monoelectronic reduction processes (see **Figure IV. 6A**). Each redox system's electron count (z) equaled one when determined using **Eq. IV. 3,** where z is the number of electrons, Q is the charge flow during electrolysis, n is the number of moles of complex in solution and F is the faradaic constant.

$$z = \frac{Q}{nF} \qquad \textbf{Eq. IV. 3}$$

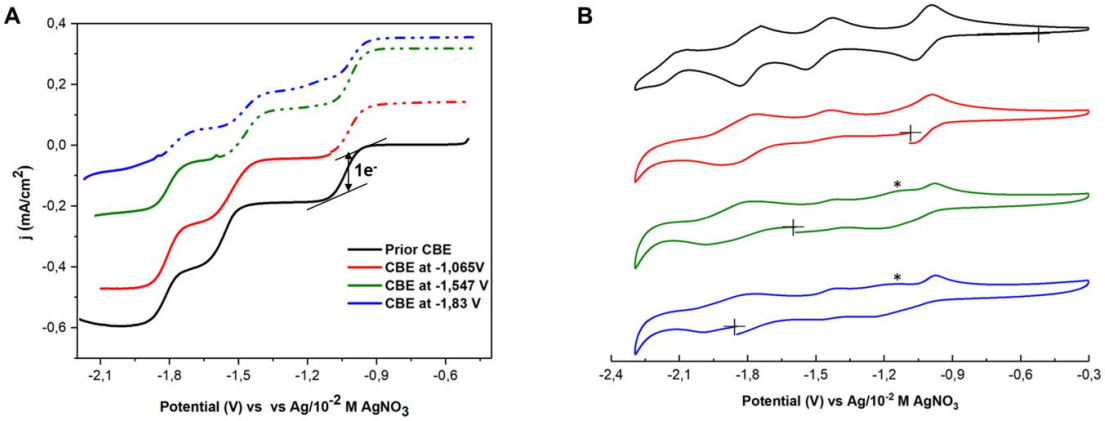

Figure IV. 6 A: Cathodic (solid lines) and anodic (dash dot dot lines) CV scans prior and after electrolysis of 1mM $[Cr(qpy)(Cl)_2]^+$ complex under argon on a RDE at different E_{red} values; **B**: Evolution of cathodic CV scans after electrolysis of 1mM $[Cr(qpy)(Cl)_2]^+$ complex under argon on a GCE in DMF/0,1M $TBAPF_6$ at ν = 0.1Vs^{-1}.

The incoming added electrons are most likely localized on the quaterpyridine ligand, since the Cr^{3+} core is thought to be redox inert.[1,15] In the CV time scale prior to electrolysis, these reduction processes are considered to reversible with no formation of chemically transformed species as indicated in **Eq. i-iii**.

i. $[Cr^{III}(qpy)(Cl)_2]^+ + e^- \xleftrightarrow{E_1: R1/O1} [Cr^{III}(qpy^{\bullet -})(Cl)_2]$ $\quad E_{1/2} = -1{,}06$ V

ii. $[Cr^{III}(qpy^{\bullet -})(Cl)_2] + e^- \xleftrightarrow{E_2: R2/O2} [Cr^{III}(qpy^{2-})(Cl)_2]^-$ $\quad E_{1/2} = -1{,}55$ V

iii. $[Cr^{III}(qpy^{2-})(Cl)_2]^- + e^- \xleftrightarrow{E_3: R3/O3} [Cr^{III}(qpy^{3-})(Cl)_2]^{2-}$ $\quad E_{1/2} = -1{,}83$ V

However, after performing electrolysis at the second reduction wave the recorded cathodic CV scan indicates a shift in the reduction potential values as well as a formation on a new oxidation peak (≈ -1.12V) * in its reverse scan as shown in **Figure IV. 6B**.

A study on the oxidation systems of the complex prior electrolysis displayed an oxidation peak at 0.6V vs Ag/10^{-2}M $AgNO_3$ (**Figure IV. 7**), corresponding to the oxidation of the chloride counter ion. After the first electrolysis process, the current magnitude corresponding to the chloride oxidation process was not modified; however, upon electrolysis at the second reduction peak some changes in the CV scans were detected (see **Figure IV. 6-B and Figure IV. 7A)**.

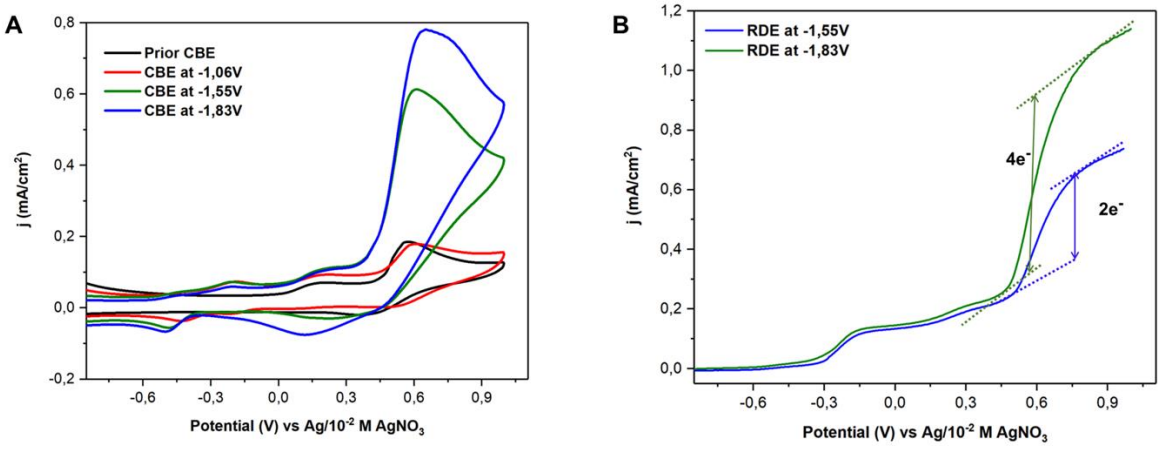

Figure IV. 7 Anodic CV scans of 1mM $[Cr(qpy)(Cl)_2]Cl$ complex prior and after electrolysis at different E_{red} values on a GCE (**A**), and on a RDE (**B**) under argon in DMF/0,1M $TBAPF_6$ at v = 0.1Vs^{-1}.

Upon electrolysis of the complex at the second wave (-1.55V), the oxidation peak at 0.6V demonstrated an increase of current density which might suggest an accumulation of released

chloride ions in solution upon further electrolysis of the $[Cr(qpy^{\cdot -})(Cl)_2]$ complex. This oxidation process was deduced to be a 2-electron oxidation process (attributed to two chloride ions, one Cl ion released in solution after electrolysis at -1.55V and one Cl counter ion) as indicated by the RDE experiment (blue) as seen in **Figure IV. 7B**.

By considering the increase of current after electrolysis at -1.55V and a two-electron oxidized reaction occurring at 0.6V, a chemical transformation of the bis-reduced $[Cr(qpy)(Cl)_2]^+$ complex is assumed to take place. This transformation is associated to the release of one chloride ion from the $[Cr(qpy^{2-})(Cl)_2]^+$ complex resulting into a formation of chemically transformed species, i.e. $[Cr^{III}(qpy^{2-})(Cl)]^-$. These new species can account for the appearance of an oxidation peak (≈ -1.12V vs $Ag/10^{-2}M\ AgNO_3$)* in the reverse scan of the cathodic CV scan (**Figure IV. 6B**). Reaction equations (**Eq. iv, v**) suggest a formation of bi-reduced species $[Cr^{III}(qpy^{2-})(Cl)_2]^-$ upon electrolysis which can lead to formation of $[Cr^{III}(qpy^{2-})(Cl)]$ species after one chloride ligand dissociation.

iv. $[Cr^{III}(qpy^{\cdot -})(Cl)_2] + e^- \longleftrightarrow [Cr^{III}(qpy^{2-})(Cl)_2]^-$ $\quad E_{onset} = -1{,}55\ V$

v. $[Cr^{III}(qpy^{2-})(Cl)_2]^- \longrightarrow [Cr^{III}(qpy^{2-})(Cl)] + Cl^-$

The formation of reduced species upon electron reduction (**Eq. iv**) and new chemical species (**Eq. v**) due to the release of chloride might suggest an occurrence of an EC mechanism (with E: electron transfer step and C: the chemical reaction step). The subsequent electrolysis process at the third reduction wave results in a 4-electron oxidation process at 06V which might suggest the release of another Cl^-. However, the magnitude of 4 electrons indicates that another one-electron oxidation process is superimposed. The formation of other chemically transformed species could be associated with the detected reduction peaks at 0.11V and -0.5V on the reversed scan of **Figure IV. 7A**.

The three electron transfer steps appear to be reversible in a timescale of the CV (**Figure IV. 4**). However, the emerging peaks in the CV scans obtained after electrolysis suggest a formation of new chemical species as a result of chloride ligand dissociation (**Figure IV. 6B**). This observation might suggest a slow kinetic rate for the chemical transformation step hence the quasi-reversibility behavior of the 2nd and 3rd redox systems during the CV timescale.

UV-visible absorption spectra were recorded after exhaustive electrolysis of the $[Cr(qpy)(Cl)_2]^+$ complex performed in DMF, in order to characterize the different redox states of the complex.

Prior electrolysis, one strong absorption band in the UV region at 326 nm and a weak absorption band at 540 are observed, these bands are assigned to the ligand centered and forbidden metal centered transitions respectively (**Figure IV. 8**).

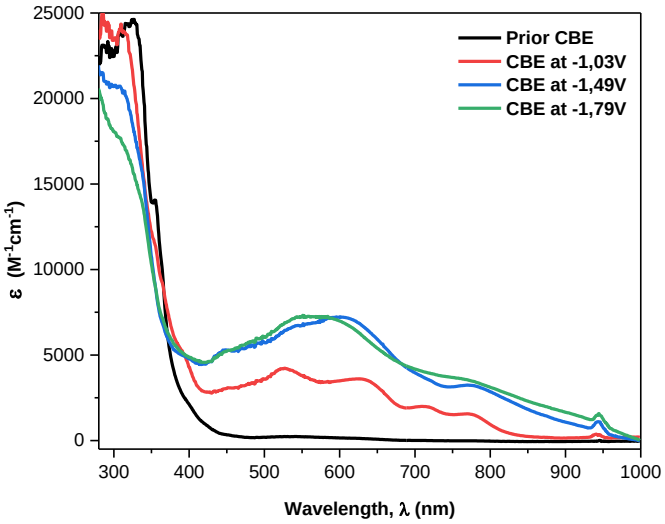

Figure IV. 8 UV-Vis absorption spectra of 1mM $[Cr(qpy)(Cl)_2]^+$ complex in DMF prior and after electrolysis at different $E_{1/2}$ values.

The mono-reduced $[Cr(qpy)^{\bullet-}(Cl)_2]$ species exhibit two strong absorption bands at 528 nm and 628 nm, plus other two weak shoulder bands around 713 nm and 773 nm. These spectroscopic signatures of Cr (III) metal center with mono-reduced polypyridyl ligand are characteristic to that of the ligand-to-metal charge transfer in the visible region.

Further reduction led to the formation of bi-reduced species whose absorption bands (601 nm and 774 nm) were red-shifted in comparison to the mono-reduced $[Cr(qpy)^{\bullet-}(Cl)_2]$ species. Evolution of the solution color from faint golden-brown solution to a purple solution was observed in the course of electrolysis, with the final tris-reduced species absorbing at around 568 nm as indicated in **Figure IV. 8**.

iii. EPR characterization and DFT calculations for the $[Cr(qpy)(Cl)_2]^+$ complex

Electron paramagnetic resonance (EPR) spectroscopy was employed to study the changes of spin state upon reduction of the parent $[Cr(qpy)(Cl)_2]^+$ complex. Consequent to electrolysis experiments carried out under Ar at each reduction potential, samples were collected for EPR

spectroscopy which aided in identifying the chemical species formed after every redox process. **Figure IV. 9** presents EPR spectra recorded at the X-band frequency ($\nu \approx 9.65$GHz) at 20K.

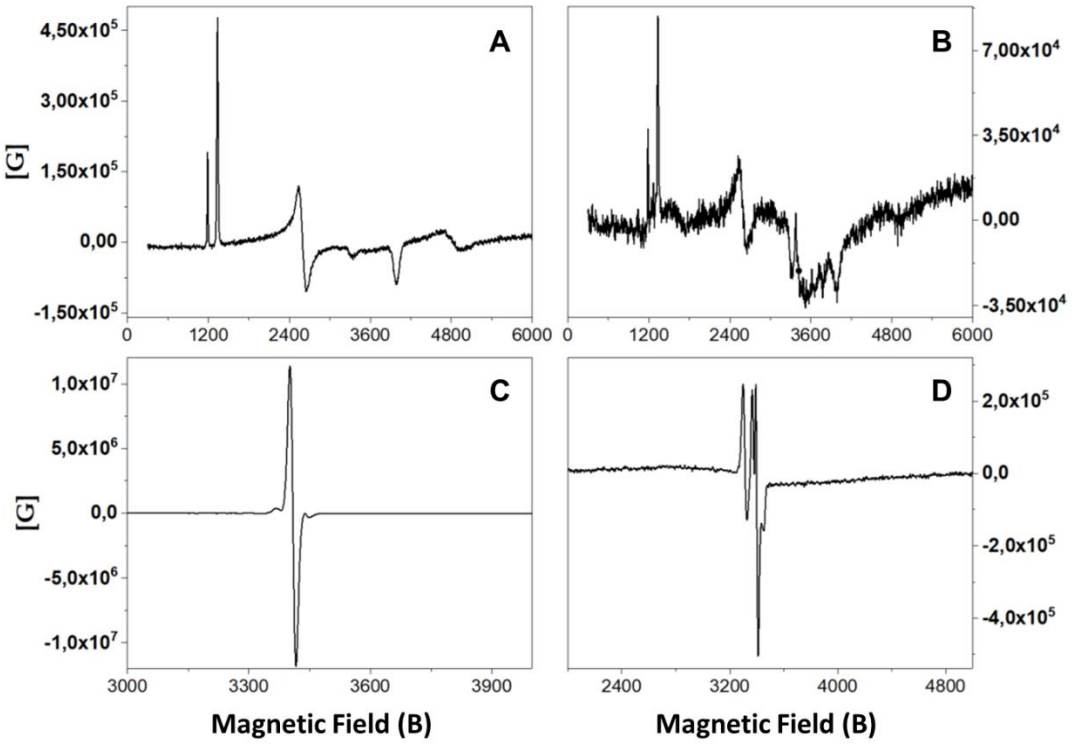

Figure IV. 9 EPR spectra of 1mM $[Cr(qpy)(Cl)_2]^+$ in DMF/0.1M $TBAPF_6$ prior (**A**) and after electrolysis at the first (**B**) and second (**C**) reduction peaks at T= 20K.

The EPR spectrum of $[Cr(qpy)(Cl)_2]^+$ (**Figure IV. 9A**) covers a large spectral window, with resonances at g = 5.7, 5, 2.6, 1.7 and 1.4. Thus, the initial compound is a high spin (S =3/2) Cr (III) complex. By taking into consideration a monoelectronic reduction, the putative spin states are S = 2, 1, and 0 (**Figure IV. 9B**). The spectrum depicted in **Figure IV. 9B** shows that the species generated upon one-electron reduction are X-Band EPR silent. An (S = 0) ground spin state is very unlikely, since it would imply a low spin metal center. We rather propose that $[Cr(qpy)(Cl)_2]$ is an integer spin system, but the zero field splitting parameters are too large to allow for its detection at the X-band frequency.

Accordingly, the two-electron reduction of $[Cr(qpy)(Cl)_2]^+$ results in the growing of a strong signal at g = 1.98, which is reminiscent of an (S = ½) spin state. The g value is close to 2, indicative of a significant radical character of the complex. Finally, three electron reduction is accompanied by a quenching of the (S = ½) resonance, concomitant with the appearance of minor resonances attributed to decomposition products.

In pursuance of insight into the spin states during subsequent reduction steps, DFT calculations were performed by Pr. Fabrice Thomas (DCM Grenoble) by using the B3LYP hybrid functional. Full geometry optimization was conducted, while free energies were computed for the $[Cr(qpy)(Cl)_2]^{+1}$. The added electrons may result to spin populations on either the Cr atom or the qpy ligand.

Based on the Mulliken spin population calculations, the monocation starting complex $[Cr(qpy)(Cl)_2]^{+}$ with two axially bound chloride ligands was deduced to have quartet spin state with spin population being mainly localized on the metal center (**Figure IV. 10a)**. Formation of a ligand radical ($qpy^{\bullet-}$) was observed upon one-electron reduction as a result of electronic spin density population on the central bisphenyl bipyridine as shown in **Figure IV. 10d**.

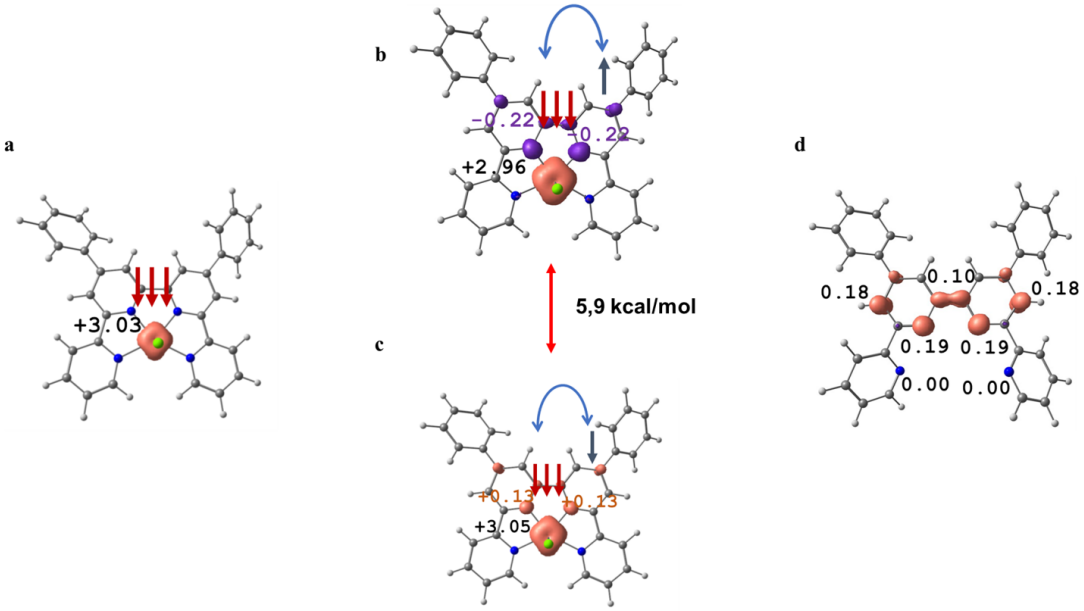

Figure IV. 10 Calculated Mulliken spin density distribution on $[Cr(qpy)(Cl)_2]^{+}$ complex; starting complex with S= 3/2 (**a**), mono-reduced complex with S= 1 (**b**), and S= 2 (**c**) and that of a qpy radical, $(qpy)^{\bullet-}$ with S=½ (**d**).

Depending on the alignment of spins localized on the ligand radical and the Cr atom, ferromagnetic and antiferromagnetic interactions resulted in two different spin states; a quintet state (**c**) and a triplet spin state (**b**) respectively as reported in **Figure IV. 10.** From energy calculations, the triplet state was reported to be more stable in comparison to the quintet state suggesting an antiferromagnetic coupling of a ligand radical ($qpy^{\bullet-}$) and the Cr^{3+} atom.

Following the second e^- reduction process, calculations for different spin states were considered: doublet, quartet and sextet. Based on the Mulliken spin analysis all are assigned to Cr^{3+} complexes involving a diradical ligand $qpy^{2\bullet 2-}$, which can be formulated as $[Cr^{III}(qpy^{2\bullet 2-})(Cl)_2]^-$. The doublet and quartet spin states result from antiferromagnetic interactions within the spin frustrated system caused by two ligand radicals and one (S=3/2) Cr^{3+} metal ion. The sextet spin state is achieved through ferromagnetic coupling of spins localized on the Cr^{3+} atom and a biradical ligand ($qpy^{2\bullet 2-}$). The doublet state is the lowest energy state, thus the most favorable one (see **Figure IV. 11A**). This conclusion is supported by the EPR signal (**Figure IV. 9C**) obtained after the second e^- reduction process, which discloses an (S = ½) species.

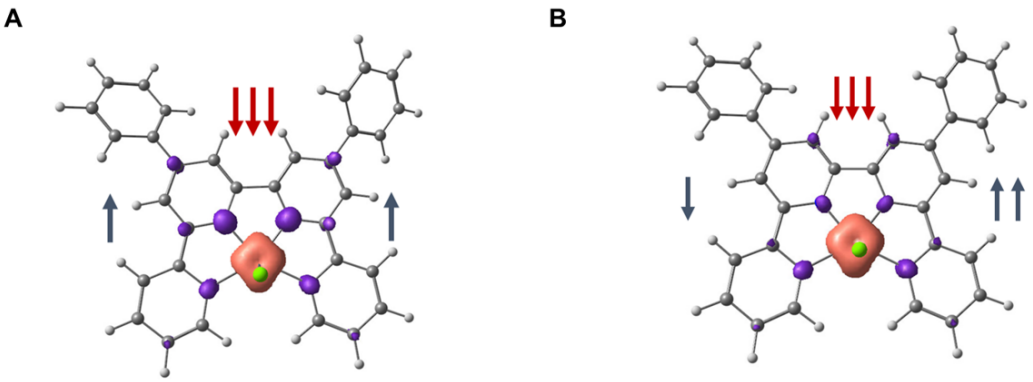

Figure IV. 11. Spin density plot on a bis-reduced $[Cr^{III}(qpy^{2-})(Cl)_2]^-$ complex (S = ½) (**A**), and a tris-reduced complex (S= 1) (**B**).

The tris-reduced complex was computed under singlet, triplet quintet and heptet states. The triplet state was calculated to be the most stable state for the tris-reduced complex. These calculations supported the localization of the third incoming electron on the qpy ligand leading to the formation of the qpy^{3-} ligand radical, as indicated in **Figure IV. 11B**.

Conclusively, **Table IV.2** summarizes the energy and spin density calculations of the reduced Cr (III) complexes. Only the most stable states are indicated, together with the Mulliken spin population on representative atoms. When three values are given, they correspond to the spin population on the N atoms on the central bipyridine core and the N atoms of the peripheral pyridines. The spin density is equally distributed on each ligand half.

Table IV.2 Mulliken charge and spin populations on the Cr atom and the qpy ligand of $[Cr(qpy)(Cl)_2]^+$ complex (with AF= antiferromagnetic coupling).

Complex oxidation state	Mull. Spin pop at Cr/N*	Formulation	Spin state
$[Cr(qpy)(Cl)_2]^+$	3.03/-0.05	Cr^{3+}/ qpy	Quartet
$[Cr(qpy)(Cl)_2]^0$	2.96/-0.22	Cr^{3+}/ $qpy^{\bullet-}$	Triplet (AF)
$[Cr(qpy)(Cl)_2]^-$	2.94/-0.27/-0.15	Cr^{3+}/ $qpy^{2\bullet 2-}$	Doublet (AF)
$[Cr(qpy)(Cl)_2]^{2-}$	2.95/-0.13/-0.11	Cr^{3+}/ $qpy^{\bullet 3-}$	Triplet

iv. Electrocatalytic reduction of CO_2 using $[Cr(qpy)(Cl)_2]^+$ complex

Further electrochemical analyses of the $[Cr(qpy)(Cl)_2]^+$ complex were carried out under carbon dioxide saturated atmosphere as means of investigating the electrocatalytic properties of this given complex. 1mM of the $[Cr(qpy)(Cl)_2]^+$ complex was solubilized in DMF/0.1M $TBAPF_6$ and then purged with CO_2 gas followed by a cathodic CV scan.

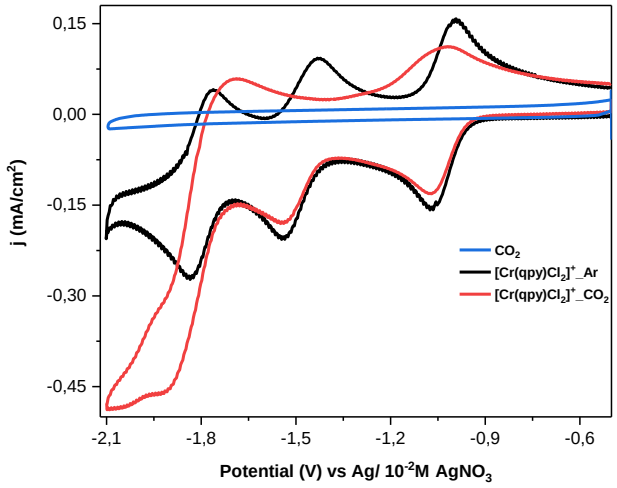

Figure IV. 12 Cathodic scan CVs of a 1mM $[Cr(qpy)(Cl)_2]^+$ complex under argon (black), CO_2 (red) and a CV of blank CO_2 saturated electrolyte (blue) on GCE in DMF/0,1M $TBAPF_6$ at v = 0.1Vs^{-1}.

As shown in **Figure IV. 12**, the Cr (III) complex under CO_2 saturated conditions resulted in a current increase at an onset potential of -1.77V vs Ag/10^{-2}M $AgNO_3$. This proves the catalytic

properties of this complex towards CO_2 reduction. And interestingly, the reported onset potential for this experiment was evidently low in comparison to most of the other reported complexes thus a decrease of the overpotential value.

As shown in the cathodic scan of the complex under CO_2 conditions, the 1st and 2nd reduction peak currents decreased as well as the loss of the reversibility behavior of these reduction waves was noted. This observation indicates an irreversible chemical transformation of the reduced species as suggested in **section 2.3 ii**, **eq. iv**, **v**. In the presence of CO_2, a rate to which this chemical reaction step occurs is assumed to be higher than a reaction rate under argon conditions.

The formation of these new chemically transformed species could be justified by the reverse scan which indicates only two oxidation waves at -1.69V and -1.02V instead of three as reported in the argon saturated CV scan (**Figure IV. 12**). Additionally, the foot of the 3rd reduction wave under CO_2 was found to be less negative (by 20mV) than that of the 3rd reduction wave under argon.

The dissociation of the chloride ligand occurring at each of the reduction waves results in an open space/room around the complex for CO_2 to coordinate to the chromium metal center. These newly formed CO_2 adduct species upon further reductions will eventually result in an electrochemical conversion of CO_2.

In efforts of improving the electroreduction process of CO_2, different weak acids were introduced as a source of protons. Firstly, the use of water was employed, by adding x% v/v of water to a CO_2 saturated electrolyte solution containing the $[Cr(qpy)(Cl)_2]^+$ complex.

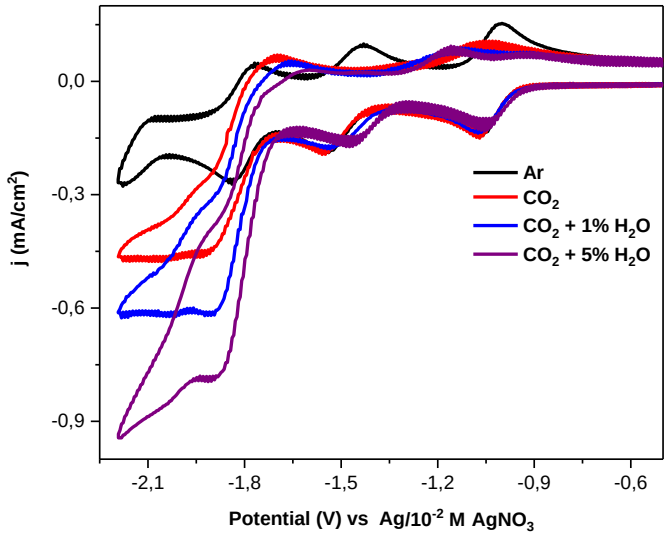

Figure IV. 13 Cathodic CV scans of a 1mM $[Cr(qpy)(Cl)_2]^+$ complex under argon (black) and CO_2 (red) with 1%v/v (blue) and 5% v/v (purple) H_2O on GCE in DMF/0,1M $TBAPF_6$ at $v = 0.1Vs^{-1}$.

This experiment resulted to an increase of current at the onset potential of -1.77V vs $Ag/10^{-2}M$ $AgNO_3$ as indicated in **Figure IV. 13**. And by varying the % of water added, the peak current and onset potential values improved.

As means of quantifying the efficiency and selectivity of this complex, gas chromatography measurements were carried out (**Table IV. 3**). These analyses were done on 1mM $[Cr(qpy)(Cl)_2]^+$ complex under CO_2 saturated conditions in the presence of 1%v/v water.

Table IV. 3 Faradaic efficiencies of the $[Cr(qpy)(Cl)_2]^+$ complex in the presence of 1%v/v H_2O at -1.85V vs $Ag/10^{-2}M$ $AgNO_3$ in DMF/0.1M $TBAPF_6$ at $v = 0.1Vs^{-1}$ on a carbon foam (8 ppi).

Complex	E_{onset} (V)	Time (mins)	Q (C)	%CO	%HCOOH
$[Cr(qpy)(Cl)_2]^+$	-1.85	60	-2.98	11.32	
		120	-4.12	8.75	
		180	-5.07	6.04	
		240	-7.05	2.46	0

As shown in **Table IV. 3**, at low % of water, there was no H_2 gas formed as a result of it being a competing reaction against CO gas and HCOOH acid formation, which is most likely to occur in the presence of high % of water. Despite the selectivity of this complex, the CO gas formation did not increase over time, instead it decreased. This decrease could be due to a number of reasons such as degradation of the complex, poisoning of the working electrode with CO or even cell leakage.

Further efforts of improving the current response of the complex involved the use of other weak acids such as methanol and phenol. Using 1.5 M of CH_3OH as a different proton source resulted in a better current response and an even less negative onset potential in comparison to when water was used (**Figure IV. 14**). An onset potential shift of 40mV was noted between the catalytic wave of CO_2 in the absence (-1.74V) and presence of methanol (-1.76V).

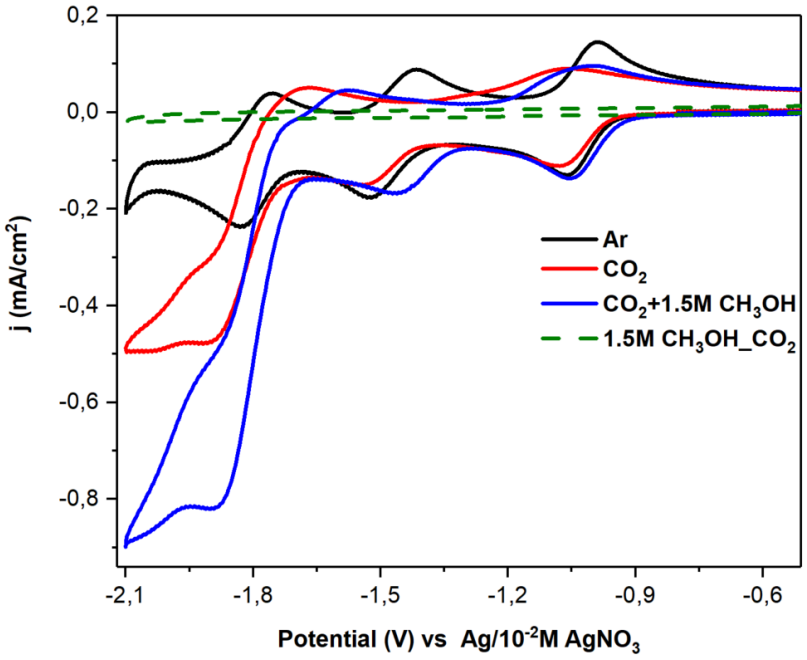

Figure IV. 14. Cathodic CV scans of 1.5M CH_3OH (green) and of 1mM $[Cr(qpy)(Cl)_2]^+$ complex under argon (black), under CO_2 (red), in the presence of 1.5M CH_3OH (blue) on GCE in DMF/0,1M $TBAPF_6$ at v = 0.1Vs^{-1}.

Finally, one more weak acid was investigated as means of finding the most efficient proton source for the reduction of CO_2. By using 1.5M phenol (PhOH), the cathodic CV scans of 1mM $[Cr(qpy)(Cl)_2]^+$ complex were once again recorded in the presence of phenol under CO_2 saturated conditions as shown in **Figure IV. 15**.

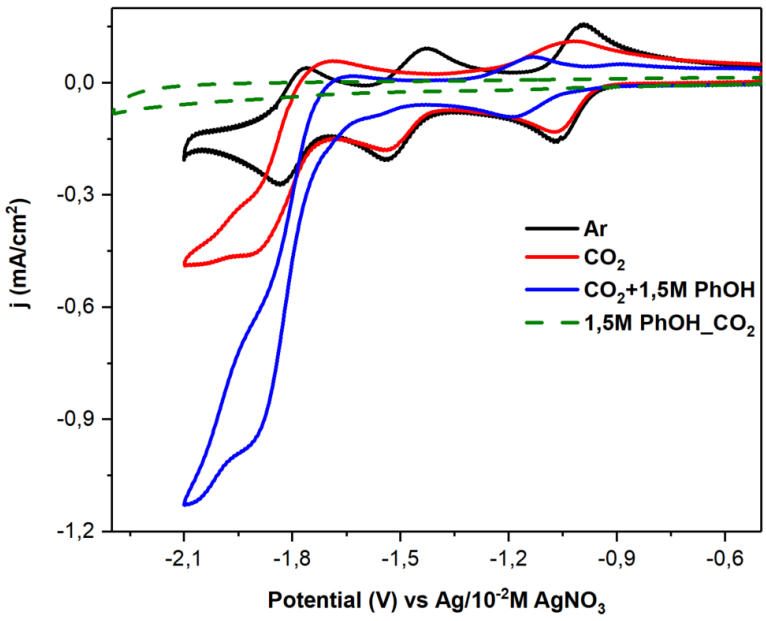

Figure IV. 15. Cathodic CV scans of 1.5M PhOH under CO_2 (green) and of 1mM $[Cr(qpy)(Cl)_2]^+$ complex under argon (black) and CO_2 (red) saturated conditions with 1.5M PhOH (blue) on GCE in DMF/0,1M $TBAPF_6$ at v = 0.1Vs^{-1}.

As indicated in **Figure IV. 15**, the use of phenol resulted in a high current response which was the best to be reported among all other weak acids (water and methanol). It was therefore interesting to continue investigating the catalysis of CO_2 using the Cr (III) complex with phenol as the proton source.

It is important to note that all the weak acids used as proton sources did not demonstrate any of their direct reduction processes in the presence of argon and CO_2 within the given electrochemical window. Further electrochemical measurements were performed while varying the concentration of phenol from 0.25M to 1.75M.

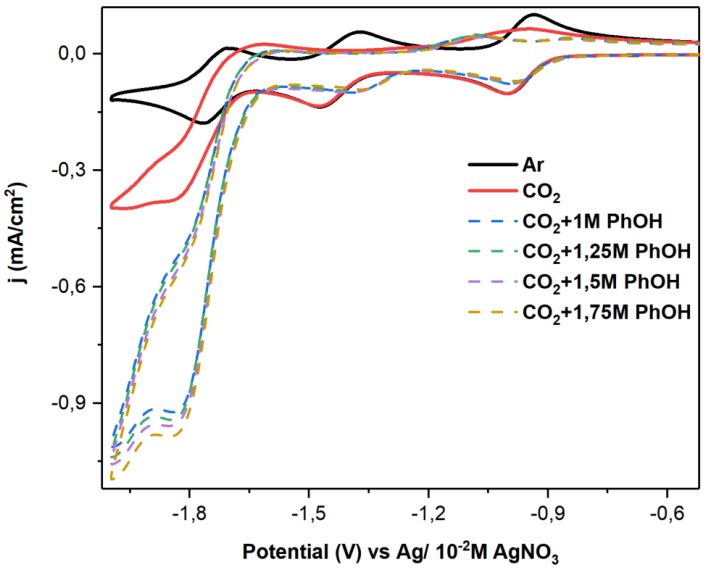

Figure IV. 16 Cathodic CV scans of a 1mM $[Cr(qpy)(Cl)_2]^+$ complex under argon (black) and CO_2 (red) saturated conditions with varying concentration of [PhOH] on GCE in DMF/0,1M $TBAPF_6$ at v = 0.05Vs^{-1}.

The varying concentrations of phenol did not necessarily result in noticeable difference of the onset potential values, but a significant onset potential shift of ~50mV was noted upon the first addition of 1M of phenol. An increase of phenol concentration mainly resulted in an increment of the catalytic peak current.

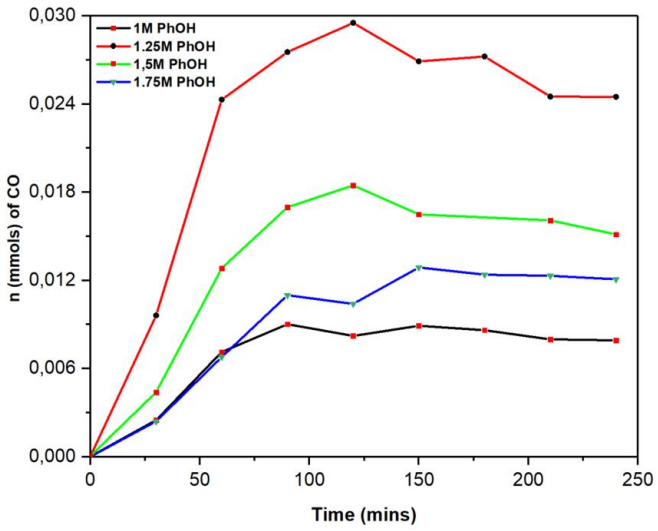

Figure IV. 17 Evolution of the number of moles of CO produced during electrolysis of 1mM $[Cr(qpy)(Cl)_2]^+$ complex at -1.85V Ag/10^{-2}M $AgNO_3$ under CO_2 saturated conditions with varying concentration of [PhOH] on a carbon foam in DMF/0,1M $TBAPF_6$.

From gas chromatography measurements, the evolution of the number of moles of CO produced during 4 hours of exhaustive electrolysis of 1mM $[Cr(qpy)(Cl)_2]^+$ complex in the presence of different concentrations of phenol at an onset potential of -1.85 V vs $Ag/10^{-2}M$ $AgNO_3$ was reported. As shown in **Figure IV. 17**, these gas injection analyses were done in an interval of 30 minutes throughout the 4 hours of electrolysis measurements.

Table IV. 4 Evolution of current during the electrolysis of 1mM $[Cr(qpy)(Cl)_2]^+$ complex in the presence of varying concentration of [PhOH] at -1.85 V vs $Ag/AgNO_3$ on a carbon foam (8 ppi with A=0.8-1 cm^2) in DMF/0,1M $TBAPF_6$.

Different phenol concentrations	Current, i_c (mA) at different injection time		
	30 mins	60 mins	180 mins
1M	-2.06	-2.01	-1.24
1.25 M	-1.73	-1.56	-0.93
1.5 M	-2.73	-2.52	-1.63
1.75 M	-1.95	-1.85	-1.45

The evolution of current with time during the electrolysis of 1mM $[Cr(qpy)(Cl)_2]^+$ complex in the presence of different concentrations of phenol indicated better current values when working with 1.5M of phenol (see **Table IV. 4**).

Electrolysis of 1mM $[Cr(qpy)(Cl)_2]^+$ complex under CO_2 saturated conditions in the presence of 1.25M PhOH resulted in a high production of CO among all varied concentrations. In the presence of 1M and 1.75 M of phenol, the production of CO increased during the first two hours and then stabilized for the rest of the remaining hours.

Given the number of parameters involved in carrying out these experiments, the reproducibility of data was somehow challenging. As indicated in **Figure IV. 18**, the electrolysis experiments of 1mM $[Cr(qpy)(Cl)_2]^+$ complex under CO_2 saturated conditions in the presence of 1.5M phenol resulted in a different production of CO moles when conducted in two different days despite working with the same electrochemical setup.

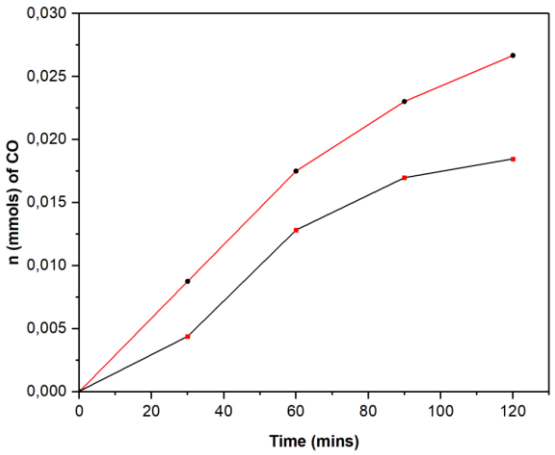

Figure IV. 18 Evolution of the number of moles of CO produced in two different days during electrolysis of 1mM $[Cr(qpy)(Cl)_2]^+$ complex at -1.85V Ag/10^{-2}M $AgNO_3$ under CO_2 saturated conditions with 1.5M of PhOH on a carbon foam in DMF/0,1M $TBAPF_6$.

This variation of results obtained in different days could be associated with a number of factors such as concentration of CO_2 saturated in the given electrolyte, leakage of the electrochemical cell, surface area of the carbon foam used as a working electrode etc. In an effort to reproduce data and minimize the electrochemical cell's leakage, the frequency of gas injections was decreased, resulting in minimal harm to the septum cap enclosing the electrochemical cell openings. And as a result, both the faradaic efficiency and the quantity of CO moles produced improved as shown in **Table IV. 5** where two different concentrations of phenol were investigated.

Table IV. 5 Faradaic efficiencies of 1mM $[Cr(qpy)(Cl)_2]^+$ complex in the presence of varying concentration of [PhOH] at -1.85 V vs Ag/$AgNO_3$ on a carbon foam in DMF/0,1M $TBAPF_6$ at v = 0.05Vs^{-1}.

[Phenol], M	E_{onset} (V)	Time (mins)	Q (C)	%CO	%H_2	%HCOOH
1.5	-1.85	60	-5	38	-	
		120	-8	48	-	
		180	-9	36	-	0
1.75	-1.85	60	-6	47	-	
		120	-8	45	1	
		180	-11	33	2	0

As demonstrated in **Table IV. 5**, the $[Cr(qpy)(Cl)_2]^+$ complex yielded around 50% faradaic efficiency regardless of the concentration of the phenol. With 1.5M of phenol, the Cr (III) complex was selective towards CO formation, with neither H_2 gas nor formic acid formation. The absence of HCOOH acid formation was common in both concentrations of phenol; however, a small amount of H_2 gas was detected at a concentration of 1.75M of phenol.

Conclusively, the use of phenol as a proton source resulted in a better catalytic current response in comparison to the use of other weak acids (water and methanol). By increasing the concentration of phenol, the efficiency of the complex improved towards the formation of CO. However, at higher concentrations of phenol there is a possibility of favoring H_2 gas formation as a result of electroreduction of protons in the electrolyte.

To account for the remaining faradaic efficiency, detection and quantification of formaldehyde was considered as suggested in the work of Abruña.[16] Using the Nash reagent mixture and the Tryptophan reagent mixture, two sensitive formaldehyde quantification methods were investigated using the absorption spectra measurements.[17-18] Using the formaldehyde detection reagents on electrolyte solutions from electrolysis measurements, no formaldehyde was detected.

With faradaic efficiency of 50%, the remaining value could be associated with formation of oxalate (very low concentration was detected using the ionic chromatography) and carbonates (failed to analyze due to the lack of an appropriate right technique).

Conclusively, the "Foot of the wave" (FOW) analysis previously reported in chapter II, was conducted using **Eq. IV. 4** for the $[Cr(qpy)(Cl)_2]^+$ under CO_2 saturated conditions in the presence of varying concentrations of phenol to analyze the influence of phenol on the catalytic rate constant.

$$\frac{i_p}{i_p^0} = \frac{2.24\sqrt{\frac{RT}{Fv}2k_{cat}c_{cat}}}{1+exp\left[\frac{F}{RT}\left(E-E_{cat}^0\right)\right]} \qquad \textbf{Eq. IV. 4}$$

To recall **Eq IV. 4**, i_p represents the catalytic current in the presence of CO_2, i_p^0 is the peak current intensity in the absence of CO_2 (under argon), F is the Faraday constant, R is the perfect gas constant, T is the absolute temperature, v is the scan rate expressed in Vs^{-1}, c_{cat} is the initial

concentration of a catalyst, E is the applied potential and $E^0_{cat}$is the standard potential of the reversible reduction peak of the active form of the catalyst.

A linear correlation between the current ratio ip/i_p^0 and the term 1/(1+$exp[F/RT(E\text{-}E^0_{cat})]$) was developed using standard CV measurements of $[Cr(qpy)(Cl)_2]^+$ complex under CO_2 and varying concentrations of phenol as presented in **Figure II. 19**.

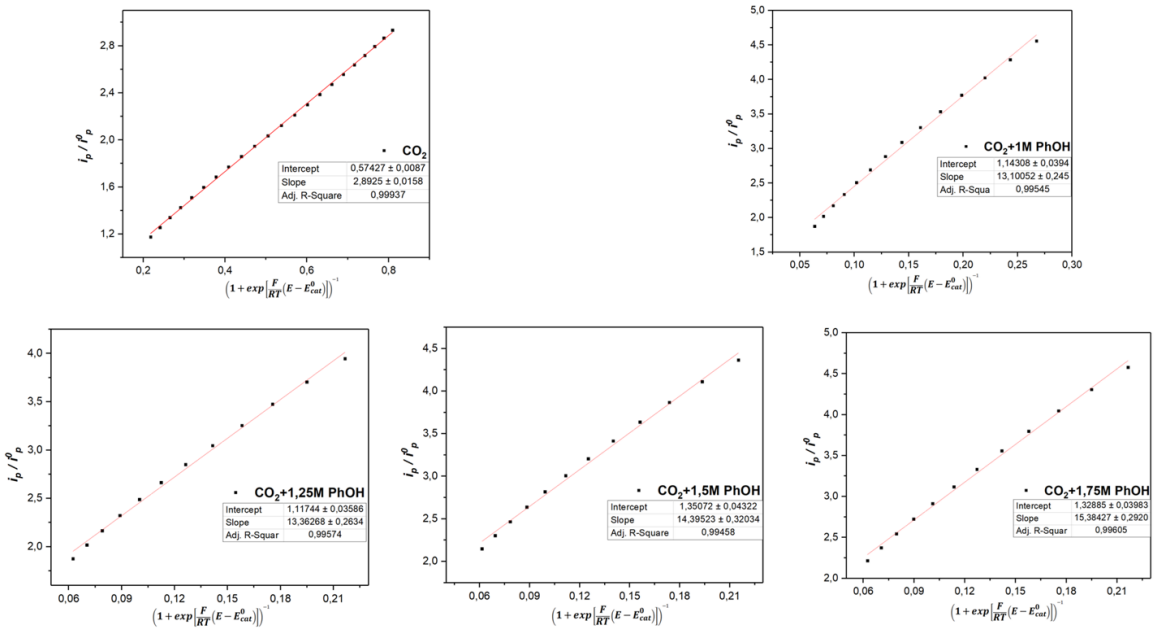

Figure IV. 19 FOW analysis of the catalysis of CO_2 reduction by 1 mM $[Cr(qpy)(Cl)_2]^+$ complex under CO_2 and varying concentrations of phenol on a GCE in DMF/0,1M $TBAPF_6$ at v =0.1Vs^{-1}.

By equating slopes obtained from linear correlations presented in **Figure IV. 19** between ip/i_p^0 and 1/(1+$exp[F/RT(E\text{-}E^0_{cat})]$) with the slope of **Eq IV.4**, theoretical k_{cat} values were calculated and presented in **Table IV.6**.

Table II. 6 Theoretical k_{cat} values of the catalysis of CO_2 reduction by 1 mM $[Cr(qpy)(Cl)_2]^+$ complex under CO_2 and varying concentrations of phenol on a GCE in DMF/0,1M $TBAPF_6$ at v =0.1Vs^{-1}.

$[Cr(qpy)(Cl)_2]^+$	**Slope**	**k_{cat} ($M^{-1}s^{-1}$)**
CO_2	2.89	3241
CO_2+1 M PhOH	13.10	6.65×10^4
CO_2 +1.25 M PhOH	13.36	6.93×10^4
CO_2 +1.5 M PhOH	14.39	8.04×10^4
CO_2 +1.75 M PhOH	15.38	9.18×10^4

The theoretical k_{cat} value in the absence of phenol was reported to be quite low in comparison to the theoretical k_{cat} values obtained in the presence of phenol (**Table II. 6**). This observation confirms the importance of adding proton sources as means of achieving an efficient conversion of CO_2 towards reduced carbon-based products.

2.4. Photocatalysis of CO_2 in homogeneous system using Cr (III) complex

From the electrochemical characterization of the Cr (III) complex, the catalytic role of this complex towards CO_2 reduction was confirmed, hence electrocatalysis of CO_2. The low onset potential at which CO_2 is reduced (as reported in **Figure IV. 12)**, presented an opportunity of associating this metal complex with a molecular photosensitizer.

The mechanism of photocatalysis of CO_2 involves three main steps: light absorption, charge separation and electron transfer to activate the catalytic reaction; different molecular components are of importance in each step. During the initiation of a photocatalytic reaction under light, an interaction of a photosensitizer (**PS**) in its excited state (**PS***) with a sacrificial electron donor (**SD**) or a catalyst (**Cat**) can occur in either of the two ways; **a**) reductive quenching through which a **PS*** is reductively quenched by a **SD** to form a one-electron reduced specie of **PS**$^{\bullet -}$ which then interacts with a **Cat** ; and **b**) oxidative quenching where a **PS*** transfers an electron to a **Cat** and a transient **PS**$^{\bullet +}$ is then reductively quenched by a **SD** which restores a **PS** in its initial state (**Scheme IV. 3)**.

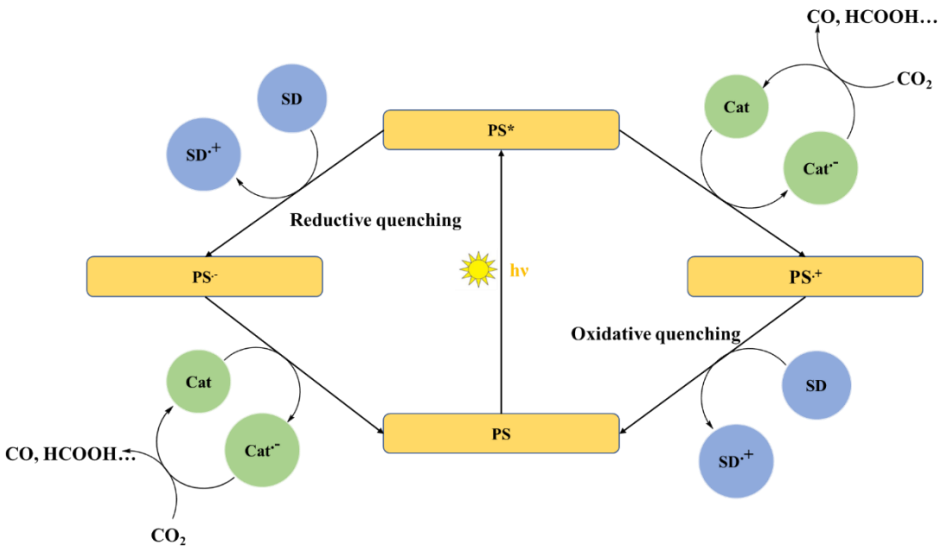

Scheme IV. 3 The photocatalytic reaction mechanism of CO_2 following either a reductive or an oxidative quenching mechanism consisting of photosensitizer (**PS**), a sacrificial electron donor (**SD**) and a catalyst (**Cat**).

Given the reported reduction potentials for most CO_2 reducing catalysts are highly negative, the most probable interaction with a **PS*** is that of reductive quenching using a **SD**. This can be explained by failure of a **PS*** to inject an electron effectively into a **Cat** due its weaker reducing power in comparison to a reduced state of a **PS**, i.e. **PS**$^{\bullet-}$.

Moreover, to favor the reductive quenching of **PS*** and sustain the photocatalytic cycle, a **SD** is usually added in excess compared to a **Cat** and as a result the interaction probability between a **PS** and a **SD** increase. Working in such reductive environment prevents the formation of possibly strong and stable oxidants (**PS**$^{\bullet+}$) which might interfere with the reduction process of CO_2; by having electrons redirected towards the reduction of **PS**$^{\bullet+}$ instead of CO_2.

In the light absorption step, the photophysical properties of the given catalyst determine whether the use of a **PS** is of necessity. Therefore, the non-emissive behavior and a very efficient deactivation of the excited state of the $[Cr(qpy)(Cl)_2]^+$ complex deemed the use of a photosensitizer necessary.

In search for an appropriate photosensitizer, the onset potential of the Cr(III) complex needed to be less negative compared to the cathodic potential value(s) of the chosen photosensitizer. Recently, heteroleptic diimine-diphosphine Cu(I) complexes have been well investigated as one of the most remarkable candidates because of their great potentials as efficient photosensitizers.[19-22]

In this work, the reductive quenching mechanism employed the use of a heteroleptic $[Cu(bph)(POP)]^+$ photosensitizer which gained interest due to its strong metal-to-ligand (MLCT) excited state emission with long lifetime in solution. This long-lived luminescent MLCT excited state of the Cu(I) **PS** is attributed to a number of factors, such as the efficient steric and electron-withdrawing effects of the POP ligand, the closed shell d^{10} configuration of the Cu(I) metal center which prevents d-d metal-centered (MC) electronic transitions that are prone to undergo non-radiative deactivation pathways and photochemical degradation.[23,24]

And within the same mechanism, BIH was employed as a sacrificial electron donor given its strong reducing power (E_{ox} = 0.33 V vs. SCE ≈ 0.026V vs $Ag/AgNO_3$ in CH_3CN) and absent absorption properties in the visible region.[25] In its neutral state, BIH can donate an electron to an excited **PS***; and in its radical form, these BIH radical species (i.e. BI$^\bullet$) species can induce a second electron injection either to a ground state of a **PS** or into a CO_2-reducing catalyst given their strong reducing power (E_{ox} = -2.06 V vs. Fc^+/Fc ≈ -1.97 V vs $Ag/AgNO_3$) of the BI$^\bullet$

species.[25] The formation of these radical species occurs upon deprotonation of the oxidized species of BIH (i.e. $BIH^{\bullet+}$) in the presence of triethanolamine (TEOA).[26]

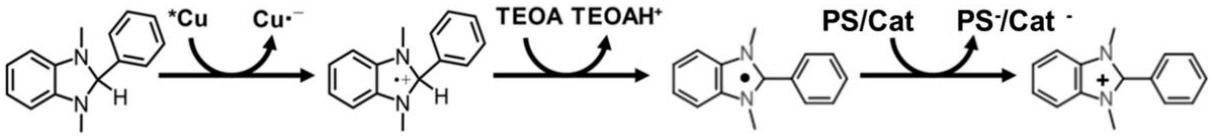

Scheme III. 4 Evolution of BIH in the presence of a **PS*** and TEOA (adapted from literature).[25]

Prior to performing the photocatalytic reduction of CO_2, the photophysical and electrochemical properties of the Cu(I) **PS** were studied. The knowledge of these properties is crucial in determining the probability in which appropriate interactions might occur between the **PS*** and the **SD** as well as between the **Cat** and **PS•⁻**.

i. Synthesis of $[Cu(bph)(POP)]^+$ photosensitizer

Following previously reported literature,[27,28] the Cu(I) complex was synthesized in two steps; the first step involved a reaction between a tetrakis(acetonitrile)copper(I) hexafluorophosphate $[Cu^I(CH_3CN)_4](PF_6)$ and bis-[2-diphenylphosphinophenyl]ether, dppe (POP) in a dichloromethane solution at room temperature.

In the second step, product from the first step was reacted with bathocuproine (bph) in dichloromethane overnight resulting to a final product of $[Cu(bph)(POP)]^+$, collected by filtration and re-concentration of the filtrate.

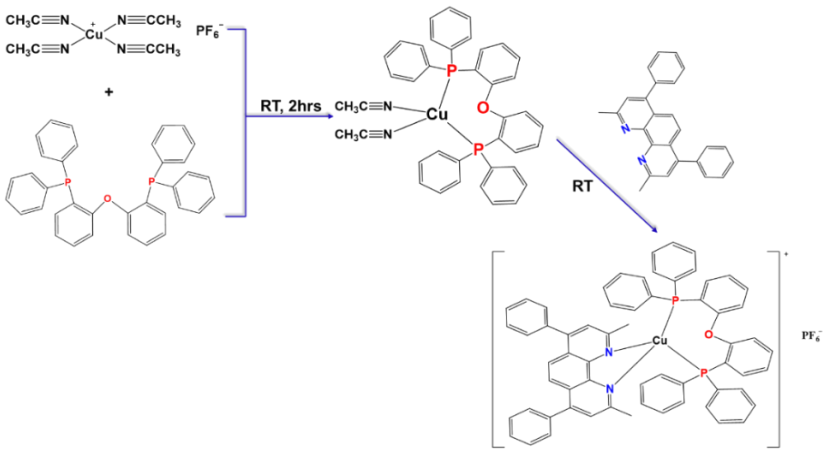

Scheme IV. 5 Molecular structure of the PF_6^-,$[Cu(bph)(POP)]^+$ complex.

ii. Photophysical properties of the $[Cu(bph)(POP)]^+$ complex.

From the electronic absorption spectra of this orange-colored complex in DMF solution, two absorption bands were observed. The first absorption band detected in the UV region (λ =288 nm) was assigned to the ligand-centered $\pi \rightarrow \pi^*$ electronic transitions; whereas the second absorption band in the 350-450 nm spectral window associated to a metal-to-ligand charge electronic transfer (MLCT) typical of heteroleptic Cu^I complex was reported (see **Figure IV. 20)**.

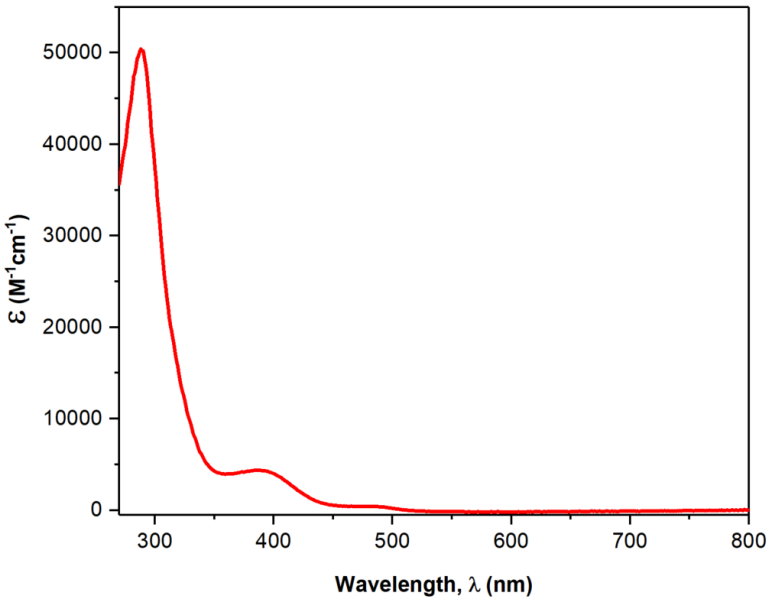

Figure IV. 20. Absorption spectra of $[Cu(bph)(POP)]^+$ complex in DMF.

As the MLCT transition being the lowest in energy as shown in the spectrum, this strongly suggests the lowest excited state of this complex to be that of the MLCT. Despite, the possible thermal relaxation of the higher in energy $\pi \rightarrow \pi^*$ excited state populating the lowest state, direct excitation of the lowest MLCT transition in the visible region almost certainly remains to be the most significant transition in a redox-photosensitizing reaction.

As indicated in **Figure IV. 21**, this complex exhibited an emission band at around 580 nm associated with the deactivation from MLCT excited levels.[29-31] Lifetime measurements attributed to the decay of these excited MLCT levels was found to be around 12 ns. The resulting weak emission intensity and short emission lifetime of this Cu(I) complex might be caused by the exciplex quenching by the DMF molecules.[30,32]

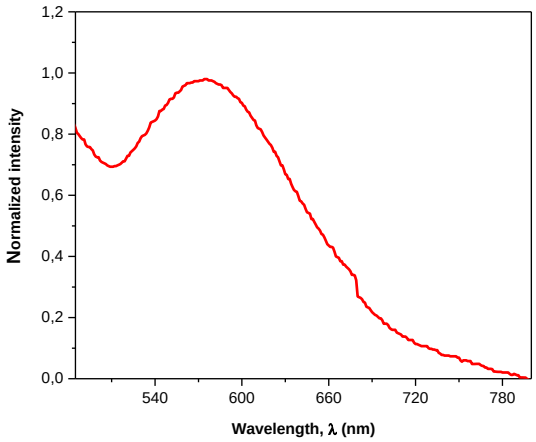

Figure IV. 21. Emission spectra of $[Cu(bph)(POP)]^{+}$ complex in DMF.

During excitation, the formation of the MLCT excited state results in a redistribution of electron density around the metal complex due to an electron transfer from the d-orbital of the Cu(I) to the antibonding orbital (π^*) of one of the coordinated bidentate ligands. This electron transfer will lead to a hole formation at the metal center that will enable an electron withdrawing behavior of the complex. Hence, the Cu(I) complex in its excited state will exhibit an oxidizing character that will aid in the interaction between the sacrificial electron donor BIH and the excited Cu **PS*.**

During photophysical measurements, the occurring radiative and non-radiative deactivation processes of **PS*** tend to compete with the second order reaction of charge separation and transfer between the excited state of the Cu(I) complex and the sacrificial electron donor BIH (**Eq. c**). Moreover, the short lifetime of the excited Cu(I) complex might further hinder this reaction between **PS*** and BIH.

$$\boldsymbol{PS}^{*} + BIH \rightarrow \boldsymbol{PS}^{-} + BIH^{\cdot +} \qquad \textbf{Eq. c}$$

By considering all these possible hindering factors for the deactivation of **PS***, conducting the quenching experiments using BIH was of necessity in verifying whether the excited state of the Cu(I) complex can be quenched by BIH and to determine the kinetic rate constant of **Eq. c**. Thus, by using the emission and lifetime decay measurements of the excited Cu(I) complex in the presence of varying concentrations of BIH in DMF: TEOA mixed solution (5:1 v/v), a Stern-Volmer plot was developed as shown in **Figure IV. 22**.

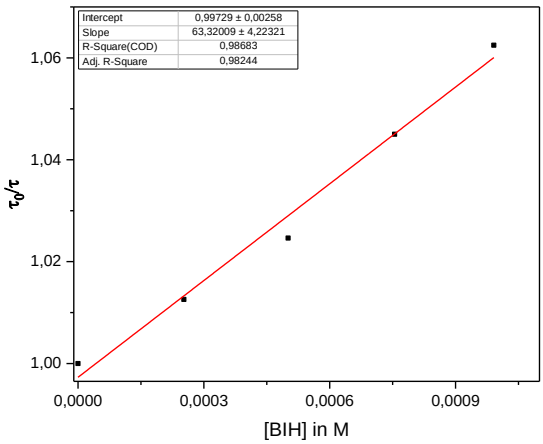

Figure IV. 22. The Stern-Volmer plot of Cu(I) **PS** consisting the ratio of lifetime decay (τ) to the lifetime decay in the absence of BIH (τ_0) with varying concentrations of BIH.

By employing the Stern-Volmer equation (**Eq. d**) with τ_0 as the lifetime of the Cu **PS*** in the absence of BIH, τ as the lifetime of the Cu **PS*** in the presence of BIH, and K_{SV} as the Stern-Volmer constant, a slope was obtained from a correlation between $^{\tau_0}/_{\tau}$ and the concentration of BIH added (**Figure IV. 20**). And through **Eq. e**, the quenching rate coefficient k_q was calculated from the K_{SV} and τ_0 values.

$$^{\tau_0}/_{\tau} = 1 + K_{SV}[BIH] \qquad \textbf{Eq. d}$$

$$K_{SV} = k_q \tau_0 \qquad \textbf{Eq. e}$$

Using the slope of the fitting curve ($K_{SV} = k_q * \tau_{em} = 63.32\ M^{-1}$) and the emission lifetime τ_{em} = 12.07 ns, the quenching rate constant (k_q) was determined to be $5.25 \times 10^9\ M^{-1}\ s^{-1}$. From the quenching constant value (k_q), the reaction between the excited Cu **PS*** and BIH is deduced to be an efficient electron transfer process almost limited by the diffusion rate constant of molecules in DMF.

iii. Electrochemical properties of the $[Cu(bph)(POP)]^+$ complex.

Electrochemical properties of this Cu(I) complex were examined through cyclic voltammetry (CV) measurements in DMF/0.1M $TBAPF_6$ electrolyte. As shown in **Figure IV. 23**, this complex demonstrated a quasi-reversible redox couple at -2,019V vs Ag/0.01M $AgNO_3$ as the first reduction wave. This one-electron reduction process is attributed to the reduction of the diimine ligands.

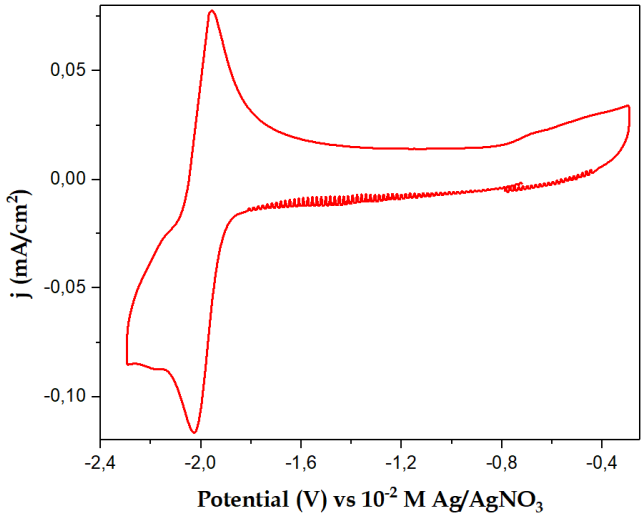

Figure IV. 23 Cathodic CV scan of a 1mM $[Cu(bph)(POP)]^+$ complex under argon saturated conditions on GCE in DMF/0,1M $TBAPF_6$ at v = 0.1 Vs^{-1}.

Upon electrolysis of the Cu(I) complex at -2V vs Ag/10^{-2}M $AgNO_3$, UV-Vis absorption spectral changes were recorded as shown in **Figure IV. 24**. A formation of new broad bands varying in absorbance intensities were noted at 557, 719 and 847 nm.

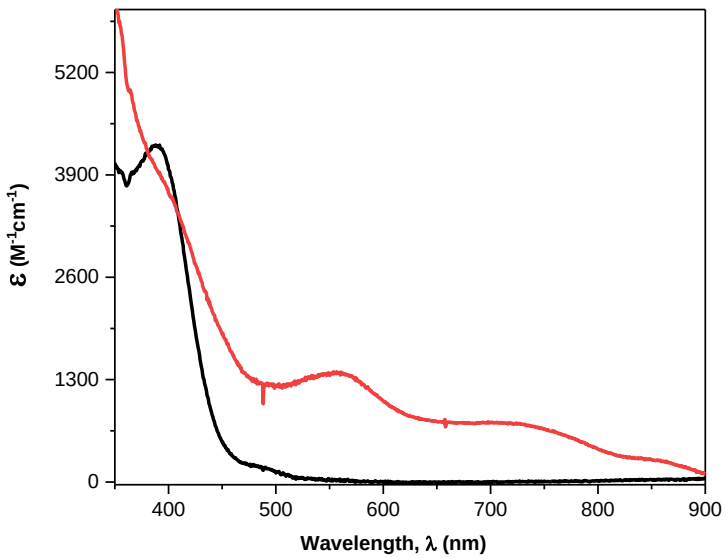

Figure IV. 24 Evolution of the absorption spectra of Cu(I) complex prior (black) and after (red) electrolysis at -2V vs Ag/10^{-2}M $AgNO_3$ complex in DMF/0.1M $TBAPF_6$.

The knowledge of the reduction potential of the Cu(I) **PS** confirms the possible quenching reaction with BIH. The ΔG° of the reaction is estimated by the difference of the redox potentials of the couples involved as shown in **Eq. f**.

$$\Delta G° = -nF\Delta E° = -nF(E_{Cu\,PS^*} - E_{BIH}) \qquad \textbf{Eq. f}$$

Where E_{BIH} is the oxidation potential of BIH (0.026V vs Ag/$AgNO_3$) and $E_{Cu\,PS^*}$ is the reduction potential of the excited state of the Cu(I) **PS*** calculated using **Eq. g**. The obtained $\Delta G°$ equates to -10.6 kJ/mol (-0.11 eV) concluding that this reaction between a Cu(I) PS and BIH is an exergonic reaction.

$$E_{Cu\,PS^*} = E_{Cu\,PS} + E_{em} \qquad \textbf{Eq. g}$$

Where; $E_{Cu\,PS}$ = -2.019V

$E_{em} = {}^{1240}/_{\lambda}$ with $\lambda = 575nm$

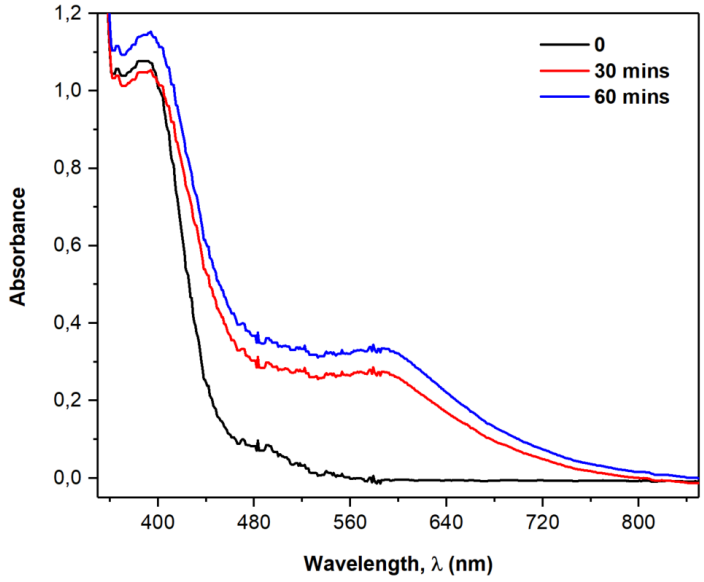

Figure IV. 25 Evolution of the absorption spectra of 0.2mM of Cu(I) complex in the presence of 10mM BIH in DMF:TEOA (5:1 v/v) upon photo irradiation under inert atmosphere.

UV-vis absorption spectral changes during photo-irradiation of a DMF:TEOA mixed solution (5:1 v/v) containing 0.2 mM $[Cu(bph)(POP)]^+$ and 10 mM BIH under Ar were measured. As shown in **Figure IV. 25**, a broad absorption band between 500-750 nm was formed during the first 30 minutes of photo irradiation. This evolution of the absorbance spectrum was found to

be similar to that reported in **Figure IV. 24** during electrolysis of the Cu(I) complex at -2V vs $Ag/10^{-2}M\ AgNO_3$ showing the formation of $[Cu(bph)(POP)]^0$ by photoreduction.

Interestingly, after 60 minutes of photo irradiation the absorbance intensity started to decrease. This observation could possibly be a result of either other competing radiative and non-radiative reactions that will hinder the reduction of the excited Cu(I) complex by BIH, or poor stability of the reduced species of $[Cu(bph)(POP)]^+$.[20]

This reported evolution of the absorption spectrum in **Figure IV. 25** was only detected during photo-irradiation, whereas in similar conditions in the absence of light (dark) no change of the absorption spectrum was seen. These results clearly indicate that the quenching of the excited state of $[Cu(bph)(POP)]^+$ is a reductive quenching process, which gives one-electron reduced species of [Cu(bph)(POP)]. With the reduction waves of the Cr (III) complex being at less negative potential values than that of Cu(I) complex, an expected reaction between one-electron reduced species of the Cu(I) PS and the $[Cr(qpy)Cl_2]^+$ catalyst should be thermodynamically favorable.

iv. Photocatalysis of CO_2 using the Cr (III) catalyst in the presence of the Cu(I) photosensitizer

After investigating the reducing power of the Cu(I) complex in its reduced state through photo irradiation and electrochemical measurements, photocatalysis of CO_2 using the $[Cr(qpy)(Cl)_2]^+$ catalyst was investigated in the presence of the $[Cu(bph)(POP)]^+$ photosensitizer and BIH under light irradiation.

An expected reaction mechanism involves an excitation of the Cu(I) PS to an excited state which is then reductively quenched by the sacrificial electron donor BIH forming a $[Cu(bph)(POP)]^0$ complex. Afterwards, an electron transfer occurs from transient reduced Cu^0 $\mathbf{PS}^{\cdot-}$ to the Cr (III) catalyst which in its reduced form then catalyzes the reduction process of CO_2 into other carbon-based products.

The photocatalytic measurements were carried out in mainly two organic solvents, CH_3CN and DMF. The presence of triethanolamine (TEOA) in both organic solvents leads to deprotonation of the oxidized $BIH^{\bullet+}$radical formed after an electron transfer from BIH to the Cu(I) PS. The reduced and deprotonated $BI^{\bullet}$ was reported to have strong reducing power that could promote reduction of either a ground state PS or that of a catalyst.[19]

Photocatalysis of CO_2 was firstly investigated in a DMF:TEOA solution for 3 hours with two gas injections carried out during the first and the last hour of the reaction. These measurements resulted in a low production of CO and H_2 gas moles in the order of 10^{-6}. Assuming the short lifetime of the Cu(I) PS in DMF being the hindering factor towards the photocatalytic reaction, the use of CH_3CN was employed given the long lifetime (0.98µs) of this Cu(I) PS in CH_3CN.

Table IV. 7 Photocatalytic reduction of CO_2 during photo irradiation of 1mM $[Cr(qpy)(Cl)_2]^+$ catalyst in the presence of a 10mM $[Cu(bph)(POP)]^+$ PS and 50mM BIH under CO_2 saturated conditions.

Mixed solutions (5:1 v/v)	Time (mins)	CO (µmols)	H_2 (µmols)
DMF:TEOA	60	2.39	3.99
	180	2.53	5.48
CH_3CN:TEOA	60	3.74	3.41
	180	4.33	6.54
CH_3CN:TEOA + 1.5M CH_3OH	60	3.32	6.75
	180	1.8	13.5

While working in CH_3CN:TEOA, a minor improvement in the number of moles of CO and H_2 gas produced was detected. However, in both organic solvents, the production of H_2 gas was found to be a bit higher than that of CO gas (**Table IV. 7**). In a further attempt to improve the efficiency of the photocatalytic reaction, the use of methanol as a source of protons was introduced. This experiment resulted mainly in the improvement of the number of moles of H_2 gas produced which suppressed the production of CO gas.

With the same concentration of catalyst in solution, the electrocatalytic process of CO_2 was reported to be more efficient and selective in converting CO_2 into CO than the photocatalytic process (**Figure IV. 26**). The production of CO was reported to increase throughout electrolysis in 3 hours; whereas in the photocatalytic process, an increase of CO production was seen only during the first hour followed by a steady decrease of CO formed.

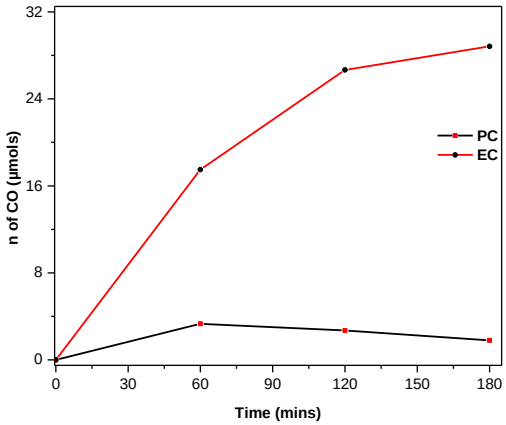

Figure IV. 26 CO gas production using 1mM $[Cr(qpy)(Cl)_2]^+$ during electrocatalysis (in DMF with 1.5M PhOH) and photocatalysis of CO_2 (in CH_3CN:TEOA solution with 10 mM of Cu(I) PS, 50mM BIH and 608µL CH_3OH) in CO_2 saturated conditions.

The weak production of CO during photocatalysis can be due to a number of factors; the (photo)stability of both the Cr (III) catalyst and the excited state of the Cu(I) PS over time, the competing radiative and non-radiative reactions hindering the interaction of BIH with the excited Cu(I) PS and also the lifetime of the Cu(I) PS.

It is important to note that we observed a formation of insoluble purple-like deposits on the surface of the irradiated test tube in which the photocatalytic reaction was taking place during the first hour of the reaction. These precipitates could possibly block further photo irradiation of the sample and indicate a formation of species that are inactive towards CO_2 reduction.

2.5. Photoelectrocatalysis of CO_2 in heterogeneous system using Cr(III) complex

In this part of the report, a heterogeneous photoelectrochemical reduction of CO_2 on semiconductor surfaces has been explored. Such a system tends to offer a number of benefits; the catalyst does not need to be soluble in the reaction medium hence a wider range of solvents is accessible. The catalyst can also be more easily separated from the reaction medium for recycling. The design of the substrate can be exploited for the benefit of the catalytic system as a porous material can favor the high loading of the catalyst due to its high surface area and offer a protective environment for the catalyst hence improving the stability.

In our collaborative work, we chose to work with the p-type semiconductor introduced in Chap III, i.e. $Cu_2O/Ga_2O_3/TiO_2$ semiconductor where the active Cu_2O layer with a suitable band gap energy of 2 eV is coated with two protective layers; an n-type gallium oxide Ga_2O_3 layer and a TiO_2 layer. Both of these protective layers were deposited as means of favoring electron conduction and improving stability of the electrode in different solvents hence formation of $Cu_2O/Ga_2O_3/TiO_2$ semiconductor.[33-37]

Using an approach realized in dye sensitized solar cells in which metal oxide overlayers are used as substrates for the covalent binding of dye molecules through anchoring groups such as carboxylates and phosphonates; we explored this approach while using the molecular Cr (III) catalyst and the $Cu_2O/Ga_2O_3/TiO_2$ semiconductor as a photocathode for photo-electrochemical CO_2 reduction. This was done with the aim of improving the efficiency of CO_2 reduction through achieving maximum catalyst loading on the surface of the photocathode.[38-40]

Prior to developing a modified Cr (III) catalyst with anchoring groups, we first investigated the already synthesized Cr (III) catalyst whose results have been discussed from the beginning of this chapter. Using this complex, heterogenization of a homogeneous catalyst was achieved through adsorption of the complex onto the mesoporous TiO_2 surface of $Cu_2O/Ga_2O_3/TiO_2$ semiconductor as it will be proved later through photoelectrochemical measurements.

ii. Photoelectrochemical reduction of CO_2 using a Cr (III) molecular catalyst on the surface of the $Cu_2O/Ga_2O_3/TiO_2$ photocathode.

In this part of the discussion, we replaced using the glassy carbon electrode as our frequent working electrode and mainly worked with $Cu_2O/Ga_2O_3/TiO_2$ semiconductor. Using the photocathodes samples sent to us from our collaborators, we began studying these pristine electrodes in a clean CH_3CN/0.1M $TBAPF_6$ electrolyte while using platinum and silver as the counter and reference electrodes respectively.

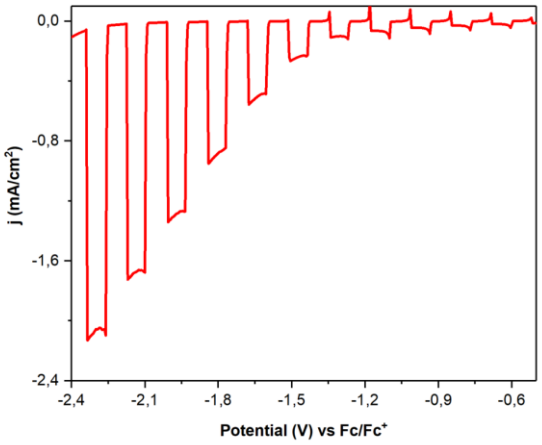

Figure IV. 27 Linear sweep voltammetry (LSV) of a $Cu_2O/Ga_2O_3/TiO_2$ photocathode under chopped light under CO_2 saturated conditions in CH_3CN/0,1M $TBAPF_6$ at v = 0.01 Vs^{-1}.

As reported in **Figure IV. 27**, the $Cu_2O/Ga_2O_3/TiO_2$ photocathode in a CO_2 saturated solution displayed a good steady photocurrent response in the presence of light. However, above -1.8V a significant increase of photocurrent was noted which could be due to the reduction of water traces in CH_3CN.

From faradaic efficiency (FE) measurements performed using the pristine $Cu_2O/Ga_2O_3/TiO_2$ photocathode under CO_2 saturated conditions, a production of H_2 gas was measured to be around 80% - 90% capacity at different potential values as recalled in **Figure IV. 28**. Apart from H_2 gas, CO and CH_4 gases were produced as the C1 products and minor C_2H_4 gas was detected as the C2 product.

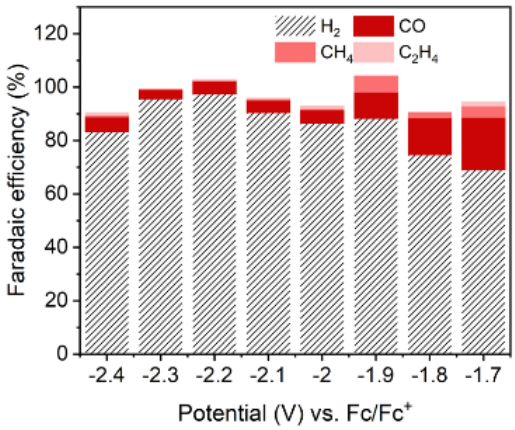

Figure IV. 28 Faradaic efficiency measurements of a $Cu_2O/Ga_2O_3/TiO_2$ photocathode under light at different reduction potentials under CO_2 saturated conditions in CH_3CN/0,1M $TBAPF_6$ under 1 sun illumination at AM 1.5G.

Using the same photocathode as that of **Figure IV. 27**, a 1mM of $[Cr(qpy)(Cl)_2]^+$ complex was added into the electrochemical cell. In CO_2 saturated conditions, the addition of the complex greatly improved the photocurrent density as shown in **Figure IV. 29**.

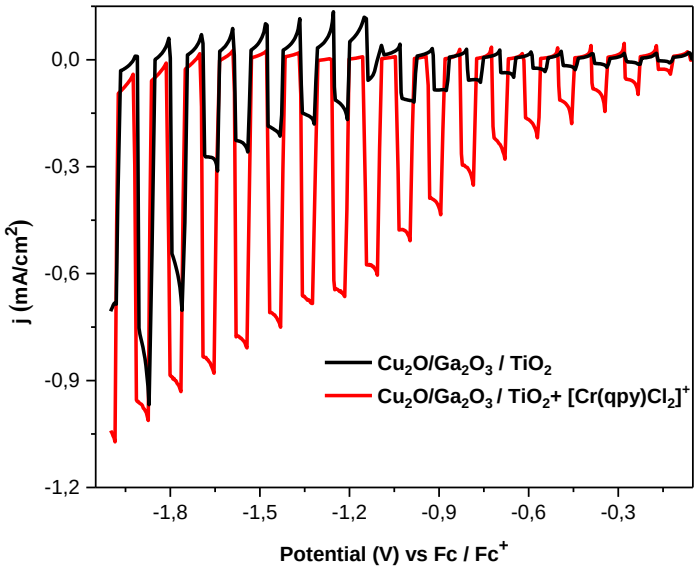

Figure IV. 29 LSV scans of 1mM $[Cr(qpy)(Cl_2)]^+$ complex in CH_3CN/0,1M $TBAPF_6$ solution at v = 0.01 Vs^{-1} on a $Cu_2O/Ga_2O_3/TiO_2$ photocathode under chopped light and CO_2 saturated conditions.

As shown in **Figure IV. 29**, the increase of photocurrent density was detected from very low potential values with significant current increase starting from around -0.6V vs Fc/Fc^+. These results once again prove the catalytic properties of the Cr(III) complex towards the reduction of CO_2 and remarkably highlights how the use of this given photocathode plays an important role not only in improving the current response of CO_2 reduction but also in lowering the onset potential at which the reduction of CO_2 commences.

Once again faradaic efficiency measurements were carried out upon the addition of the Cr(III) complex at different applied potentials. As recorded in **Figure IV. 30**, the presence of a $[Cr(qpy)(Cl_2)]^+$ catalyst resulted in a better amount of CO gas produced compared to the faradaic efficiencies reported in the absence of a catalyst. It was also noted that in the presence of a catalyst, the production of C_2H_4 gas was a bit higher than that of CH_4 gas.

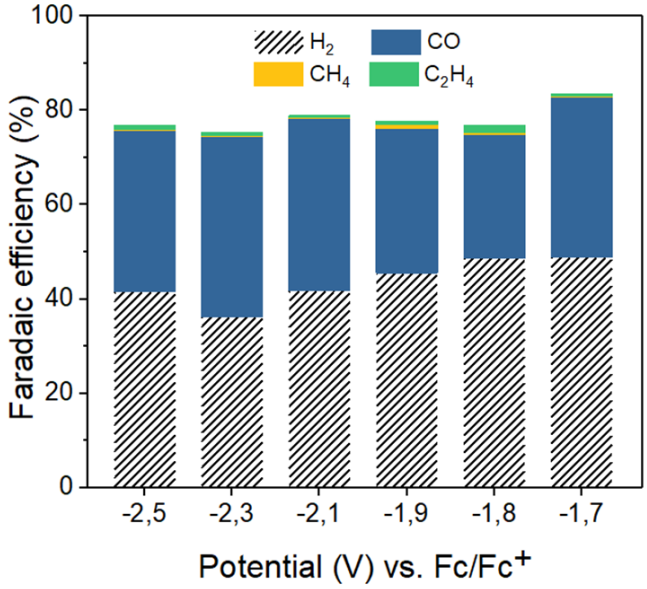

Figure IV. 30 Faradaic efficiency measurements of 1mM $[Cr(qpy)(Cl_2)]^+$ complex in a CO_2 saturated CH_3CN/0,1M $TBAPF_6$ solution at ν = 0.01 Vs^{-1} on a $Cu_2O/Ga_2O_3/TiO_2$ photocathode at different reduction potentials under simulated light (1 sun illumination at AM 1.5G).

As a way of confirming the physisorption of the $[Cr(qpy)(Cl_2)]^+$ complex in solution onto the surface of the $Cu_2O/Ga_2O_3/TiO_2$ photocathode used during the reported electrochemical measurements, this formerly used photocathode was stored for a couple of days and then re-investigated in clean blank electrolyte without the Cr(III) complex in solution.

From the comparison of these LSV scans under CO_2 and continuous light irradiation in **Figure IV. 31**, it was evident that this already-used photocathode had no similarity in electrochemical properties with a pristine electrode. However, it displayed similar electrochemical properties to the LSV scan recorded when the Cr(III) complex was in solution. This observation confirmed the physical adsorption of the complex onto the mesoporous TiO_2 layer of the $Cu_2O/Ga_2O_3/TiO_2$ photocathode.

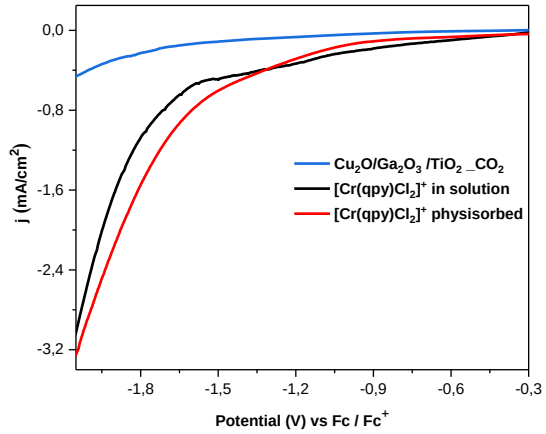

Figure IV. 31. Comparison of LSV scans $Cu_2O/Ga_2O_3/TiO_2$ photocathode in the absence (blue) and presence of 1mM $[Cr(qpy)(Cl_2)]^+$ complex in solution (black) and on the surface of the photocathode (red), under light irradiation and CO_2 saturated conditions at v = 0.01 Vs^{-1}.

Conclusively, the use of $Cu_2O/Ga_2O_3/TiO_2$ photocathode in the photoelectrochemical reduction of CO_2 using the Cr(III) catalyst greatly improved the onset potential value hence low overpotential values. This improvement could be associated with a catalyst loading that could possibly improve the electron relay transfer between the surface of the photocathode and the catalyst.

We then decided to employ the approach used in dye-sensitized solar cells by modifying the complex with some anchoring groups[40] that could facilitate the formation of a self-assembled layer of the molecular catalyst on a surface of the photocathode.

iii. Synthesis of a modified Cr(III) complex using a quaterpyridine ligand modified with a silatrane anchoring group.

Using a quaterpyridine ligand that was previously used to synthesize the $[Cr(qpy)(Cl)_2]^+$ complex, a modified quaterpyridine ligand with a silatrane anchoring group was designed (**Scheme IV.6**). The choice of this anchoring group was a result of various reported literature works that suggested this tripodal anchoring group to be stable in a wide range of pH (2 to 11) as well as its ability to form strong siloxane surface bonds to metal oxides surfaces. These formed surface bonds were reported to be much more resistant to hydrolysis relative to phosphonic acids and carboxylic acids.[41-43]

The 1-(3-aminopropyl)silatrane was prepared following a procedure reported in literature,[44] parallel to this a modified quatepyridine ligand: potassium 4,4'-([2,2':6',2":6",2"'-quaterpyridine]-4',4"-diyl)dibenzoate, $(COOK)_2$-qpy was synthesized using a microwave technique almost similar to the procedure reported in previous literature work.[11]

As a final step of ligand modification, 1-(3-aminopropyl)silatrane and $(COOK)_2$-qpy were reacted together in the presence of (2-(1h-benzotriazol-1-yl)-1,1,3,3-tetramethyluronium hexafluorophosphate), HBTU coupling reagent to form a 4,4'-([2,2':6',2":6",2"'-quaterpyridine]-4',4"-diyl)bis(N-(3-(2,8,9-trioxa-5-aza-1-silabicyclo[3.3.3]undecan-1-yl)propyl)benzamide), $(SiO_3N)_2$-qpy ligand. This final qpy ligand modified with the silatrane cage was then reacted with the $CrCl_3.6H_2O$ salt following previous reported synthetic procedure[1] to form a $[Cr((SiO_3N)_2\text{-qpy})(Cl)_2]Cl.4H_2O$ complex.

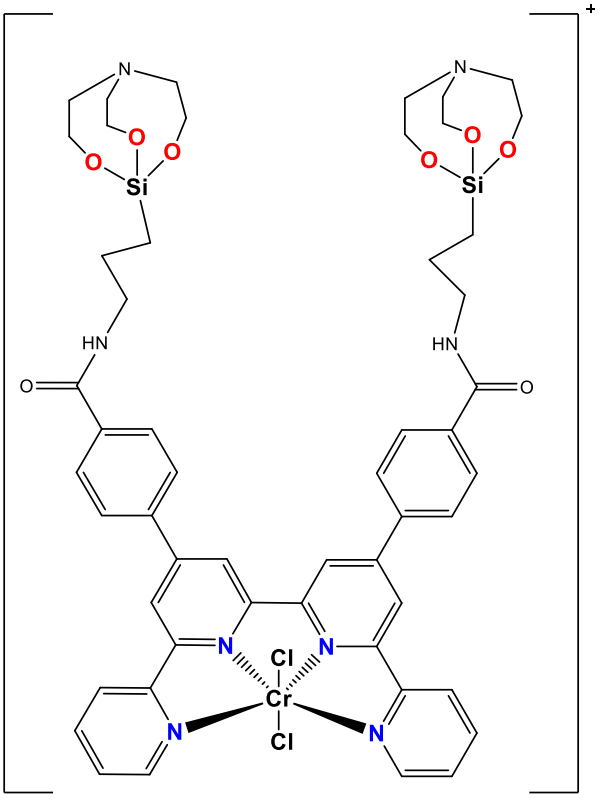

Scheme IV.6 Molecular structure of the modified Cr(III) complex, $[Cr((SiO_3N)_2\text{-qpy})(Cl)_2]^+$.

iv. Electrochemical characterization of the modified $[Cr((SiO_3N)_2\text{-qpy})(Cl_2)]^+$ complex

a) In solution

Cyclic voltammetry of this complex was recorded in DMF/0.1M $TBAPF_6$ electrolyte using GCE as the working electrode. 1mM of this modified $[Cr((SiO_3N)_2\text{-qpy})(Cl)_2]^+$ complex solubilized in the given electrolyte was studied under argon saturated condition as shown in **Figure IV. 32**.

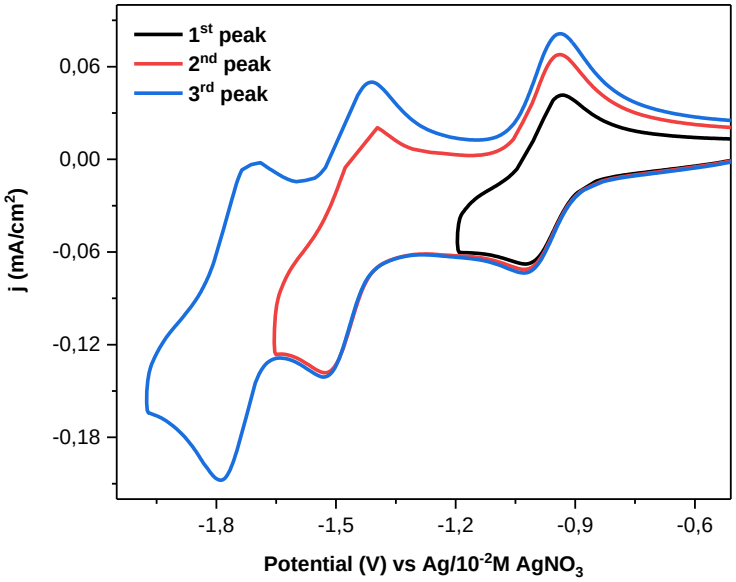

Figure IV. 32 Cathodic scan CV of a 1mM modified $[Cr((SiO_3N)_2\text{-qpy})(Cl)_2]^+$ complex under argon atmosphere on a GCE in DMF/0,1M $TBAPF_6$ at $v = 0.1Vs^{-1}$.

As indicated in **Figure IV. 32**, the synthesis of the modified Cr(III) was a success as it represented almost similar electrochemical behavior as that reported in **Figure IV. 4** for the Cr (III) complex. The redox behavior of all the reduction waves remained similar however an improvement of the redox potential values towards less negative potential was noted as shown in **Table IV. 8**. This shift in potential (~50mV) could be associated to the electron-withdrawing properties of the new substituent groups with an amide function introduced on the para position of the outer phenyl rings.

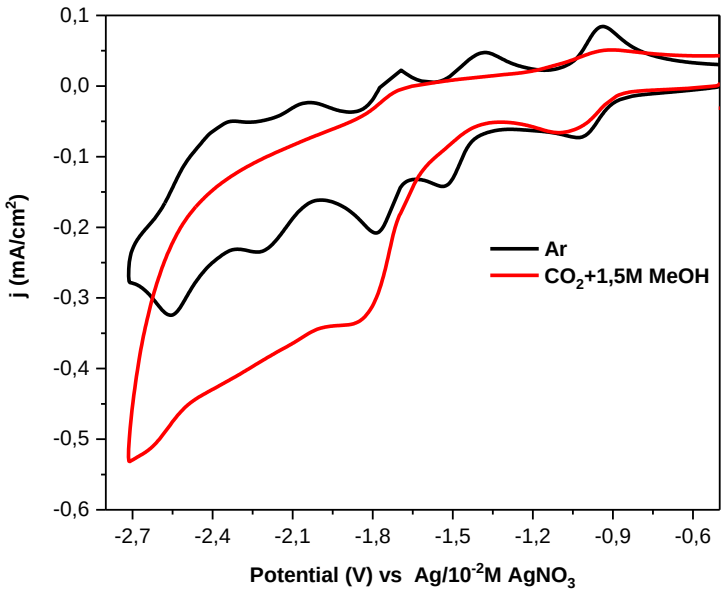

Figure IV. 33 Cathodic CV scan of a 1mM modified $[Cr((SiO_3N)_2\text{-}qpy)(Cl)_2]^+$ under argon (black) and under CO_2 in the presence of methanol (red) in DMF/0,1M $TBAPF_6$ on a GCE at $v = 0.1Vs^{-1}$.

The study of this modified $[Cr((SiO_3N)_2\text{-}qpy)(Cl)_2)]^+$ complex under CO_2 saturated conditions in the presence of methanol displayed catalytic current confirming the catalytic properties of this complex towards CO_2 reduction. **Figure IV. 33** shows a catalytic process occurring at potential values similar to those reported for the parent complex $[Cr(qpy)(Cl)_2]^+$

Table IV. 8 Redox potentials of 1mM of $[Cr(qpy)(Cl)_2]^+$ and 1mM of $[Cr((SiO_3N)_2\text{-}qpy)(Cl)_2]^+$ complexes in DMF/0.1TBAPF6 at $v = 0.1\ Vs^{-1}$

Reactants [1mM]	$E_{1/2}$ (ΔE_p), V vs Ag/10^{-2} M $AgNO_3$		
	$E_{red\ (1)}$	$E_{red\ (2)}$	$E_{red\ (3)}$
$[Cr(qpy)(Cl)_2]^+$	-1.03 (0.07)	-1.48 (0.11)	-1.79 (0.07)
$[Cr((SiO_3N)_2\text{-}qpy)(Cl)_2]^+$	-0.98 (0.09)	-1.47(0.11)	-1.75(0.08)

v. On the surface of FTO

After verifying the electrochemical properties of the $[Cr((SiO_3N)_2\text{-qpy})(Cl)_2]^+$ complex in solution, we further worked on immobilizing this complex on the surface of a clean FTO electrode. Two immobilization procedures were employed; the room temperature immobilization technique and the 70°C heating immobilization techniques. Following the sensitization procedure reported in literature, [45] we decided to combine different steps that could result in a better anchorage of the complex on the FTO surface. All FTO electrodes were clean in an acidic phosphate buffer and then separated into two batches assigned to the two immobilization techniques. The first immobilization technique involved dip-coating an FTO electrode in a DMF solution containing 1mM of complex at RT; whereas in the second immobilization technique, an FTO electrode was dip-coated in a heated complex solution (at 70°C in an oil bath).

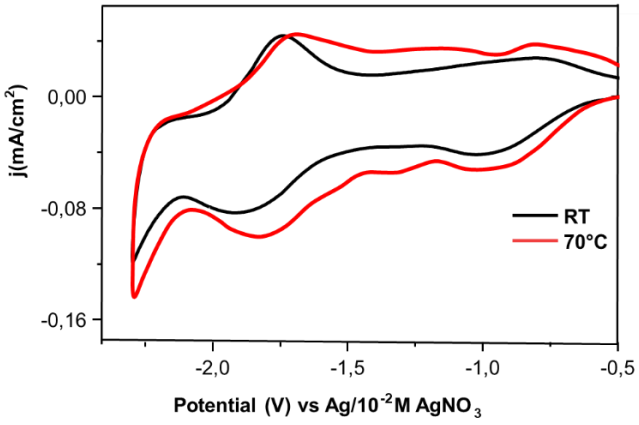

Figure IV. 34 Cathodic CV scans of FTO electrodes coated in 1mM modified $[Cr((SiO_3N)_2\text{-qpy})(Cl)_2]^+$ in DMF/0,1M $TBAPF_6$ solutions at RT and 70°C under argon atmosphere at v = $0.1Vs^{-1}$.

As indicated in **Figure IV. 34**, our preliminary experiments suggest that immobilization of the complex on the FTO surface was successful with both CV scans showing redox signals of the complex present on the surface of the FTO electrode. The 70°C heating immobilization technique presented a bit higher current density in comparison to the RT technique; this suggests that a better loading of the complex can be achieved at high temperatures rather than low temperature.

Consequently, we investigated the coated FTO from the 70°C heating technique and studied its response under CO_2 saturated conditions as shown in **Figure IV. 35**.

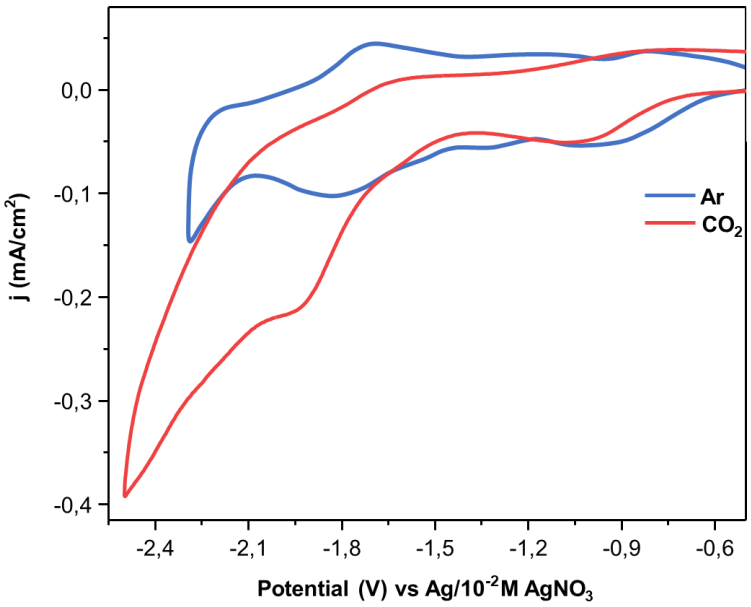

Figure IV. 35 Cathodic CV scans of FTO electrode coated in 1mM modified $[Cr((SiO_3N)_2\text{-}qpy)(Cl)_2]^+$ complex at 70°C in DMF/0,1M $TBAPF_6$ solutions under argon and CO_2 saturated atmosphere at $v = 0.1Vs^{-1}$.

In **Figure IV. 35**, our first attempt at studying these modified FTO electrodes showed a current response under CO_2 saturated conditions suggesting a catalytic activity taking place. An increase of current density was detected from an onset potential of -1.75V vs $Ag/10^{-2}M\ AgNO_3$, with an onset potential at almost similar value as that of the complex in solution. And since these results are our first findings on the modification of electrodes with a silatrane anchoring group, there is a need to further investigate better anchoring conditions to ensure a proper immobilization of the modified Cr(III) complex on electrode surface prior to implementing the procedure on a p-type semiconducting electrode.

Indeed, we did notice a short-term stability of these modified FTO electrodes. Upon running various CV scans using the same FTO electrode, the reduction waves corresponding to the modified Cr(III) complex disappeared which further indicates the need to conduct more studies on proper immobilization techniques.

3. Conclusion

In the course of this chapter, we successfully designed a Cr(III) complex that displayed great catalytic activity towards CO_2 reduction at a very low onset potential compared to other complexes reported in the other chapters. With this complex, we managed to lower the overpotential to 0.78V which is an interesting progress in comparison to other reported chromium complexes.

This complex was reported to have an average faradaic efficiency and yet it did display some selectivity behavior. In further studying the catalytic properties of this complex in solution, we explored its photocatalytic behavior in the presence of a Cu(I) photosensitizer and a sacrificial electron donor BIH. In this case the reduction of CO_2 gas was not as effective as in electrocatalysis, which could be due to a number of reasons that are mainly attributed to the photophysical and photochemical properties of the Cu(I) PS used.

In a heterogeneous system, photoelectrochemical reduction of CO_2 using the Cr (III) catalyst physisorbed on the surface of $Cu_2O/Ga_2O_3/TiO_2$ photocathode demonstrated interesting results with a number of carbon-based products (CO, CH_4, C_2H_4) being formed as result of CO_2 reduction. With the bare $Cu_2O/Ga_2O_3/TiO_2$ semiconductor mainly producing H_2 gas, the addition of the Cr(III) complex helped in suppressing the competing reaction of H_2 gas formation and mainly favored the formation of the intended carbon products.

As an attempt of forming a covalent linkage between the molecular catalyst and the surface of the electrode, a modified Cr(III) complex was successfully synthesized and anchored on the ITO surface. Despite the short-term stability of this linkage between the catalyst and the ITO electrode, we did manage to still observe the catalytic properties of this modified complex at a very low onset potential. And finally, we achieved our goal of synthesizing a novel Cr(III) complex with a silatrane anchoring group which to our knowledge has not been done before.

Bibliography

1. E. C. Constable, S. M. Elder, D. A. Tocher, *Polyhedron*., **1992,** *11*, 1337-1342.
2. N. A. P. Kane-Maguire, *Top. Curr. Chem*., **2007**, *280*, 37-67
3. S. L. Hooe, J. M. Dressel, D. A. Dickie, C. W. Machan, *ACS Catal*., **2020**, *10* (2), 1146-1151.
4. E.C. Constable, S.M. Elder, M.J. Hannon, A. Martin, P.R. Raithby, D.A. Tocher, *J. Chem. Soc., Dalton Trans*., **1996**, 2423-2433.
5. E. C. Constable, M. J. Hannon, P. Harverson, M. Neuburger, D. R. Smith, V. F. Wanner, L. A. Whall, M. Zehnder, *Polyhedron*., **2000**, *19*(1), 23-34.
6. K. T. Potts, M. Keshavarz-K, F. S. Tham, H. D. Abruna, C. R. Arana, *Inorganic Chem*., **1993**, *32* (20), 4422-4435.
7. Z. Guo, F. Yu, Y. Yang, C.-F. Leung, S.-M. Ng, C.-C. Ko, C. Cometto, T.-C. Lau, M. Robert, *ChemSusChem*., **2017**,*10*, 4009−4013.
8. K.-M. Lam, K.-Y. Wong, S.-M. Yang, C.-M. Che, J. *Chem. Soc., Dalton Trans.*, **1995**, 1103-1107.
9. Z. Guo, S. Cheng, C. Cometto, E. Anxolabéhère-Mallart, S.-M. Ng, C.-C. Ko, G. Liu, L. Chen, M. Robert, T.-C. Lau, *J. Am. Chem. Soc*., **2016**, *138* (30), 9413-9416.
10. C. Cometto, L.Chen, E. Anxolabéhère-Mallart, C. Fave, T.-C. Lau, M. Robert, *Organometallics*., **2019**, *38* (6), 1280-1285.
11. P. B. Pati, R. Wang, E. Boutin, S. Diring, S. Jobic, N. Barreau, F. Odobel, M. Robert, *Nat. Commun*., **2020**, *11*, 3499.
12. L. Chen, G. Chen, C.-F. Leung, C. Cometto, M. Robert, T.-C. Lau, *Chem. Soc. Rev*., **2020**, *49*, 7271-7283.
13. E. C. Constable, S. M. Elder, J. Healy, D. A. Tocher, *J. Chem. Soc. Dalton. Trans*., **1990**, 1669-1674.
14. V. Balzani, F. Scandola, Supramolecular photochemistry., **1991**.
15. C. C. Scarborough, K. M. Lancaster, S. DeBeer, T. Weyhermüller, S. Sproules, K. Wieghardt; *Inorg. Chem*., **2012**, *51* (6), 3718-3732.
16. J. A. Ramos Sende, C. R. Arana, L. Hernhndez, K. T. Potts, M. Keshevarz-K, H. D. Abruña; *Inorg. Chem*., **1995**, *34* (12), 3339-3348.
17. J. Chrastil, J. T. Wilson, *Anal. Biochem*., **1975**, *63* (1), 202-207.
18. U. Kleeberg, W. Klinger, *J. Pharmacol. Methods*., **1982**, *8* (1), 19-31.

19. Y. Yamazaki, T. Onoda, J. Ishikawa, S. Furukawa, C. Tanaka, T. Utsugi, T. Tsubomura, *Front. Chem*., **2019**, *7*, 288.
20. H. Takeda, K. Ohashi, A. Sekine, O. Ishitani, *J. Am. Chem. Soc*., **2016**, *138*, 4354−4357.
21. P. A. Forero-Cortés, M. Marx, N. G. Moustakas, F. Brunner, C. E. Housecroft, E. C. Constable, H. Junge, M. Beller and J. Strunk, *Green Chem*., **2020**,22, 4541-4549.
22. T. Tsubomura, K. Kimura, M. Nishikawa and T. Tsukuda, *Dalton Trans*., **2015**, *44*, 7554-7562.
23. M. Ruthkosky, C. A. Kelly, F. N. Castellano, G. J. Meyer, *Coord. Chem. Rev*., **1998**, *171*, 309–322.
24. D.F. Watson, H. S. Tan, E. Schreiber, C. J. Mordas, A. B. Bocarsly, *J. Phys. Chem. A*., **2004**, *108* (16), 3261-2367.
25. Y. Tamaki, K. Koike, T. Morimoto, O. Ishitani, *J. Catal*., **2013**, *304*, 22–28.
26. X.-Q. Zhu, M.-T. Zhang, A. Yu, C.-H. Wang, J.-P. Cheng, *J. Am. Chem. Soc*., **2008**, *130*, 2501–2516.
27. N. Armaroli, G. Accorsi, M. Holler, O. Moudam, J.-F. Nierengarten, Z. Zhou, R. T. Wegh, R. Welter, *Adv. Mater*., **2006**, *18*, 1313 – 1316.
28. H. Takeda, Y. Monma Y, H. Sugiyama, H. Uekusa, O. Ishitani, *Front. Chem*., **2019**, *7*, 418.
29. D. G. Cuttell, S. M. Kuang, P. E. Fanwick, D. R. McMillin, R. A.Walton, *J. Am. Chem. Soc*., **2002**, *124*, 6-7.
30. S. M. Kuang, D. G. Cuttell, D. R. McMillin, P. E. Fanwick, R. A. Walton, *Inorg. Chem*., **2002**, *41*, 3313-3322.
31. L. Yang, J. K. Feng, A. M. Ren, M. Zhang, Y. G. Ma, X. D. Liu, *Eur. J. Inorg. Chem*., **2005**, 1867-1879.
32. A. Kaeser, M. Mohankumar, J. Mohanraj, F. Monti, M. Holler, J.-J. Cid, O. Moudam, I. Nierengarten, I. Karmazin-Brelot, C. Duhayon, B. Delavaux-Nicot, N. Armaroli, J.-F. Nierengarten, *Inorg. Chem*., **2013**, *52* (20), 12140−12151.
33. D. R. McMillin, K. M. McNett, *Chem. Rev*., **1998**, *98*, 1201–1220.
34. A. Paracchino, V. Laporte, K. Sivula, M. Grätzel, E. Thimsen, *Nat. Mater*., **2011**, *10*, 456–461.
35. M. Schreier, P. Gao, M. T. Mayer, J. Luo, T. Moehl, M. K. Nazeeruddin, S. D.Tilley, M. Grätzel, *Energy Environ. Sci*., **2015**, *8*, 855-861.

36. L. Pan, J. H. Hyun, M. T. Mayer, M. K. Son, A. Ummadisingu, J. S. Lee, A. Hagfeldt, J. Luo, M. Grätzel, *Nat. Catal*., **2018**, *1*, 412-420.
37. L. Pan, Y. Liu, L. Yao, D. Ren, K. Sivula, M. Grätzel, A. Hagfeldt, *Nat Commun*., **2020**, *11*(1), 318
38. C. Li, T. Hisatomi, O. Watanabe, M. Nakabayashi, N. Shibata, K. Domen, J.-J. Delaunay, *Energy Environ. Sci*., **2015**, *8*, 1493–1500.
39. C. D. Windle, E. Pastor, A. Reynal, A. C. Whitwood, Y. Vaynzof, J. Durrant, R. Perutz, E. Reisner, *Chem. Eur. J*., **2015**, *21* (9), 3746-3754.
40. E.-G. Ha, J.-A. Chang, S.-M. Byun, C. Pac, D.-M. Jang, J. Park, S. O. Kang, *Chem. Commun*., **2014**, *50* (34), 4462-4464.
41. T. M. Suzuki, H. Tanaka, T. Morikawa, M. Iwaki, S. Sato, S. Saeki, M. Inoue, T. Kajino, T. Motohiro, *Chem. Commun*., **2011**, *47* (30), 8673-8675.
42. B. J. Brennan, A. E. Keirstead, P. A. Liddell, S. A. Vail, T. A. Moore, A. L. Moore, D. Gust, *Nanotechnology*., **2009**, *20*, 505203.
43. B. J. Brennan, M. J. Llansola Portoles, P. A. Liddell, T. A. Moore, A. L. Moore, D. Gust, *Phys. Chem. Chem. Phys*., **2013**, *15*, 16605–16614.
44. K. L. Materna, B. J. Brennan, G. W. Brudvig, *Dalton Trans*., **2015**, *44*, 20312-20315.
45. A. M.-C. Dumitriu, M. Cazacu, S. Shova, C. Turta, B. C. Simionescu; *Polyhedron*., **2012**, *33*, 119–126.
46. K. L. Materna, J. Jiang, R. H. Crabtree, G.W. Brudvig, *ACS. App. Mater. Interfaces*., **2019**, *11* (6), 5602-5609.

General conclusion and perspectives

The work of this thesis focuses on the study of the conversion of CO_2 into valuable synthetic fuels using polypyridinyl group VI metal complexes in solution. To achieve this goal, these metal complexes were synthesized and characterized for their photophysical and electrochemical properties. The molecular composition and structure of the metal complexes was modified by working with different coordinating ligands (bidentate and tetradentate) that result to the alteration of the intrinsic nature of these complexes (i.e. their electro- and photochemical properties) which directly influences the mechanistic behavior during catalysis.

The photo- and physicochemical characterization of these metal complexes involved the use of different techniques mainly IR, NMR, MS-ESI and UV-Vis. These techniques were used in determining compositions of molecular structures of synthesized complexes, confirming their purity as well as investigating absorption and emission properties of designed complexes.

The investigation of the electrochemical properties performed in organic solvents saturated with either argon or CO_2 gave an insight as to whether these complexes possess catalytic properties towards the reduction of CO_2. During this work, cyclic voltammogram and spectroelectrochemical measurements were crucial to understanding the step-by-step evolution of complex species during electrolysis that eventually reveal active species involved in the reduction of CO_2.

A study of bipyridyl tetracarbonyl metal complexes presented in Chapter II reveal bi-reduced tricarbonyl species of the group VI metal complexes $[M(bpy)(CO)_3]^{2-}$ as active species that bind with the CO_2 substrate and further reduce CO_2 through the inner sphere CO_2 reducing mechanism. By replacing one carbonyl ligand with a halide ligand, a new family of complexes was developed $[M(bpy)(CO)_3Cl]^-$ having a geometry closely corresponding to that of rhenium and manganese tricarbonyl complexes. These tricarbonyl group VI metal complexes demonstrated a positive shift of the reduction onset potential due to the presence of a chloride ligand that can easily be released in comparison to a carbonyl ligand.

Subsequent to the investigation of bipyridyl metal complexes, another family of tetracarbonyl species with a different diimine ligands (pyridine imidazole-based ligands) was investigated as discussed in Chapter III. This study was done in an attempt of understanding and utilizing the photophysical properties of the pyridine-imidazole-based metal complexes (specifically $[W(\mathbf{LI})(CO)_4]$) towards achieving photocatalytic conversion of CO_2 in solution. And although

this metal complex exhibited both photophysical and electrocatalytic activities, the short lifetime of its excited state rendered efforts to execute CO_2 photocatalysis ineffective. Nonetheless, this tungsten pyridine imidazole complex demonstrated an effective photoelectroreduction of CO_2 to CO with a FE of 88% in heterogeneous conditions on the $Cu_2O/Ga_2O_3/TiO_2$ photocathode.

Conclusively, a Cr (III) polypyridyl metal complex was synthesized and investigated. This complex, despite being previously synthesized, had not been investigated for the electrocatalytic conversion of CO_2. As compared to earlier reported group VI metal complexes, this complex demonstrated electrocatalytic properties towards CO_2 reduction in protic organic solvent at the least negative onset potential (-1.85V vs $Ag/10^{-2}$ M $AgNO_3$) due to its high oxidation state and utilization of a novel polypyridyl ligand. Given the low onset potential, photocatalytic conversion of CO_2 was investigated using the Cr (III) catalyst in the presence of a Cu(I) photosensitizer and a sacrificial electron donor BIH. Both experiments (electrocatalytic and photocatalytic) showed that this Cr (III) complex is a far more effective electrocatalyst than a photocatalyst under homogeneous conditions resulting mainly in the formation of CO. On the other hand, under heterogeneous conditions, the photoelectrochemical reduction of CO_2 with the Cr (III) catalyst adsorbed on the surface of the $Cu_2O/Ga_2O_3/TiO_2$ photocathode showed intriguing results, with different carbon-based products (CO, CH_4, and C_2H_4) being produced as a result of CO_2 photoelectroreduction. These valuable carbon-based products could be a result of a cooperative effect of the catalytic properties of the complex and the semi-conducting electrode.

Clearly, these results indicate a potential for further research and development of complexes using earth abundant group VI metals. Very few examples of complexes with metal centers of higher oxidation state than zero have been investigated. However, our findings with others suggest this approach being effective towards the future development of efficient catalysts based on such metals.

As means of improving the efficiency of CO_2 reduction using group VI metal complexes, the modification of the complex structure should be considered. This structural modification of the complex should mainly be focused on altering the ligand structure by introducing different substituents groups with electron-withdrawing properties that can aid in achieving CO_2 reduction at less negative reducing potentials.

Other types of ligand substituents groups to be considered should be those with anchoring properties that can favor immobilization of complexes on different conductive surfaces resulting to an improved electrocatalytic properties due to better reaction rates by eliminating the mass transportation hindrance of a catalyst to an electrode surface.

Another possible approach may involve incorporating catalysts in a polymer matrix or modify the ligand structure with polymerizable groups (i.e. pyrrole, vinyl, thiophene). Such polymer films deposited on an electrode surface could also offer interesting properties due to high catalysts loading. An example was reported by Abrunã et al., with a Cr (III) terpyridine core bearing vinyl substituted groups. The electropolymerization of this complex film on a carbon electrode led to the formation of formaldehyde. However, this approach has not been further investigated yet.

Exploration and investigation of other porous molecular inorganic structures such as MOFs, zeolites for their electrocatalytic properties towards CO_2 reduction should be taken into consideration. Given their ability to selectively capture and store CO_2, these porous structures associated with efficient catalysts and/or incorporated to conductive electrode surfaces can result in the development of devices and novel technology applicable in industries for CO_2 capture and utilization.

1. Instrumentation and characterization techniques

Nuclear Magnetic Resonance: ^{1}H NMR, ^{13}C NMR and ^{15}N NMR were recorded at room temperature on Bruker Avance 400 or 500 MHz spectrometers. ^{1}H chemical shifts were referenced to residual solvent peaks. Coupling constant values (J) are given in hertz and chemical shift (δ) in ppm. The abbreviations used are: s= singlet, d= doublet, dd= doublet of doublet, t= triplet and m= multiplet, dt= doublet of triplet, q= quartet.

UV-visible absorption spectroscopy (UV-vis): UV-vis spectra of complexes in solution were recorded on a Cary 50 Probe UV−vis spectrophotometer (VARIAN) or on Zeiss MC5601 spectrophotometer, using either a 1mm quartz immersion probe (Hellma Inc.) or a quartz cuvette of optical path length l =1 cm.

Infra-red spectroscopy: The complexes of interest were analyzed using the "Golden Gate" ATR system on a Nicolet iS10 FTIR thermo Scientific spectrometer. This system features a brazed diamond ATR crystal and a signature "Golden Gate" sample loading bridge. The complex samples in solid form were loaded on this bridge which contains the required mirrors for beam transmission.

Luminescence: Emission spectra were recorded with a Fluoromax-4 (Horiba Scientific) in a quartz cuvette with 4 transparent faces. Samples were purged with Ar for 15 minutes prior to experiment. The FluoTime 200 time-resolved spectrometer is used for decay acquisition. It consists of a GaAs microchannel plate photomultiplier tube (Hamamatsu model R3809U-50) coupled to a time-correlated single photon counting system from PicoQuant (PisoHarp300).

Mass Spectroscopy: The electrospray ionization mass spectrometry (ESI-MS) experiments were performed on a triple quadrupole mass spectrometer Amazon speed (BRUKER). The ESI source was heated to 80° C. The sampling cone voltage was set within the range 14 - 18 V. Complex in different organic solvents were injected using a syringe pump at a flow rate in the range of 5 mL.min^{-1}. Matrix assisted laser desorption/ionization time-of-flight MALDI-TOF were recorded on a Bruker Maldi-TOF/TOF Speed.

EPR spectroscopy: X and Q band EPR spectra were recorded with a Bruker EMX, equipped with the ER-4192 ST Bruker and ER-4121 VT for the X-band at 100 K experiments and the ER5106 QTW Bruker cavity and an Oxford Instruments ESR-900 continuous-flow helium cryostat for the Q-band at 4.5 K experiments.

Electrochemistry: Electrochemical measurements were performed in a standard three-electrode cell at RT under a continuous argon flow or in a glovebox. Electrolytes were purchased and used without further purification (minimum purity 99%): tetra-n-butylammonium hexafluorophosphate ($TBAPF_6$, Aldrich) and silver nitrate ($AgNO_3$, Prolabo). A platinum (Pt) coil in CH_3CN/0.1M $TBAPF_6$ or DMF/0.1M $TBAPF_6$ and a silver (Ag) coil in 0.01M $AgNO_3$ solubilized in CH_3CN/0.1M $TBAPF_6$ or DMF/0.1M $TBAPF_6$ were used as counter electrode and reference electrode, respectively. A glassy carbon disk electrode, GCE (3 mm in diameter) was used as a working electrode. Before experiments, the GCE was polished using diamond paste and cleaned with acetone.

Cyclic voltammograms (CV) were recorded with an Ametek® Solartron analytical potentiostat/galvanostat controlled by a modulab XM ECS software or a CHI 630 potentiostat (CH Instrument), or a Biologic SP300 potentiostat (Science Instruments). All reported potentials are against the $Ag/AgNO_3$ 0.01 M reference electrode, unless otherwise stated. One should subtract 0.087 V from them to convert them against Fc^+/Fc reference.

Half-wave potential ($E_{1/2}$) and peak-to-peak splitting (ΔE_p) are calculated as follows:

$$E_{1/2} = \frac{E_{pa}+E_{pc}}{2} \qquad \Delta E_p = E_{pa} - E_{pc}$$

where E_{pa} and E_{pc} are anodic and cathodic peak potentials respectively.

Exhaustive electrolysis: these experiments were carried out under argon atmosphere (glove box) at RT using vitreous carbon plate or carbon foam as the working electrode and Pt wire as counter electrode isolated from the electrolytic working solution through an CH_3CN/0.1M $TBAPF_6$ or DMF/0.1 M $TBAPF_6$ solution bridge. The reference electrode was $Ag/AgNO_3$ (0.01 M) electrode in CH_3CN/0.1M $TBAPF_6$ or DMF/0.1 M $TBAPF_6$.

The process of electrolysis was followed by monitoring the changes in the UV-Vis spectra of the solution by spectro-electrochemical measurements at RT using a BioLogic SP300 potentiostat controlled by an EC-Lab® software coupled with either an MCS 501 UV-NIR (Carl Zeiss) spectrophotometer or a Zeiss MC5601 spectrophotometer using an additional 1 mm quartz immersion probe (Hellma).

Electrocatalysis: Experiments were carried out at room temperature in a CO_2 saturated environment to analyze the reduction of CO_2 in a sealed conventional three-electrode cell. The solvent was either CH_3CN/0.1M $TBAPF_6$ or DMF/0.1 M $TBAPF_6$, to which a weak acid as a proton source may be added in some CO_2 reduction experiments. Reference and counter electrodes were $Ag/AgNO_3$ 0.01 M and Pt plate, respectively, with the use of a carbon foam as working electrode.

In a normal setting with 3 electrodes and 10 mL solution, the headspace volume was measured to be 140 mL. During the experiments, at each time interval a 100 µL sample was taken from the headspace gas using a gas tight injection syringe. Gas products were analyzed with the chromatographic techniques described below. At the end of the experiments, a liquid sample was taken for HCOOH analysis.

Photocatalysis: these experiments were performed using 5 mL of organic solvent (CH_3CN: TEOA or DMF: TEOA with a 5:1 v/v ratio) in a glass tube with 17 mL total volume. Unless otherwise stated, the amounts of BIH, **PS** and the given complex were calculated so that their final concentrations were 50 mM, 10 mM and 1 mM, respectively. The glass tube was tightly sealed using a rubber septum and the resultant solution was degassed with a CO_2 for 15-30 min. The cell was then transferred to the irradiation setup bench.

The photoirradiation measurements were performed using a Xenon-Mercury lamp (LC8, HAMAMATSU) in association with a 400-750 nm filter (03MHG101, MELLES GRIOT). The setup was composed of three sections, a holder for the lamp fibre, a filter holder and the clamp to keep the cell in position, accompanied by a magnetic stirring bar. Gas and liquid product detection were performed using gas chromatograph and ionic chromatography described below.

Gas chromatography: Gas samples (100 µL) were taken from the headspace of the tube containing the reaction mixture using a syringe. This sample was then injected and analyzed using a Perkin Elmer Clarus 560 gas chromatography equipped with a thermal conductivity detector.

The H_2 gas was detected with the TCD system whereas CO and CH_4 are detected with the FID system. The number of moles of gas contents was calculated using the quantity of charge passing through the cell which was consequently compared to a standard gas mixture of 1% CO, 5% H_2 and 1% CH_4 (from Air Liquid).

Ionic chromatography: Content of HCOOH and oxalate ($C_2O_4^{2-}$) produced by electrocatalysis was determined by manual injection of 100 µL on a Metrohm Eco ionic chromatography equipped with a Metrosep A Supp 19 column and Na_2CO_3 8mM / $NaHCO_3$ 0.25mM in water as mobile phase for formate and oxalate detection by conductivity.

Chemicals

Solvents: Acetonitrile (CH_3CN), Xylene, dichloromethane (CH_2Cl_2) and methanol (CH_3OH), all purchased from Fisher, HPLC grade), dimethyl sulfoxide (DMSO, Acros, anhydrous 99.7%), *N*,*N*-dimethylformamide (DMF, Acros, anhydrous 99.8%), chloroform ($CHCl_3$, Carlo Erba, HPLC grade), diethyl ether (Aldrich, 99.8%), hexane (95%), and acetone (Aldrich, 99.5%) were used as purchased without any further purifications. Dry solvents were obtained by distillation under Argon. Distilled water was prepared with a Milli-Q system.

Reagents: all reagents have been used without further purifications, unless otherwise stated.

2. Synthesis procedures

Most of the synthetic procedures were performed either in oven-dried glassware attached to a vacuum and argon gas line with Schlenk techniques or in a glovebox. The synthesis of ligands and complexes will be detailed chapter wise.

2.1. Chapter II complexes

i. Synthesis of [M(bpy)(CO)$_4$] complexes

These complexes were synthesized following two different synthetic routes, the reflux and the irradiation routes as described below;

- The reflux synthetic route

For [M(bpy)(CO)$_4$] with M = Cr, Mo

1.36 mmol of [M(CO)$_6$] hexacarbonyl complexes (0.299 g and 0.359 g for M= Cr and M=Mo respectively) and 1.4 mmol (0.218 g) of 2,2′-bipyridine ligand were dissolved in 50 mL of dry toluene. The resulting solution was refluxed for 2h under argon atmosphere, then cooled down at room temperature. Upon cooling, deep orange precipitates settled down in solution which

were then filtered and rinsed thoroughly by diethyl ether. Yield: 18% (0.077g for M=Cr) and 61% (0.3034 g for M=Mo).

[Cr(bpy)(CO)$_4$]:

^{1}H NMR (400 MHz, DMSO-d_6) δ 9.06 (s, 1H), 8.53 (s, 1H), 8.12 (s, 1H), 7.61 (s, 1H). **FT-IR** (ν (CO)): 1999, 1892, 1859, 1828.

ESI-MS: *m/z* $[M+nCl]^-$ = 354.96 (calculated for $C_{14}H_8CrN_2O_4$ [M] = 320.22).

[Mo(bpy)(CO)$_4$]:

^{1}H NMR (400 MHz, CD_3CN) δ 9.04 (d, J = 4.9 Hz, 1H), 8.31 (t, J = 14.1 Hz, 1H), 8.06 (td, J = 8.0, 1.5 Hz, 1H), 7.62 – 7.30 (m, 1H). **FT-IR** (ν (CO)): 2006, 1912, 1858, 1825.

ESI-MS: *m/z* $[M+nCl]^-$ = 400.92 (calculated for $C_{14}H_8MoN_2O_4$ [M] = 364.19).

For [W(bpy)(CO)$_4$]

1.36 mmol (0.478 g) of $[W(CO)_6]$ hexacarbonyl complex and 1.4 mmol (0.218 g) of 2,2′-bipyridine ligand were dissolved in 80 mL of dry xylene. The dissolved solution was refluxed for 3h under inert conditions. Upon cooling, the deep maroon precipitates were filtered and rinsed using diethyl ether. Yield: 58% (0.0.493 g).

^{1}H NMR (400 MHz, CD_3CN) δ 9.15 (d, J = 4.9 Hz, 1H), 8.37 (d, J = 8.2 Hz, 1H), 8.10 (td, J = 8.1, 1.6 Hz, 1H), 7.65 – 7.33 (m, 1H). **FT-IR** (ν (CO)): 2000, 1906, 1826, 1802.

ESI-MS: *m/z* $[M+nCl]^-$ = 486.97 (calculated for $C_{14}H_8WN_2O_4$ [M] = 452.07).

- The irradiation synthetic route

1.36 mmol of $[M(CO)_6]$ hexacarbonyl complexes (0.299 g, 0.359 g, 0.478 g for M= Cr, Mo and W respectively) and 1.4 mmol (0.218 g) of 2,2′-bipyridine ligand were dissolved in 50 mL of degassed isooctane. These solutions were photo-irradiated at 50% lamp intensity in the visible region of 300-400 nm for 2-3 hours using a Xenon Hamamatsu Lightnincure LC8 lamp.

[Cr(bpy)(CO)$_4$]:

^{1}H NMR (400 MHz, DMSO-d_6) δ 9.06 (s, 1H), 8.53 (s, 1H), 8.12 (s, 1H), 7.61 (s, 1H). **FT-IR** (ν (CO)): 1999, 1892, 1859, 1828.

ESI-MS: *m/z* $[M+nCl]^-$ = 354.96 (calculated for $C_{14}H_8CrN_2O_4$ [M] = 320.22).

[Mo(bpy)(CO)$_4$]:

^{1}H NMR (400 MHz, CD3CN) δ 9.04 (d, J = 4.9 Hz, 1H), 8.31 (t, J = 14.1 Hz, 1H), 8.06 (td, J = 8.0, 1.5 Hz, 1H), 7.62 – 7.30 (m, 1H). **FT-IR** (ν (CO)): 2006, 1912, 1858, 1825.

ESI-MS: *m/z* $[M+nCl]^-$ = 400.92 (calculated for $C_{14}H_8MoN_2O_4$ [M] = 364.19).

[W(bpy)(CO)$_4$]:

^{1}H NMR (400 MHz, CD_3CN) δ 9.15 (d, J = 4.9 Hz, 1H), 8.37 (d, J = 8.2 Hz, 1H), 8.10 (td, J = 8.1, 1.6 Hz, 1H), 7.65 – 7.33 (m, 1H). **FT-IR** (ν (CO)): 2000, 1906, 1826, 1802.

ESI-MS: *m/z* $[M+nCl]^-$ = 486.97 (calculated for $C_{14}H_8WN_2O_4$ [M] = 452.07).

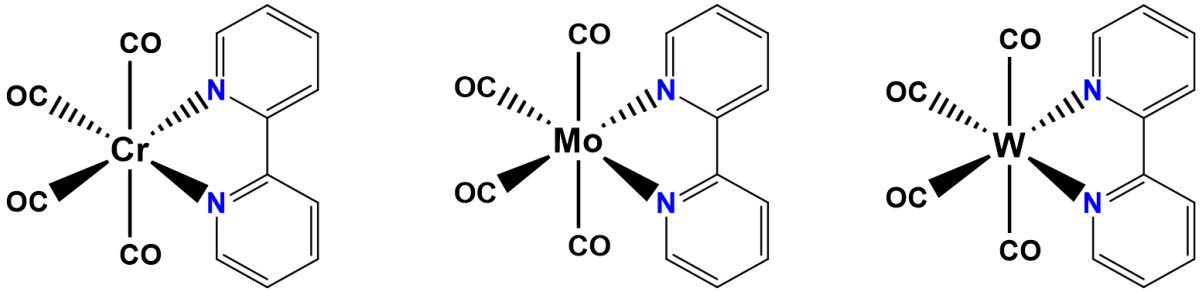

ii. Synthesis of PPh$_4$[M(bpy)(CO)$_3$Cl] complexes

PPh$_4$[W(bpy)(CO)$_3$Cl]: 0.5 mmol (0.2252 g) of [W(bpy)(CO)$_4$] complex was solubilized with 0.75 mmol (0.283 g) of PPh_4Cl in 40 mL solution of xylene: acetonitrile (8:1) then refluxed for 16h under argon. On cooling, the precipitates were filtered and rinsed with cold methanol resulting in a dark purple solid product. Yield: 87% (0.3453 g)

^{1}H NMR (400 MHz, DMSO-d6) δ 8.71 – 8.64 (m, 1H), 8.38 (d, J = 8.0 Hz, 1H), 7.46 (ddd, J = 7.5, 4.7, 1.2 Hz, 1H). **FT-IR** (ν (CO)): 1874, 1759, 1739.

PPh$_4$[Mo(bpy)(CO)$_3$Cl]: 0.51 mmol (0.1849 g) of [Mo(bpy)(CO)$_4$] complex was reacted with 0.75 mmol (0.283 g) of PPh_4Cl in 40 mL solution of toluene: acetonitrile (4:1) in a reflux reaction of 1h under argon conditions. A purple solid was collected upon filtration and rinse using cold methanol. Yield: 54% (0.1938 g).

^{1}H NMR (400 MHz, DMSO-d6) δ 8.71 – 8.64 (m, 1H), 8.40 – 8.32 (m, 1H), 7.45 (ddd, J = 7.5, 4.8, 1.2 Hz, 1H). **FT-IR** (ν (CO)): 1885, 1765, 1744.

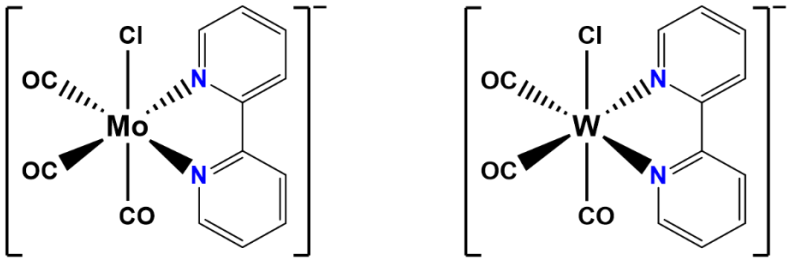

2.2. Chapter III complexes

i. Synthesis of [M(L1)(CO)$_4$] complexes

The [M(**L1**)(CO)$_4$] complexes were synthesized using 1.36 mmol of metal hexacarbonyl complexes [M(CO)$_6$] (0.299 g, 0.359 g, 0.478 g for M= Cr, Mo and W respectively) and 1.41 mmol of 2-(1H-Imidazol-2-yl) pyridine (0.204 g) refluxed in either 50 mL of dry toluene (for M= Cr, Mo) or 80 mL of xylene (for M= W) for 2 h under argon. Upon filtration, a greenish-yellow precipitate was collected and rinsed with diethyl ether (Yield ~30%).

[Cr(L1)(CO)$_4$]:

^{1}H NMR (400 MHz, DMSO) δ 8.96 (d, 1H), 8.07 (s, 2H), 7.65 (s, 1H), 7.46 (s, 1H), 7.34 (s, 1H). **FT-IR** (ν(CO)): 2004, 1908, 1851, 1767 cm^{-1}.

ESI-MS: *m/z* [M+NO$_3$]$^-$ = 370.97 (calculated for $C_{12}H_7CrN_3O_4NO_3$: 309.12).

[Mo(L1)(CO)$_4$]:

^{1}H NMR (400 MHz, CD$_3$CN) δ 8.96 (d, 1H), 8.03 (td, 1H), 7.93 (d, 1H), 7.45 – 7.37 (m, 2H), 7.31 (d, 1H). **FT-IR** (ν(CO)): 2010, 1912, 1851, 1762 cm^{-1}.

ESI-MS: *m/z* [M+H]$^-$ =353.94 (calculated for $C_{12}H_7MoN_3O_4$: 353.11).

[W(L1)(CO)$_4$]:

^{1}H NMR (400 MHz, CD$_3$CN) δ 9.07 (d, 1H), 8.11-8.01 (m, 1H), 7.95 (d, 1H), 7.86-7.77 (m, 1H), 7.47-7.33 (m, 2H). **FT-IR** (ν(CO)): 2002, 1902, 1846, 1753 cm^{-1}.

ESI-MS: *m/z* [M-nH]$^-$ =439.99 (calculated for $C_{12}H_7WN_3O_4$: 441).

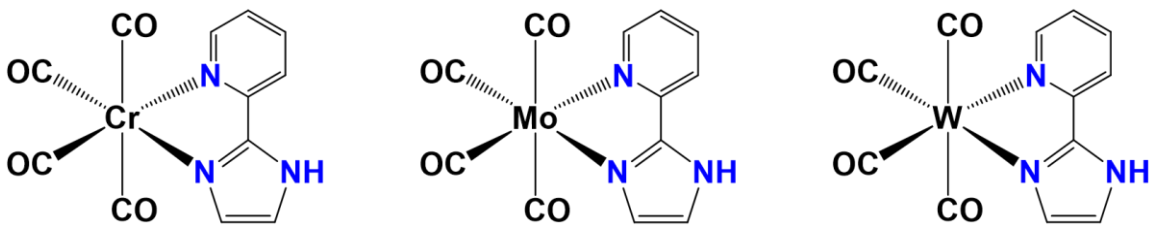

ii. Synthesis of [W(L2)(CO)$_4$] complex

1.36 mmol (0.479 g) of tungsten hexacarbonyl [W(CO)$_6$] solubilized with 1.4 mmol (0.273 g) of **L2** = 2-(pyridin-2-yl)-1H-benzo[d]imidazole in 50 mL of degassed xylene was refluxed for 2h under argon saturated conditions. Upon cooling, deep orange solid was collected through filtration and then rinsed with diethyl ether resulting in a yield of 21% (0.139 g).

^{1}H NMR (400 MHz, DMSO-d6) δ 9.15 (d, J = 5.5 Hz, 1H), 8.45 (d, J = 7.9 Hz, 1H), 8.30 (d, J = 6.8 Hz, 1H), 8.02 (t, J = 7.8 Hz, 1H), 7.88 (dt, J = 7.8, 3.2 Hz, 1H), 7.82 – 7.75 (m, 1H), 7.73 – 7.59 (m, 2H). **FT-IR** (ν(CO)): 2007, 1870, 1845, 1765 cm^{-1}.

ESI-MS: *m/z* [M-nH]$^-$ = 490 (calculated for $C_{12}H_9N_3WC_4O_4$: 491).

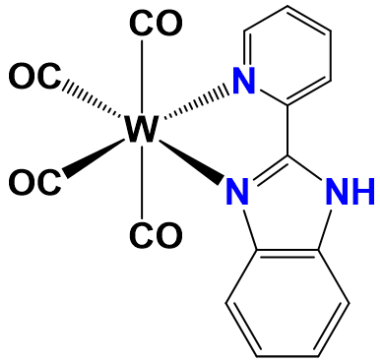

iii. Synthesis of [W(L3)(CO)$_4$] complex

This complex was synthesized using 0.679 mmol (0.239 g) of tungsten hexacarbonyl [W(CO)$_6$] reacted with 0.7 mmol of **L3** = 1-methyl-2-(pyridin-2-yl)-1H-benzo[d]imidazole) solubilized and refluxed for 2h in 50 mL of degassed xylene. On cooling, filtration of this copper-red solution rendered copper-red solid which was then rinsed and dried with diethyl ether. Yield: 85% (0.293 g).

^{1}H NMR (400 MHz, DMSO-d6) δ 9.25 (dd, J = 5.5, 1.3 Hz, 1H), 8.62 (d, J = 8.3 Hz, 1H), 8.29 (ddd, J = 8.0, 6.8, 1.6 Hz, 1H), 8.00 – 7.89 (m, 2H), 7.77 – 7.64 (m, 1H), 7.63 – 7.50 (m, 2H), 4.35 (s, 3H). **FT-IR** (ν(CO)): 1994, 1894, 1834, 1794cm^{-1}.

ESI-MS: *m/z* [M+NO$_3$]$^-$ =567 (calculated for $C_{13}H_{11}N_3WC_4O_4$: 505).

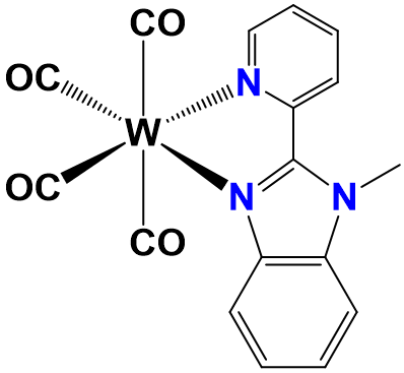

2.3. Chapter IV complexes

i. Synthesis of quaterpyridine ligand

This 4',4''-diphenyl-2,2':6',2'':6'',2'''-quaterpyridine ligand (qpy) was synthesized in two consecutive steps.

Step I: the first step involved a preparation of the 1,6-Diphenylhexa-1,5-diene-3,4-dione ligand done in a 100-mL flask with magnetic stirring within which 141 mmol (15 g) of benzaldehyde and 47 mmol (4.01 g) of diacetyl were mixed in 20mL of methanol. To this solution, 5 mmol of piperidine and 5 mmol of acetic acid were added. The overall mixture was stirred at 65°C overnight, then left to cool at RT without stirring for 24h. Orange crystals precipitated out of the dark reaction mixture resulting in a yield of 4% (0.459 g).

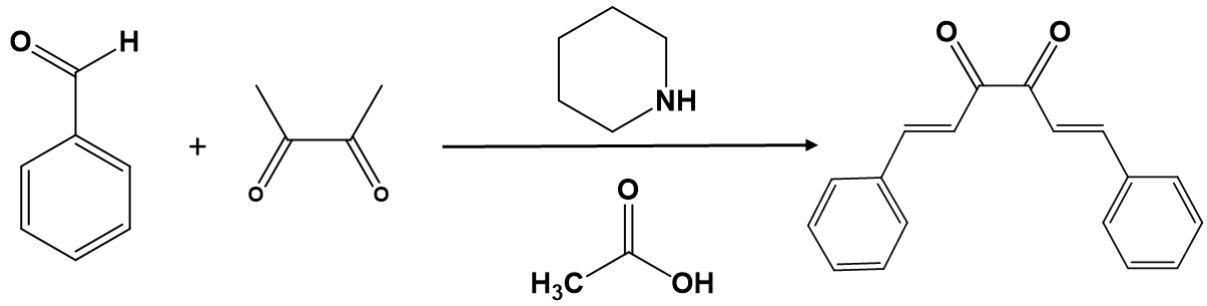

Step II: Consequent to former step, 1.75 mmol of the crude dione from step one along with 4.2 mmol (1.37 g) of Krohnke's reagent and 2.06 mmol (1.08 g) of ammonium acetate were mixed and dissolved in 20mL of ethanol and then refluxed for 6h. Upon RT cooling for 18h, gray precipitates were collected by filtration and rinsed with ethanol. Yield: 65% (526.1mg)

^{1}H NMR (500 MHz, CDCl3) δ 8.94 (d, J = 1.3 Hz, 2H), 8.77 (d, J = 1.3 Hz, 2H), 8.75 (d, J = 4.4 Hz, 2H), 8.71 (d, J = 7.9 Hz, 2H), 7.97 – 7.86 (m, 6H), 7.57 (t, J = 7.5 Hz, 4H), 7.50 (t, J = 7.3 Hz, 2H), 7.37 (dd, J = 6.7, 5.1 Hz, 2H).

^{13}C NMR (126 MHz, CDCl3) δ 156.37(q), 156.25(q), 156.05(q), 150.53(q), 149.26, 139.04(q), 137.13, 129.16, 129.14, 127.56, 124.01, 121.63, 119.48, 119.35, 77.16.3

^{15}N NMR (50 MHz, CDCl3, GHMQC experiment) δ 293 (4,4'-N), 305.

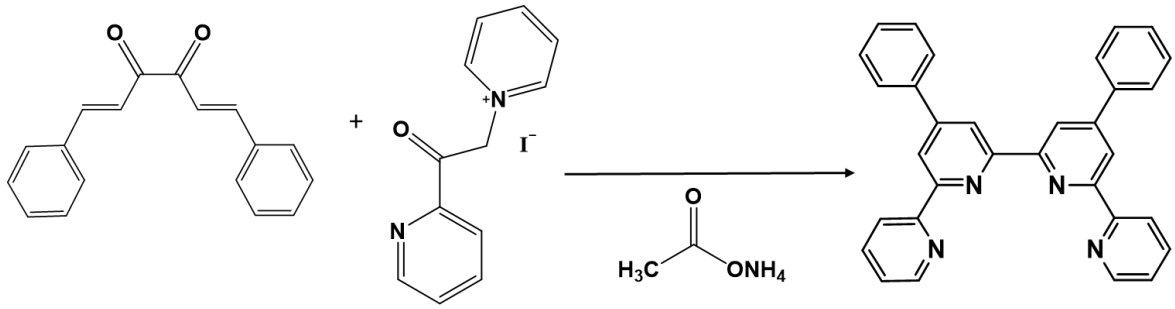

ii. Synthesis of [Cr(qpy)(Cl)$_2$]Cl.4H$_2$O

0.1 mmol (0.027 g) of hydrated chromium (III) chloride salt $CrCl_3.6H_2O$ was mixed with 0.2 mmol (0.046 g) of 4',4''-diphenyl-2,2':6',2'':6'',2'''-quaterpyridine ligand in 15mL of ethanol, this solution was refluxed for 30h. After cooling, this solution was filtered resulting in a greenish-gray solid product that was then rinsed and dried using diethyl ether. Yield: 56% (38.8 mg).

FT-IR: 1603w, 1545w, 1487s, 1461w, 1407w, 1242w, 1049s, 1024w, 886s, 830s, 787s, 769w, 731w, 689w, 679s, 661s, 651w, 640w, 633s cm^{-1}.

ESI-MS: *m/z* $[M]^+$ =584 (calculated for $C_{13}H_{11}N_3WC_4O_4$: 584).

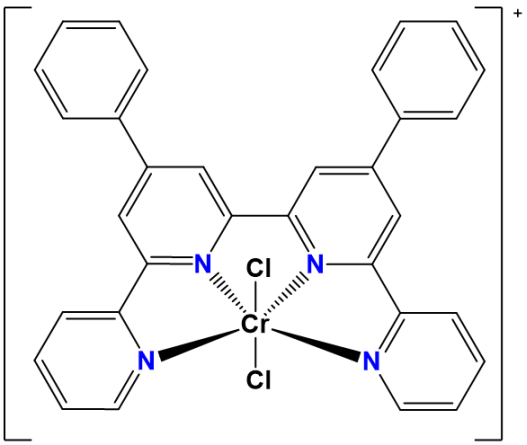

iii. Synthesis of [Cu(bph)(POP)]$^+$

This Cu(I) complex used as a photosensitizer was synthesized in the glove box following the two steps details below;

Step I: 0.3 mmol (0.1123 g) of tetrakis(acetonitrile)copper(I) hexafluorophosphate $[Cu^{I}(CH_3CN)_4](PF_6)$ was reacted with 0.3 mmol (0.1628 g) of bis-[2-diphenylphosphinophenyl]ether, dppe (POP) in 20 mL of dichloromethane solution at RT for 2h.

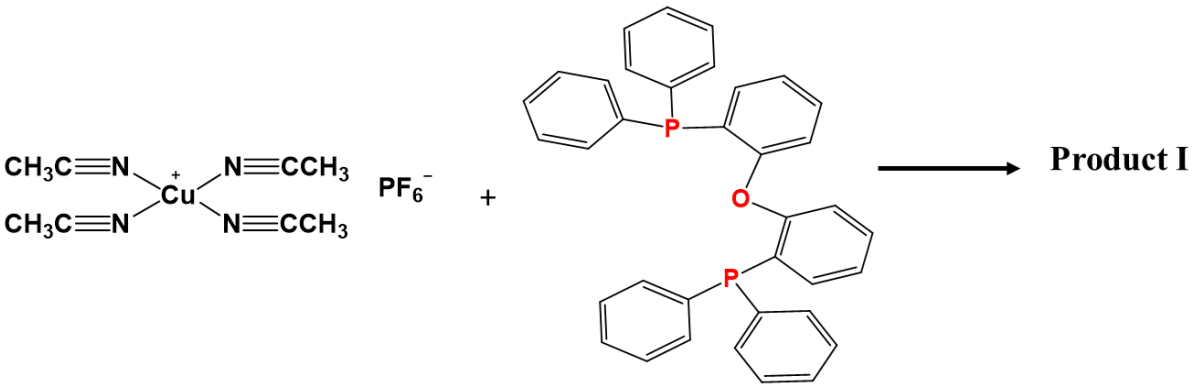

Step II: 0.3 mmol (0.1093 g) of bathocuproine (bph) solubilized in 5mL of dichloromethane was added into the reaction mixture of **step I** (i.e. **product I**) after two hours of the **step I** reaction. The addition of bph resulted into a yellow reaction mixture that was left stirring overnight at room temperature. Afterwards, the final reaction solution was filtered and the collected filtrate was evaporated under vacuum resulting in a bright orange powder that was rinsed with diethyl ether. Yield: 80% (266 mg).

ESI-MS: *m/z* $[M]^+$ = 961.25 (calculated for $C_{62}H_{48}CuN_2OP_2$: 961.25).

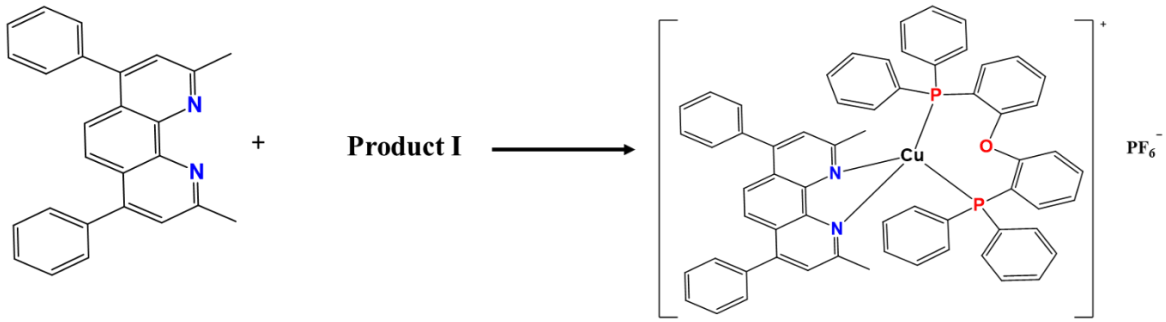

iv. Synthesis of the silatrane modified quaterpyridine ligand

To achieve the synthesis of the 4,4'-([2,2':6',2":6",2"'-quaterpyridine]-4',4"-diyl)bis(N-(3-(2,8,9-trioxa-5-aza-1-silabicyclo[3.3.3]undecan-1-yl)propyl)benzamide), two major chemical ingredients were to be synthesized. The preparation of the first ingredient which is the 1-(3-aminopropyl)silatrane is described in detail in **part a**; whereas the synthesis of the potassium

4,4'-([2,2':6',2":6",2"'-quaterpyridine]-4',4"-diyl)dibenzoate as the second ingredient is detailed in **part b**. The complete synthesis of this silatrane modified quaterpyridine ligand will be concluded in **part c**.

- **Part a: synthesis of 1-(3-aminopropyl)silatrane**

44.6 mmol of 3-aminopropyltrimethoxysilane (8g, 7.8 mL) and 44.6 mmol of triethanolamine (6.8 g, 5.9 mL) were added to 100 mL of toluene in a 250 mL flask equipped with a Dean Stark apparatus. KOH (77 mg) was added and the mixture was vigorously refluxed at 125°C under argon saturated conditions for 3h (at this point no more CH_3OH/water was collected in the Dean Stark apparatus).

Afterwards, this mixture was cooled down to RT and then toluene was evaporated. The collected crude oil was then triturated in hexanes (150 mL) several times until a formation of white precipitates was detected. By filtration this white solid was collected and washed with hexanes (200 mL), and dried under vacuum to yield ~ 5.2 g of the desired product as a white solid.

^{1}H NMR (400 MHz, Chloroform-d) δ 3.75 (t, J = 5.8 Hz, 8H), 3.64 (dt, J = 14.4, 5.0 Hz, 1H), 2.79 (t, J = 5.8 Hz, 8H), 2.61 (d, J = 7.0 Hz, 3H), 1.51 (dtd, J = 12.0, 8.4, 7.7, 6.1 Hz, 3H), 0.45 – 0.36 (m, 3H).

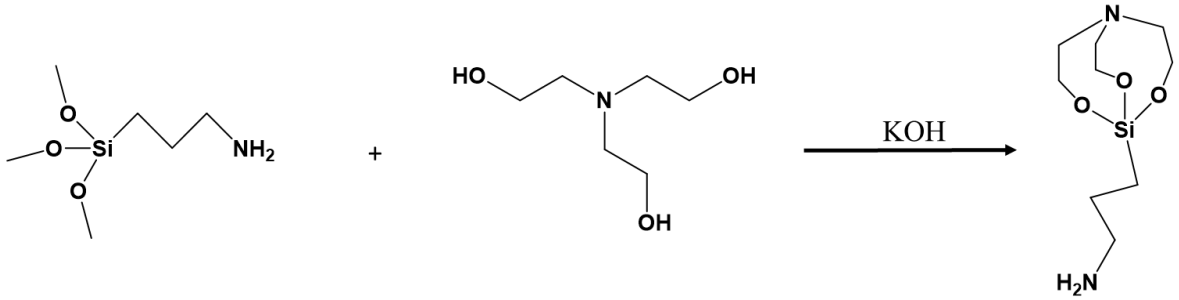

- **Part b: synthesis of potassium 4,4'-([2,2':6',2'':6'',2'''-quaterpyridine]-4',4''-diyl)dibenzoate**

As means of introducing the silatrane anchoring group to this tetradentate ligand, it was decided to first develop a quaterpyridine ligand with ester groups on the furthest phenyl rings of this given ligand. These ester substituent groups were expected to facilitate a linkage between the quaterpyridine ligand and the silatrane anchoring group.

The preparation of the quaterpyridine ligand with ester substituent groups was carried out in several steps as described below;

Step I: Methyl-4-formylbenzoate (182.75 mmol, 30.035 g) was mixed with diacetyl (60.91 mmol, 0.981 g) in 20 mL of methanol. To this mixture piperidine (6.48 mmol) and glacial acetic acid (6.48 mmol) was added. This reaction mixture was stirred overnight at 65°C and then cooled at RT for 24h. Afterwards, a yellow powder was collected by filtration resulting in a yield of 17% (3.989 g).

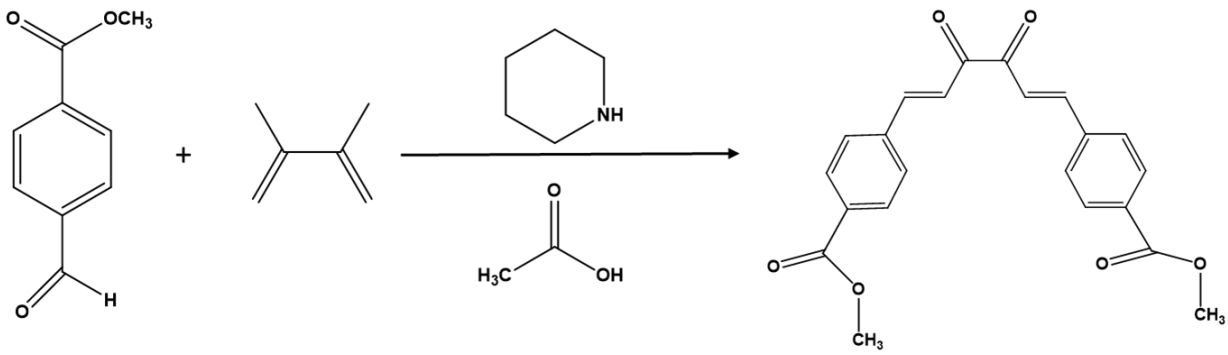

Step II: 3.705 mmol (1.409 g) of the yellow product from step I was mixed with 7.45 mmol (2.431 g) of Krohnke's reagent and 53 mmol (4.05 g) of ammonium acetate in 20mL of ethanol. This mixture was refluxed for 6h and then left to cool for 18h, leading to pale gray precipitates formation that were collected by filtration and washed by ethanol.

1H NMR (400 MHz, Chloroform-d) δ 8.98 (d, J = 1.7 Hz, 2H), 8.85 – 8.70 (m, 6H), 8.30 – 8.22 (m, 4H), 8.06 – 8.00 (m, 4H), 7.96 (td, J = 7.7, 1.8 Hz, 2H), 7.42 (ddd, J = 7.5, 4.8, 1.2 Hz, 2H), 4.01 (s, 5H), 3.75 (q, J = 7.0 Hz, 7H).

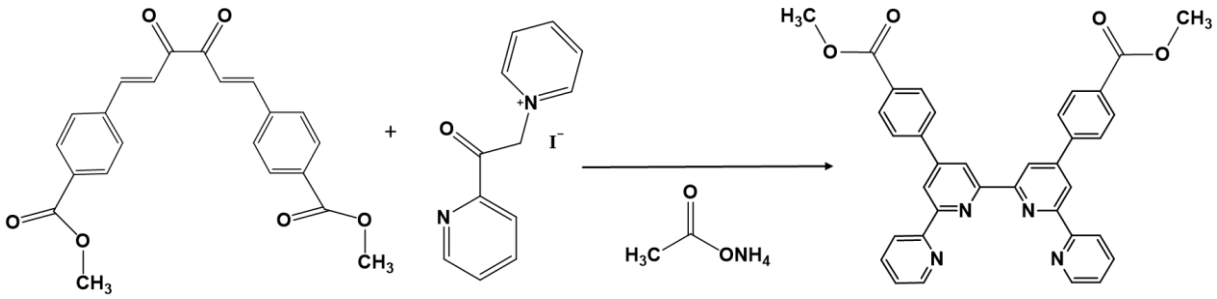

Step III: The synthesis of the potassium 4,4'-([2,2':6',2":6",2"'-quaterpyridine]-4',4"-diyl)dibenzoate ligand was finalized using a microwave reaction of the dimethyl 4,4'-([2,2':6',2":6",2"'-quaterpyridine]-4',4"-diyl)dibenzoate with KOH under argon in a 10mL microwave vial for 3hrs at 100°C.

1H NMR (400 MHz, DMSO) δ 7.57 (2H, ddd, J = 7.5, 5.5, 1.7 Hz), 7.93-8.21 (12H, 7.99 (ddd, J = 7.2, 1.5, 0.5 Hz), 8.03 (ddd, J = 8.2, 7.5, 1.9 Hz), 8.08 (ddd, J = 7.2, 2.2, 0.5 Hz), 8.14 (ddd, J = 8.2, 1.7, 0.5 Hz)), 8.56-8.67 (4H, 8.61 (d, J = 1.9 Hz), 8.62 (d, J = 1.9 Hz)), 9.02 (2H, ddd, J = 5.5, 1.9, 0.5 Hz).

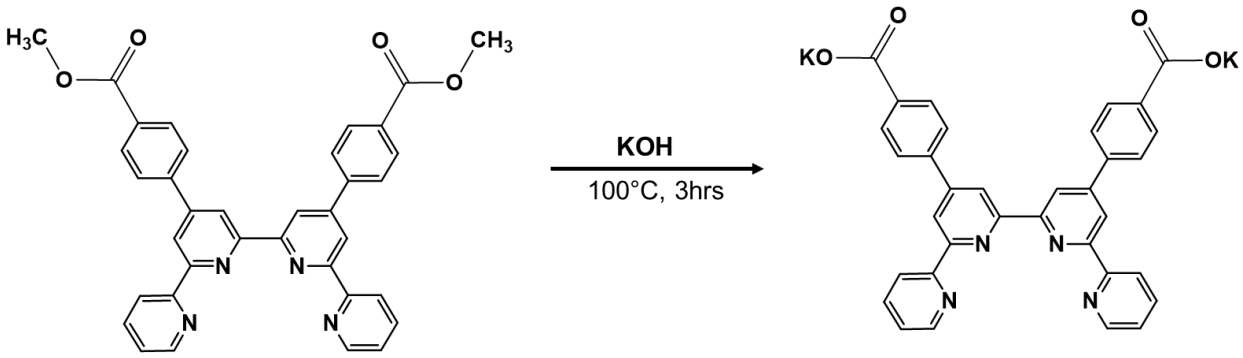

- **Part c: synthesis of 4,4'-([2,2':6',2'':6'',2'''-quaterpyridine]-4',4''-diyl)bis(N-(3-(2,8,9-trioxa-5-aza-1-silabicyclo[3.3.3]undecan-1-yl)propyl)benzamide)**

As a final step to developing modified quaterpyiridine ligand with a silatrane anchoring group, 0.2 mmol (0.128 g) of qpy-$(COO^-)_2$ was mixed with 0.48 mmol (0.183 g) of (2-(1h-benzotriazol-1-yl)-1,1,3,3-tetramethyluronium hexafluorophosphate) HBtu in 10 mL of DMF, this reaction mixture was heated. After 30-45 mins of observation, this mixture solution turned milky-white to which 0.42 mmol (0.987 g) of aminopropylsilatrane solubilized in 5mL of DMF was added and continued to be heated. After 2h of reaction, a colorless reaction solution was left to cool at RT. This solution was then mixed with diethyl ether which resulted into a formation of a white suspension which upon filtration a white powder product was collected. Yield: 74% (148.2 mg)

1H NMR (500 MHz, DMF-d7) δ 8.96 – 8.90 (m, 1H), 8.26 – 8.18 (m, 2H), 8.03 (s, 7H), 3.70 (t, J = 5.9 Hz, 3H), 3.48 (s, 24H), 3.39 – 3.27 (m, 1H), 2.93 – 2.85 (m, 5H), 2.75 (d, J = 7.8 Hz, 4H), 1.77 – 1.66 (m, 1H).

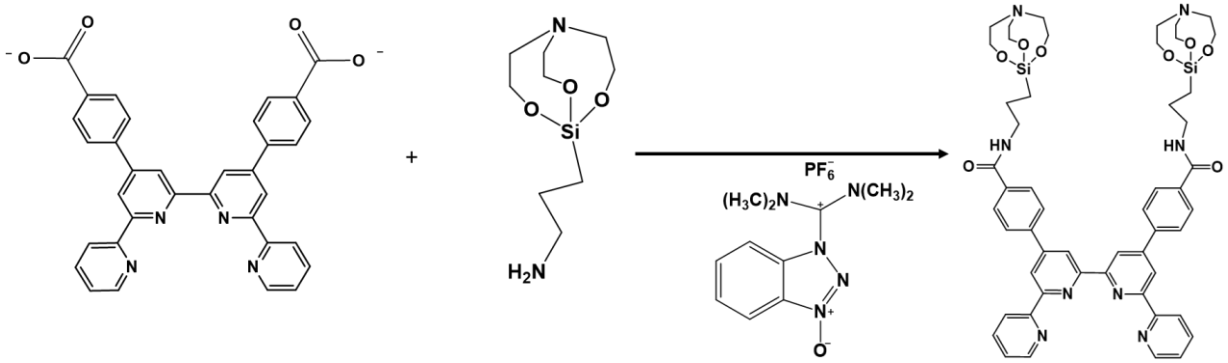

v. Synthesis of $[Cr((SiO_3N)_2\text{-}qpy)(Cl)_2]Cl.4H_2O$

0.86 mmol (0.23 g) of hydrated chromium (III) chloride salt $CrCl_3.6H_2O$ was solubilized with 0.86 mmol (0.845 g) of the modified quaterpyridine ligand $(SiO_3N)_2$-qpy in 30 mL of ethanol:DMF solvent mixture (1:1) under argon atmosphere. This reaction mixture was refluxed for 30h and then left to cool overnight. Consecutively, maximum solvent was eliminated by evaporation of the reaction mixture and then addition of diethyl ether to the remaining solvent resulted in the formation of a brown suspension. Upon filtration, a mud brown paste was collected, and rinsed with diethyl ether then dried under vacuum resulting in faded brown powder. Yield: 31% (309 mg)